Future DC Smart Homes: Key Power Electronics Development

Bandyopadhyay, S.

DOI
10.4233/uuid:26692245-3fb7-460e-8d3a-419301eef8e7

Publication date
2021

Document Version
Final published version

Citation (APA)
Bandyopadhyay, S. (2021). *Future DC Smart Homes: Key Power Electronics Development*. [Dissertation (TU Delft), Delft University of Technology]. https://doi.org/10.4233/uuid:26692245-3fb7-460e-8d3a-419301eef8e7

Important note
To cite this publication, please use the final published version (if applicable).
Please check the document version above.

Future DC Smart Homes

Key Power Electronics Development

Soumya Bandyopadhyay

Future DC Smart Homes

Key Power Electronics Development

Proefschrift

ter verkrijging van de graad van doctor aan de Technische Universiteit Delft,
op gezag van de Rector Magnificus, Prof.dr.ir. T.H.J.J. van der Hagen,
voorzitter van het College voor Promoties,
in het openbaar te verdedigen op

Woensdag 2 juni 2021 om 12:30 uur

door

Soumya BANDYOPADHYAY

Elektrotechnisch ingenieur, Technische Universiteit Delft, Nederland,
geboren te Bankura, India

Dit proefschrift is goedgekeurd door de promotoren.

Samenstelling promotiecommissie bestaat uit:

• Rector Magnificus	voorzitter
• Prof.dr.ir. P. Bauer	Technische Universiteit Delft, promotor
• Dr. Z. Qin	Technische Universiteit Delft, copromotor

Onafhankelijke leden:

• Prof.dr. M. Liserre	Universiteit van Kiel
• Dr. P.H. Nguyen	Technische Universiteit Eindhoven
• Prof.dr. P. Palensky	Technische Universiteit Delft
• Prof.ir. P.T.M. Vaessen	Technische Universiteit Delft
• Dr. T.Batista Soeiro	Technische Universiteit Delft

This project is part of the research programme P 13-21 with project number A, which is funded by the Netherlands Organisation for Scientific Research (NWO).

Printed by: Ridderprint BV

ISBN: 978-94-6384-220-4

An electronic version of this dissertation is available at http://repository.tudelft.nl

Summary

By contributing up to almost 40% of the total consumed energy, residential households and commercial buildings are major consumers, which will play an essential role in the world's upcoming energy transition. Hence, ensuring high energy-efficiency from generation to consumption is of paramount importance to achieving sustainability.

The advent of Smart grids (SGs) with renewable energy sources (RESs), electric vehicles (EVs), and energy storage offers a lot of flexibility in how the energy is used, stored, and locally produced. In addition to that, the resurgence of direct current (DC) distribution system due to: (a) advancements in power electronics, and (b) inherent DC nature of renewable energy sources, storages, modern loads, provides an interesting opportunity to reconceptualize residential distribution geared with the goal of achieving high energy efficiency. To that end, the goal of this thesis is to develop a highly efficient, safe, sustainable, economically feasible EV charging enabled future DC smart home concept suitable for smart DC grid integration. This thesis is comprised of four main elements:

Optimal smart DC home architecture

Developing robust, available, decentralized, Smart Grids (SGs) require a bottom to top modular approach. Further, the individual modules should be capable of independently performing multiple functions while using locally available information. To that end, the functional requirements of a future smart house architectur are identified so that they can act as modules or agents to form a robust, decentralized SGs. Based on those metrics, the existing state of the art alternating current (AC) household architecture is evaluated. A case for DC-based distribution is presented as it provides potentially higher energy efficiency due to the inherent DC nature of sources like photo-voltaic (PV) panels, storages like the battery, and loads like modern electronic appliances. Several existing DC system architectures and voltage levels for integrating PV, EV, storage, and loads are compared based on scalability, flexibility, availability, and robustness. After a detailed comparison, it is concluded that a smart power router-based DC system architecture that integrates PV, battery storage, the grid in a multi-port converter is the optimal architecture for future household grids.

Multi-port power electronic converter

The multi-active bridge (MAB) converter topology is selected as the smart power router capable of functions like controlling bi-directional power flow, islanding during abnormal grid conditions, providing high-level energy management, supporting the grid autonomously based on price incentives, etc. Derived from the dual-active bridge (DAB) converter family, the MAB converter not only integrates

and exchanges the energy from/to all ports, but also provides full isolation among all ports and matches the different port voltage levels. Additionally, the MAB converter realizes bidirectional power flow by adjusting the phase-shift angle between the high-frequency AC voltages generated by the inverter module at each port.
A key challenge in the design and control of the MAB converter is the inherent cross-coupling of power flows between ports due to the inter-winding magnetic coupling of the transformer. Therefore, the MAB converter behaves as a multi-input multi-output (MIMO) system with coupled power loops, which is difficult to control. Thus, they inhibit the scalability of the number of ports in MAB converters and increases the complexity of the control reduces their applicability. In this thesis, two solutions, a hardware based solution and a control based solution are presented to decouple the power flows in MAB converter. A 2 kW, 100 kHz Si-C based four port MAB converter laboratory prototype is developed and tested extensively to validate the decoupling control strategies.

EV charging integration

Electric vehicles (EV) will be an integral part of future smart homes. Therefore, efficient charging infrastructure is needed for integration of EVs in the DC house. Inductive power transfer (IPT) based charging system is a promising candidate for household EV charging applications since it is more user-friendly and safer than conventional wired charging due to absence of electrical or mechanical contacts. Hence, a wireless inductive power transfer (IPT) based EV charging station for residential applications is developed in this thesis. A multi-objective optimization (MOO) framework is developed to provide a platform to design efficient, light, and misalignment tolerant magnetic couplers for IPT based EV charging. The existing state of the art magnetic couplers like uni-polar couplers like circular, rectangular and bi-polar couplers like DD, DDQ, and BPP are quantitatively compared using the developed MOO framework, and their relative advantages and disadvantages are highlighted.

System sizing and economics of DC homes

Significant investment cost is associated with PV-battery based smart DC homes. In addition to battery and PV, the sizing of the grid-interfacing AC-DC converter connecting the nanogrid to the utility grid needs to be considered in the optimization. Since there are numerous design degrees of freedom like PV design variables, storage sizes, the converter rating and battery technologies, a fundamental question arises: What is the optimal and cost-effective PV installed power, converter rating and storage capacity mix that minimises the annual cost of electricity, maximises self-sufficiency while considering battery degradation? A multi-objective optimization-based framework is developed to draw simple PV-battery sizing guidelines considering the effect of solar potential, degree of temporal mismatch between load and PV generation, battery degradation, and tariff incentives. Economic metrics like simple payback time and net savings are considered to evaluate the economic feasibility of PV-battery powered smart DC homes. Additionally, the effect of meteorology on the optimal sizing problem is investigated by selecting two case studies in the Netherlands and the US.

Samenvatting

Door tot bijna 40 % van de totale verbruikte energie bij te dragen, zijn residentiële huishoudens en commerciële gebouwen grote verbruikers, die een essentiële rol zullen spelen in de aanstaande wereldwijde energietransitie. Daarom is het waarborgen van een hoge energie-efficiëntie van opwekking tot verbruik van het grootste belang om duurzaamheid te bereiken.

De komst van Smart grids (SG's) met hernieuwbare energiebronnen, elektrische voertuigen en energieopslag biedt veel flexibiliteit in hoe de energie wordt gebruikt, opgeslagen en lokaal geproduceerd. Daarnaast biedt de heropleving van het gelijkstroom (DC) distributiesysteem als gevolg van: (a) vooruitgang in vermogenselektronica en (b) de inherente gelijkstroom-aard van hernieuwbare energiebronnen, opslagplaatsen, moderne belastingen, een interessante gelegenheid om opnieuw te begrijpen woningdistributie gericht op het bereiken van een hoge energie-efficiëntie. Daartoe is het doel van dit proefschrift om een zeer efficiënt, veilig, duurzaam, economisch haalbaar toekomstig DC smart homeconcept te ontwikkelen dat geschikt is voor slimme DC-netintegratie. Dit proefschrift bestaat uit vier hoofdelementen:

Optimale slimme DC-huisarchitectuur

Het ontwikkelen van robuuste, beschikbare, gedecentraliseerde Smart Grids (SG's) vereist een modulaire aanpak van onder naar boven. Verder moeten de afzonderlijke modules in staat zijn om onafhankelijk meerdere functies uit te voeren terwijl ze lokaal beschikbare informatie gebruiken. Hiertoe worden de functionele vereisten van een toekomstige slimme huisarchitect geidentificeerd, zodat deze kunnen fungeren als modules of agenten om robuuste, gedecentraliseerde SGs te vormen. Op basis van die meetgegevens wordt de bestaande state-of-the-art architectuur van een huishouden geevalueerd. Er wordt een voorbeeld gegeven van op gelijkstroom gebaseerde distributie, omdat het potentieel hogere energie-efficientie biedt vanwege de inherente gelijkstroom-aard van bronnen zoals PV, opslagplaatsen zoals de batterij en belastingen zoals moderne elektronische apparaten. Verschillende bestaande DC-systeemarchitecturen en spanningsniveaus voor het integreren van PV, EV, opslag en belastingen worden vergeleken op basis van schaalbaarheid, flexibiliteit, beschikbaarheid en robuustheid. Na een gedetailleerde vergelijking wordt geconcludeerd dat een op slimme stroomrouter gebaseerde gelijkstroom-systeemarchitectuur die PV, batterijopslag en het net in een multi-port converter integreert, de optimale architectuur is voor toekomstige huishoudelijke netten.

Multi-port power elektronische converter

De topologie van de multi-actieve bridge (MAB) -convertor is geselecteerd als de slimme stroomrouter die functies kan uitvoeren zoals het regelen van de bidirectionele stroomtoevoer, eilandbewaking tijdens abnormale netomstandigheden, het verstrekken van hoogwaardig energiebeheer, het autonoom ondersteunen van het net op basis van prijsprikkels , enz. Afgeleid van de familie van de dual-active bridge (DAB) omvormers, integreert en wisselt de MAB-omvormer niet alleen de energie van / naar alle poorten, maar biedt hij ook volledige isolatie tussen alle poorten en komt hij overeen met de verschillende poortspanningsniveaus. Bovendien realiseert de MAB-omzetter een bidirectionele stroomtoevoer door de faseverschuivingshoek tussen de hoogfrequente wisselspanningen die door de invertermodule bij elke poort worden gegenereerd, aan te passen.

Een belangrijke uitdaging bij het ontwerp en de besturing van de MAB-omzetter is de inherente kruiskoppeling van stroomstromen tussen poorten als gevolg van de onderling wikkelende magnetische koppeling van de transformator. Daarom gedraagt de MAB-converter zich als een multi-input multi-output (MIMO) -systeem met gekoppelde stroomlussen, wat moeilijk te besturen is. Ze verhinderen dus de schaalbaarheid van het aantal poorten in MAB-converters en vergroten de complexiteit van de besturing en verminderen hun toepasbaarheid. In dit proefschrift worden twee oplossingen, een op hardware gebaseerde oplossing en een op controle gebaseerde oplossing, gepresenteerd om de stroomstromen in de MAB-omvormer te ontkoppelen. Een laboratoriumprototype van 2 kW, 100 kHz op Si-C gebaseerde MAB-converters met vier poorten is ontwikkeld en uitgebreid getest om de ontkoppelingsregelstrategieën te valideren.

EV-laadintegratie

Elektrische voertuigen (EV) zullen een integraal onderdeel zijn van toekomstige slimme huizen. Daarom is een efficiënte laadinfrastructuur nodig voor de integratie van EV's in het DC-huis. Op inductief vermogenoverdracht (IPT) gebaseerd laadsysteem is een veelbelovende kandidaat voor huishoudelijke EV-laadtoepassingen, aangezien het gebruiksvriendelijker en veiliger is dan conventioneel bedraad opladen vanwege de afwezigheid van elektrische of mechanische contacten. Daarom is in dit proefschrift een draadloos, op inductief vermogenoverdracht (IPT) gebaseerd EV-laadstation voor residentiële toepassingen ontwikkeld. Een multi-objectief optimalisatie (MOO) raamwerk is ontwikkeld om een platform te bieden voor het ontwerpen van efficiënte, lichte en foutieve uitlijningstolerante magnetische koppelingen voor IPT-gebaseerd EV-opladen. De bestaande state-of-the-art magnetische koppelaars zoals unipolaire koppelingen zoals ronde, rechthoekige en bipolaire koppelingen zoals DD, DDQ en BPP worden kwantitatief vergeleken met behulp van het ontwikkelde MOO-raamwerk, en hun relatieve voor- en nadelen worden benadrukt.

Systeemafmetingen en economie van DC-huizen

Aanzienlijke investeringskosten worden in verband gebracht met op PV-batterijen gebaseerde slimme gelijkstroomwoningen. Naast de batterij en PV, moet bij de optimalisatie rekening worden gehouden met de dimensionering van de wisselstroom-gelijkstroomomzetter die de nanogrid met het openbare stroomnet verbindt. Aangezien er talrijke ontwerpvrijheidsgraden zijn, zoals PV-ontwerpvariabelen, opslaggroottes, het vermogen van de omvormer en batterijtechnologieën, rijst een fundamentele vraag: wat is het optimale en kosteneffectieve geïnstalleerde PV-vermogen, het vermogen van de omvormer en de opslagcapaciteit die de jaarlijkse kosten van elektriciteit, maximale zelfvoorziening, rekening houdend met de degradatie van de batterij? Er is een op optimalisatie gebaseerd raamwerk

met meerdere doelen ontwikkeld om eenvoudige richtlijnen voor de dimensionering van PV-batterijen te trekken, rekening houdend met het effect van het zonnepotentieel, de mate van tijdelijke mismatch tussen belasting en PV-opwekking, batterijdegradatie en tariefprikkels. Economische statistieken zoals eenvoudige terugverdientijd en nettobesparingen worden overwogen om de economische haalbaarheid van door PV-batterijen aangedreven slimme gelijkstroomwoningen te evalueren. Daarnaast wordt het effect van meteorologie op het optimale dimensioneringsprobleem onderzocht door twee case studies in Nederland en de VS te selecteren.

Contents

1 Introduction

1.1 Motivation: A Brave New Grid

1.1.1 Why the grid is changing?

"*Either you die a hero, or you live long enough to see yourself become the villain*"- visionary filmmaker Christopher Nolan had a unique observation regarding the eroding effect of time on the human character in an ever-changing society. However, in reality, the statement is more universally applicable to a multitude of things ranging from political ideology, technology to even in some cases well-tested scientific theories. The latest victim of this test of time is the electricity grid.

The alternating-current (AC) based grid driven by cheap fossil fuels has been performing satisfactorily since its inception in the late 19^{th} century. However, in recent years, two fundamental aspects of the current electricity grid are subjected to increased scrutiny. First, its over-reliance on conventional energy sources has created significant environmental problems due to the emission of greenhouse gases.

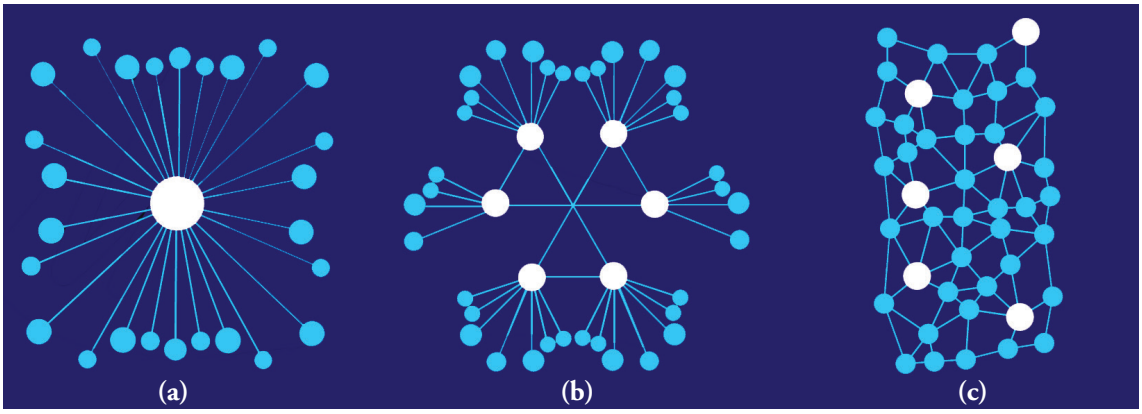

Figure 1.1: Overview of complex networks: (a) centralized: where all the nodes are connected under a single entity, (b) decentralized: all the nodes have individual autonomy , and (c) distributed: every node is independent and inter-connected with each other.

Second, the structural limitations of the hyper-centralized grid are exposed by the considerable stress caused by an ever-growing demand for electrical energy due to rapid development and industrialization.

As a response to the polluting fossil fuel-based generation, a new sustainable energy supply chain is emerging due to increasing penetration of renewable energy sources (RES) like solar and wind, coupled with recent developments in energy storage technologies like the battery, supercapacitor, and fuel cells. However, sustainability is not only about efficiency and wise use of resources, but it is also about the fundamental structure of that system.

1.1.2 Advent of smart grid

The primary function of the grid is to provide energy to where it is demanded most efficiently and reliably. Each source and loads constitute a node in a multi-agent-based complex network. There are three ways of realizing a complex system: (a) centralized, (b) decentralized, (c) distributed as shown in Figure 1.1. The current grid structure is a highly centralized complex network. Hence, it is inherently more vulnerable to fluctuations, less adaptable to changing conditions, and requires large capital investment in both the system itself and its supporting infrastructure. On the other hand, decentralized or distributed systems tend to be more flexible, able to adapt to local conditions, and can take advantage of mass production and modularity to be cheap and accessible. To that end, a new field of research into "Smart grids" (SG) is created to envision a renewable energy-driven efficient, resilient, and reliable decentralized grid for the future. "Smart grid" focuses on the integration of highly decentralized distributed sources, loads and storage systems. As an example, Figure 1.2 shows the evolution of the electricity grid of Denmark from 1985 to 2015. The rapid change of the fundamental structure of the grid from a centralized network to a decentralized network is evident.

The main flexibility of smart grids comes from its modular bottom-to-top approach towards designing grids. The main building blocks of SGs is known as "Microgrids". The idea of a microgrid is based on an aggregation of micro sources, loads and storage systems which collectively results in a unique entity which is interpreted as a single dispatch-able prosumer [2]. To incorporate further modularity, the concept of nanogrid as building blocks for individual microgrids has also been proposed [3]. A cluster of autonomous nanogrids result in an autonomous microgrid. Building on the next layer, a cluster of autonomous microgrids leads to a reliable, available and fault-tolerant smart grid as shown in Figure 1.3.

1.1.3 Role of households in smart grid: challenges and opportunities

Similar to the main grid, the residential grid is going through a radical transition of its own. The future households face several challenges as highlighted in the following:

1. **Rising energy demand:** By contributing up to almost 30% of the total consumed energy (see Figure 1.4a), residential households will play a crucial role in the upcoming energy transition in Europe. The overall energy consumption in the residential sector is expected to increase further, as shown in Figure 1.4b. Hence, ensuring energy-efficiency from source to consumption is of paramount importance towards sustainability.

2. **Electrification of heating:** According to Figure 1.4b, a significant amount of energy consumption in the residential sector is in the space and water heating which is currently supplied by fossil-fuelled heat generation technologies. The EU strategic long-term vision is to electrify the heating by replacing fossil fuels with heat pumps which would further increase the electricity demand by up to 26% [4, 5] in 2050.

3. **Integration of EVs:** Future households have to integrate charging of electric-vehicles (EVs). The high power requirement of EVs coupled with its inherent stochastic nature will put significant stress on the residential grids.

4. **Interface with weak grids:** Due to high penetration of RESs interfaced with power electronic converters, smart grids are expected to be weaker than conventional grids due to the lack of energy storage. Thus, for stable and robust operation of the grid, future nanogrids will have to provide additional functionalities like fast control, grid-support via demand response, and islanding capability.

The above challenges make the interaction of the buildings/households with the microgrid as a design bottleneck of the new energy transition. However, there are several reasons to be optimistic. Recent scientific and technological advancements have given grid engineers the required tools to tackle the challenges adequately. Some of them are highlighted in the following:

- **Development in solar power technology:** The cost of solar photo-voltaics (PV) in the residential

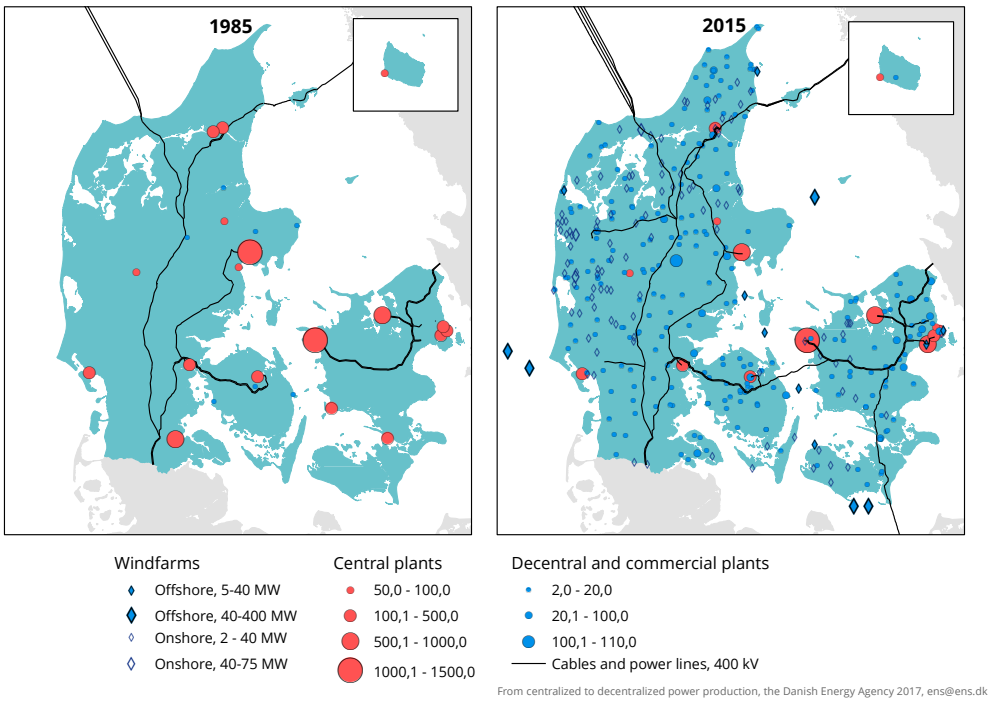

Figure 1.2: Evolution of the electricity grid of Denmark from a centralized network to de-centralized network [1].

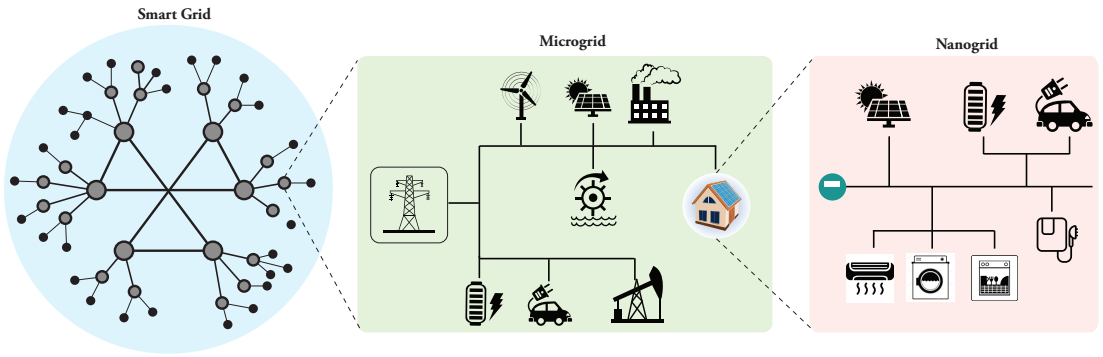

Figure 1.3: Modular building blocks of future decentralized Smart grids composed of multiple inter-connected microgrids which consist of mutiple nanogrids.

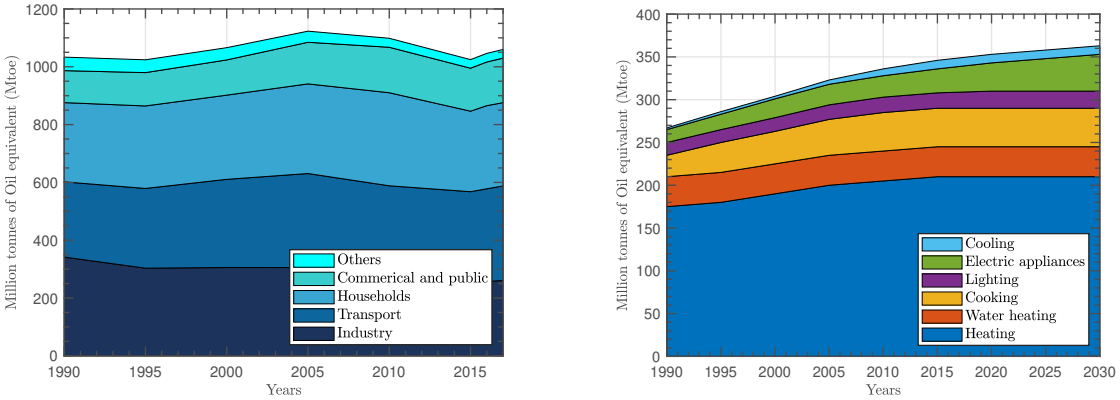

(a) (b)

Figure 1.4: Overall energy consumption data in Europe: (a) contribution of individual sectors from 1990 to 2017, (b) combined historical data and forecasted data of energy consumption by use in the residential sector from 1990 to 2030. [Source: Eurostat]

sector is consistently falling over the past decade and is expected to go from 1350 €/kWp in 2016 [6] to as low as 300 €/kWp in 2050 [7]. Therefore, the low Levelized cost of electricity (LCOE) for rooftop PV systems will incentivise residential users to produce and consume the energy locally leading to higher grid-independence and lower transmission losses.

- **Advancements in storage technology:** The advancements in energy storage technology in the last two decades, combined with an exponential reduction in production costs in the previous ten years have provided the right conditions for the deployment of mature battery storage technologies. Based on conservative estimates, the latest Tesla Powerwall system based on Li-ion costs just under 600 €/kWh. Forecasts suggest that will reduce even further to 100 €/kWh in 2050 [8]. Additionally, innovation in new battery technologies like the solid-state battery, lithium-sulphur (Li-S), and vanadium redox flow batteries is expected to improve further the lifetime, round-trip efficiency, and safety [9–11].

- **Towards a direct current (DC) grid:** Most renewable distributed generators for residential systems like solar photovoltaics (PV), fuel cells (FCs) are inherently DC. Additionally, energy storage systems (ESS) as batteries and even the modern AC based electronic appliances like refrigerators, dishwashers are all intrinsically DC in nature. Thus, a DC-based distribution architecture is a natural interface between mostly DC-based devices which leads to significant power conversion stages reduction, hence achieving considerable loss reduction, in addition to simplicity and potential cost reduction in power conversion units [12].

- **Emerging technology integration:** Emerging technology like Internet of Things (IoT) [13] provides exciting opportunities for conceptualizing safe, efficient, and smart future residential households. Additionally, with the commercialization of wide-bandgap (WBG) semiconductor devices inductive wireless Power transfer (WPT) has become feasible for a range of residential applications from low power [14] to high power [15].

Therefore, rooftop PV panels, coupled with battery storage on a DC architecture, can genuinely make future households sustainable, self-sufficient or grid-independent, and energy-efficient. Further, future homes will also have emerging technologies like wireless EV charging capable of vehicle-to-home (V2H) and vehicle-to-grid (V2G) depending on demand response. In summary, the motivation of this thesis is to envision the future house nanogrid, which plays an integral role in the formation of a stable, reliable and efficient smart grid.

1.2 Research objective

The main objective of this doctoral thesis is as follows:

"To develop a highly efficient, safe, sustainable, economically feasible EV charging enabled future DC smart home concept suitable for smart DC grid integration"

The main goal of this thesis can be divided into two sequential steps. First, to conceptualize the house of the future powered by rooftop PV coupled with battery-based energy storage in DC distribution and able to integrate high power stochastic EV load. Second, to develop the required hardware and control to realize the concept in its full potential. To that end, four key research questions are essential to answer:

1. What is the optimal architecture for integrating PV, EV, battery, and loads to realize future smart grid-connected residential households?

2. How to design and construct key power electronic converter technology to realize a robust, safe, scalable, and reliable household nanogrid?

3. How to integrate EV charging in future homes while ensuring user safety and high efficiency?

4. What is the techno-economic feasibility of PV-battery integrated smart household nanogrids?

1.3 Research questions and thesis outline

The four main research components identified above are organized into five chapters. Figure 1.5 shows the thesis outline along with the chapters. The corresponding research questions answered in each chapter of the thesis are presented below:

Chapter 2: Optimal architecture for Smart DC homes

- *What additional functions are required of a future residential nanogrid?*
- *What are the advantages and drawbacks of the existing AC architecture for residential grids?*
- *What is the optimal architecture for integrating PV, storage, and EV in future residential grids?*

This chapter reviews the current AC-based architecture of residential grids and identifies the technological gap that hinders integration into smart-grids. A case for DC distribution for future residential grids is presented based on qualitative comparison. Several existing DC system architectures for integrating PV, EV, storage and loads are compared based on scalability, flexibility, availability, and robustness. Based on the analysis, a smart power router-based DC system architecture which integrates PV, battery storage, grid in a multi-port converter is selected for future household grids.

Chapter 3: Smart power router for DC Homes

- *How the functional requirements of future residential grids influence the power router design?*
- *Which multi-port power converter topology is suitable to function as a smart power router?*
- *What are the design or control challenges associated with the multi-port converter topology?*

A smart power-router based future DC house concept is introduced in chapter 2. Chapter 3 investigates the optimal multi-port converter topology to satisfy the functionalities of the intelligent power router. The multi-active bridge (MAB) converter is selected as the topology for the smart power-router. MAB converter is challenging to design and control as it is a highly coupled multi-input multi-output (MIMO) system. To that end, two solutions are presented to decouple the intra-port power flows of the MAB converter. One approach decouples the power flows using hardware design, and the other approach solves it in the control domain. A 5 kW four-port MAB converter laboratory prototype is developed and extensively tested to validate the theoretical claims.

Chapter 4: Wireless EV charging integration

- *What are the advantages of inductive wireless charging for EV integration in future homes?*
- *How to design highly efficient, high power density and misalignment tolerant static inductive power transfer (IPT) systems?*

- *What are the advantages and drawbacks of different magnetic coupler topologies for IPT based residential EV charging?*

Chapter 4 develops an efficient charging infrastructure based on wireless inductive power transfer (IPT) for integration of EVs in the DC house. IPT technology is more user-friendly and safer than conventional wired charging due to absence of electrical or mechanical contacts. With the aim of building a professional prototype, efficiency, volume, weight and misalignment performance are considered in a multi-objective optimization based IPT system design framework.

Chapter 5: Optimal system sizing & economics of DC smart homes

- *How to build a comprehensive optimization framework for PV, battery and converter system sizing which incorporates multiple objectives?*
- *How to derive simple sizing rules based on load profile, PV profile, and specific storage technology?*
- *What is the return-on-investment (ROI) on a PV, storage integrated household in terms of savings in cost of electricity?*

This chapter examines the optimal system design of the PV system, local energy storage, and grid converter in residential grids. A multi-objective optimization framework is developed to incorporate the design complexity arising from multiple design variables and mutually conflicting design objectives. Using the optimization framework, the effect of meteorological conditions, electricity tariffs, choice of battery storage technology, and temporal mismatch between load and PV profile on optimal system sizing is investigated. Lifetime system cost and savings on electricity costs are also considered in the optimal system sizing problem.

Chapter 6: Conclusions & future Work

Chapter 6 summarizes the key outcomes obtained from the thesis corresponding to the main research questions formulated in chapter 1. Additionallty, recommendations regarding future research directions are provided.

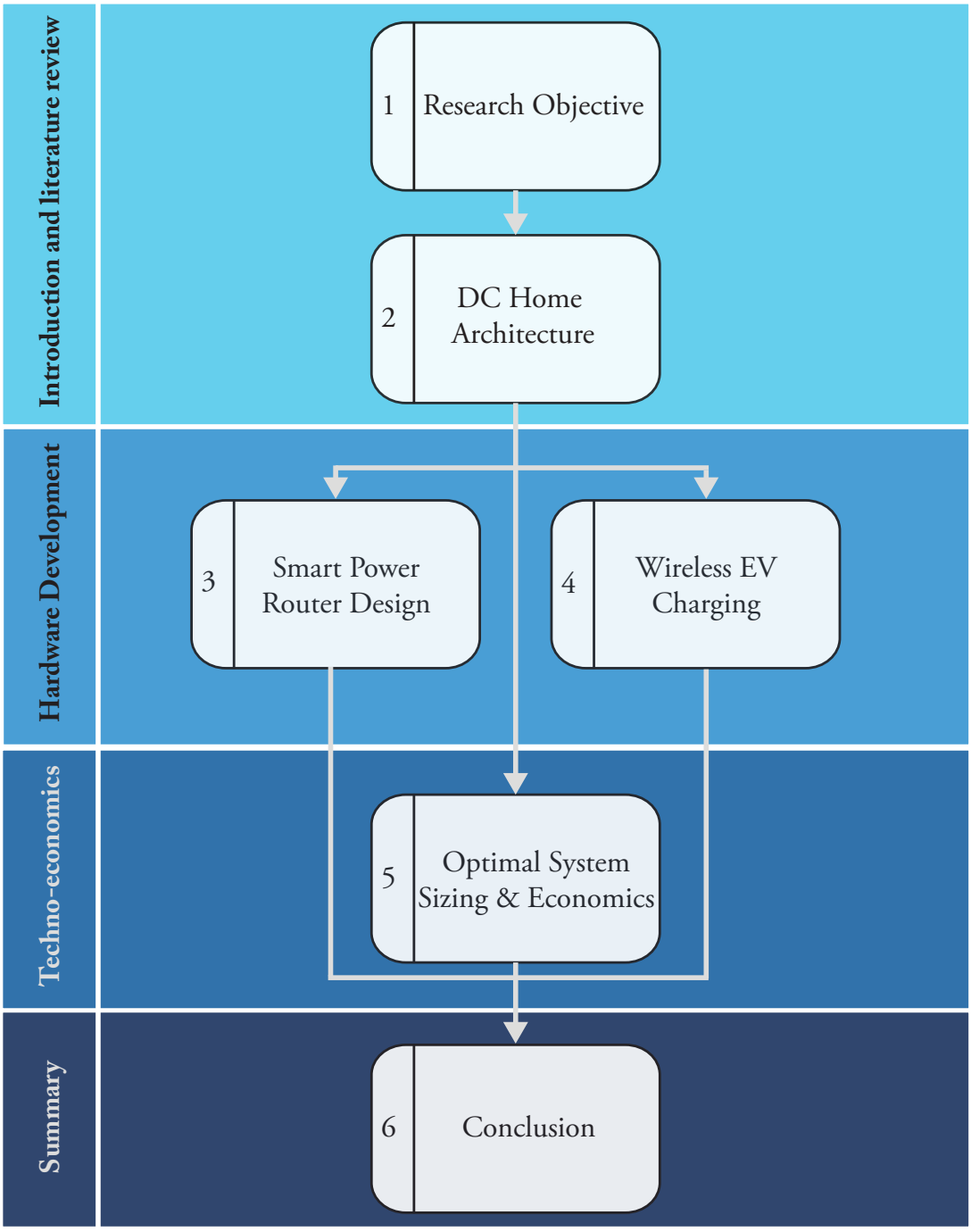

Figure 1.5: Outline and flow of thesis.

1.4 Research contributions

The list of relevant publications to the thesis and the corresponding chapters are presented in the following:

Journal publications:

1. S. Bandyopadhyay, P. Purgat, Z. Qin, and P. Bauer, "A Multi-Active Bridge Converter with Inherently Decoupled Power Flows," in IEEE Transactions on Power Electronics, vol. 36, no. 2, pp. 2231-2245, Feb. 2021 (Chapter 3)
2. S. Bandyopadhyay, Z. Qin, and P. Bauer, "Decoupling control of Multi-Active Bridge Converter using Active Disturbance Rejection," in IEEE Transactions on Industrial Electronics (Chapter 3)
3. S. Bandyopadhyay, P. Venugopal, J. Dong and P. Bauer, "Comparison of Magnetic Couplers for IPT-Based EV Charging Using Multi-Objective Optimization," in IEEE Transactions on Vehicular Technology, vol. 68, no. 6, pp. 5416-5429, June 2019 (Chapter 4)
4. S. Bandyopadhyay, G. R. C. Mouli, Z. Qin, L. R. Elizondo and P. Bauer, "Techno-Economical Model Based Optimal Sizing of PV-Battery Systems for Microgrids," in IEEE Transactions on Sustainable Energy, vol. 11, no. 3, pp. 1657-1668, July 2020 (Chapter 5)

Conference publications:

1. S. Bandyopadhyay, V. Prasanth, P. Bauer and J. A. Ferreira, "Multi-objective optimisation of a 1-kW wireless IPT systems for charging of electric vehicles," IEEE Transportation Electrification Conference and Expo (ITEC), Dearborn, MI, 2016, pp. 1-7 (Chapter 4)
2. S. Bandyopadhyay, V. Prasanth, L. R. Elizondo and P. Bauer, "Design considerations for a misalignment tolerant wireless inductive power system for electric vehicle (EV) charging," 2017 19th European Conference on Power Electronics and Applications (EPE'17 ECCE Europe), Warsaw, 2017, pp. 1-10 (Chapter 4)
3. S. Bandyopadhyay, J. Dong, L. Ramirez-Elizondo and P. Bauer, "Determining Relation Between Size of Polarized Inductive Couplers and Nominal Airgap," IEEE 18th International Power Electronics and Motion Control Conference (PEMC), Budapest, 2018, pp. 248-255 (Chapter 4)
4. S. Bandyopadhyay, Z. Qin, L.R. Elizondo, and P. Bauer, "Comparison of Battery Technologies for DC Microgrids with Integrated PV," 2019, International Conference on DC Microgrids (ICDCM), Matsue, Japan, 2019, pp. 1-9 (Chapter 5)

References

[1] D. E. Agency, "Overview map of the danish power infrastructure in 1985 and 2015," 2017.

[2] T. Dragičević, X. Lu, J. C. Vasquez, and J. M. Guerrero, "DC Microgrids - Part II: A Review of Power Architectures, Applications, and Standardization Issues," 2016.

[3] B. Nordman and K. Christensen, "Local power distribution with nanogrids," *2013 Int. Green Comput. Conf. Proc.*, pp. 1–8, 2013.

[4] D. Connolly, H. Lund, B. V. Mathiesen, S. Werner, B. Möller, U. Persson, T. Boermans, D. Trier, P. A. Østergaard, and S. Nielsen, "Heat roadmap europe: Combining district heating with heat savings to decarbonise the eu energy system," *Energy policy*, vol. 65, pp. 475–489, 2014.

[5] T. G. Kavvadias K., Jiménez-Navarro J.P., "Decarbonising the eu heating sector," *JRC Technical Reports*, 2019.

[6] C. N. Truong, M. Naumann, R. C. Karl, M. Müller, A. Jossen, and H. C. Hesse, "Economics of residential photovoltaic battery systems in germany: The case of tesla's powerwall," *Batteries*, vol. 2, no. 2, p. 14, 2016.

[7] I. Fraunhofer and A. Energiewende, "Current and future cost of photovoltaics. long-term scenarios for market development, system prices and lcoe of utility-scale pv systems," *Agora Energiewende*, vol. 82, 2015.

[8] W. J. Cole and A. Frazier, "Cost projections for utility-scale battery storage," tech. rep., National Renewable Energy Lab.(NREL), Golden, CO (United States), 2019.

[9] N. Nitta, F. Wu, J. T. Lee, and G. Yushin, "Li-ion battery materials: present and future," *Materials today*, vol. 18, no. 5, pp. 252–264, 2015.

[10] M. Guarnieri, P. Mattavelli, G. Petrone, and G. Spagnuolo, "Vanadium redox flow batteries: Potentials and challenges of an emerging storage technology," *IEEE Industrial Electronics Magazine*, vol. 10, no. 4, pp. 20–31, 2016.

[11] Y.-S. Su and A. Manthiram, "Lithium–sulphur batteries with a microporous carbon paper as a bifunctional interlayer," *Nature communications*, vol. 3, no. 1, pp. 1–6, 2012.

[12] L. Mackay, N. H. v. d. Blij, L. Ramirez-Elizondo, and P. Bauer, "Toward the universal dc distribution system," *Electric Power Components and Systems*, vol. 45, no. 10, pp. 1032–1042, 2017.

[13] M. R. Alam, M. B. I. Reaz, and M. A. M. Ali, "A review of smart homes—past, present, and future," *IEEE transactions on systems, man, and cybernetics, part C (applications and reviews)*, vol. 42, no. 6, pp. 1190–1203, 2012.

[14] A. Momeneh, M. Castilla, M. Moradi Ghahderijani, J. Miret, and L. García de Vicuña, "Analysis, design and implementation of a residential inductive contactless energy transfer system with multiple mobile clamps," *IET Power Electronics*, vol. 10, no. 8, pp. 875–883, 2017.

[15] R. W. Carlson and B. Normann, "Test results of the plugless™ inductive charging system from evatran group, inc.," *SAE International Journal of Alternative Powertrains*, vol. 3, no. 1, pp. 64–71, 2014.

2 Optimal Architecture for Smart DC Homes

Developing robust, available, decentralized, modular smart Grids (SGs) require modules capable of independently performing multiple functions and using locally available information. To that end, this chapter analyses the suitability of the current AC-based architecture of residential grids as potential building blocks of smart-grids. A case for DC distribution as a better candidate for residential grids is presented based on the qualitative comparison. Several existing DC system architectures for integrating PV, EV, storage, and loads are compared based on scalability, flexibility, availability, and robustness. Based on the analysis, a smart power router-based DC system architecture that integrates PV, battery storage, grid in a multi-port converter is selected for future household grids.

2.1 Introduction

Chapter 1 presents the motivation for developing decentralized smart grids (SGs) with a flexible structure consisting of modules known as microgrids (MGs) and nanogrids (NGs). The individual microgrid or nanogrid modules are defined as groups of energy resources, both renewable and conventional, and loads located and interconnected to appear as a single entity to the overhead electric grid. The use of distributed resources to power local loads combined with the capability to operate independently of the overhead grid makes MGs/NGs a technically feasible option to address the concerns of sustainability, resilience, and energy efficiency.

The current centralized grid is comprised of distributed elements consuming energy downstream. The individual components in this complex grid network are incredibly passive, which results in a complex system consisting of simple elements. Therefore, for the overall system stability, the functions are performed in centralized control stations. The stability of the overall grid centralized grid structure is aided by the large system inertia, which is due to the stored energy in the mechanical rotating generators. As presented in the previous chapter, the future smart grid plans to deviate from the hyper-centralized fossil fuel-based grids into a decentralized grid with distributed renewable energy sources (RESs). Unlike conventional power plants, a renewable energy power plant doesn't offer the same inertia, which makes control and stability of the grid challenging. Therefore, for stable operation of a decentralized smart grid, it requires the modules or elements forming the complex grid to be actively participating in the process. To that end, this chapter focuses on developing a concept for the future residential household acting as an active nanogrid contributing towards a stable decentralized smart grid.

The future household will be powered locally by rooftop solar panels to improve energy independence and reduce the burden on the overhead grid. Further, it will consist of energy storage as an active element responsible for balancing generation with the load increasing power independence. When connected to the overhead grid, a residential nanogrid will appear as a controlled module within the complex power system that, instead of being a burden to the overhead grid power-management system, represents a resource capable of supporting the grid. The choice of system architecture and distribution at the residential nanogrid level will play a significant role in achieving a reliable, robust, efficient, and flexible smart grid. To that end, this chapter provides a detailed analysis of the choice of hardware architecture and distribution, enabling a nanogrid to function optimally as a responsible element within a decentralized smart grid.

The chapter is divided into five sections. Section 2.2 provides more insight into the functions required of a future residential nanogrid and identifies the critical aspects of an optimally functioning nanogrid. To achieve those functions, the choice of distribution and architecture is of paramount importance. To that end, section 2.3 compares an AC nanogrid and a DC nanogrid based on the desired functions of a future nanogrid to select the optimal distribution. Section 2.4 reviews the current literature and DC house pilot projects to provide a qualitative comparison of the popular architectures and voltage levels. Section 2.5 introduces the DC smart utility grid as the overhead grid integrating multiple household nanogrids. The advantages and drawbacks of having a power electronic interface between nanogrid and microgrid are presented in detail. Based on the comprehensive analysis, a centralized smart-router based DC-household nanogrid architecture is proposed in Section 2.6.

2.2 Performance requirements for SG residential applications

In this section, a critical review of the performance requirements of future residential nanogrids (NGs) is presented. A detailed analysis regarding the performance requirements is detailed in [1–3]. For a holistic review, those functions are summarized in this section. Further, the functions are divided into two categories: control and hardware architecture.

2.2.1 Control functional requirements:

1. **Stability:** The primary control of the NGs must ensure sufficient stability margins during transient operating modes. It must be noted that the choice of system architecture also influences overall system stability.

2. C**o-ordinated control:** Secondary and tertiary NG control should be able to carry out high-level functions like economic dispatch, mode changing, efficiency optimization, and power flow control between different sources, storages, and loads.

3. **Grid-support capability:** Future decentralized SGs will be dominated by power electronic converters integrating renewable energy sources (RESs), storages, and loads. These interfacing power electronic converters have a relatively low terminal capacitance, which results in low system inertia. In comparison, the current centralized AC grid has high system inertia due to the kinetic energy of the rotating generator in power plants. Therefore, future nanogrids are expected to be able to provide ancillary services to the overhead utility grid.

2.2.2 Hardware functional requirements:

1. **Energy efficient:** With ever-increasing standards of living, heating electrification, and charging of electric vehicles (EV), future households are expected to consume significantly more energy compared to current standards. Therefore, future residential nanogrids are expected to be highly energy-efficient to reduce losses and emissions.

2. **Availability:** Future residential NGs will inherently have higher availability due to multiple local energy sources [4, 5]. Availability can be further improved with the optimal choice of distribution and architecture.

3. **Flexibility:** The possibility of autonomous reconfiguration during faults or islanding can make NGs more flexible and subsequently increase overall microgrid availability.

4. **Scalability:** Residential NGs should be highly scalable as they must continue working with new appliances, sources, storage units, and loads seamlessly integrated into the household.

Among the above functional requirements, both stability and availability can be influenced by both control and hardware architecture choices. NGs need to satisfy the above functionalities to different degrees, depending on the application to form a stable, robust microgrid. For example, in the case of NG applications like data centers, the availability requirements will be much higher than that of

residential households. Since in this thesis, residential application is considered, higher priority will be given to functions like co-ordinated control, stability, and scalability.

2.3 Choice of optimal distribution: AC vs DC

An in-depth review of the different elements of the residential grid is required to select the best distribution for future smart homes. Those elements can be subdivided into three categories: sources, storages, and loads. In the upcoming subsections, a detailed analysis of the internal architecture of the categories is presented. Based on that, a comparative analysis of an AC-based nanogrid and a DC-based nanogrid is reported.

2.3.1 Sources, storages, and loads in residential grids

Renewable sources

Contemporary and future smart homes are envisioned to be energy sustainable and powered by a mix of renewable energy sources, together with the utility grid. Among the wide array of renewable resources, photo-voltaic (PV) solar cells and fuel cells (FC) [6] are the most techno-economically feasible in residential applications. Additionally, both PV panels and FCs generate power in DC.

Energy storage technologies

Energy storage technologies can be broadly classified into four categories: (a) mechanical energy storage like pumped hydro storage (PHES), flywheel energy storage (FES), (b) electrical or electromagnetic based like supercapacitors, (c) electro-chemical based like lead-acid or lithium-ion batteries, and (d) thermal-based like hot water storage [7]. In residential applications, electro-chemical or battery storage technologies are the most popular due to their high energy densities [8] and reliability. Therefore, in this thesis, the focus will be on integrating batteries as energy storage elements. Battery technologies like renewable energy sources are intrinsically DC in nature. In addition, the expected future integration of electric vehicles (EVs) is going to inevitably increase the presence of DC devices in buildings' electrical systems because, basically, EVs have batteries that can be charged or discharged.

Types of loads

In contemporary households, a majority of the appliances depend on power electronic converters to process electrical power into the form and amplitude required by the loads. Based on their internal architecture, loads can be classified into the following categories:

1. **Consumer electronics and LED lighting**: Modern consumer electronics like smart TVs, phones, computers are all internally DC loads. Further, energy-efficient light-emitting diode (LED) lights are also DC in nature.

2. **Variable-speed drive loads**: Kitchen loads like refrigerators, washing machines, dishwashers, etc. are variable speed motor drives that are intrinsically AC in nature. However, they require an additional AC-DC conversion before an inverter which controls the motor operation.

3. **Resistive loads**: Heating loads like electric oven, irons are resistive in nature, which converts electrical energy to thermal energy. Resistive loads can work with both AC and DC distribution without the need for extra power conversion.

A brief overview of the characteristics of sources, storages, and loads of residential households is presented above. In the upcoming sections, different distributions are used to interconnect them and compared them in detail.

2.3.2 AC nanogrid

Figure 2.3a presents the architecture of a grid-fed alternating current (AC)-based household in Europe. The voltage level and the fundamental frequency vary depending on the geography. However, from an architecture and distribution viewpoint, the above schematic can be considered a generic representation of a current household grid globally. A passive distribution panel acts as an interface with

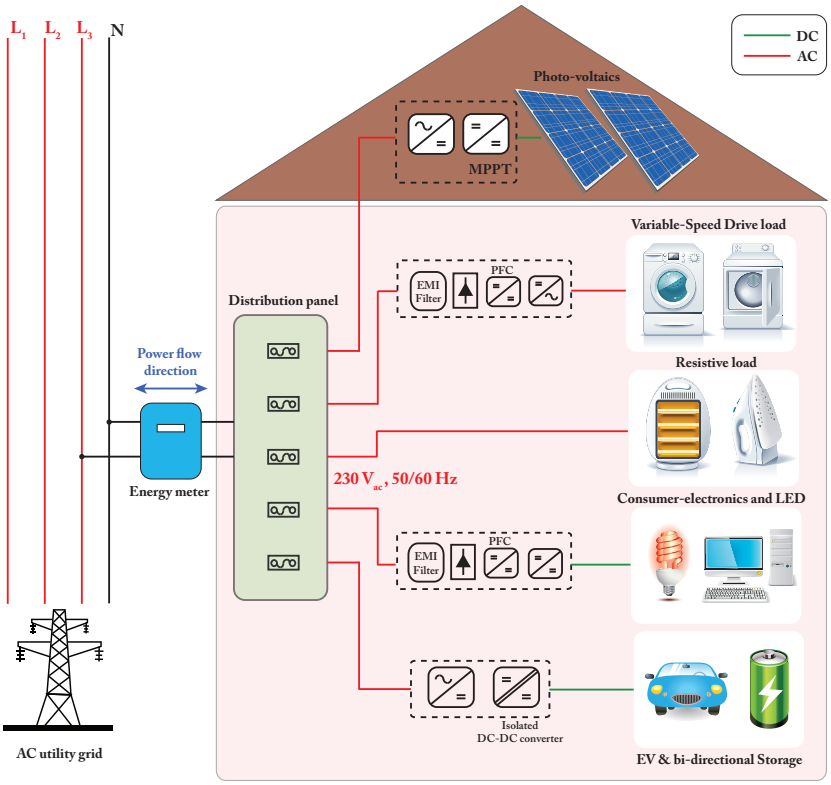

Figure 2.1: AC based legacy house architecture.

the overhead grid between one of the phases and the neutral. Within the same area, different houses are connected to different phases for balanced operation. From the distribution panel, individual feeders emerge that provides power to different load types based on their power ratings. Based on the component type, there are different power conversion steps involved.

The power converter for the PV panels is generally a unidirectional two-stage converter featuring the boost DC-DC converter stage and a single-phase voltage source inverter stage for interface with the household grid. Energy storage and EV typically require isolated bidirectional DC-DC converters for the optimal battery utilization on one side and the AC-line interfce at the other.

In the future, household loads are envisioned to contain more power electronic converters to optimize their operation and boost efficiencies. For example, a modern washing machine has a variable speed drive to provide maximum torque per ampere to a brushless motor. Thus, they are more efficient than old washing machines that used conventional induction motors. Even low power consumer electronic devices like TV, computer, audio, and other portable ones, inherently comprise the power electronics circuits for operation. Most household electronic loads have two-stage power conversion, where the front-end interface consists of electro-magnetic interference filter (EMI), a bridge rectifier, and often a power factor correction (PFC) circuit.

The AC nanogrid system described above can work in both grid-connected mode and stand-alone mode [9, 10]. It needs to perform two transitions: islanding operation during a fault or other abnormal grid condition and synchronization when the fault in the grid is cleared or during normal conditions. During islanding mode, the bi-directional converters of the storage, EV, and the PV converters perform voltage/frequency regulation of the household AC grid. Additionally, grid support can be provided via demand response during grid-connected mode operation [11]. There are two main drawbacks of the above AC-based architecture. First, for optimal co-ordinated control of different source and storage converters, dedicated real-time communication between the converter controllers [12] is necessary. Second, since the utility grid interface of the AC nanogrid is still the AC-line, the overall nanogrid stability depends on the composite of all the source, storage, and load converters, which is challenging.

2.3.3 DC nanogrid

Figure 2.2 presents the architecture of a grid-tied direct current (DC)-based household nanogrid concept. Since the utility grid is AC, a bi-directional AC-DC converter acts as an interface between the grid and the DC nanogrid. Therefore, the entire household nanogrid is seen by the utility grid as a single electronic entity dynamically decoupled from the utility grid but dispatchable by the utility grid. Compared to the AC nanogrid, the DC nanogrid has several advantages:

System efficiency

The main advantage of the DC nanogrid is the inherent high energy efficiency it offers [13, 14]. There is no skin effect in a DC system which allows the current to flow through the entire cable and not just the outer edges. This reduces losses and also provides a possibility to use a smaller cable for the same amount of the current [15, 16]. Further, most household loads, renewable energy sources, and energy storage technologies are intrinsically DC in nature. Figure 2.3 shows a single line diagram of AC and

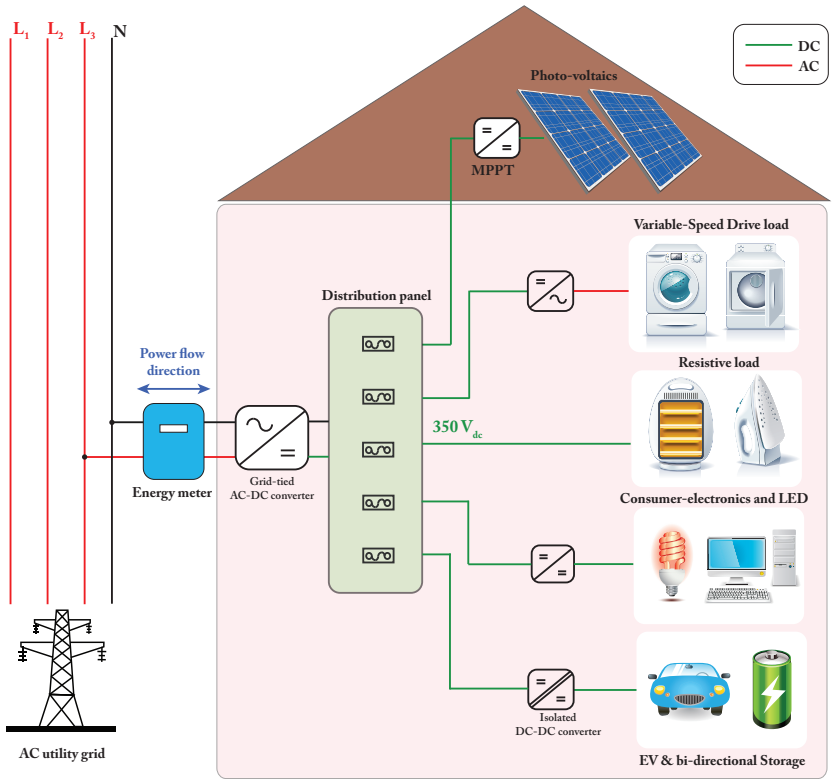

Figure 2.2: DC based house architecture.

DC nanogrids, highlighting the power conversion stages required by loads, sources, and storages. The power conversion stages for resistive loads like an oven, stove, etc. are not shown as fundamentally the choice of distribution is irrelevant for heating elements. Determining system efficiency is a challenging task since it depends on multiple variables like load profile, PV profile, battery state of charge (SoC), etc. These variables determine the dominant power flows within the system. Since future residential grids are envisioned to be self-sufficient, it can be presumed that loads will be powered by PV panels during the day and during the night or low solar irradiation battery storage will power the loads. The utility grid will be used to power the loads if only PV power is not sufficient, and the battery is completely discharged. Based on the conditions and power management implemented, the dominant power flows in the system for both AC, and DC nanogrid are illustrated in Table 2.2. The different conversion steps for every power flows can be summarized in Table 2.1.

According to Table 2.1, DC nanogrid has less conversion steps in most of the power flow conditions. Only when the loads are directly powered by the utility grid, the power conversion steps are similar to that of AC nanogrid. However, in the case of DC nanogrid, the first conversion step is the grid AC-DC interfacing converter, which is rated for high power. Thus, at a low power range, the AC-DC conversion has low partial load efficiency. Hence, it is possible for AC nanogrid to have higher efficiency than DC nanogrid only when the power flowing from the grid to household appliances is dominant compared to the other power flows. A detailed comparative analysis of overall system analysis is not in the scope of

Table 2.1: Main power flows in DC and AC nanogrids

Source	AC Grid	DC Grid
PV	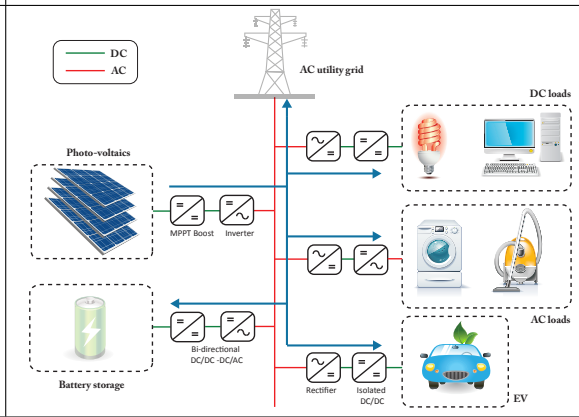	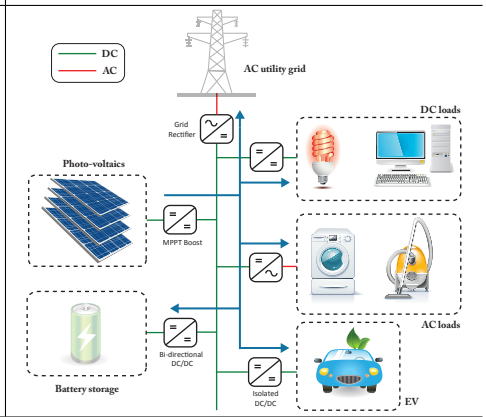
Battery	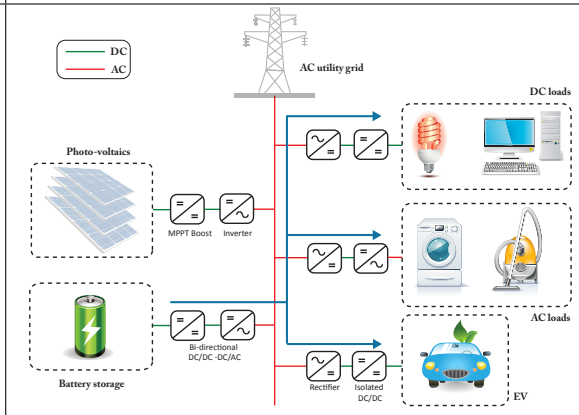	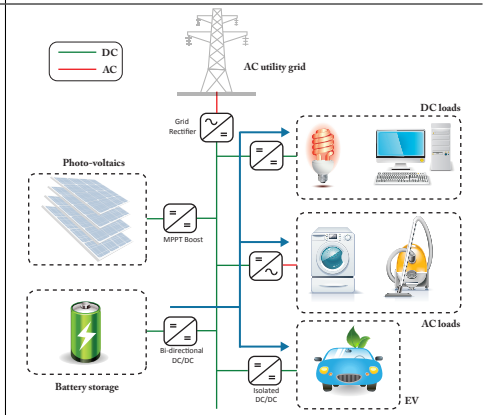
Grid	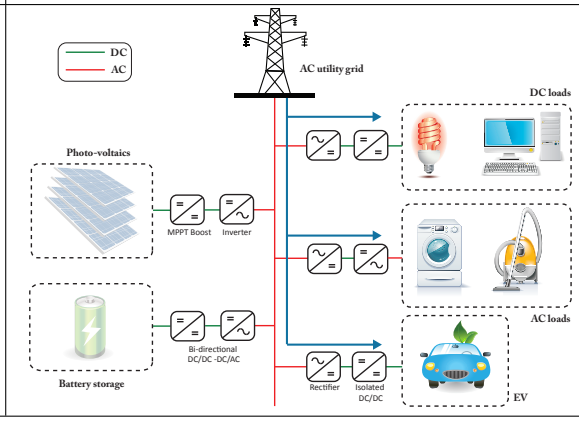	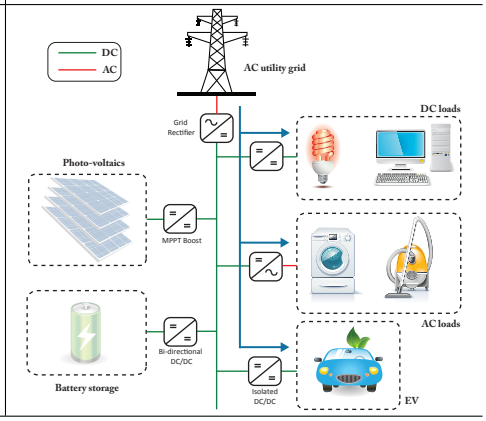

Table 2.2: Conversion steps and energy efficiency

Power Flows		Conversion Steps		Energy efficiency
Source	Load	AC	DC	DC vs AC
PV	AC load	4	2	DC
	DC load	4	2	DC
	EV	4	2	DC
	Battery	4	2	DC
	Grid	2	2	AC
Battery	AC load	4	2	DC
	DC load	4	2	DC
	EV	4	2	DC
Grid	AC load	2	2	AC
	DC load	2	2	AC
	EV	2	2	AC

this thesis. A significant amount of scientific literature regarding the comparison of AC and DC system efficiency has already been reported [14, 17].

Ease of control and stability

Unlike the AC nanogrid, the DC nanogrid has a controllable interface with the utility grid. Thus, a DC nanogrid is much less susceptible to failure due to main grid disturbances. Further, the nanogrids are fully decoupled from the grid through the converter, so that their internal architecture is completely independent. The DC bus voltage in the house can be controlled, which can be used for distributed control [18]. There is no need for any synchronization of DC nanogrid with the overhead AC grid, and also reactive power control is not required. This further reduces the operational complexity

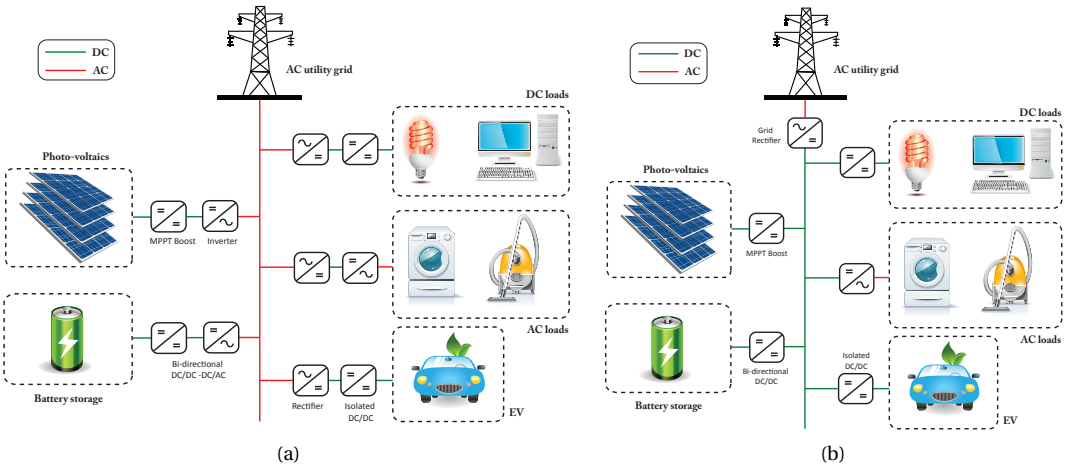

Figure 2.3: Single line diagram of: (a) AC nanogrid, and (b) DC nanogrid to hightlight the reduction of power conversion stages enabled by DC distribution.

of the system. Stability in a DC nanogrid depends on maintaining the DC bus voltage within the normal operating range for all the devices connected to the bus under every transient and steady-state condition. Although stability depends on the overall architecture of the DC distribution, the solutions are simpler than for AC nanogrids.

Advances in power electronics

Advances in DC-DC converter technology have resulted in highly efficient and reliable converters providing the "DC transformer" effect that counterbalances the decisive factor that favored AC systems in the 1900s. With the advent of wide-bandgap semi-conductors like silicon-carbide (Si-C) and galium-nitride (GaN), the switching frequencies of power converters are consistently increasing to as high as 500 kHz - 1 MHz. High switching frequencies reduce the size of the passives like magnetics and capacitors, which provide space savings and system costs.

In conclusion, strong arguments indicate that implementing nanogrid by using a common DC voltage is simpler, more reliable, and more efficient than using AC to implement nanogrids. However, there are some obstacles to the practical implementation of the DC nanogrid, which need more attention from the research community. Some of these are:

- **Lack of commercial products**: The high initial investment cost prevents the replacement of the whole AC distribution grid at one time. This results in a chicken-and-egg problem: the lack of available DC devices hinders the implementation of small DC grids while the lack of DC grids prevents manufacturers from building DC devices.

- **Lack of standards**: The lack of standards and code is probably the main issue that needs to be solved. Standardization is essential at the voltage levels where most devices will be connected and also the choice of an optimal power architecture. However, it is important not only to consider local DC nanogrids and microgrids but to consider their connection to a full universal DC distribution system. Standardization will allow developing countries to choose DC when electrifying rural areas or when investing in new infrastructure on a large scale. Several organizations such as Emerge Alliance (EA), the European Telecommunications Standards Institute (ETSI), the International Electrotechnical Commission (IEC), Institute of Electrical and Electronics Engineers (IEEE) and others, are already actively developing the necessary regulation and standards.

- **Protection**: Protection of the DC grid system is more difficult compared to the AC distribution system. Sensitive detection, differentiation, and selective clearance of parallel and series DC arc faults are important. Compared to AC microgrids, DC distribution systems are more susceptible to sustained arcs due to the absence of current zero crossing [19].

In conclusion, DC grids have certain technical and commercialization challenges to solve before proliferation into the energy market. However, they may be able to provide increased energy efficiency, power density, and reliability, at possibly lower installation and operation costs. To that end, in this thesis, DC distribution is considered as the backbone for the design of future smart homes. In the upcoming section, possible DC home architectures are introduced and compared.

2.4 DC architecture building blocks and voltage level

Significant scientific work has already been published regarding the choice of voltage level and architecture type for general DC microgrids [13, 20, 21]. In this section, a brief overview of relevant architectures for residential applications is presented for a qualitative discussion. Further, a brief overview of the voltage levels in future DC households is also presented.

2.4.1 Voltage level in DC homes

The lack of standards in low-voltage DC (LVDC) distribution systems is evident from the variety of voltage levels used in different DC home pilot projects from values as low as 48 V to as high as 400 V. However, upon close inspection, a pattern can be recognized. Based on power consumption, the following voltage levels are relevant to residential applications:

- **300 V - 400 V :** Usual AC voltage levels for residential devices range from 100 V in Japan to 230 V in the EU. The lowest RMS voltage can be 90 V and the highest 264 V considering a safety margin of ±10%. The latter has an RMS to peak voltage range from 305 V to 373 V. All devices have to be able to insulate at least this voltage. Therefore, just from the device perspective, everything is fine until this voltage if used with DC [22]. Normally, nanogrid applications with high power consumption (≥ 10 kW) prefer this voltage range to minimize distribution losses. Beyond 400 V, energy efficiency improvement becomes negligible, whereas the design of the protection system becomes challenging and costly. For example, 380 V is already a standardized voltage level in data centers [23–25]. Similar voltage levels are used in several DC buildings and house pilot projects [26, 27].
- **230 V :** Medium power elements (0.4 - 5 kW) in a DC residential nanogrid can be powered at 230 V. For given power consumption, powering loads at 230 V would keep the same current loading in the cables as in a single phase 230 V_{ac}. Additionally, this voltage level is already compatible with purely resistive loads.
- **120 V :** According to IEC61140 standard, 120 V represents the limit for extra LV, which doesn't require dedicated protection systems against indirect contacts. Using extra-low voltage is one of several means to protect against electrical shock. For low power households in developing countries, this can be an optimal choice of voltage level for supplying loads safely.
- **48/60 V:** 48 V DC and lower voltage levels are safe and relatively efficient standard for low-power appliances in home microgrids. It is already used as a standard in telecommunications applications. In certain applications, 60 V can also be used instead of 48 V to improve energy efficiency with similar advantages [26]. Consumer electronic equipment (e.g., phone chargers, computers, smart TVs, and LED lights) in residential grids can be powered by this voltage level efficiently while maximizing safety.

The selected voltage from the above choices for a residential nanogrid is inevitably related to the power rating of the different elements in the house if the same wire gauge is reused. Therefore, different voltages are more optimal for different groups while optimizing energy efficiency for each scenario,

Table 2.3: Load groups and optimal voltage levels

Group no.	Category	Loads	Power range	Optimal voltage
1	Consumer electronics and lighting	Smart TV, phone charger, computer, LED lighting	10 - 200 W	48/60 V
2	Kitchen	Electric oven, kettle, rice cooker, toasters	1 - 3 kW	230 V
3	Laundry	Washing machine, dryers, electric iron	2 - 4 kW	300-400 V
4	Electric vehicles	DC charging, wireless charging	3 - 11 kW	350-700 V

safety, and compatibility with other systems [28]. Table 2.3 summarizes the optimal voltage levels for different load groups in a DC household. In conclusion, there is no objectively best choice of voltage level in future DC households. Research trend and implementation in pilot projects suggest that future DC houses and buildings will have multiple voltage buses catering to different load groups, which optimizes efficiency and safety [26, 27, 29].

2.4.2 Classification of architecture

There are several possible architectures for DC microgrid applications reported in the literature. In this thesis, we are only focusing on those architectures suitable for DC residential applications [30]. Additionally, hybrid DC-AC residential grids are not considered in the following discussion.

A wide variety of DC architectures are possible due to numerous combinations of some basic architecture building blocks. An in-depth analysis of DC architectures for microgrids can be found in [20, 21]. Based on the polarity of the DC voltage, and the number of buses, the following basic architecture blocks can be used for future smart homes:

1. **Unipolar DC house**: In a unipolar DC residential nanogrid, sources and loads are connected between the positive and the negative pole of the DC bus, as shown in Figure **??**. Since the power is transmitted via the positive pole, the selection of the voltage level is a crucial factor in the overall design of the system. Higher voltage level increases the power transmission capability at the risk of safety [31, 32].
   Overall, the unipolar system is simple to implement and cost-effective. However, this system lacks redundancy, and therefore even a single fault can lead to a shutdown of the complete system. Moreover, this system does not offer different voltage level options to the customers. The unipolar DC system is viable for off-grid homes in remote rural areas, where no utility grid infrastructure exists.

2. **Bipolar DC house**: A bi-polar DC system addresses the limitations of a unipolar DC grid. A bipolar DC grid is a three-wire system, which consists of + V_{DC}, - V_{DC} and a neutral line as highlighted in Figure 2.4b. This configuration provides customers three voltage levels: V_{DC}, - V_{DC} and $2V_{DC}$. High power loads like EV and sources like PV can be fed by the high voltage levels. For the rest of the low and medium power loads, the normal voltage level can be used. Moreover, during

fault conditions, one of the poles can still be used to provide power to the loads. Therefore, the reliability, availability, and power quality of the bipolar system are better than the unipolar system. However, the unequal distribution of loads can lead to system unbalance in the bi-polar DC grid. Normally, a voltage balancer circuit is used in this type of system, which increases cost [33].

3. **Multi-bus DC house**: The main disadvantage of a unipolar DC nanogrid is the lack of flexibility in terms of consumer voltage. A multi-bus DC nanogrid solves that problem by introducing multiple unipolar buses of different voltage levels catering to the wide range of electronic devices in a residential grid. Thus, the loads with different power ratings can be connected to the voltage that better suits them. Figure 2.4c shows a multi-bus DC house with three unipolar voltage levels: 350 V for high power loads and sources, 60/48 V for LED lighting and consumer electronics, and 24 V for USB-C based charging. Several DC house pilot projects are based on the multi-

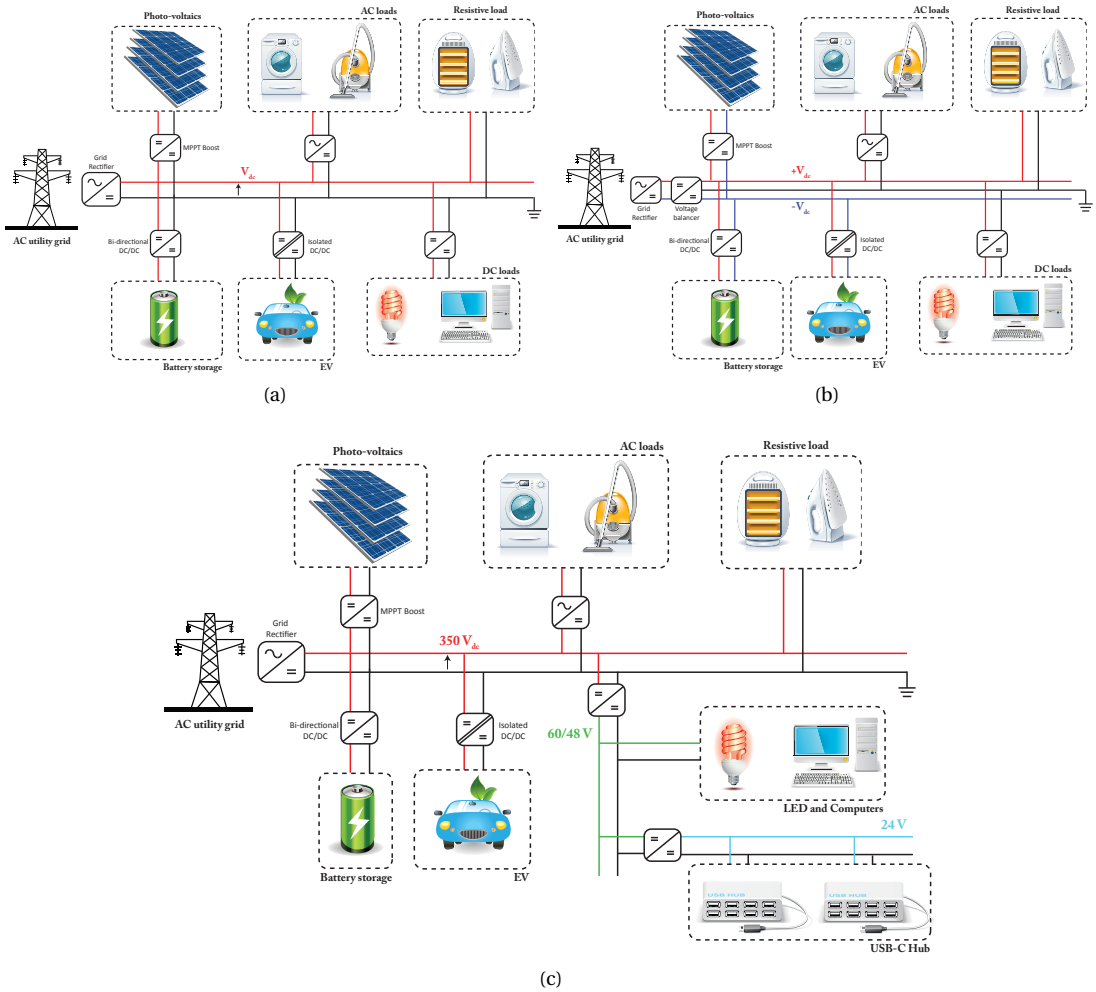

Figure 2.4: Single line diagram of different AC grid-connected DC home architectures: (a) unipolar DC grid, (b) bi-polar DC grid with voltage balancer, and (c) multi-bus DC grid with three unipolar voltage buses.

Table 2.4: Overview of architecture and voltage level in DC home pilot projects

Pilot Project	Location	Bus architecture			Voltage levels
		Unipolar	Bi-polar	Multi-bus	
Pulse Building [26]	Delft, The Netherlands	✓		✓	350 V, 60 V
ABN Amro building [27]	Amsterdam, The Netherlands	✓			350 V
Intelligent DC house [29]	Aalborg, Denmark	✓		✓	380 V, 48 V, 24 V, 12 V
Osaka university [33]	Osaka, Japan		✓		170 V, 340 V
Yokohama smart home [34]	Yokohama, Japan	✓			380 V
Solar DC homes [35]	Rajasthan, India	✓			48 V

bus architecture: Pulse building in the Delft University of Technology in the Netherlands [26], intelligent DC home at Aalborg University in Denmark [29] etc. For more flexibility of available voltages, the main bus of the house can also be bipolar.

The unipolar and bipolar topologies form the basis for the future DC nanogrid system architecture. The multi-bus DC house architecture can be considered a higher level architecture on top of either a unipolar or a bi-polar architecture. Multi-bus systems can be an interesting architecture for future households as different load groups can be powered by different bus voltages, which improve both energy efficiency and safety.

Based on the architecture building blocks and possible voltage levels, several pilot projects for implementation of DC house or buildings already exists in different parts of the world. Table 2.4 provides a brief overview of the architecture and voltage levels used in those DC nanogrid prototypes. It must be noted that the list of pilot projects shown in the table is not exhaustive.

2.5 Integration with DC utility microgrid

A significant overhaul of the current AC utility infrastructure overnight is not feasible. Therefore, the journey towards a universal DC smart grid is going to be long and arduous with small steps from both bottom to top and top to bottom directions. From the bottom, making nanogrids like households DC is a significant stepping stone towards a universal DC smart grid. Till now, all the DC home solutions reported in literature and industry considered an AC utility grid with an interfacing AC-DC converter. However, in the last decade, research has gathered significant momentum towards envisioning the utility grid as a DC microgrid consisting of multiple DC nanogrids [33, 36–38]. Bi-polar distribution connecting multiple houses and buildings is seen as a promising solution due to the advantages discussed in the previous section. Figure 2.5 presents a bi-polar architecture of a DC utility grid interfacing with an overhead AC grid [13]. Since the limit for LVDC is 1500 V, a bi-polar distribution grid of ± 750 V is proposed for minimizing distribution losses. Another bi-polar grid of ± 350 V is extracted from the overhead grid to power the residential grid consisting of different nanogrids. Medium and low power households or buildings can be connected to the 350 V and the neutral while buildings requiring high power (≥ 15 kW) can connect between +350 V and -350 V.

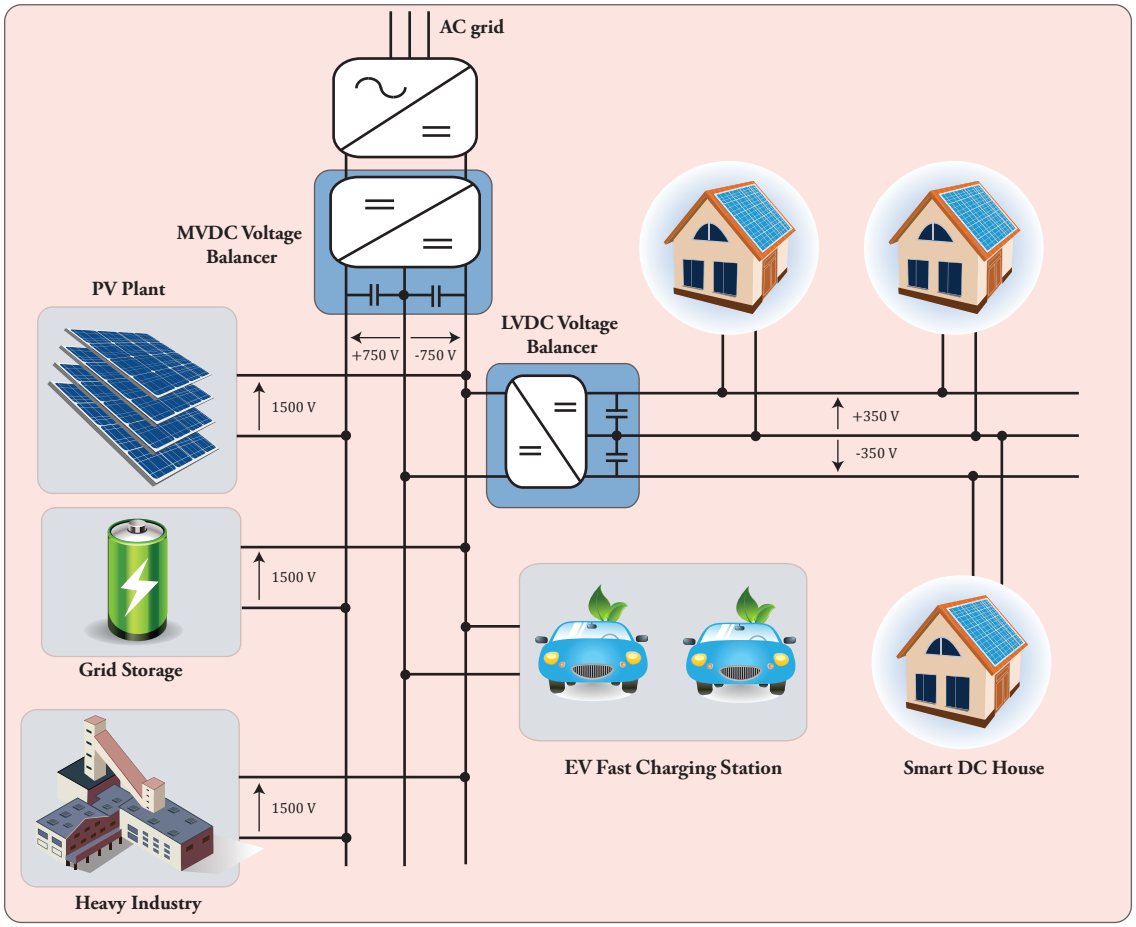

Figure 2.5: A schematic of a two-level bipolar LVDC utility distribution microgrid [13].

Conceptualizing a DC house architecture connected to an AC utility grid is fundamentally different compared to envisioning a DC house connecting a DC utility grid. While connecting a DC household to an AC overhead grid, a power electronic interface is necessary to convert AC to DC. However, two possible scenarios arise when connecting a DC house to a DC utility grid: (1) without a DC-DC power electronic converter as grid-interface, (2) With a DC-DC power electronic converter as grid-interface. The advantages and disadvantages of the above configurations are discussed in the following:

2.5.1 DC house without interfacing converter

The advantages of DC distribution in households are discussed in detail in Section 2.3. Since the final goal is to implement DC distribution in a household nanogrid grid with an overhead DC utility grid, the logical step is to directly connect the house to the utility grid, as shown in Figure 2.6. In essence, it is similar to the current AC houses being directly connected to the AC utility grid, as shown in Figure 2.1. The advantages and disadvantages of DC house without a converter as a grid interface are discussed in

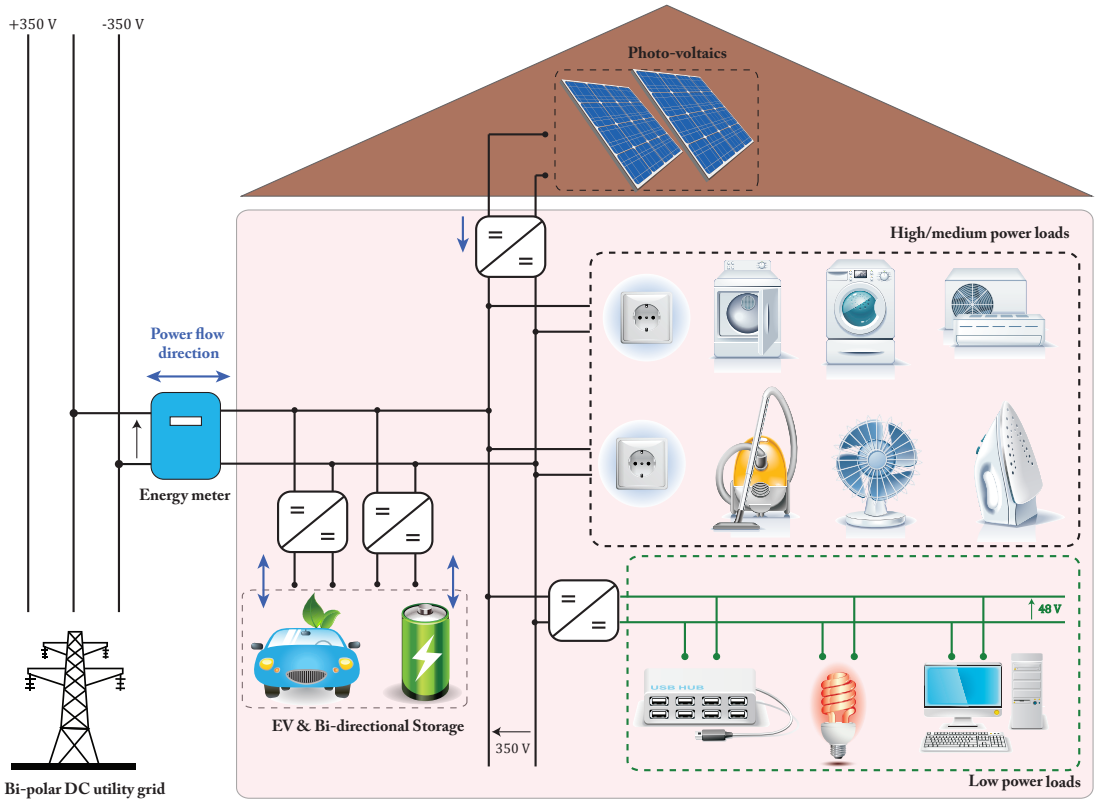

Figure 2.6: DC house architecture without a DC-DC converter interface to the DC utility grid.

the following:

Advantages

1. **Higher energy efficiency**: Since there is no converter as a grid-interface, there is one less conversion stage when loads are powered from the grid. Additionally, in scenarios that require power transfer between adjacent households, the energy-saving due to fewer conversion steps will be even higher [39].

2. **Low installation cost**: While interfacing a DC house with the utility microgrid, the interfacing converter needs to be designed for the peak demand of the nanogrid, which is expensive. Thus, removing the converter at the interface between nanogrid and the utility microgrid can reduce investment costs significantly.

3. **High scalability**: Due to the decentralized nature of the house nanogrid, sources, loads, and storages can be expanded without any constraints. Therefore, this system is very scalable.

Disdvantages

1. **Lack of electrical separation**: A significant downside of directly connecting the DC nanogrid to the microgrid is the lack of electrical separation between them. Consequently, the control of the microgrid becomes a bit challenging as the utility grid doesn't see the DC nanogrid as a single dispatchable electronic entity.

2. **Fault energy and safety**: The lack of electrical separation between the household nanogrid and utility microgrid makes the protection challenging as there is no bi-directional fault interruption. Additionally, a short circuit fault within the house nanogrid can be fed by the microgrid, which might lead to high fault energy resulting in safety concerns [40].

3. **Complex grid stability**: Future DC microgrids will be dominated mainly by renewable energy resources interfaced with power electronic converters. Therefore, compared to the existing AC grid, future DC grid will have significantly low inertia leading to the term "weak grid" [41, 42]. While interfaced directly with a weak grid, the overall DC nanogrid stability is dependent on the composite of all the source and load converters, which can be complex [43–45].

4. **Low grid-support capability**: The lack of a controllable grid interface results in a passive non-dispatchable nanogrid. Such an entity doesn't offer a lot in terms of overall grid support and re-configuration.

5. **Decentralized control and need for dedicated communication**: Since individual sources, storages and loads are connected by individual power electronic converters, high-level energy management for economic optimization requires complex decentralized control or dedicated real-time communication.

2.5.2 DC house with interfacing converter

The natural alternative to directly connecting a DC household to the utility grid is to use a DC-DC converter as an interface between the nanogrid and the microgrid, as shown in Figure 2.7. From an architecture viewpoint, it is similar to the current DC house pilot projects with an AC-DC converter as an interface to the AC utility grid (see Figure 2.2). The advantages and disadvantages of the DC nanogrid with the grid-interface concept are discussed in the following:

Advantages

1. **Decoupled from grid**: Since there is a controllable grid-interface, the household nanogrid is seen as a single electronic load/source/storage by the utility grid. The resulting nanogrid is dynamically decoupled from the grid and can be dispatched by the utility operator autonomously via price signals.

2. **Bi-directional fault interruption**: The current limit protection is integrated into the semiconductor switches of the DC-DC power converter itself, which eliminates the need for bulky and expensive protection devices, e.g., solid-state circuit breaker, on both sides [40].

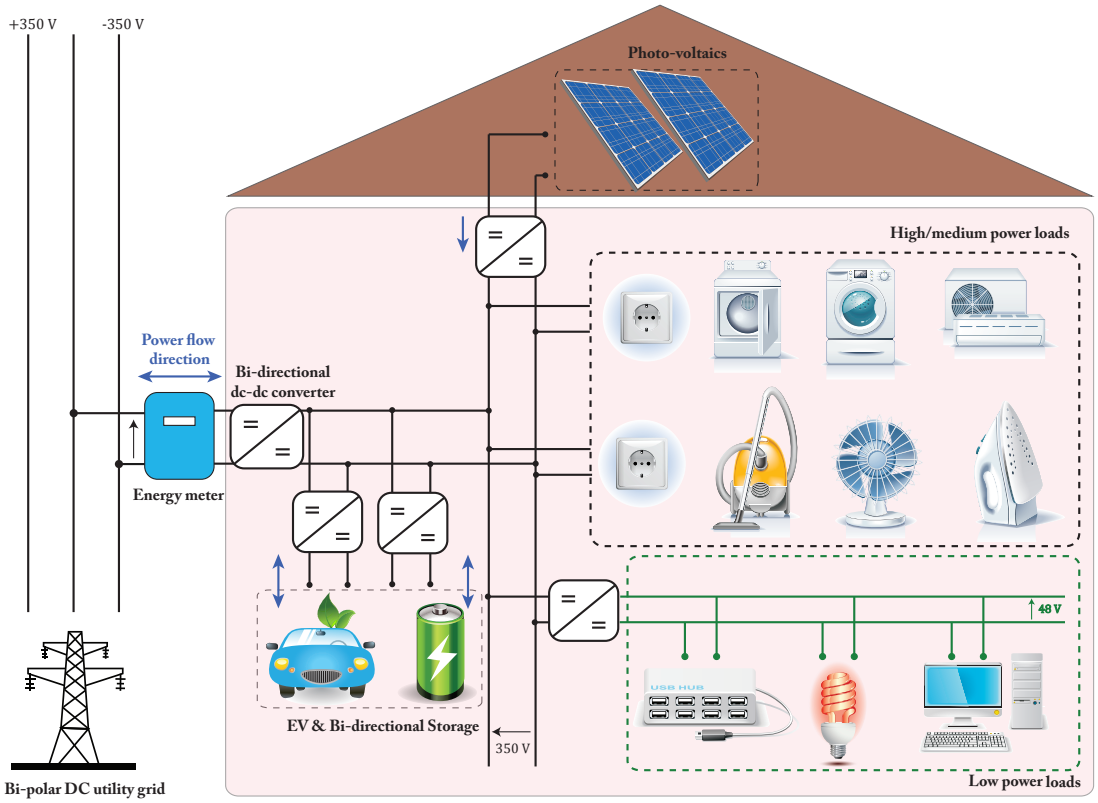

Figure 2.7: DC house architecture with a DC-DC converter interface to the DC utility grid.

3. **Controllable consumer voltage**: Due to dynamic decoupling from the grid, the voltage of the internal architecture is completely independent and can have different voltages. The variable DC bus voltage can be used as a communication signal between different source/storage converters for distributed control [18].

4. **Low fault energy and safety**: The static energy stored on the DC nanogrid side converter capacitors is small, which can reduce the transient energy spike under the short-circuit condition, thus reducing the safety challenge to users.

Disdvantages

1. **Low energy efficiency**: Using a power electronic converter as a grid interface adds an extra power conversion step between the microgrid and household loads/sources or storage, which reduces energy efficiency. However, future house nanogrids are envisioned to be highly grid-independent in terms of both energy and power. Hence, the dominant power flows in a household nanogrid will be internal, which doesn't affect overall energy efficiency.

2. **High investment cost**: The grid-interfacing converter needs to bi-directional and rated at the peak demand of the household nanogrid, which makes it expensive. Hence, this converter will

have a low utilization factor as the average demand is significantly lower (10%-20% of peak demand). Most of the time, these converters would operate at partial load conditions with poor efficiency, as modular converters might not be economically feasible at these power levels due to the overhead of modularity.

3. **Complex stability**: Even with a grid-interfacing converter, the overall nanogrid stability is dependent on the composite of the source/load converters, which can be complex.

4. **Decentralized control and communication**: Control requirements for DC nanogrid with grid converter can still be a bit challenging due to its decentralized nature. As previously discussed, the controllable DC bus voltage can be used for distributed control. However, real-time communication might still be necessary for high-level energy optimization.

2.6 Smart-power-router based DC nanogrid

In this previous section, two possible scenarios of connecting a DC nanogrid to a DC utility microgrid are discussed. The advantages and disadvantages of the two scenarios are analyzed in depth. In summary, both solutions offer a trade-off between different nanogrid functionalities. For example, a DC nanogrid without interface has more energy efficiency for nanogrid to microgrid or inter-nanogrid power transfers at the cost of controllability and ease of protection. Similarly, a DC nanogrid with grid-interface offers ease of control and protection at the expense of energy efficiency for specific power flows and high overall investment cost. However, both the solutions suffer from similar drawbacks like complex stability due to their decentralized architecture and the need for communication to achieve high-level energy management for economic optimization. To that end, a centralized smart-power-router concept for DC house is proposed in this thesis to combine the best attributes of the above solutions while eliminating their common drawbacks.

Figure 2.6 presents the schematic of a smart-power router-based DC house nanogrid. The smart-power router acts as a multi-port power processor integrating different sources, storage, grid, and household loads. The smart power router is responsible for multiple functions like controlling the charge/discharge of the batteries, MPPT control of PV panels, grid islanding/reconnecting, DC bus voltage regulation, etc. Due to its centralized nature, the need for real-time communication for low to high-level control actions is eliminated in the proposed nanogrid structure. The advantages and disadvantages of the smart-power router-based DC nanogrid are highlighted below:

Advantages

1. **Decoupled from the microgrid:** The smart power router has an integrated grid-interface which dynamically decouples the nanogrid from the microgrid. Therefore, it has all the advantages of the DC house concept with a grid interface.

2. **No need for communication:** The proposed DC nanogrid concept is centralized in nature, which integrates the individual source/storage converters into one physical, electronic entity. Thus, the proposed configuration obviates the need for communication between different sources/storage.

3. **Ease of co-ordinated control and protection:** Co-ordination between sources, storages, and

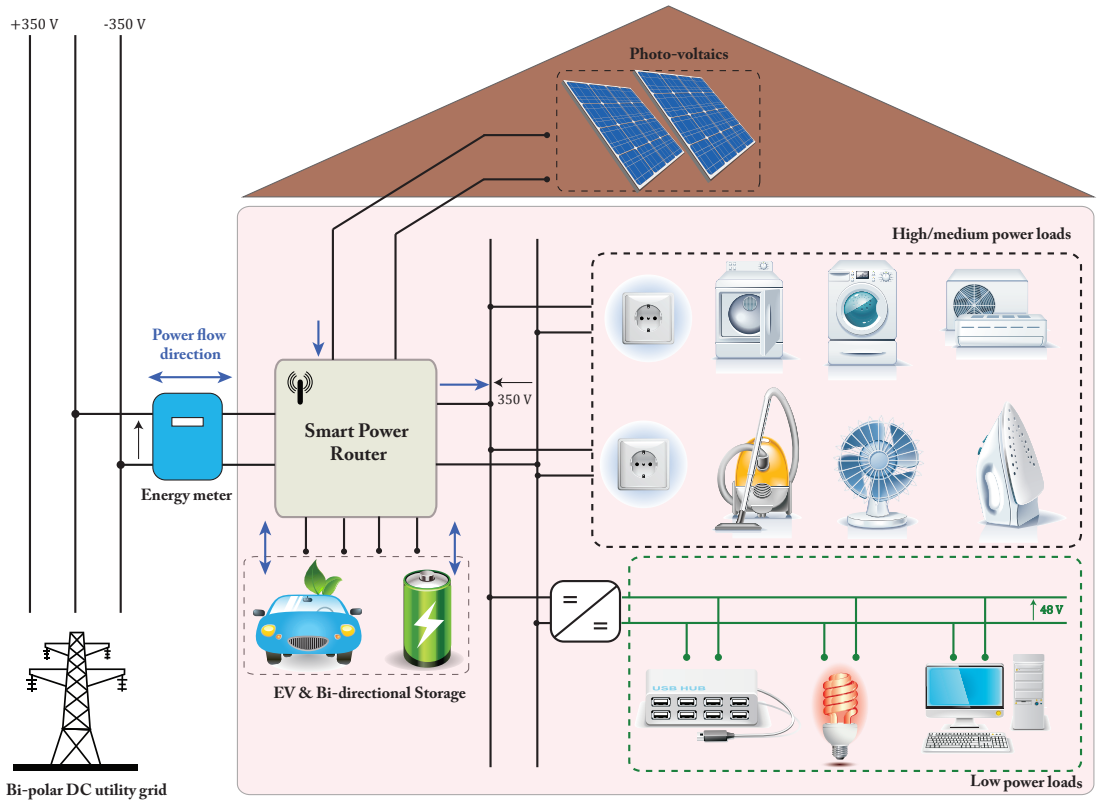

Figure 2.8: Proposed centralized smart-power-router based DC household nanogrid architecture.

loads is much simpler due to the centralized nature of the smart power router-based DC nanogrid concept. Additionally, protection and selectivity are also easier as only well-defined parts of the subsystem have to be taken into consideration.

4. **Simpler stability conditions:** The overall nanogrid stability condition is simpler to achieve as there is only one main component opposed to multiple decentralized converters used in the previous concepts.

5. **Medium installation cost:** The overall system cost can be reduced by intelligently combining multiple sources, storage converters into one main component able to perform all the major functions, and more.

Disadvantages

1. **Low reliability:** An inherent drawback of centralized architectures is the single point of failure, which decreases the overall reliability and availability of the system. However, the reliability can be improved by the innovative design of the smart power router internal architecture.

2. **Low scalability:** The expandability or scalability of the proposed smart power router DC nanogrid concept is not very straightforward. Especially in the case of residential household applications, a

Table 2.5: Comparison of different DC home architectures

Category	Function	Architecture		
		Decentralized		Centralized
		With interface	Without interface	Smart-power router
Control	Stability	++	+	+++
	Grid-support capability	+++	+	+++
	Co-ordinated control	++	+	+++
Hardware	Energy efficiency	+	+++	++
	Availablity	++	++	++
	Flexibility	++	+	+++
	Scalability	++	+++	+
	System cost	+	+++	++

consumer must be able to integrate new appliances without facing overloading issues. Therefore, the design of the smart power router needs to be modular to incorporate scalability.

Fundamentally, the proposed centralized smart power router-based nanogrid seems like an anti-thesis to the goal of forming a universal decentralized smart grid. However, on close inspection, it is evident that to realize a stable, robust, flexible, decentralized smart DC microgrid, we need to maximize the functional abilities of individual nanogrids. Since nanogrids are inherently small in terms of physical size, a centralized internal architecture improves the overall operational capabilities of the nanogrid without accentuating the inherent drawbacks of a centralized system. Therefore, the smart power router-based DC nanogrid is a promising architecture for future residential households. Table 2.5 shows a qualitative comparison of the proposed smart power router-based DC nanogrid to the previous decentralized DC home architectures.

2.7 Conclusion

In this chapter, the internal architecture of future household nanogrid capable is conceptualized with the goal of playing an essential role as an active agent in building a robust universal DC smart microgrid. To that end, critical functionalities required of such a nanogrid are identified, which includes control functions like ensuring system stability, co-ordination between different nanogrid elements, and grid-support capability based on price signals and hardware functions like energy efficiency, availability, and reliability, cost-effectiveness, and scalability. The current AC based household architecture is evaluated in the above metrics to test their suitability as a nanogrid module in a smart grid. However, their overall performance is sub-optimal due to their low energy efficiency, flexibility, and grid-support capability.

As an alternative, DC-based household nanogrid is presented. DC-based nanogrids offers potentially superior energy efficiencies as most renewable generators, storages, and appliances are inherently DC in nature. To that end, several DC pilot projects are reviewed in terms of their architecture and voltage levels. Several existing DC system architectures for integrating PV, EV, storage, and loads are compared based on scalability, flexibility, availability, and robustness. The advantages and disadvantages of different architectures are analyzed in detail.

Based on the analysis, a smart power router-based DC system architecture that integrates PV, battery storage, grid in a multi-port power processor is selected for future household grids. In conclusion, a centralized nanogrid architecture is capable of performing all the functions necessary to realize a robust, available, efficient decentralized smart grid. In the next chapter, the design and development of the proposed smart-power electronic router are presented.

References

[1] B. Wunder, L. Ott, J. Kaiser, Y. Han, F. Fersterra, and M. März, "Overview of different topologies and control strategies for dc micro grids," in *IEEE First International Conference on DC Microgrids (ICDCM)*, pp. 349–354, IEEE, 2015.

[2] R. M. Cuzner and G. Venkataramanan, "The status of dc micro-grid protection," in *IEEE Industry Applications Society Annual Meeting*, pp. 1–8, IEEE, 2008.

[3] G. Venkataramanan and C. Marnay, "A larger role for microgrids," *IEEE power and energy magazine*, vol. 6, no. 3, pp. 78–82, 2008.

[4] H. Ikebe and T. Yamashita, "Power systems for telecommunications in the it age," *IEICE transactions on communications*, vol. 87, no. 12, pp. 3414–3421, 2004.

[5] A. Kwasinski, "Quantitative evaluation of dc microgrids availability: Effects of system architecture and converter topology design choices," *IEEE Transactions on Power Electronics*, vol. 26, no. 3, pp. 835–851, 2010.

[6] R. H. Wolk, "Fuel cells for homes and hospitals," *IEEE Spectrum*, vol. 36, no. 5, pp. 45–52, 1999.

[7] F. A. Bhuiyan and A. Yazdani, "Energy storage technologies for grid-connected and off-grid power system applications," in *2012 IEEE Electrical Power and Energy Conference*, pp. 303–310, IEEE, 2012.

[8] N. Kularatna, *Energy storage devices for electronic systems: rechargeable batteries and supercapacitors*. Academic Press, 2014.

[9] T. Thacker, R. Burgos, F. Wang, and D. Boroyevich, "Single-phase islanding detection based on phase-locked loop stability," in *IEEE Energy Conversion Congress and Exposition*, pp. 3371–3377, IEEE, 2009.

[10] D. Boroyevich, I. Cvetković, D. Dong, R. Burgos, F. Wang, and F. Lee, "Future electronic power distribution systems a contemplative view," in *12th International Conference on Optimization of Electrical and Electronic Equipment*, pp. 1369–1380, IEEE, 2010.

[11] P. Palensky and D. Dietrich, "Demand side management: Demand response, intelligent energy systems, and smart loads," *IEEE transactions on industrial informatics*, vol. 7, no. 3, pp. 381–388, 2011.

[12] I. Cvetkovic, T. Thacker, D. Dong, G. Francis, V. Podosinov, D. Boroyevich, F. Wang, R. Burgos, G. Skutt, and J. Lesko, "Future home uninterruptible renewable energy system with vehicle-to-grid technology," in *IEEE Energy Conversion Congress and Exposition*, pp. 2675–2681, IEEE, 2009.

[13] E. Rodriguez-Diaz, F. Chen, J. C. Vasquez, J. M. Guerrero, R. Burgos, and D. Boroyevich, "Voltage-level selection of future two-level lvdc distribution grids: A compromise between grid compatibiliy, safety, and efficiency," *IEEE Electrification Magazine*, vol. 4, no. 2, pp. 20–28, 2016.

[14] D. J. Hammerstrom, "Ac versus dc distribution systemsdid we get it right?," in *IEEE Power Engineering Society General Meeting*, pp. 1–5, IEEE, 2007.

[15] J.-D. Park, J. Candelaria, L. Ma, and K. Dunn, "Dc ring-bus microgrid fault protection and identification of fault location," *IEEE transactions on Power delivery*, vol. 28, no. 4, pp. 2574–2584, 2013.

[16] A. Shekhar, E. Kontos, L. Ramirez-Elizondo, A. Rodrigo-Mor, and P. Bauer, "Grid capacity and efficiency enhancement by operating medium voltage ac cables as dc links with modular multilevel converters," *International Journal of Electrical Power & Energy Systems*, vol. 93, pp. 479–493, 2017.

[17] I. Sulaeman, V. Vega-Garita, G. R. C. Mouli, N. Narayan, L. Ramirez-Elizondo, and P. Bauer, "Comparison of pv-battery architectures for residential applications," in *IEEE International Energy Conference (ENERGYCON)*, pp. 1–7, IEEE, 2016.

[18] J. Schonbergerschonberger, R. Duke, and S. D. Round, "Dc-bus signaling: A distributed control strategy for a hybrid renewable nanogrid," *IEEE Transactions on Industrial Electronics*, vol. 53, no. 5, pp. 1453–1460, 2006.

[19] A. Shekhar, L. Ramírez-Elizondo, S. Bandyopadhyay, L. Mackay, and P. Bauera, "Detection of series arcs using load side voltage drop for protection of low voltage dc systems," *IEEE Transactions on Smart Grid*, vol. 9, no. 6, pp. 6288–6297, 2017.

[20] T. Dragičević, X. Lu, J. C. Vasquez, and J. M. Guerrero, "Dc microgrids—part ii: A review of power architectures, applications, and standardization issues," *IEEE transactions on power electronics*, vol. 31, no. 5, pp. 3528–3549, 2015.

[21] D. Kumar, F. Zare, and A. Ghosh, "Dc microgrid technology: system architectures, ac grid interfaces, grounding schemes, power quality, communication networks, applications, and standardizations aspects," *IEEE Access*, vol. 5, pp. 12230–12256, 2017.

[22] L. Mackay, L. Ramirez-Elizondo, and P. Bauer, "Dc ready devices-is redimensioning of the rectification components necessary?," in *Proceedings of the 16th International Conference on Mechatronics-Mechatronika*, pp. 1–5, IEEE, 2014.

[23] G. AlLee and W. Tschudi, "Edison redux: 380 vdc brings reliability and efficiency to sustainable data centers," *IEEE Power and Energy Magazine*, vol. 10, no. 6, pp. 50–59, 2012.

[24] A. Pratt, P. Kumar, and T. V. Aldridge, "Evaluation of 400v dc distribution in telco and data centers to improve energy efficiency," in *INTELEC 07-29th International Telecommunications Energy Conference*, pp. 32–39, IEEE, 2007.

[25] K. Hirose, "Consideration of voltage range of a 380 vdc distribution system for international standardization," in *Intelec 2013; 35th International Telecommunications Energy Conference, Smart Power and Efficiency*, pp. 1–6, VDE, 2013.

[26] https://dc.systems/projects/8-main/132-pulse-technical-university-of delft, "Pulse building of delft university of technology," 2016.

[27] https://www.dc.systems/projects/8-main/133-circl-pavilion-of-abn-amro bank, "Circl pavilion of abn amro bank dc building," 2016.

[28] W. Li, X. Mou, Y. Zhou, and C. Marnay, "On voltage standards for dc home microgrids energized by distributed sources," in *Proceedings of The 7th International Power Electronics and Motion Control Conference*, vol. 3, pp. 2282–2286, IEEE, 2012.

[29] E. Rodriguez-Diaz, J. C. Vasquez, and J. M. Guerrero, "Intelligent dc homes in future sustainable energy systems: When efficiency and intelligence work together," *IEEE Consumer Electronics Magazine*, vol. 5, no. 1, pp. 74–80, 2015.

[30] E. Rodriguez-Diaz, M. Savaghebi, J. C. Vasquez, and J. M. Guerrero, "An overview of low voltage dc distribution systems for residential applications," in *IEEE 5th International Conference on Consumer Electronics-Berlin (ICCE-Berlin)*, pp. 318–322, IEEE, 2015.

[31] T.-F. Wu, Y.-K. Chen, G.-R. Yu, and Y. Chang, "Design and development of dc-distributed system with grid connection for residential applications," in *8th International Conference on Power Electronics-ECCE Asia*, pp. 235–241, IEEE, 2011.

[32] E. Cetin, A. Yilanci, H. K. Ozturk, M. Colak, I. Kasikci, and S. Iplikci, "A micro-dc power distribution system for a residential application energized by photovoltaic–wind/fuel cell hybrid energy systems," *Energy and Buildings*, vol. 42, no. 8, pp. 1344–1352, 2010.

[33] H. Kakigano, Y. Miura, and T. Ise, "Low-voltage bipolar-type dc microgrid for super high quality distribution," *IEEE transactions on power electronics*, vol. 25, no. 12, pp. 3066–3075, 2010.

[34] J. S. C. Portal, "Yokohama smart city project (yscp)," *Retrieved from*, 2014.

[35] A. Jhunjhunwala, A. Lolla, and P. Kaur, "Solar-dc microgrid for indian homes: A transforming power scenario," *IEEE Electrification Magazine*, vol. 4, no. 2, pp. 10–19, 2016.

[36] L. Mackay, T. G. Hailu, G. C. Mouli, L. Ramírez-Elizondo, J. Ferreira, and P. Bauer, "From dc nano- and microgrids towards the universal dc distribution system-a plea to think further into the future," in *IEEE Power & Energy Society General Meeting*, pp. 1–5, IEEE, 2015.

[37] B. S. H. Chew, Y. Xu, and Q. Wu, "Voltage balancing for bipolar dc distribution grids: A power flow based binary integer multi-objective optimization approach," *IEEE Transactions on Power Systems*, vol. 34, no. 1, pp. 28–39, 2018.

[38] T. Dragicevic, J. C. Vasquez, J. M. Guerrero, and D. Skrlec, "Advanced lvdc electrical power architectures and microgrids: A step toward a new generation of power distribution networks.," *IEEE Electrification Magazine*, vol. 2, no. 1, pp. 54–65, 2014.

[39] L. Mackay, "Steps towards the universal direct current distribution system," 2018.

[40] D. Dong, I. Cvetkovic, D. Boroyevich, W. Zhang, R. Wang, and P. Mattavelli, "Grid-interface bidirectional converter for residential dc distribution systems—part one: High-density two-stage topology," *IEEE Transactions on Power Electronics*, vol. 28, no. 4, pp. 1655–1666, 2012.

[41] T. Hailu, L. Mackay, L. Ramirez-Elizondo, J. Gu, and J. Ferreira, "Voltage weak dc microgrid," in *IEEE First International Conference on DC Microgrids (ICDCM)*, pp. 138–143, IEEE, 2015.

[42] R. Farooq, L. Mateen, M. Ahmad, S. Q. Akbar, H. A. Khan, and N. A. Zaffar, "Smart dc microgrids: Modeling and power flow analysis of a dc microgrid for off-grid and weak-grid connected communities," in *IEEE PES Asia-Pacific Power and Energy Engineering Conference (APPEEC)*, pp. 1–6, IEEE, 2014.

[43] N. H. van der Blij, L. M. Ramirez-Elizondo, P. Bauer, and M. T. Spaan, "Design guidelines for stable dc distribution systems," in *2017 IEEE Second International Conference on DC Microgrids (ICDCM)*, pp. 279–284, IEEE, 2017.

[44] J. M. Guerrero, P. C. Loh, T.-L. Lee, and M. Chandorkar, "Advanced control architectures for intelligent microgrids—part ii: Power quality, energy storage, and ac/dc microgrids," *IEEE Transactions on industrial electronics*, vol. 60, no. 4, pp. 1263–1270, 2012.

[45] N. Bottrell, M. Prodanovic, and T. C. Green, "Dynamic stability of a microgrid with an active load," *IEEE Transactions on Power Electronics*, vol. 28, no. 11, pp. 5107–5119, 2013.

3 Smart Power Router for DC Residential Nanogrids

A smart power router based future DC house concept is introduced in this thesis. Main functionalities of the power router or DC grid manager are fast control, integration of renewables and storage, power management, demand response based on price signal, and islanding mode capability. Thus, the goal of this chapter is to develop and design a multi-port power converter as the smart power router for the DC house. The multi-active bridge (MAB) converter is selected as the toplogy for the smart power router.

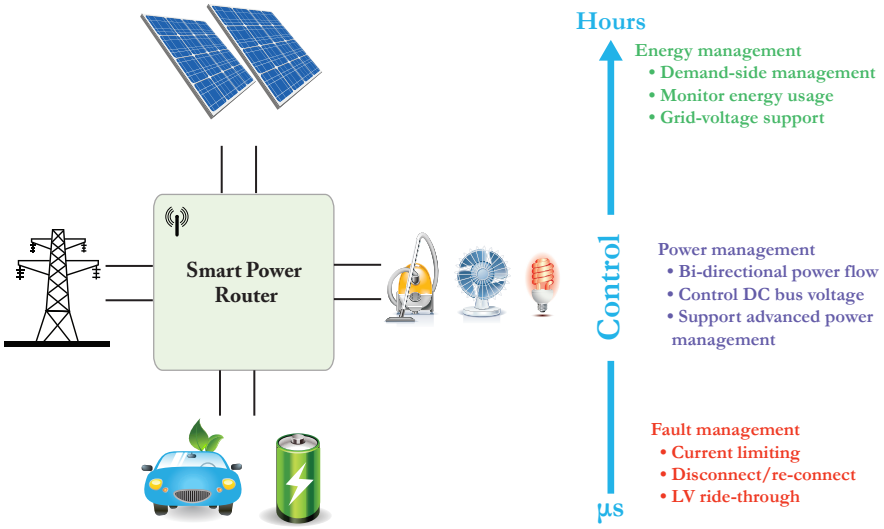

Based on:

1. "*A Multi-Active Bridge Converter with Inherently Decoupled Power Flows,*" in **IEEE Transactions on Power Electronics**, vol. 36, no. 2, pp. 2231-2245, Feb. 2021 DOI: 10.1109/TPEL.2020.3006266.
2. *"Decoupling control of Multi-Active Bridge Converter using Linear Active Disturbance Rejection"* in **IEEE Transactions on Industrial Electronics**, 2021 DOI: 10.1109/TIE.2020.3031531.

3.1 Introduction

In Chapter 2, a smart power-router based nanogrid concept is introduced as a promising architecture for future DC smart homes. The concept of 'smart power router' as a flexible interface of the different areas (cells) has been proposed previously for AC based active distribution networks (ADNs) grids [1]. In this thesis, the similar concept is used for DC low-voltage distribution grids and realized using a multi-port power electronic converter. The internal architecture of the proposed nanogrid and its integration to the DC utility microgrid is shown in Figure 3.1. The smart power router acts as the backbone of the DC nanogrid performing multiple hardware and control functions resulting in a safe, efficient, and robust operation.A multi-port power electronic converter is designed and developed in this chapter to serve as a smart power router.

Functions of a smart power router

As a smart power router, the primary purpose of the multi-port converter (MPC) is to integrate multiple sources/storages with different voltage and current ratings into a single power stage, allowing bi-directional power flow each port. Apart from bi-directional power flow, specific components like integrating electric vehicle (EV) also require galvanic isolation between the different ports for safety reasons. Further, the MPC is entrusted with the operation of the local renewable generation, load shedding, utilization of the static or mobile battery energy and other power management functions, as well as nanogrid stabilization and advanced, active islanding in the event of outages or other disturbances on the utility side. Finally, the MPC is expected to support the "weak" DC microgrid during congestion enabled by the utility operator's price tariff incentives.

Literature review

Many different multi-port power converter topologies that integrate photo-voltaics (PV), storage, and grid systems have been proposed in the literature. The topologies can be divided into categories: (a) non-isolated topologies, and (b) isolated topologies. Non-isolated topologies combine the single source, storage, or load converters via a common DC link [2–5]. On the other hand, isolated topologies combine the individual converters via one or more transformers. Therefore, isolated MPCs incorporate galvanic isolation and boost/buck functionalities using the transformer turns ratio. However, non-isolated MPC topologies are more efficient as there are fewer loss mechanisms compared to transformer-based

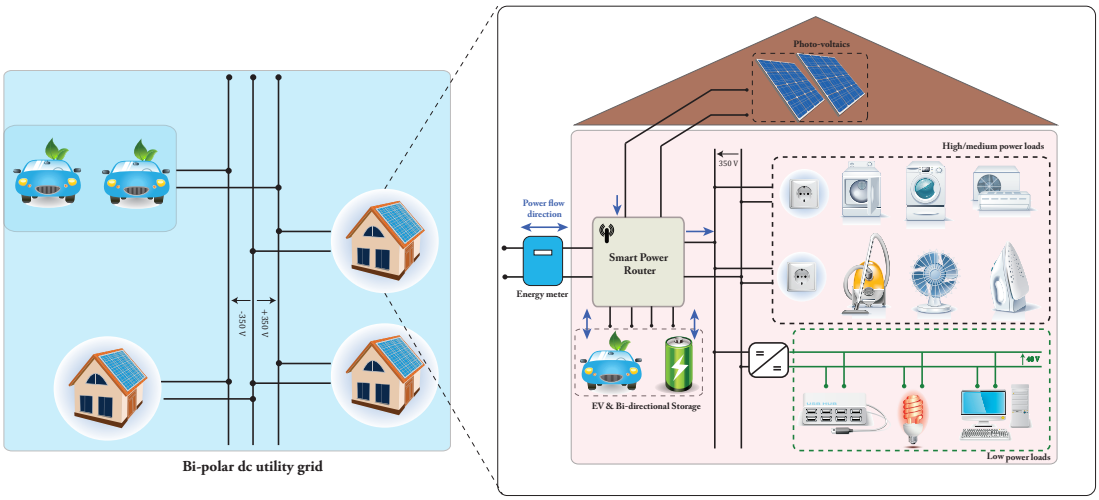

Figure 3.1: A smart power router based DC household nanogrid capable of integrating renewable sources, static or mobile battery storage, and supporting the utility DC microgrid.

MPCs. Figure 3.2 highlights a general classification of different multi-port converter families [6]. In this thesis, the isolated MPC family is selected as the focus for the search for a smart power router. The isolated multi-port converter family can be divided into two categories depending on the number of transformers: (a) multi-winding transformer-coupled MPC [7, 8], and (b) multi-transformer coupled MPC [9].

Multi-active bridge (MAB) converter

One of the promising topologies in the multi-winding transformer-coupled MPC family is the multi-active bridge (MAB) converter. The MAB converter consists of multiple inverter bridges (half-bridge or full-bridge) connected via a high frequency (HF) multi-winding transformer [7, 10, 11]. Derived from the dual-active bridge (DAB) converter family [12], the MAB converter not only integrates and exchanges the energy from/to all ports, but also provides full isolation among all ports and matches the different port voltage levels. Additionally, the MAB converter realizes bidirectional power flow by adjusting the phase-shift angle between the high-frequency AC voltages generated by the inverter module at each port. Figure 3.3 shows the topology of a generic n-port MAB converter.

A key challenge in the design and control of the MAB converter is the inherent cross-coupling of power flows between ports due to the inter-winding magnetic coupling of the transformer. Therefore, the MAB converter behaves as a multi-input multi-output (MIMO) system with coupled power loops, which is difficult to control. Thus, they inhibit the scalability of the number of ports in MAB converters and reduces their applicability.

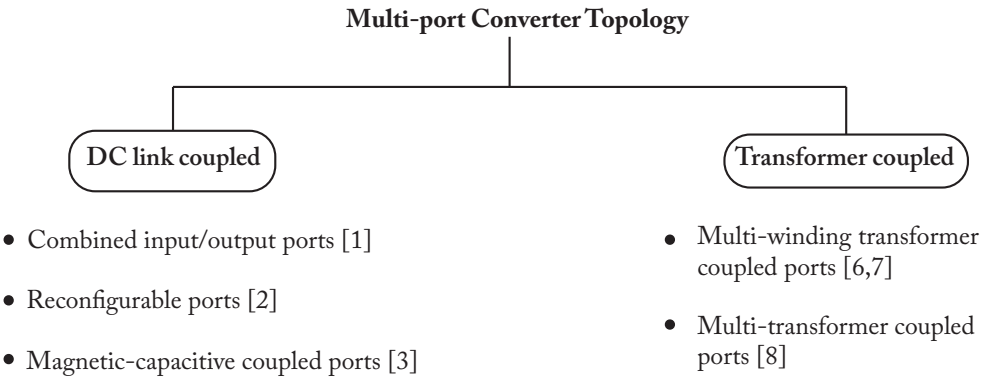

Figure 3.2: Classification of Multi-port converter topologies

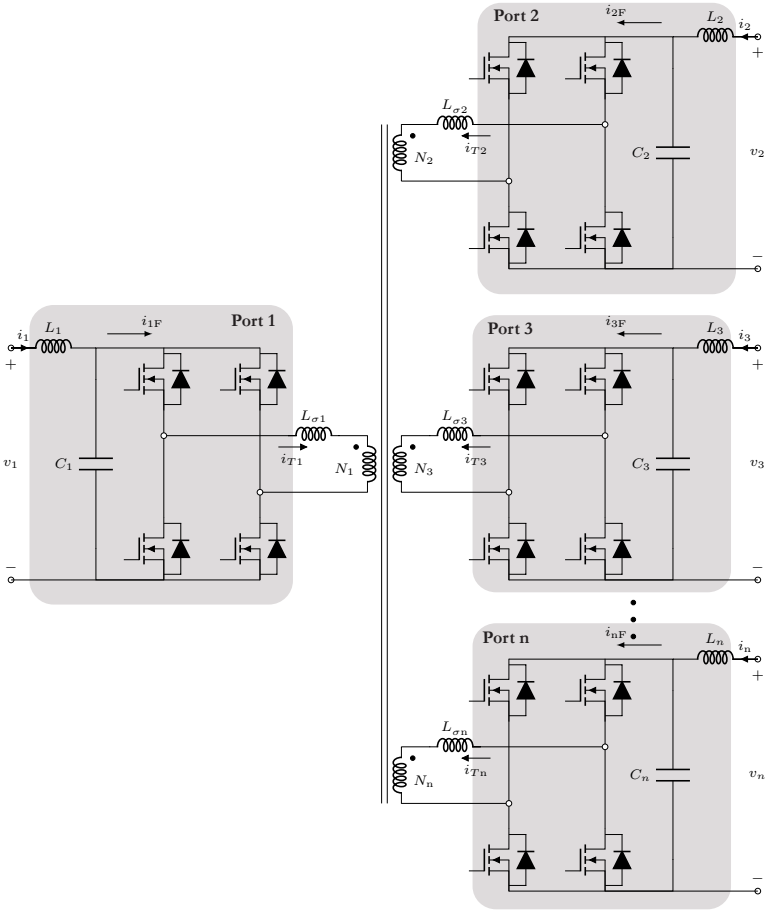

Figure 3.3: Topology of a Multi-active bridge (MAB) converter.

Contributions

This thesis proposes two solutions to the inherent coupling problem: (a) hardware solution, and (b) control solution. The proposed methods decompose the multivariable coupled control system into a series of independent single-loop subsystems. As a result, high bandwidth for each control loop and rapid dynamic response can be achieved independently. Besides, due to simple control requirements, this configuration enables the scalability of the number of ports without increasing any control complexity. A 2 kW, 100 kHz, Si-C based prototype of a four-port multi-active bridge converter or a quad-active bridge converter (QAB) is built and successfully tested in this thesis. The experimental results confirm the theoretical analysis and show the inherent decoupling and fast dynamic response. In summary, compared to existing literature, the main contributions of this work are:

1. Develop a generic Thevenin-Superposition based analytical power flow model for multi-active bridge (MAB) converters.
2. Introduce a hardware-based solution to the inherent coupling problem of MAB converters without adding extra hardware.
3. Derive design thumb rules to achieve near decoupling using an asymmetrical distribution of leakage inductances.
4. Introduce a distributed decoupling control strategy to solve MAB converters' inherent coupling problem using minimal system information.
5. Provide experimental validation of the proposed decoupling approaches in a four-port MAB converter prototype.
6. Present an in-depth analysis of the distribution of losses in the proposed asymmetric four-port MAB converter with experimental validation.

Chapter outline

This chapter is organized into six parts. The MAB converter's theory, along with the analysis of the power flow coupling, are reviewed in Section 3.2. Section 3.3 presents a hardware solution to the coupling problem of MAB converters along with an in-depth study on the limits of decoupling strategy. A control-based solution, the MAB coupling problem, is presented in Section 3.4. Simulations are performed on a four-port MAB converter or a quad-active bridge converter (QAB) to validate the theoretical claims in Section 3.5. Section 3.6 analyze the experimental results on the QAB converter laboratory prototype. Finally, general conclusions are summarized based on the analysis and the results.

3.2 Analysis of Multi-active bridge (MAB) topology

3.2.1 Operational theory and equivalent circuit

Figure 3.3 presents the topology of an n-port MAB converter comprised of n full-bridge modules magnetically coupled via an n-winding HF transformer. A star-equivalent model is used for analysing

the operation and switching conditions of the MAB converter as shown in Figure 3.4. The ports of the MAB converter are replaced by rectangular voltages sources in the equivalent circuit. For convenience, the magnetizing inductance L_{m}, the leakage inductances $L_{\sigma\mathrm{k}}$ and the generated AC voltages and AC currents are referred to port #1:

$$V_{\mathrm{k}}^{'} = \frac{N_1}{N_{\mathrm{k}}} V_{\mathrm{k}}, \quad i_{\mathrm{Tk}}^{'} = \frac{N_{\mathrm{k}}}{N_1} i_{\mathrm{Tk}}, \quad L_{\sigma\mathrm{k}}^{'} = \left(\frac{N_1}{N_{\mathrm{k}}}\right)^2 L_{\sigma\mathrm{k}} \tag{3.1}$$

The expression for voltage at the star-point (V_{x}) is obtained by applying theory of superposition to estimate the Thevenin voltage contribution of all the ports:

$$V_{\mathrm{x}} = \sum_{\mathrm{i}=1}^{n} \frac{\left(\sum\limits_{\mathrm{j}=1,\mathrm{j}\neq\mathrm{i}}^{n} \frac{1}{L_{\sigma\mathrm{j}}^{'}}\right)^{-1}}{L_{\sigma\mathrm{i}}^{'} + \left(\sum\limits_{\mathrm{j}=1,\mathrm{j}\neq\mathrm{i}}^{n} \frac{1}{L_{\sigma\mathrm{j}}^{'}}\right)^{-1}} V_{\mathrm{i}}^{'} \tag{3.2}$$

Therefore, the current slopes of the transfomer windings of the MAB equivalent circuit can be expressed as the following:

$$\frac{di_{\mathrm{Ti}}^{'}}{dt} = \frac{V_{\mathrm{x}} - V_{\mathrm{i}}^{'}}{L_{\sigma\mathrm{i}}^{'}} \tag{3.3}$$

The actual transformer currents can be obtained by integrating (3.3) over a switching period. The shape of the transformer currents is dependent on the type of modulation strategy used to modulate the star-point voltage V_{x}. Classically single phase-shift modulation strategy (SPS) is applied to most MAB converter solutions [10, 13]. According to the operating principles of SPS modulation, the MAB bridges generate the square-wave voltages V_{i} with a 50% duty cycle, and the phase shift between the driving signals for the bridges determines the power magnitude and direction. Figure 3.5 shows the idealized

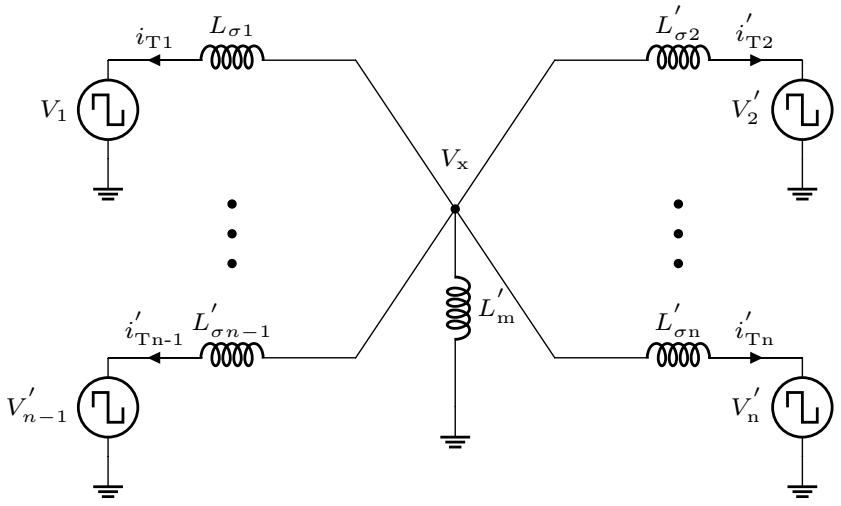

Figure 3.4: Star-equivalent model of a MAB topology.

transformer waveforms of a four-port MAB converter with SPS modulation strategy assuming unity DC conversion ratios. The expressions for the effective inductance between the ports and the power flow are derived in the upcoming scetion.

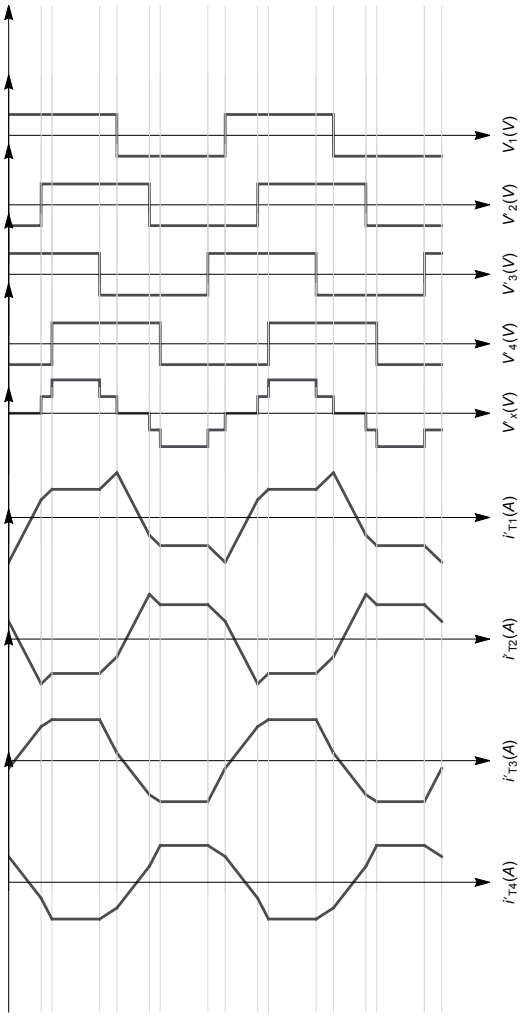

Figure 3.5: Idealized steady-state switching waveforms for unity-DC-conversion ratios and equal leakage inductances of a four-port MAB converter or a quad-active-bridge (QAB) converter.

3.2.2 Power flow and link inductances

MAB converter is a natural extension of the dual-active bridge (DAB) converter introduced in [12]. A DAB converter can be considered as a MAB converter with two active ports. Therefore, the power flow equations derived for DAB converters can be extended to a MAB converter. The cycle-to-cycle average

power transferred between port #i and port #j of a MAB converter is given by:

$$P_{\mathrm{ij}} = \frac{V_{\mathrm{i}}^{'} V_{\mathrm{j}}^{'}}{2\pi f_{\mathrm{s}} L_{\mathrm{ij}}} \phi_{\mathrm{ij}} \left(1 - \frac{|\phi_{\mathrm{ij}}|}{\pi}\right), \qquad \phi_{\mathrm{ij}} = \phi_{\mathrm{i}} - \phi_{\mathrm{j}} \tag{3.4}$$

where $V_{\mathrm{i}}^{'}$, $V_{\mathrm{j}}^{'}$ are the port DC voltages; L_{ij} is the equivalent inductance between ports #i and #j; f_{s} is the switching frequency; ϕ_{ij} is the phase-shift between the two square wave voltages at the corresponding transformer terminals. It is evident from (3.4) that to compute the power flow between ports #i and #j the equivalent inductance (L_{ij}) between two ports need to be calculated.

The star-equivalent circuit of MAB converters is already introduced in the previous section. However, the effective inductance between two ports is not readily obtained from the star representation. To that end, a delta MAB equivalent power flow model (see Figure 3.6) is built to analyze the power flow between the MAB ports. The MAB delta power flow model represents point to point DAB power flow between any two ports of an MAB converter. The computation of the effective link inductance between two MAB ports in the delta power flow model is presented next.

The Thevenin-equivalent inductance between any two ports #i and #j represented as L_{ij} is obtained by applying the theory of superposition on the star-equivalent MAB circuit. Thus, the voltage sources except the considered ports are shorted, resulting in the circuit shown in Figure 3.7a. The Thevenin inductance ($L_{\mathrm{TH,x}}$) between the rest of the circuit and the star-point is the parallel combination of leakage inductance of the remaining ports and the transformer magnetizing inductance:

$$L_{\mathrm{TH,x}}^{'} = \left(\frac{1}{L_{\mathrm{m}}^{'}} + \sum_{k\neq i,j}^{n} \frac{1}{L_{\sigma\mathrm{k}}^{'}}\right)^{-1} \simeq \left(\sum_{k\neq i,j}^{n} \frac{1}{L_{\sigma\mathrm{k}}^{'}}\right)^{-1} \tag{3.5}$$

Furthermore, it is assumed that the transformer magnetizing inductance is significantly higher than the leakage inductances of the port windings. The Thevenin equivalent AC voltage $V_{\mathrm{TH,x}}$ at the star port

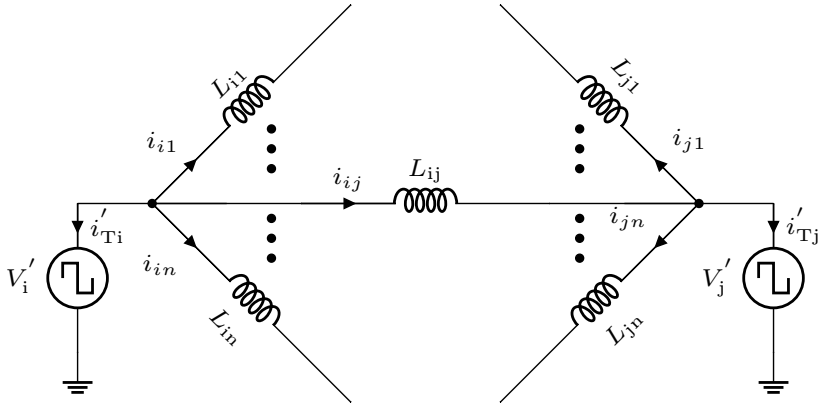

Figure 3.6: Delta power flow model of MAB converter topology.

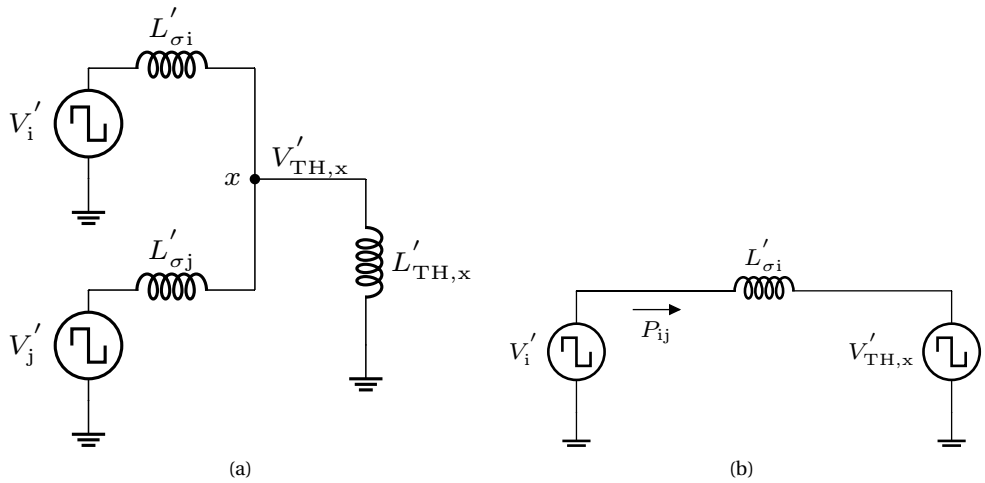

Figure 3.7: (a) Thevenin-equivalent impedance of the rest of the ports with the voltage sources short-circuited, (b) obtained thevnin-equivalent circuit of port #i with respect to star point x with the thevenin voltage contribution of port #j.

can be obtained as the superposition of voltages from ports #i and #j :

$$V'_{\mathrm{TH,x}} = \left(\frac{L'_{\sigma\mathrm{i}} \| L'_{\mathrm{TH,x}}}{L'_{\sigma\mathrm{i}} + L'_{\sigma\mathrm{i}} \| L'_{\mathrm{TH,x}}}\right) V'_{\mathrm{i}} + \left(\frac{L'_{\sigma\mathrm{j}} \| L'_{\mathrm{TH,x}}}{L'_{\sigma\mathrm{j}} + L'_{\sigma\mathrm{j}} \| L'_{\mathrm{TH,x}}}\right) V'_{\mathrm{j}} \tag{3.6}$$

Since the active power transfer from star point x to the ground is zero, the active power transfer between port #i and port #j is equal to the active power transfer between port #i and star point x resulting the DAB equivalent circuit between port #i and star-point x as seen in Figure 3.7b. Therefore, applying the DAB power flow equation (3.4) between V'_{i} and $V'_{\mathrm{TH,x}}$, the active power can be written as:

$$P_{\mathrm{ij}} = \frac{V'_i V'_{\mathrm{TH,x}}}{2\pi f_{\mathrm{s}} L'_{\sigma\mathrm{i}}} \phi_{\mathrm{ij}} \left(1 - \frac{|\phi_{\mathrm{ij}}|}{\pi}\right) \tag{3.7}$$

Further, it must be noted that while computing the power flow between port #i and star point x, the voltage contribution of V'_{i} in $V'_{\mathrm{TH,x}}$ would not result in active power flow since it is in phase with itself. Therefore, substituting only the contribution of V'_{j} in (3.6) into (3.7), the generic power flow equation between two ports in a MAB converter can be derived as:

$$P_{\mathrm{ij}} = \frac{V'_{\mathrm{i}} V'_{\mathrm{j}}}{2\pi f_{\mathrm{s}} \left(L'_{\sigma\mathrm{i}} + L'_{\sigma\mathrm{j}} + \frac{L'_{\sigma\mathrm{i}} L'_{\sigma\mathrm{j}}}{L'_{\mathrm{TH,x}}}\right)} \phi_{\mathrm{ij}} \left(1 - \frac{|\phi_{\mathrm{ij}}|}{\pi}\right) \tag{3.8}$$

Therefore, comparing (3.8) to the DAB power flow form (3.4) and combining with (3.5), the link induc-

tance L_{ij} between ports #i and #j can be formulated as:

$$L_{ij} = \begin{cases} \text{NA}, & \forall i = j \\ L'_{\sigma i} + L'_{\sigma j} + L'_{\sigma i} L'_{\sigma j} \left(\sum_{k \neq i,j}^{n} \frac{1}{L'_{\sigma k}} \right), & \forall i \neq j \end{cases} \tag{3.9}$$

3.2.3 Dynamic model and control of MAB converter

The power flow between any two ports in a MAB converter is presented in equation (3.8). Based on the equation, the power flow can be controlled by: (a) the phase-shift angle ϕ_{ij} between the square wave voltages, (b) the switching frequency f_s, and (c) the port voltages V_i and V_j which can be altered by the pulse-width of the square wave voltages. Among the possible solutions, the single phase shift modulation (SPS) is considered to be the simplest as both the magnitude and the direction of the power flow can be controlled by the single variable phase-shift angle ϕ_{ij} [13]. Additionally, a hybrid approach of both phase-shift and duty-cycle modulation can be employed to achieve soft-switching and thus lead to the higher efficiency of MAB converters [14]. Since the goal of this thesis is to investigate the power flow decoupling of the MAB converter, single phase-shift modulation is considered as the modulation strategy. The MAB control formulation and the dynamic modeling of the converter are discussed in the following.

For controlling a generic n-port MAB system, (n-1) degrees of freedom [ϕ_i, i$\in (2, n)$] are available as the control variables. Based on the application, different control objectives can be set at different ports of the MAB converter. For example, the port current will be the control objective for the port connected to a battery. On the other hand, ports connected to sources like photo-voltaic (PV) panels or loads, voltage regulation will be the control objective. For simplicity, the port currents are considered as control objectives in this thesis. This approach is sufficient to analyze the power flow coupling of MAB converter systems without loss of generality.

Analyzing the controllability of the MAB system requires a small signal model describing the relationship between the control inputs and outputs. Generally, state-space averaging technique is used to model the dynamic behavior of DC-DC converters [15, 16]. However, in the case of isolated DC-DC converters like the MAB converter, one of the state-variable is the transformer current, which does not satisfy the small-ripple approximation [17–19]. Since the power flow coupling can be analyzed by low-frequency dynamics, the influence of the high-frequency leakage inductor dynamics of the transformer can be neglected [10, 14, 20]. To that end, an approximate control-oriented small signal system model can be derived by linearizing the system at a DC operating point. The currents at different ports of the MAB converter before the DC side filters, as shown in Figure 3.3 can be expressed in equation form in the following:

$$i_{Fi} = \frac{P_i}{V_i} = \frac{\sum_{j \neq i}^{n} P_{ij}}{V_i}, \qquad \forall i \in (1, n) \tag{3.10}$$

Combining (3.10) with (3.4) the following expression for the ith port current is obtained:

$$i_{\mathrm{Fi}} = \sum_{j \neq i}^{n} \frac{V_{\mathrm{j}}}{2\pi f_{\mathrm{s}} L_{\mathrm{ij}}} f(\phi_{\mathrm{ij}}), \quad \forall i \in (1,n) \tag{3.11}$$

where $f(\phi)$ is a non-linear function of the control variables defined as following based on power flow equation (3.8):

$$f(\phi_{\mathrm{ij}}) = f(\phi_{\mathrm{i}} - \phi_{\mathrm{j}}) = \phi_{\mathrm{ij}}\left(1 - \frac{|\phi_{\mathrm{ij}}|}{\pi}\right) \tag{3.12}$$

Since the state variables or port currents are a non-linear function of the control inputs, the system needs to linearzied at a DC operating point. The nominal plant is assumed to be lossless, and only the predominant dynamics associated with the filters at the DC side of each port have been considered herein. The Taylor series expansion of above port currents at an operating point A is:

$$I_i = I_{\mathrm{i,A}} + \Delta I_{\mathrm{i,A}} \tag{3.13}$$

$$\Delta I_{\mathrm{i,A}} = \sum_{j \neq i}^{n} G_{\mathrm{ij}} \Delta\phi_{\mathrm{ij}}, \qquad \forall \mathrm{i} \in (1,n) \tag{3.14}$$

$$G_{\mathrm{ij}} = \frac{\partial I_{\mathrm{i,A}}}{\partial \phi_{\mathrm{ij}}} \qquad \forall \mathrm{i} \in (1,n) \tag{3.15}$$

Since it is always the phase shift between ports enable the power transfer, in order to simply the control, the phase of port 1 can be fixed to be zero. Therefore, the small signal gain matrix of the MAB converter can be expressed as:

$$\Delta\mathbf{I} = \begin{bmatrix} \Delta I_2 \\ \Delta I_3 \\ \vdots \\ \Delta I_{\mathrm{i}} \\ \vdots \\ \Delta I_{\mathrm{n}} \end{bmatrix} = \begin{bmatrix} G_{22} & G_{23} & .. & .. & G_{2n} \\ G_{32} & G_{33} & .. & .. & G_{3n} \\ \vdots & \vdots & .. & .. & \vdots \\ G_{\mathrm{i2}} & G_{\mathrm{i3}} & .. & .. & G_{\mathrm{in}} \\ \vdots & \vdots & .. & .. & \vdots \\ G_{\mathrm{n2}} & G_{\mathrm{n3}} & .. & .. & G_{\mathrm{nn}} \end{bmatrix} \begin{bmatrix} \Delta\phi_2 \\ \Delta\phi_3 \\ \vdots \\ \Delta\phi_{\mathrm{i}} \\ \vdots \\ \Delta\phi_{\mathrm{n}} \end{bmatrix} = \mathbf{G}\Delta\phi \tag{3.16}$$

where, the expressions of the gain elements $G_{\mathbf{ij}}$ $\forall[i,j]$ in the matrix can be expressed as:

$$G_{\mathrm{ij}} = \begin{cases} \sum\limits_{p \neq i}^{n} \dfrac{V_{\mathrm{p,A}}}{2\pi f_{\mathrm{s}} L_{\mathrm{ip}}}\left(1 - \dfrac{2|\phi_{\mathrm{i,A}} - \phi_{\mathrm{p,A}}|}{\pi}\right), & \forall[i=j] \\ -\dfrac{V_{\mathrm{j,A}}}{2\pi f_{\mathrm{s}} L_{\mathrm{ij}}}\left(1 - \dfrac{2|\phi_{\mathrm{j,A}} - \phi_{\mathrm{i,A}}|}{\pi}\right), & \forall[i \neq j] \end{cases} \tag{3.17}$$

Since G_{ij} $\forall[i,j]$ are all non-zero entities, the resulting control input to output gain matrix **G** becomes a non-diagonal matrix. The ratio of the non-diagonal terms G_{ij} $\forall[i \neq j]$ to the diagonal elements of the gain matrix **G** represents the degree of cross-coupling between the individual control loops [21]. This concludes the mathematical analysis to quantify the power flow coupling of MAB converters.

3.2.4 Decoupling control of MAB converter: conventional approach

The mutual interaction can be eliminated by using a special pre-compensator or decoupling network which decomposes a multivariable control system into a series independent single-loop subsystems. Thus, the system can be controlled via independent loop controllers. This is known as the conventional decoupling control (CDC) for MAB converters [14].

To achieve independent control loops, the effective input to output gain matrix **X** needs to be a diagonal matrix:

$$\mathbf{X} = \mathbf{GH} = \begin{bmatrix} x_2 & 0 & 0 \\ 0 & x_3 & 0 \\ 0 & 0 & x_4 \end{bmatrix} \tag{3.18}$$

Therefore, the decoupling network can be designed as :

$$\mathbf{H} = \begin{bmatrix} H_{22} & H_{23} & H_{23} \\ H_{32} & H_{33} & H_{34} \\ H_{42} & H_{43} & H_{44} \end{bmatrix} = \mathbf{G}^{-1}\mathbf{X} \tag{3.19}$$

For every operating point, the small signal transfer function matrix of the converter **G** is only a constant, i.e., no pole or zero is involved since the inductor dynamics are already neglected, and so does the

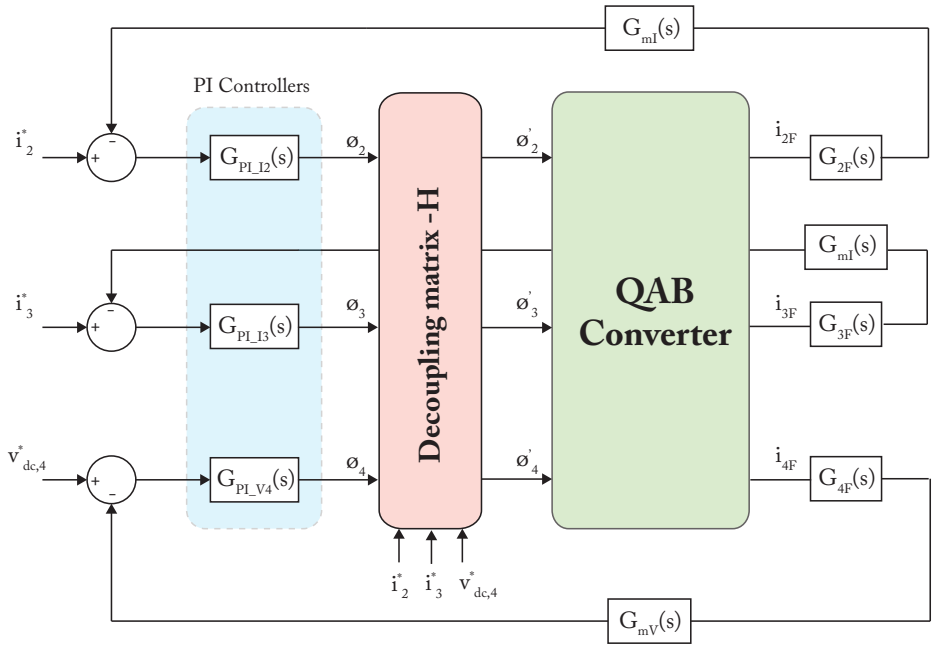

Figure 3.8: Conventional decoupling control (CDC) of MAB converter with a pre-compensator decoupling network **H**. The gains of decoupling matrix are pre-calculated and stored as look-up table for optimal decoupling performance.

decoupling network , which is the inverse matrix of the plant matrix **G**. Therefore, based on the operating point, the elements of the decoupling matrix **H** can be calculated in advance and be stored as lookup tables.

3.3 Decoupling control of MAB converters: hardware approach

A modified configuration of the MAB is proposed and described in detail in this section, which inherently decouples inter-port flows. The small-signal model developed in Section 3.2.3 is applied to investigate the degree of the cross-coupling associated with the proposed configuration. Finally, a qualitative comparison between the proposed solution and the existing solution reported in the literature.

Section 3.2.4 showed that the inter-port MAB power flow is dependent on the leakage inductance associated with the individual ports. The leakage inductances can be realized by incorporating them into the design of the multi-winding transformer. This approach, however, results in higher losses in the transformer. As a result, the leakage inductances are realized by adding external inductors to the windings of the transformer, resulting in higher design flexibility [10, 14]. Figure 3.9 presents the star equivalent model of the proposed MAB configuration based on external leakage inductors. Compared to the conventional MAB configuration (see figure 3.3), an external leakage inductor of one of the ports is omitted. This port is referred to as the 'master' port and all other ports are referred to as the 'slave port'. Depending on the application, a stiff-voltage source like a grid or a battery should be connected to the

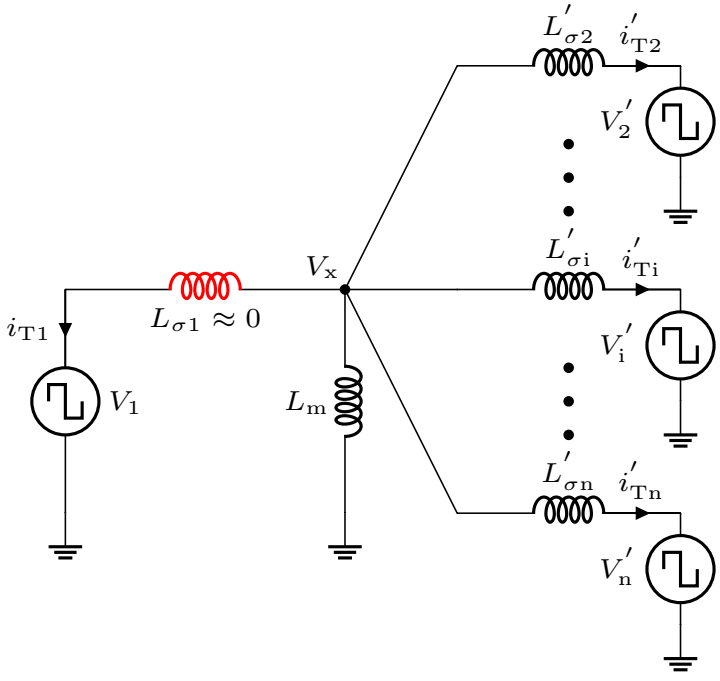

Figure 3.9: Star equivalent circuit of the proposed MAB converter configuration with port #1 as the master port, i.e $L_{\sigma 1} \approx 0$.

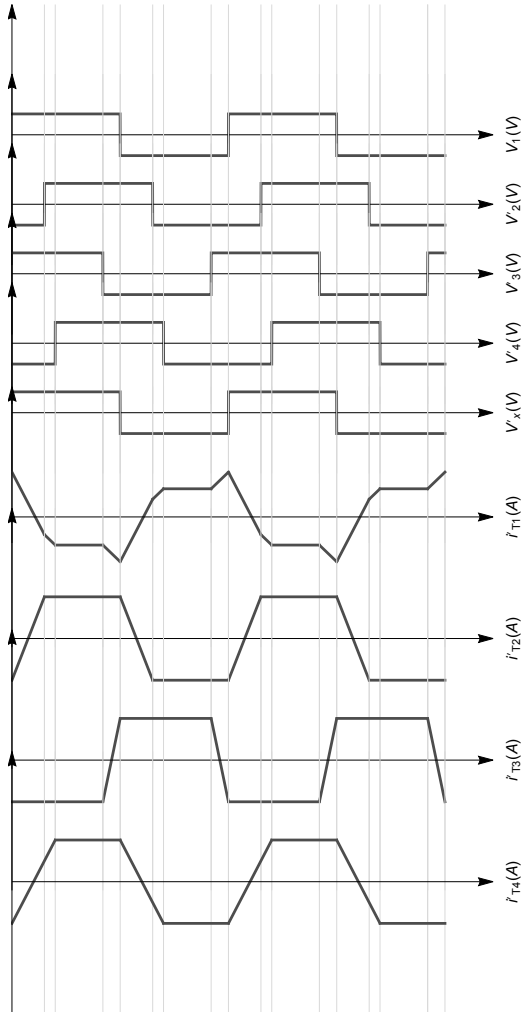

Figure 3.10: Idealized steady-state switching waveforms for unity-DC-conversion ratios and equal link inductances of the proposed four-port MAB converter.

master port. Since the leakage inductance of the master port transformer winding is significantly lower than the slave ports, it essentially regulates the voltage across the magnetizing impedance transformer, thus decoupling the power flow between the slave ports. However, the 'master' port leakage inductance is not zero in practical applications. The winding of the transformer linked to the master port has its own leakage inductance. A sensitivity analysis of the 'master' port leakage inductance on the dynamic decoupling performance of the control loops is conducted in Section 3.5.2.

3.3.1 Equivalent circuit and waveforms

Figure 3.9 shows the star-equivalent circuit of the proposed configuration. Similar to the analysis presented in Section 3.2, the voltage at the star-point (V_X) and the current slopes of the transfomer

windings of the proposed MAB converter can be expressed as the following:

$$V_{\mathrm{x}} = V_1 \tag{3.20}$$

$$\frac{\mathrm{d}i_{\mathrm{Ti}}^{'}}{\mathrm{d}t} = \frac{V_1 - V_{\mathrm{i}}^{'}}{L_{\sigma\mathrm{i}}^{'}}, \qquad \forall i \in [2,n] \tag{3.21}$$

The inductor currents of the ports of the proposed MAB converter can be obtained by integrating (3.21). Figure 3.10 shows the idealized waveforms of a four-port MAB converter with a null-leakage inductor at port #1. Comparing the waveforms in Figure 3.10 to the conventional MAB converter waveforms in Figure 3.5, it can be observed that the shape of the slave port inductor currents ($i_{\mathrm{T2}}^{'}, i_{\mathrm{T3}}^{'}, i_{\mathrm{T4}}^{'}$) are trapezoidal in nature similar to DAB converter. However, the master port inductor current (i_{T1}) is not trapezoidal since it is a superposition of the all the trapezoidal slave port inductor currents.

Since the slave port transformer currents are essentially similar to that of DAB converters, all modulation strategies applicable to DAB converters like trapezoidal modulation (TZM), triangular modulation (TRM), and hybrid methods can be applied to improve efficiency. Additionally, the soft switching boundaries of the ports are independent of the operating points of the other ports. Therefore, it is easier to design duty-cycle based soft-switching control of the proposed low leakage port MAB Configuration [14, 22].

3.3.2 Link inductances and power flow

The proposed MAB configuration is a special case of the conventional configuration with the leakage inductance of the master port reduced removed. Re-writing the link inductance expression L_{ij} of (3.9) with selecting port #1 as the master port, i.e $L_{\sigma 1} \approx 0$:

$$L_{\mathrm{ij}} = \begin{cases} \mathrm{NA}, & i = j \\ L_{\sigma\mathrm{j}}^{'}, & i = 1, j \neq 1 \\ L_{\sigma\mathrm{i}}^{'}, & i \neq 1, j = 1 \\ \infty, & i \neq 1, j \neq 1, i \neq j \end{cases} \tag{3.22}$$

Therefore, the generic power flow equation for the proposed configuration can be subdivided into two cases: (a) power flow equation between the master port and any slave port, and (b) power flow between any two slave ports:

$$P_{\mathrm{ij}} = \begin{cases} 0, & i \neq 1, \forall j \in [2,n] \\ 0, & j \neq 1, \forall i \in [2,n] \\ \dfrac{V_{\mathrm{i}}^{'} V_{\mathrm{j}}^{'}}{2\pi f_{\mathrm{s}} L_{\mathrm{ij}}} \phi_{\mathrm{ij}} \left(1 - \dfrac{|\phi_{\mathrm{ij}}|}{\pi}\right), & i = 1, \forall j \in [2,n] \\ \dfrac{V_{\mathrm{i}}^{'} V_{\mathrm{j}}^{'}}{2\pi f_{\mathrm{s}} L_{\mathrm{ij}}} \phi_{\mathrm{ij}} \left(1 - \dfrac{|\phi_{\mathrm{ij}}|}{\pi}\right), & j = 1, \forall i \in [2,n] \end{cases} \tag{3.23}$$

Based on the power flow equation derived for the proposed MAB configuration, a small signal model is developed in the following section.

3.3.3 Small signal model and controllability

The pre-filtered currents at different ports of the proposed MAB converter can be expressed in equation form in the following:

$$i_{\mathrm{Fi}} = \begin{cases} \dfrac{\sum_{j\neq i}^{n} P_{\mathrm{ij}}}{V_{\mathrm{i}}}, & i = 1 \\ \dfrac{P_{\mathrm{i1}}}{V_{\mathrm{i}}}, & i \neq 1, i\forall \in [2,n] \end{cases} \tag{3.24}$$

Combining the above equations with the power flow equation (3.4), they can be expressed as the following:

$$i_{\mathrm{Fi}} = \begin{cases} \sum_{j\neq i}^{n} \dfrac{V_{\mathrm{j}}}{2\pi f_{\mathrm{s}} L_{\sigma \mathrm{j}}} f(\phi_{\mathrm{i}} - \phi_{\mathrm{j}}), & i = 1 \\ \dfrac{V_1}{2\pi f_{\mathrm{s}} L_{\sigma \mathrm{j}}} f(\phi_1 - \phi_{\mathrm{i}}), & \forall i \in [2,n] \end{cases} \tag{3.25}$$

Since the port #1 is selected as the "master" port, it acts as the slack bus and the phase shift of this port is fixed at 0. The phase shifts of the slave ports are used to control their respective currents. Linearizing the system at a certain operating point A, and applying the Taylor series expansion of above port currents as carried out previously in (3.13) - (3.15) the small signal gains from input (ϕ_2, ... , ϕ_{n}) to output (i_2, ... , i_{n}) can be derived as following:

$$G_{\mathrm{ij}} = \begin{cases} 0, & \forall [i \neq j] \\ \dfrac{V_{1,\mathrm{A}}}{2\pi f_{\mathrm{s}} L_{\sigma \mathrm{i}}} \left(1 - \dfrac{2|\phi_{\mathrm{i,A}} - \phi_{1,\mathrm{A}}|}{\pi}\right), & \forall [i = j] \in [2,n] \end{cases} \tag{3.26}$$

Therefore, the small signal gain matrix of the proposed MAB converter configuration can be expressed as:

$$\Delta \mathbf{i} = \begin{bmatrix} \Delta i_2 \\ \Delta i_3 \\ : \\ \Delta i_{\mathrm{i}} \\ : \\ \Delta i_n \end{bmatrix} = \begin{bmatrix} G_{22} & 0 & .. & .. & 0 \\ 0 & G_{33} & .. & .. & 0 \\ : & : & .. & .. & : \\ 0 & 0 & .. & G_{ii} & 0 \\ : & : & .. & .. & : \\ 0 & 0 & .. & .. & G_{nn} \end{bmatrix} \begin{bmatrix} \Delta\phi_2 \\ \Delta\phi_3 \\ : \\ \Delta\phi_i \\ : \\ \Delta\phi_n \end{bmatrix} = \mathbf{G}\Delta\phi \tag{3.27}$$

It can be observed that the small-signal gain matrix of the proposed configuration is a diagonal matrix with all the non-diagonal elements approaching zero. Therefore, there is no cross-coupling between the control loops. Compared to existing solutions for the power flow decoupling in literature, the proposed MAB configuration has several advantages. The main advantage of the proposed topology is that it is essentially decomposing a tightly coupled MIMO network into multiple independent SISO systems.

3.4 Decoupling of MAB converters: control approach

In this section, a control strategy known as active disturbance rejection control (ADRC) is introduced as a solution to decouple the control loops in MAB converters. ADRC belongs to the class of control algorithms designed to control systems with uncertainities and disturbances [23]. In essence, ADRC uses an observer to track disturbances in real-time and actively compensates for it. Therefore, it has found use in a wide range of industrial application like mechatronics, chemical or process, aerospace etc. which require robust control for higher reliability [24–26]. In general, ADRC is used in removing disturbances in single input-single output (SISO) systems. However, the versatility and flexibility of ADRC has led to its utilization for multi-variable decoupling control for non-linear multiple-input multiple-output (MIMO) systems [27–29].

3.4.1 Fundamentals of ADRC

To explain ADRC, an approximate second order plant is considered in the following form:

$$\ddot{y} = -a_1\dot{y} - a_2 y + w + bu \tag{3.28}$$

where y is the output, u is the input, and w is the disturbance term which can be a combination of external and internal factors. The second-order plant can be re-written as the following:

$$\begin{aligned}\ddot{y} &= -a_1\dot{y} - a_2 y + w + (b - b_0)u + b_0 u \\ &= f(t, y, \dot{y}, w) + b_0 u\end{aligned} \tag{3.29}$$

where the lumped term $f(t, y, \dot{y}, w)$ represents the combination of internal dynamics $-a_1\dot{y} - a_2 y + (b - b_0)u$ and the extrenal disturbance w. The term b_0 takes into account the possible disturbances coming from the input signal. It is approximated from nominal values of the energy storage elements in the plant equation.

ADRC principle stipulates that if the lumped disturbances represented by $f(t, y, \dot{y}, w)$ can be estimated (or observed) in real time, they can be actively compensated without the need for a mathematical model. To that end, a linear extended state observer (ESO) is built to observe the states of the system including the disturbance in real time.

ESO Observer Design

To observe the second order plant in (3.29), the following states are defined:

$$x_1 = y, \qquad x_2 = \dot{y}, \qquad x_3 = f(t, y, \dot{y}, w) \tag{3.30}$$

Additionally, we assume that the dynamics of the disturbance term $h = \dot{f}(t, y, \dot{y}, w)$ is bounded. Therefore, the state space form becomes:

$$\begin{aligned}\dot{x} &= Ax + Bu + Eh \\ y &= Cx\end{aligned} \tag{3.31}$$

where the state-space matrices are $A = \begin{bmatrix} 0 & 1 & 0 \\ 0 & 0 & 1 \\ 0 & 0 & 0 \end{bmatrix}$, $B = [0 \quad b_0 \quad 0]^{\mathrm{T}}$, $C = [1 \quad 0 \quad 0]$, and $E = [0 \quad 0 \quad 1]^{\mathrm{T}}$.
A standard linear Luenberger observer can be designed based on this system:

$$\begin{aligned} \dot{z} &= Az + Bu + L(y - \hat{y}) \\ \hat{y} &= Cz \end{aligned} \tag{3.32}$$

where L = $[\beta_1 \ \beta_2 \ \beta_3]^{\mathrm{T}}$ is the observer gain and z is the observer estimate for the system states x. Using bandwidth parameterization [30], the gains of the observer can be chosen as:

$$\beta_1 = 3\omega_{\mathrm{o}} \quad \beta_2 = 3\omega_{\mathrm{o}}^2 \quad \beta_3 = \omega_{\mathrm{o}}^3 \tag{3.33}$$

where ω_{o} is the bandwidth of the observer. Higher the ω_{o}, faster the observer. However, in practical implementation, the observer bandwidth is limited by hardware constraints like sensor noises and sampling rates. Since the lumped disturbance is defined as a state, this is also known as extended state observer (ESO).

Control law

Once the observer is well tuned, the outputs can track the y, $\dot{y}$ and the lumped disturbance term $\dot{f}(t, y, \dot{y}, w)$ via the terms z_1, z_2, and z_3 respectively. Hence, ADRC actively compensates the influence of the disturbance term by cancelling the z_3 term of the ESO. The control law can be formulated as the following:

$$u = \frac{u_0 - z_3}{b_0} \tag{3.34}$$

which effectively reduces the second order plant as described in (3.29) into:

$$\ddot{y} = u_0 \tag{3.35}$$

which is a straightforward control problem to solve since the steady state error is zero. A simple PD controller of the following form is sufficient:

$$u_0 = k_{\mathrm{p}}(r - z_1) - k_{\mathrm{d}} z_2 \tag{3.36}$$

The ADRC controller schematic for a second-order plant is shown in Figure 3.11. However, this approach is not exclusive to second order systems. With few modifications it can be applied to first-order systems as well. In case of first-order plants, the derivative term $\dot{y}$ is absent in the lumped disturbance term $f(t, y, \dot{y}, w)$. Thus, the ESO observes only the state y and the disturbance term. Hence, a proportional controller is sufficient in ADRC control design of first-order plants.

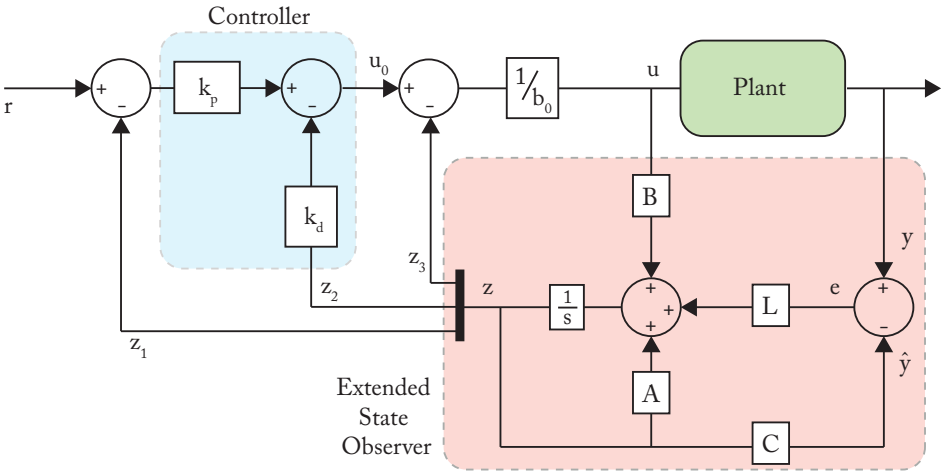

Figure 3.11: ADRC controller schematic of a second-order plant.

3.4.2 ADRC formulation of QAB converter

Conventional control methods to decouple MIMO interactions like traditional feed-forward compensator [14] require detailed understanding of the term term $f(t, y, \dot{y}, w)$ before the control design can be carried out. Classic ADRC approach observes the lumped disturbance to a system and actively compensates for it in real-time. Therefore, ADRC can be used as decoupling control of a MIMO system like multi-active bridge (MAB) converter by modeling the inherent coupling as an observable disturbance. A SISO ADRC controller is then designed for each port of the converter. A four-port MAB converter or a quad-active bridge converter (QAB) is shown in Figure 3.14.

The QAB converter comprises of four ports: three bi-directional voltage sourced ports, and a load port consisting of a resistor in parallel with a capacitor. In the control system, there are three control loops: two current loops for the bi-directional voltage sources in port #2 and port #3; and a voltage control loop for the resistive load in port #4 with R_{load}. This particular combination is selected as it includes the two typical operation modes. Therefore, it is representative and generic. Designing SISO ADRC controllers for each port requires information about the order of that port. The order of a port is decided by the order of the DC side filter. Thus, current controlled ports (#2 and #3) with LC filter are second order plants and the RC load port is a first order plant. The ADRC formulation described in Section 3.4.1 is applied to the individual port control loops of the QAB converter.

Current controlled ports

Port #2 and #3 are the current controlled ports in the QAB converter with LC filter. The ADRC formulation of port #2 is shown here which is also applicable to port #3. Figure 3.12a shows the circuit schematic of port #2 with the relevant filter current components. The ADRC modelling of a second order plant as shown in section 3.4.1 is applied to this port. Applying KVL and KCL at the node O, the

following inductor current and capacitor voltage dynamics are obtained:

$$L_{f2}\frac{di_2}{dt} = V_{DC,2} - V_{Cf2} - r_{f2}i_2 \tag{3.37}$$

$$\begin{aligned} C_{f2}\frac{dV_{Cf2}}{dt} &= i_2 - i_{2F} \\ &= i_2 - (G_{22}\phi_2 + G_{23}\phi_3 + G_{24}\phi_4) \end{aligned} \tag{3.38}$$

where r_{f2} is the lumped parasitic resistance of the LC filter. Differentiating (3.37) and combining with (3.38) the following is obtained:

$$\begin{aligned} \frac{d^2i_2}{dt^2} &= -\frac{1}{L_{f2}}\frac{dV_{Cf2}}{dt} - \frac{r_{f2}}{L_{f2}}\frac{di_2}{dt} \\ &= -\frac{1}{L_{f2}C_{f2}}[i_2 - (G_{22}\phi_2 + G_{23}\phi_3 + G_{24}\phi_4)] - \frac{r_{f2}}{L_{f2}}\frac{di_2}{dt} \\ &= -\frac{i_2}{L_{f2}C_{f2}} - \frac{r_{f2}}{L_{f2}}\frac{di_2}{dt} + \frac{G_{23}}{L_{f2}C_{f2}}\phi_3 + \frac{G_{24}}{L_{f2}C_{f2}}\phi_4 + \left(\frac{G_{22}}{L_{f2}C_{f2}} - b_{2,0}\right)\phi_2 + b_{2,0}\phi_2 \\ &= f_2(t, i_2, \dot{i}_2, w_b) + b_{2,0}\phi_2 \end{aligned} \tag{3.39}$$

where $f_2(t, i_2, \dot{i}_2, w_b)$ represents the combined disturbances due to internal dynamics and external disturbances due to the inherent coupling of state i_2 with inputs of other ports ϕ_3 and ϕ_4. The term $b_{2,0}$ can be estimated by the following:

$$b_{2,0} = \frac{G_{22,0}}{L_{f2,0}C_{f2,0}} \tag{3.40}$$

where $G_{22,0}$, $L_{f2,0}$ and $C_{f2,0}$ are the nominal values of the parameters G_{22}, L_{f2} and C_{f2}. In theory, ADRC is capable to rejecting uncertainities in estimating $b_{2,0}$.

Based on the methodology introduced in section 3.4.1, an extended-state-observer (ESO) is designed

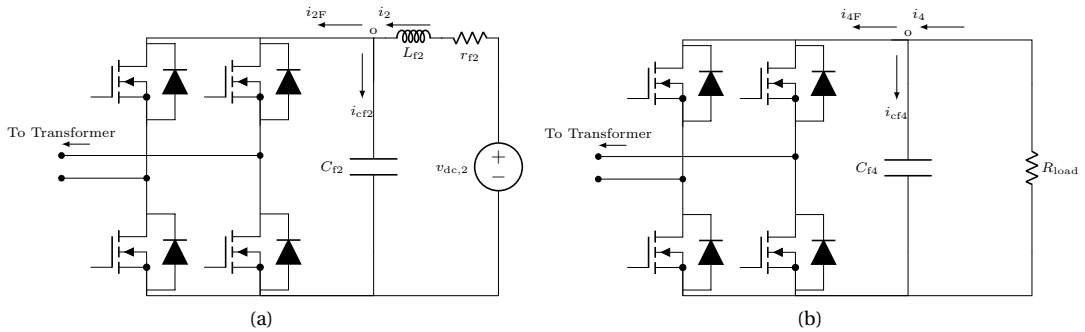

Figure 3.12: Circuit schematic of QAB converter ports: (a) second order current control port #2 with LC filter, (b) first order voltage control port #4 with only capacitor filter.

to observe the disturbance $f_2(t, i_2, \dot{i}_2, w_\mathrm{b})$:

$$\begin{cases} \dot{z}_\mathrm{c} = [A_\mathrm{c} - L_\mathrm{c}C_\mathrm{c}]z_\mathrm{c} + [B_\mathrm{c} \quad L_\mathrm{c}]u_\mathrm{c} \\ y_\mathrm{c} = z_\mathrm{c} \end{cases}$$

where $z_\mathrm{c} = [z_{\mathrm{c}1} \quad z_{\mathrm{c}2} \quad z_{\mathrm{c}3}]^\mathrm{T}$ is the observer output tracking i_2, $\dot{i}_2$, and $f_2(t, i_2, \dot{i}_2, w_\mathrm{b})$ respectively. The state space matrices are $A_\mathrm{c} = \begin{bmatrix} 0 & 1 & 0 \\ 0 & 0 & 1 \\ 0 & 0 & 0 \end{bmatrix}$, $B_\mathrm{c} = [0 \quad b_{2,0} \quad 0]^\mathrm{T}$, $C_\mathrm{c} = [1 \quad 0 \quad 0]$. The input vector u_c is $[\phi_2 \quad i_2]^\mathrm{T}$ and the observer gain vector is $\mathrm{L} = [3\omega_{\mathrm{o}2} \; 3\omega_{\mathrm{o}2}^2 \; \omega_{\mathrm{o}2}^3]^\mathrm{T}$ where $\omega_{\mathrm{o}2}$ is the observer bandwidth of port #2.

Voltage controlled ports

The voltage of port #4 is regulated at a nominal value of $V_{\mathrm{DC,load}}$ which is a first order port. The current and the voltage dynamics of the filter as shown in Figure 3.12b are as follows:

$$\begin{aligned} C_{\mathrm{f}4}\frac{\mathrm{d}V_{\mathrm{cf}4}}{\mathrm{d}t} &= i_4 - i_{4\mathrm{F}} \\ &= \frac{V_{\mathrm{DC,load}}}{R_{\mathrm{load}}} - G_{42}\phi_2 - G_{43}\phi_3 - G_{44}\phi_4 \end{aligned} \tag{3.41}$$

The goal of the controller is to control the voltage of the house load to a fixed value. It can be acheived by an inner current loop combined with an outer voltage loop. Therefore, the load subsystem can be formulated as an ADRC problem using the same methodology applied in case of the battery subsystem.

The first-order ADRC formulation of the filter dynamics of the load port is as follows:

$$\begin{aligned} \frac{\mathrm{d}V_{\mathrm{DC},4}}{\mathrm{d}t} &= \frac{V_{\mathrm{DC},4}}{C_{\mathrm{f}4}R_{\mathrm{load}}} - \frac{1}{C_{\mathrm{f}4}}(G_{42}\phi_2 + G_{43}\phi_3) - \frac{1}{C_{\mathrm{f}4}}G_{44}\phi_4 \\ &= \frac{V_{\mathrm{DC},4}}{C_{\mathrm{f}4}R_{\mathrm{load}}} - \frac{1}{C_{\mathrm{f}4}}(G_{42}\phi_2 + G_{43}\phi_3) - \left(\frac{G_{44}}{C_{\mathrm{f}4}} - b_{4,0}\right)\phi_4 - b_{4,0}\phi_4 \\ &= f_4(t, V_{\mathrm{DC},4}, w_\mathrm{b}) - b_{4,0}\phi_4 \end{aligned} \tag{3.42}$$

where $f_4(t, V_{\mathrm{DC},4}, w_\mathrm{b})$ represents the combined disturbances due to internal dynamics and external disturbances due to the inherent coupling of state $V_{\mathrm{DC},4}$ with inputs of other ports ϕ_2 and ϕ_3. Similar to $b_{2,0}$, the input gain term $b_{4,0}$ can be estimated by the following:

$$b_{4,0} = \frac{G_{44,0}}{C_{\mathrm{f}4,0}} \tag{3.43}$$

Similar to the current controlled ports, an ESO is designed for port #4 to observe $f_4(t, V_{\mathrm{DC},4}, w_\mathrm{b})$:

$$\begin{cases} \dot{z}_\mathrm{v} = [A_\mathrm{v} - L_\mathrm{v}C_\mathrm{v}]z_\mathrm{v} + [B_\mathrm{v} \quad L_\mathrm{v}]u_\mathrm{v} \\ y_\mathrm{v} = z_\mathrm{v} \end{cases}$$

Table 3.1: ADRC formulation of QAB converter ports

System Order	Schematic	Governing equations	ADRC Formulation ÿ	f	b_0
1	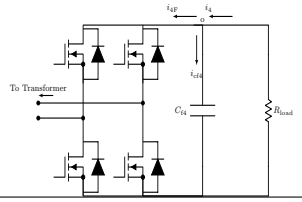	$C_{f4}\dot{v}_{cf,4} = i_4 - i_{4F}$ $i_{4F} = G_{42}\phi_2 + G_{43}\phi_3 + G_{44}\phi_4$	$\dot{V}_{cf4}$	$f_4 = \frac{v_{DC,4}}{C_{f4}R_{load}} - \frac{(G_{42}\phi_2+G_{43}\phi_3)}{C_{f4}} - ...(\frac{G_{44}}{C_{f4}} - \frac{G_{44,0}}{C_{f4,0}})\phi_4$	$\frac{G_{44,0}}{C_{f4,0}}$
2	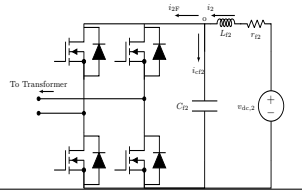	$L_{f2}\dot{i}_2 = v_{DC,2} - v_{cf,2} - r_{f2}i_2$ $C_{f2}\dot{v}_{cf,2} = i_2 - i_{2F}$ $i_{2F} = G_{22}\phi_2 + G_{23}\phi_3 + G_{24}\phi_4$	$\ddot{i}_2$	$f_2 = -\frac{i_2}{L_{f2}C_{f2}} - \frac{r_{f2}}{L_{f2}}\dot{i}_2 + ... \frac{(G_{23}\phi_3+G_{24}\phi_4)}{L_{f2}C_{f2}} + ...(\frac{G_{22}}{L_{f2}C_{f2}} - \frac{G_{22,0}}{L_{f2,0}C_{f2,0}})\phi_2$	$\frac{G_{22,0}}{L_{f2,0}C_{f2,0}}$

where $z_v = [z_{v1} \quad z_{v2}]^T$ is the observer output tracking $V_{DC,4}$, and $f_4(t, V_{DC,4}, w_b)$ respectively. The state space matrices are $A_v = \begin{bmatrix} 0 & 1 \\ 0 & 0 \end{bmatrix}$, $B_c = [b_{4,0} \quad 0]^T$, $C_c = [1 \quad 0]$. The input vector u_c is $[\phi_4 \quad V_{DC,4}]^T$ and the observer gain vector is $L = [2\omega_{o4} \; \omega_{o4}^2]^T$ where ω_{o4} is the observer bandwidth of port #4. Table 3.1 details the governing equations and the equivalent expressions of the ADRC parameters (f, b_0) of the QAB converter ports.

3.4.3 Controller design

Well-tuned observers can track the coupling disturbance terms ($f_{2,3,4}$) in the system dynamics of the QAB converter ports. Thus, the control inputs of $\phi_2 = \frac{u_{i2} - f_2}{b_{2,0}}$, $\phi_3 = \frac{u_{i3} - f_3}{b_{3,0}}$, and $\phi_4 = \frac{u_{v4} + f_4}{b_{4,0}}$, reduces the the individual port dynamics to:

$$\ddot{i}_2 = u_{i2}, \quad \ddot{i}_3 = u_{i3}, \quad \dot{v}_{DC,4} = u_{v4} \tag{3.44}$$

All the above systems have no steady state error and therefore can be easily controlled by a P controller or a PD controller depending on the system order. Hence, the control laws for the current loops and the voltage loop can be written as:

$$u_i = k_{pc}(r_c - z_{c1}) - k_{DC}z_{c2} \tag{3.45}$$

$$u_v = k_{pv}(r_v - z_{v1}) \tag{3.46}$$

where k_p, k_d are the proportional and the derivative gains of the controllers. Based on the formulation presented till now, the ADRC decoupling control schematic of the QAB converter is shown in Figure 3.13.

The open loop transfer functions of the individual systems along with the controllers can be expressed

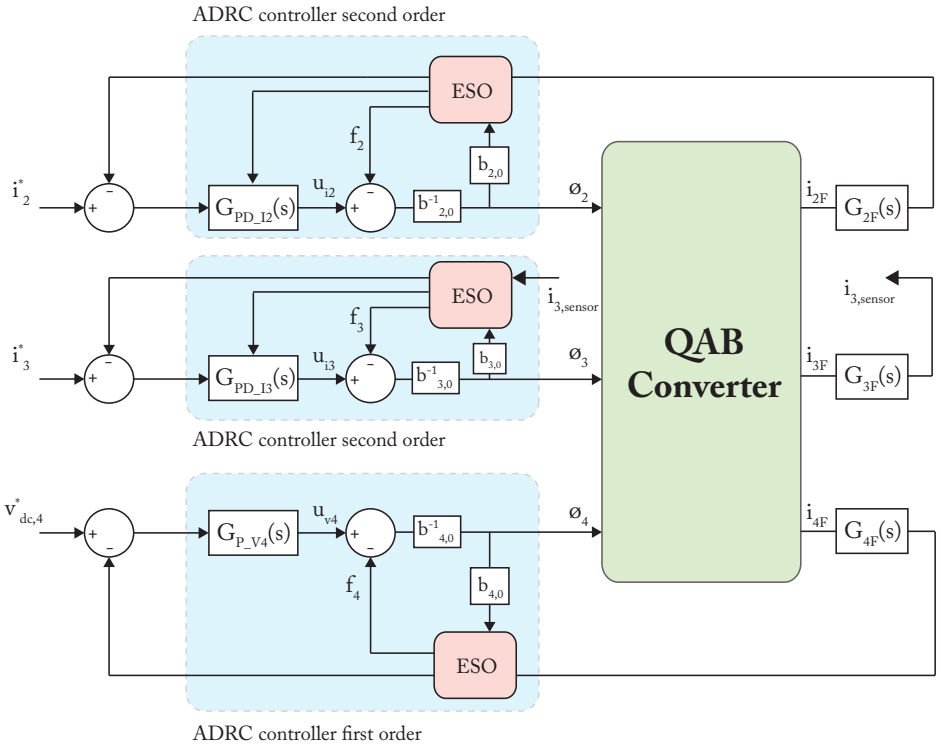

Figure 3.13: Active disturbance rejection decoupling control (ADRC) schematic of QAB converter.

as:

$$G_{\mathrm{OL,i}} = \frac{k_{\mathrm{pc}} + s k_{\mathrm{DC}}}{s^2} e^{-s\tau} \tag{3.47}$$

$$G_{\mathrm{OL,v}} = \frac{k_{\mathrm{pv}}}{s} e^{-s\tau} \tag{3.48}$$

where $e^{-s\tau}$ is the inherent delay associated with practical implementation of the system. For digital controllers, the time delay τ can be represented as $\tau = 1.5T_{\mathrm{s}}$, where T_{s} is the sampling period of the controller. Neglecting the delay term in the open-loop transfer functions, it is evident that the systems are inherently stable since the phase is not crossing -180^o. Further, considering the delay, the gains (k_{p},k_{d}) can easily be tuned to make sure the gain of the transfer function is below 0 dB when the phase is crossing -180^o. Therefore, using ADRC controllers, system stability is relatively easy to ensure. However, it must be noted that the choice of the control gains is limited by the observer bandwidth due to hardware constraints like sampling frequency and sensor noise.

3.5 Simulation results

Simulations on a four-port MAB converter or a quad-active bridge (QAB) converter are carried out and analyzed in this section to validate the theoretical considerations presented in the previous section.

Initially, the QAB converter specifications and control strategy considered in the simulation are discussed. The selected simulation package is MATLAB/Simulink augmented with the PLECS blockset. A detailed analysis of the results obtained from the simulations is presented at the end of this section.

3.5.1 QAB converter specifications and control strategy

The QAB converter schematic used for the simulation study is presented in Figure 3.14. The converter is comprised of four ports: three bi-directional voltage ports, and a load port consisting of a resistor in parallel with a capacitor. The voltage sourced port #1 is used as the "master port" as introduced in Section 3.3 which acts as the slack bus of the multi-port converter. Table 3.2 presents the simulation parameters of the different ports of the QAB converter. The base inductance L_{base} value is obtained by using the maximum power flow equation between two ports of a MAB converter when $\phi_{\text{ij}} = \frac{\pi}{2}$ resulting in the following expression:

$$P_{\text{rated}} = \frac{V_{\text{rated}}^2}{8 f_{\text{sw}} L_{\text{base}}} \tag{3.49}$$

Using the values of switching frequency, rated power and rated voltage from the QAB converter specifications in Table II in revised manuscript,the base inductance L_{base} results in 25 µH.

In the control system, there are three control loops: two current loops for the bi-directional voltage sources in port #2 and port #3; and a voltage control loop for the resistive load in port #4 with R_{load} = 35 Ω.

3.5.2 Results: hardware decoupling

Therefore, the voltage source in port #1 acts as the "master" port or the slack bus. Simple phase shift control is used to control the QAB converter. Figure 3.15a shows the block diagram of the QAB control system. The PI controller for the voltage loop is designed to be slower than the current loops to investigate the interactions between the individual loops. For the current control, a crossover frequency of 1.5 kHz is selected, while for the load voltage control only 10 Hz is chosen as shown in the open loop Bode plots Figure 3.15b and Figure 3.15c. The small signal gain matrix for MAB converters derived

Table 3.2: QAB converter specifications for hardware decoupling

Description	Symbol	Unit	Port			
			#1	#2	#3	#4
Voltage rating	V_{rated}	V	200	200	200	160
Current rating	I_{rated}	A	10	10	10	10
Leakage inductance	L_σ	pu	0/1	1	1	1
LC filter inductance	L_{f}	µH	3	3	3	3
LC filter capacitance	C_{f}	µF	500	500	500	100
Phase-shift angle range	ϕ	rad	0	$-\frac{\pi}{2}$ to $\frac{\pi}{2}$	$-\frac{\pi}{2}$ to $\frac{\pi}{2}$	0 to $\frac{\pi}{2}$
Switching frequency	f_{sw}	kHz	100	100	100	100

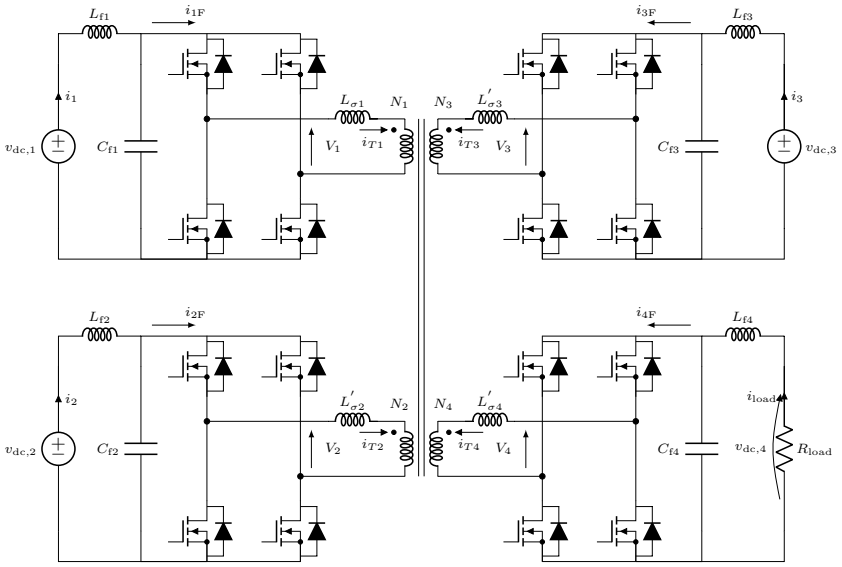

Figure 3.14: QAB converter schematic for simulation. Port #1, port #2 and port #3 are connected with a voltage source and port #4 is connected with an RC load.

in (3.16) can be re-written for the QAB converter:

$$\begin{bmatrix} \Delta i_{2F} \\ \Delta i_{3F} \\ \Delta i_{4F} \end{bmatrix} = \begin{bmatrix} G_{22} & G_{23} & G_{23} \\ G_{32} & G_{33} & G_{34} \\ G_{42} & G_{43} & G_{44} \end{bmatrix} \begin{bmatrix} \Delta\phi_2 \\ \Delta\phi_3 \\ \Delta\phi_4 \end{bmatrix} \tag{3.50}$$

where i_{iF} (i $\in [1,4]$) are the pre-filter currents of the DC ports. The dynamics of the DC port currents (i_i) can be obtained combining (3.50) with the transfer functions of the DC side filters of the QAB ports which are defined as:

$$G_{2I}(s) = \frac{\Delta i_2}{\Delta i_{2F}}, \quad G_{3I}(s) = \frac{\Delta i_3}{\Delta i_{3F}}, \quad G_{4I}(s) = \frac{\Delta V_{DC,4}}{\Delta i_{4F}} \tag{3.51}$$

The goal of the simulations is to prove the the effectiveness of the proposed converter configuration in terms of decoupling the power flows to gain precise and independent control on the individual ports. To that end, two case studies are considered:

1. Case study I: load step in the resistive load port #4 to investigate the effect of the relatively slower voltage loop on the faster current loops.

2. Case study II: simultaneous step change of current reference points in the current controlled ports #2 and #3 to study the effect of the faster current loops on the efficacy of the voltage control loop.

In addition, simulations were performed of various leakage inductances in the master port to test the sensitivity analysis of the degree of the control loop decoupling. The simulations are carried out at the

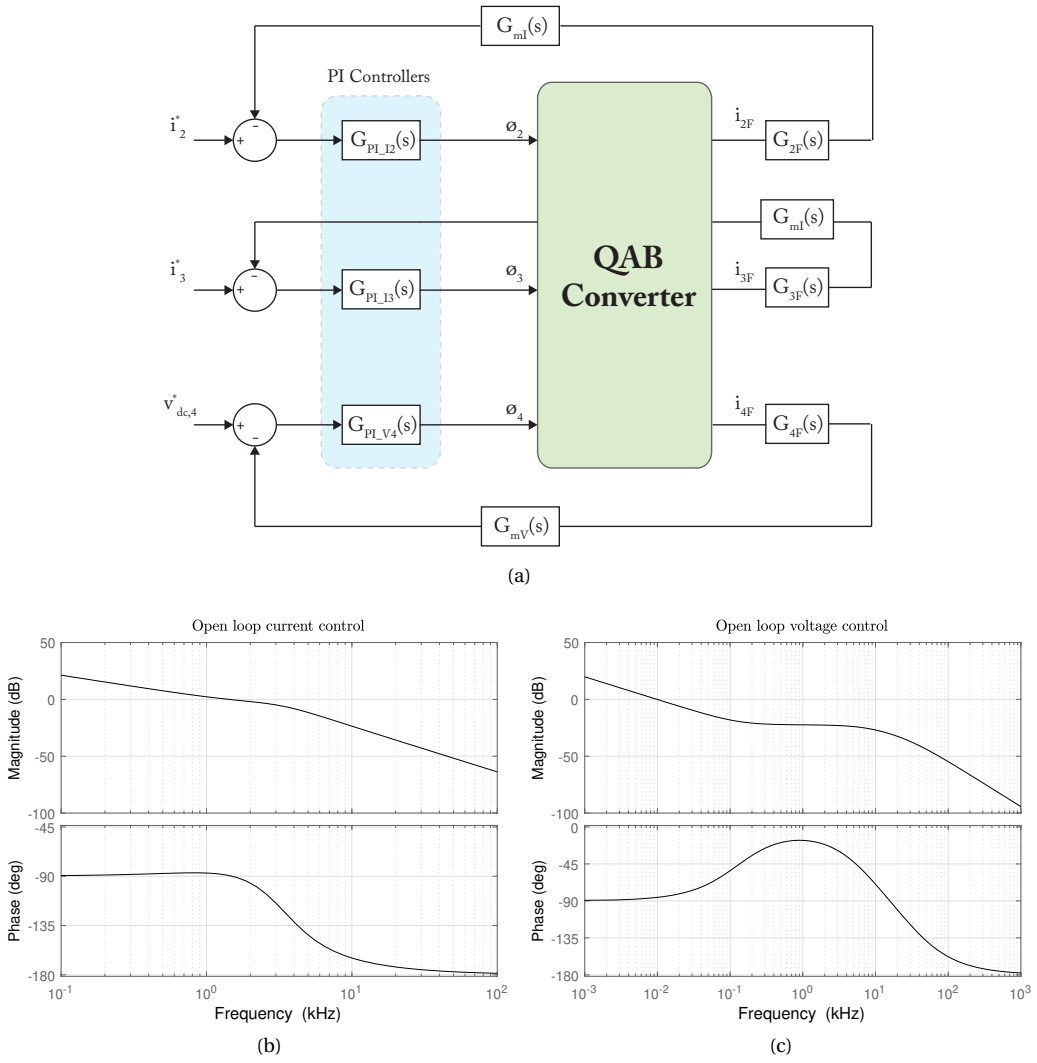

Figure 3.15: (a) Block diagram of the QAB control system with three control loops: port #2 current control loop, port #3 current control loop, and port #4 voltage control loop; (b) open loop response of current control loops of port #2 and port #3, and (c) open loop response of voltage control loop of port #4.

following operating point: $P_{\text{load},4}$ = -700 W; P_2 = 800 W; P_3 = -800 W. At this operating point, the QAB converter acts in the 2 source-2 load configuration (2S-2L) with port #1 and port #2 as the sources and port #3 and port #4 as the loads. The obtained simulation results are analyzed in the following.

Case Study I

The load step is realized by switching a resistor of R_{sw} = 130 Ω across the existing load resistor R_{load}. Figure 3.16a presents the dynamic performance of the current loops and voltage loops of the ports during the load step in the load port at a certain instant (t = 0.11 s). It is noted that the voltage restoration control during the load step has no major effect on the current loops in port #2 and port #3, which are capable of holding currents at their set-points irrespective of the master port leakage inductance. As the current loops are much faster than the voltage loop, they reject the interference independently of the leakage inductance of the master port. However, the dynamic performance of the load port voltage loop deteriorates with increasing leakage inductance in the master port which is observed in the 12.5% drop of the nominal voltage when $L_{\sigma 1}$ = 0.8 pu compared to only 7% drop when $L_{\sigma 1}$ = 0.04 pu. The increasing leakage inductance of the master port increases the effective inductance between the load port and the master port, thereby reducing the plant control to output gain; G_{44} in the small-signal gain matrix (3.50).

Case study II

At a certain time instant (t = 0.04 s), the current reference point in the source port #2 is changed from 4A to 2A. Simultaneously, the current set-point in the load port #3 is changed from -2A to -4A. Similar to the case study I, the simulations are repeated for different master-port leakage port inductances. Figure 3.16b shows the dynamic performance of the current loops and voltage loop of the ports around t = 0.04 s. The port #4 bus voltage disruption during the current set-point adjustments in the current-controlled ports is visible when the voltage drops by 24 V when the master port leakage inductance is 0.8 pu. Unlike the case study I, there is a significant interaction between the current and the voltage control loops. The slow voltage loop is not capable of rejecting the interference caused by the current set-points adjustments when the master port leakage inductances are 0.2 pu and 0.8 pu. However, when the leakage inductance of the master port is 0.04 pu, the bus voltage disturbance is negligible.

The obtained simulation results can be explained by the analysis presented in Section 3.2.4. At the end of the Section 3.2.3, it was inferred that the degree of cross-coupling of the control loops is directly proportional to the relative value of the non-diagonal elements with the diagonal elements. To that end, the small signal gain matrix of the QAB converter as shown (3.50) is normalized as the following:

$$G_{\text{norm}} = \begin{bmatrix} 1 & |\frac{G_{23}}{G_{22}}| & |\frac{G_{24}}{G_{22}}| \\ |\frac{G_{32}}{G_{33}}| & 1 & |\frac{G_{34}}{G_{33}}| \\ |\frac{G_{42}}{G_{44}}| & |\frac{G_{43}}{G_{44}}| & 1 \end{bmatrix} \tag{3.52}$$

Figure 3.17 shows the area-plot of the normalized gain matrix G_{norm} at different values of the master port leakage inductance. At $L_{\sigma 1}$ = 0.04 pu, the matrix is essentially a diagonal matrix with the non-diagonal gain terms approaching zero. Nonetheless, as the leakage inductance reaches the base value of 1 pu, non-diagonal gain terms are increasingly comparable to diagonal terms leading to cross-coupling

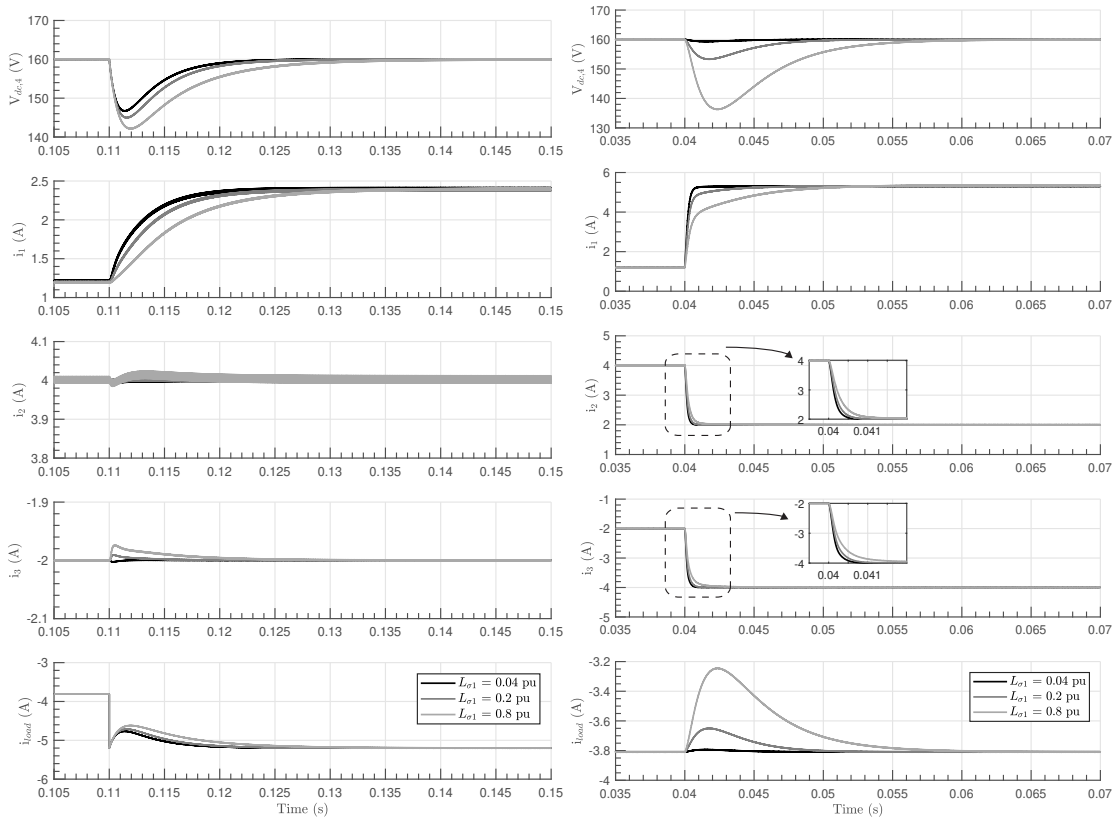

(a) (b)

Figure 3.16: Transient response of port voltages and currents at different master port leakage inductances during: (a) case study I: a load step on load port #4 by switching a parallel resistor ; (b) case study II: simultaneous changes in the current set-points; 4A to 2A for i_2^* and -2A to -4A for i_3^*. In both the case studies, port #1 acts as the slack bus.

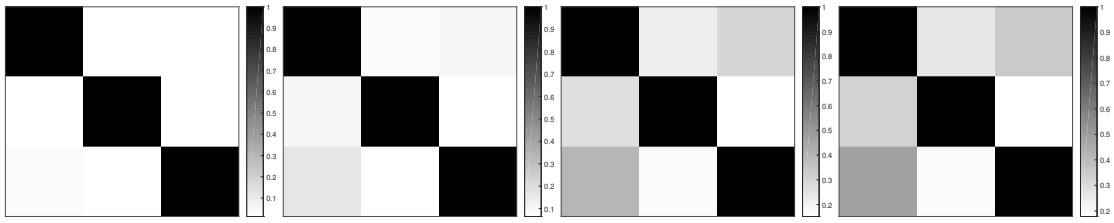

(a) (b) (c) (d)

Figure 3.17: 2-D area plot of normalized gain matrix G_{norm} as expressed in (3.52) with master port leakage inductance $L_{\sigma 1}$: (a) 0.04 pu, (b) 0.2 pu, (c) 0.8 pu, and (d) 1 pu.

between control loops.

In addition to the gain matrix approach, a disturbance to the output bode plot can be used to study

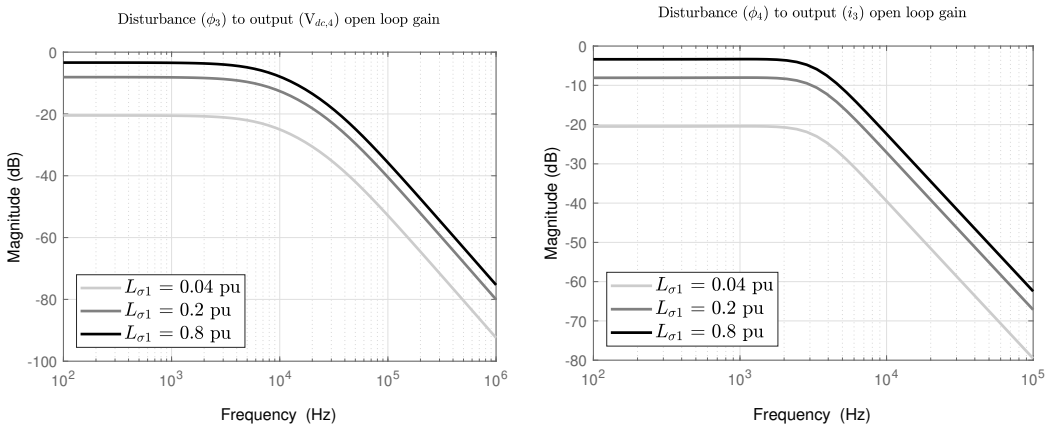

Figure 3.18: Open loop response of disturbance to control output: (a) current control variable ϕ_3 to voltage loop control output $V_{\mathrm{DC},4}$, (b) voltage control variable ϕ_4 to current loop control output i_3.

the effect of the master port leakage inductance on the decoupling performance. Figure 3.18a shows the disturbance (ϕ_3) to output ($V_{\mathrm{DC},4}$) bode plot for port #4. Similarily, Figure 3.18b depicts the disturbance (ϕ_4) to output (i_3) bode plot for port #3. All cases show that the low-frequency disturbance to output gain decreases by approximately 20 dB as the master port leakage inductance decreases from 0.8 pu to 0.04 pu. Therefore, when the master port leakage inductance is low ($\leq$ 0.05 pu), the PI controller gains of the individual control loops are sufficient to reject the cross-loop intereference. It must be noted that the above decoupling design criteria becomes difficult to achieve as the power rating and switching frequency of the MAB converter increases as the base inductance is inversely proportional to them as per equation (3.49).

In summary, the results of the simulation show that the proposed MAB configuration has inherently decoupled power flows if the master port leakage inductance is sufficiently low ($\leq$0.05 pu). In addition, it is shown that selecting different control bandwidths for the control loops in the MAB [31] does not guarantee power flow decoupling. The technique eliminates the noise due to the slower loop on the faster loop. However the slower control loop becomes more vulnerable to disruption caused by faster control loops.

3.5.3 Results: ADRC control decoupling

Dynamic simulations are performed to validate the the effectiveness of the proposed ADRC control in terms of decoupling the power flows. The selected simulation package is MATLAB/Simulink augmented with the PLECS blockset. The QAB converter schematic used for the simulation study is presented in Figure 3.14. The performance of ADRC decoupling control is compared with the matrix based conventional decoupling control (CDC). Finally, simulations are also carried out on the QAB converter without any decoupling control, i.e, with only decentralized PI controllers for individual ports. The PI controller for the voltage loop is designed to be slower than the current loops to investigate the interactions between the individual loops. It must be noted that the PI controller gains highlighted in

Table 3.3: Controller gains for simulation study

Type	Description	Symbol	Unit	Port			
				1	2	3	4
ADRC control & observer gains	Observer bandwidth	ω_o	rad/s	-	20,000	50,000	50,000
	Proportional	k_p	-	-	3	2	0.06
	Differential	k_d	-	-	800	500	-
CDC controller PI gains	Proportional	k_P	-	-	2.5	1.8	0.06
	Integral	k_I	-	-	5000	3000	10

the specifications are applicable to simulations with CDC control and with only PI control. Dynamic simulations are carried out at the following operating point: P_2 = 800 W; P_3 = -400 W, and $P_{load,4}$ = -740 W. The current set-point of the port #2 is changed from 4A to 2A and the behavior of the current of port #3 and voltage of port #4 are observed to evaluate the performance of the decoupling control strategies.

Performance comparison of decoupling control methods

The performance of the proposed active-disturbance rejection control (ADRC) is compared to the performance of the conventional decoupling control (CDC) used for decoupling control of MAB converters. Table 3.3 presents the controller gains of the ADRC controllers along with the CDC controllers. Further, the behavior of the converter without any decoupling control is also analyzed to create a baseline performance. For the converter system without decoupling control, only decentralized PI controllers with similar gains to the CDC control (Table 3.3). Figure 3.19 shows the dynamic waveforms of the relevant QAB port currents and voltages using different control strategies. Figure 3.19a and 3.19b show the terminal voltage and current of port #4 while Figure 3.19c shows the current of port #3. The cross-coupling of the QAB converter control loops is evident from the disturbance caused in the port voltages and currents when no decoupling controller is used. Thus, the dynamic behavior is highly coupled and will lead to stability issues. The decoupling performance of ADRC controller is evident

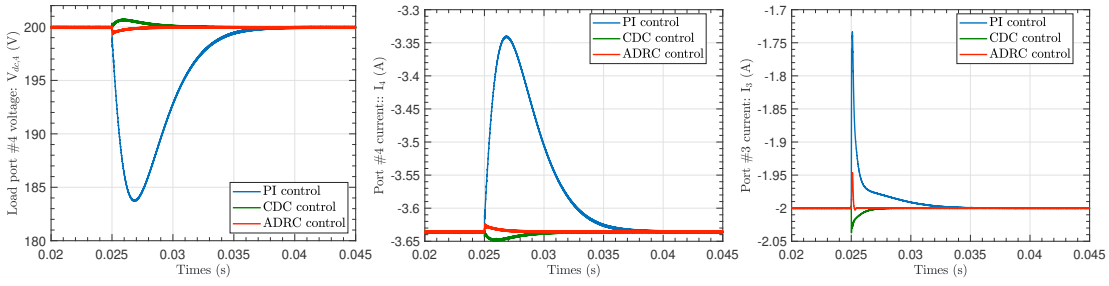

(a) (b) (c)

Figure 3.19: Comparison of decoupling performance of different control strategies; without decoupling control (only PI controllers), conventional decoupling control, and active disturbance rejection control during a step-change in set-point of port #2 current i_2 from 4A to 2A. Disturbance in different QAB converter ports: (a) $v_{DC,4}$: voltage of load port #4, (b) i_4: current of load port #4, and (c) i_3: current of port #3.

from the dynamic behavior of the port currents and voltage. The deviations in the transient response of i_3, i_4 and $v_{DC,4}$ are less than 1% compared to 10% in the simulation study without decoupling control. Additionally, the ADRC performance is comparable to the CDC decoupling control, thus validating its performance.

Robustness analysis of decoupling controllers

Compared to CDC control, ADRC needs less information regarding the plant. The individual port ADRC controllers only require the information regarding the order of the port filter. On the other hand, the centralized CDC control needs internal information of the QAB converter model which includes the nominal values of link inductances between the ports (L_{ij}), rated port voltage ($v_{DC,i}$), phase shifts during an operating point (ϕ_{ij}) and switching freqeuncy (f_{sw}). Therefore, it is necessary to investigate the decoupling performance of the CDC and ADRC controllers when there is a deviation in values extracted from plant models. The above dynamic simulation is repeated for both the control strategies with deviations in relevant model parameter values. Figure 3.20a shows the dynamic response of the port #4 voltage $v_{DC,4}$ using CDC control with deviations in the value of the link inductance between port #3 and #4; L_{34} in the plant model. Similarily, figure 3.20b shows the decoupling of $v_{DC,4}$ using ADRC control with deviations in the value of the input gain b_4 in the controller model. The CDC decoupling performance is sensitive to under-compensation or over-compensation depending on the deviation in the nominal value of L_{34} in the QAB plant model. However, in the case of ADRC control, the decoupling performance is robust. It can dynamically decouple the port voltage independent of the deviations in the input gain values in the controller. In practical scenarios, the term b_0 is used as an additional tuning parameter besides observer (ω_o) and controller gains.

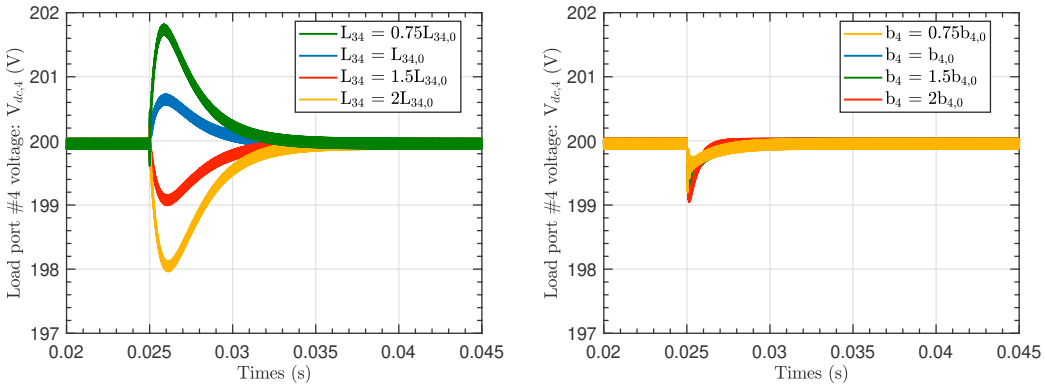

Figure 3.20: Dynamic behavior of port #4 voltage $v_{DC,4}$ to investigate sensitivity of decoupling performance to deviation in model parameters: (a) CDC decoupling performance when the value of the link inductance L_{34} is changed in the plant model from it's nominal value $L_{34,0}$, and (b) ADRC decoupling performance when the value of the input gain b_4 is changed from it's nominal value $b_{4,0}$.

Effect of observer bandwidth and sampling frequency

The decoupling performance of the ADRC controllers is dependent on the choice of observer bandwidth and the sampling frequency of the digital controller. To analyze the effect of the digital control delay and the observer time constant, the transfer functions of the individual QAB converter ports or sub-systems are used. Using a first order approximation of the time delay, the open loop transfer functions of the current controlled and voltage controlled ports introduced in (3.47) and (3.48) can be re-written as:

$$G_{\mathrm{OL,i}} = \frac{k_{\mathrm{pc}} + s k_{\mathrm{DC}}}{s^2(1+s\tau)} \tag{3.53}$$

$$G_{\mathrm{OL,v}} = \frac{k_{\mathrm{pv}}}{s(1+s\tau)} \tag{3.54}$$

It must be noted that the validity of the above mentioned open loop transfer functions is contingent on the cancellation of lumped disturbance of the system by the output of the ESO. Therefore, the bandwidth of the observer has to be sufficiently higher compared to that of the controller for optimal decoupling performance. However, the bandwidth of the observer is dependent on the sampling time of the digital controller T_{s}. To that end, the bode plots of the control to output loop gains for varying sampling times are analyzed and presented in Figure 3.21. Figure 3.21a shows the open loop Bode plot of the port #2 current control loop gain with different digital time delays ranging from 100 ms to 10 µs. It is evident from the Bode plots that lower the digital control delay, higher the control bandwidth and the phase margin for fixed controller gains. For higher delays, the controller gains can be increased to make sure there is sufficient phase margin when the transfer function gain is 0 dB.

As mentioned above, the ports' open-loop transfer functions are only valid if the extended state observer (ESO) is sufficiently fast. To that end, the effect of the ESO bandwidth on the decoupling dynamics of the QAB converter obtained from simulations is shown in Figure 3.22. As expected, the higher the LESO bandwidth, the better the disturbance rejection by the ADRC voltage and current

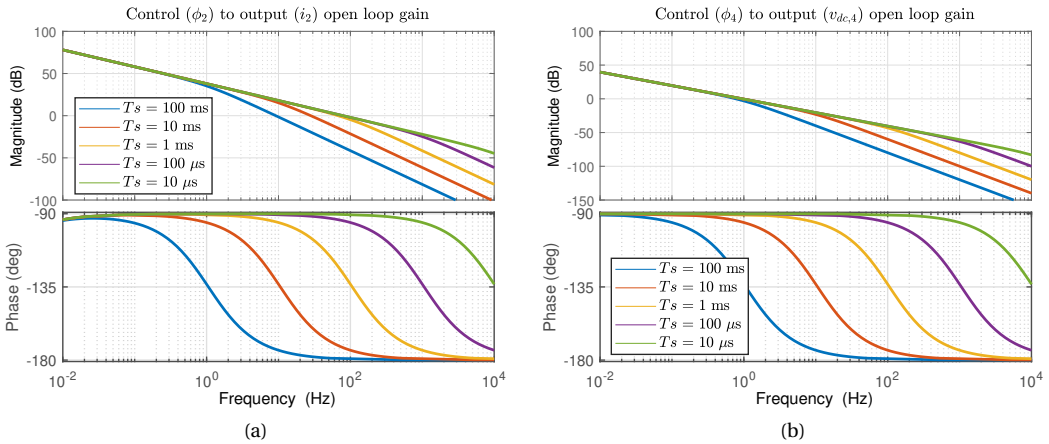

(a) (b)

Figure 3.21: Open loop Bode plots of: (a) port #2 current adrc control loop at different digital time delays. The controller gains are fixed with k_{pc}= 2 and k_{DC}= 500, and (b) port #4 voltage first order adrc control loop at different digital time delays with a gain of k_{pv}= 0.06.

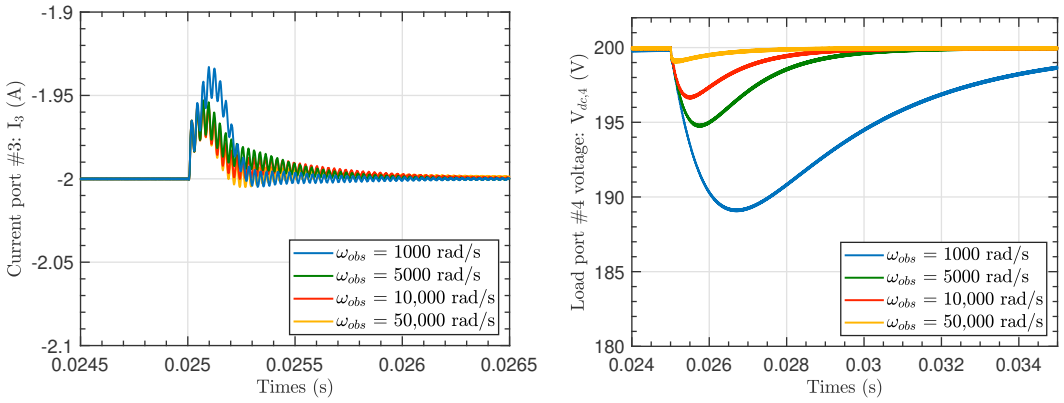

Figure 3.22: Decoupling performance of ADRC controllers at four observer bandwidths (ω_{obs}): (a) port #3 current dynamic behavior at different observer bandwidths, and (b) decoupling performance of ADRC voltage controller $v_{\text{DC},4}$ for different observer bandwidths.

controllers. The decoupling performance of the ADRC voltage controller is really sensitive to the choice of the observer bandwidth as shown in Figure 3.22b since the voltage control bandwidth is much slower compared to the current controller bandwidth. In conclusion, the lower controller bandwidth can be compensated by a high observer bandwidth in case of disturbance rejection. However, it must be noted that the observer bandwidth cannot be increased indefinitely as the sensor noise starts to dominate, which might lead to unstable operation.

In summary, the results of the simulation show that the proposed ADRC control approach for MAB converters is able to dynamically decouple the individual power flows. The main advantage of the proposed control strategy is that it requires much less information regarding the converter model compared to the matrix based approach of conventional decoupling control [14]. Additionally, the gains of the ADRC controller are independent of the operating point unlike in case of CDC control which needs a look up table to update the gains at different operating points. Further, the ADRC decoupling performance is robust to the deviation of the controller gains derived from model parameters.

3.6 Experimental results

Experiments are performed on a quad-active bridge (QAB) converter prototype to demonstrate the efficacy of the proposed power flow decoupling strategies. To that end, the overall experimental setup, along with the system components, is addressed in the next segment. Additionally, the efficiency of operation and distribution of losses are presented. The dynamic decoupling performance of the QAB converter prototype is presented at the end.

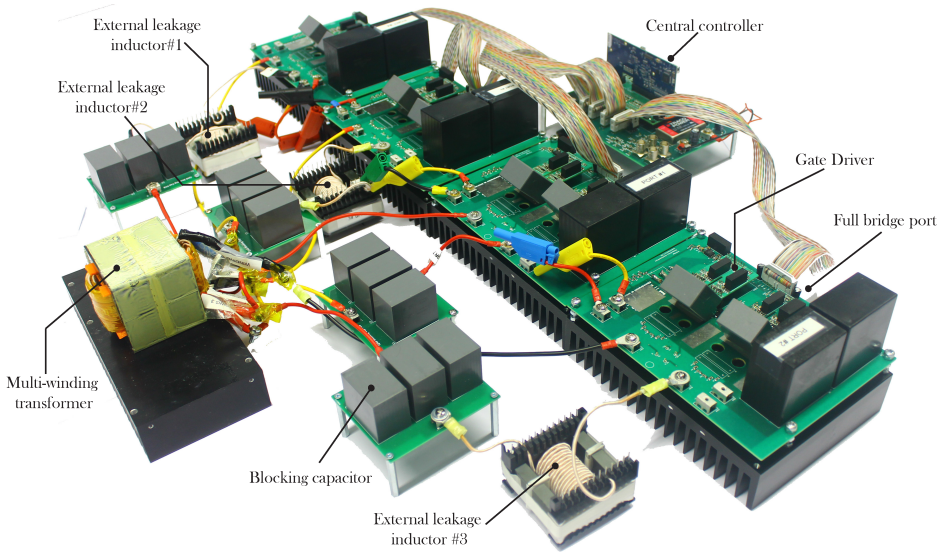

Figure 3.23: QAB experimental laboratory prototype.

3.6.1 Laboratory prototype

The experimental QAB prototype is identical to the simulation schematic (Figure 3.14) without the DC-side filter inductors with all other parameters remaining the same (Table 3.2). The laboratory QAB converter setup is presented in Figure 3.23. The overall system consists of four full-bridge modules connected via a high-frequency multi-winding transformer with three bi-directional DC power supplies (SM 500 CP-90 Delta Elektronika) and a resistive load of 35 Ω. Si-C MOSFETs (Wolfspeed C3M0065100K) are used for the full-bridge modules. Three external leakage inductors of value 25 µH for the three slave ports are highlighted in Figure 3.23. Blocking capacitors are connected to each transformer winding to ensure the transformer is not saturated due DC bias during transient and steady state operating conditions. The central controller is implemented on a Texas Instruments TMS320F28379D DSP. The high-frequency (HF) transformer is implemented by using two stacks of E-70/33/32 cores (core material N87) in parallel. The transformer windings are interleaved to ensure low leakage inductance of the windings. Leakage impedance tests on the HF transformer are conducted to evaluate the inter-winding leakage inductances. Table 3.4 presents the design specifications of the HF transformer along with the experimentally obtained values of the leakage inductances of the delta-equivalent circuit. The transformer winding #1 is designed to have the lowest leakage among all the windings, as evident from the experimentally obtained leakage inductance values in Table 3.4. Therefore, the port connected to the winding #1 is used as the master port.

3.6.2 Steady-state waveforms

Figure 3.25 presents the operating steady-state winding current and voltage waveforms of the four-port MAB converter prototype in its conventional configuration with symmetric distribution of leakage inDCutances. The operating point is identical to the operating point OP#1 chosen for the simulation study ($P_{\text{load},4}$ = -730 W; P_2 = 800 W; P_3 = -400 W) where the MAB converter acts in 2 source-2 load (2S-2L)

Table 3.4: HF Transformer Specifications

Design parameter	**Details**
Core	2 stacks E-70/33/32
Material	N87 (EPCOS TDK)
Layer insulation	Kapton tape
Number of turns (N_1, N_2, N_3, N_4)	8,8,8,8
Parallel turns	4,2,2,2
Litz wire details	r_{strand} = 0.05 mm n_{strand} = 420
Leakage inductances (µH)	L_{12} = 8; L_{13} = 1.8; L_{14} = 6.7 L_{23} = 9; L_{34} = 9; L_{24} = 19

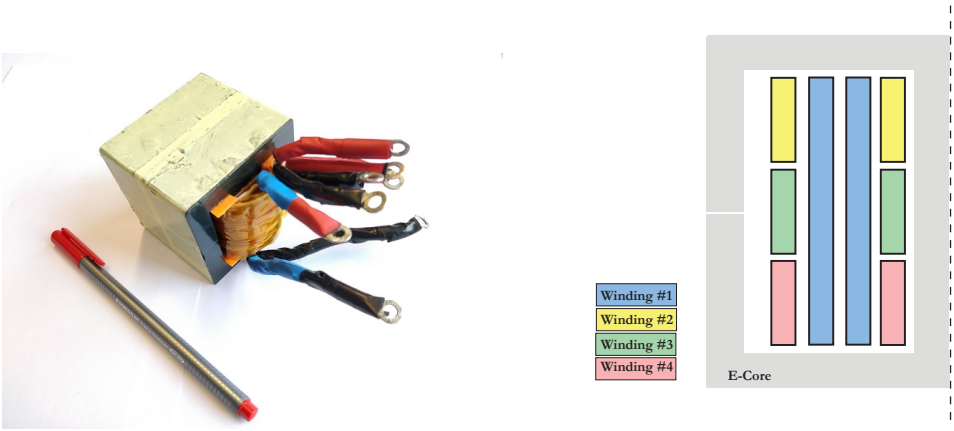

(a) (b)

Figure 3.24: (a) Four-winding transfer for the multi-active bridge converter, (b) interleaved winding strategy of the multi-winding transformer to ensure low leakage inductance for winding #1.

mode. It is evident that the experimentally obtained waveforms are similar to the theoretical waveforms presented in Figure 3.5.

Similarly, Figure 3.26 presents the operating steady-state winding current and voltage waveforms of the modified MAB converter with port #1 as the 'master' port with zero leakage inductance at the same operating point. The winding currents of the slave ports are trapezoidal in shape similar to dual-active bridge (DAB) converters operating with sibgle-phase shift (SPS) modulation. The winding current of the 'master' port (i_{T1}) is a superposition of the slave port currents. The transformer widning current shapes are similar to the theoretical waveforms presented in Figure 3.10.

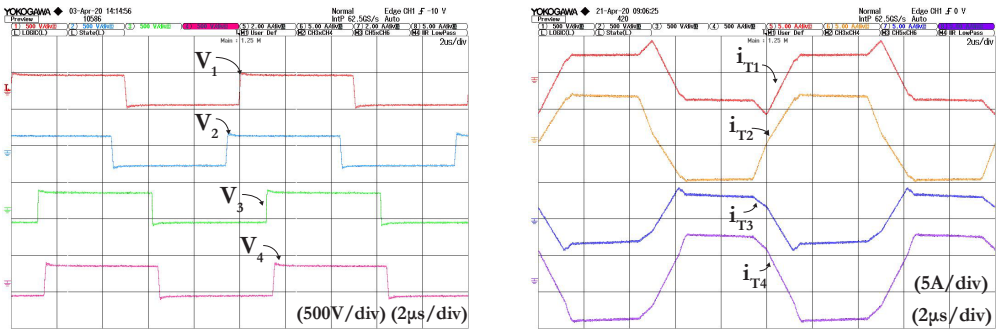

(a) (b)

Figure 3.25: Steady state waveforms of the conventional MAB configuration with symmetrical leakage inductance distribution in 2S-2L mode at the operating point OP#1: (a) transformer winding voltages, (b) transformer winding currents.

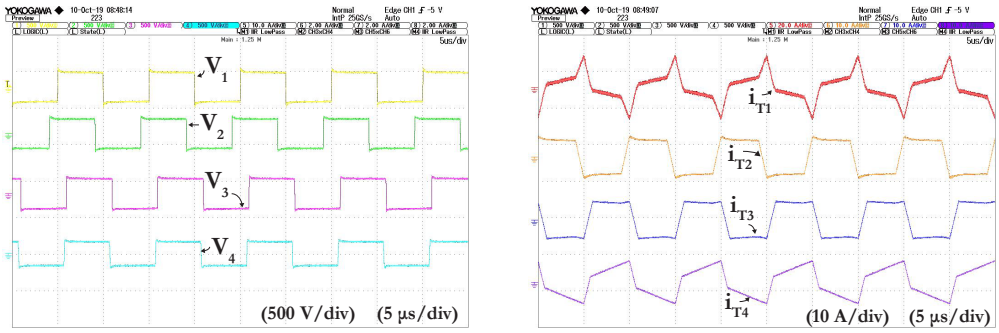

(a) (b)

Figure 3.26: Steady state waveforms of the modfied MAB configuration with asymmetrical leakage inductance distribution in 2S-2L mode at the operating point OP#1: (a) transformer winding voltages, (b) transformer winding currents..

3.6.3 Bi-directional power flow control

As highlighted previously, one of the significant advantages of the MAB converter family is the capability of controlling the power of ports in both directions. Figure 3.27 demonstrates a case study where the power in port #2 is controlled in both directions. The port #2 current alters direction tracking the ramped power set-point. It can be further observed that port #1 acts as the slack port of the converter as the QAB converter transitions from a 2 source-2 load (2S-2L) mode of operation to a 1 source-3 load (1S-3L) mode. Thus, the bi-directional power flow control of the QAB converter is validated.

3.6.4 Dynamic behavior: hardware decoupling

The power flow dynamic decoupling performance of the proposed QAB converter is validated by performing multiple experiments on the prototype. The experiments are divided into two case studies

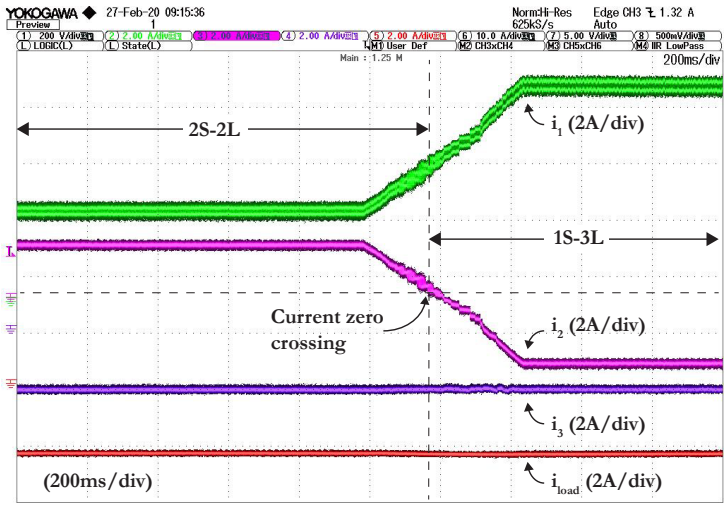

Figure 3.27: Bi-directional power flow control in port #2 in the QAB converter prototype by ramping down the port power set-point. The converter mode of operation transitions from a 2S-2L to a 1S-3L.

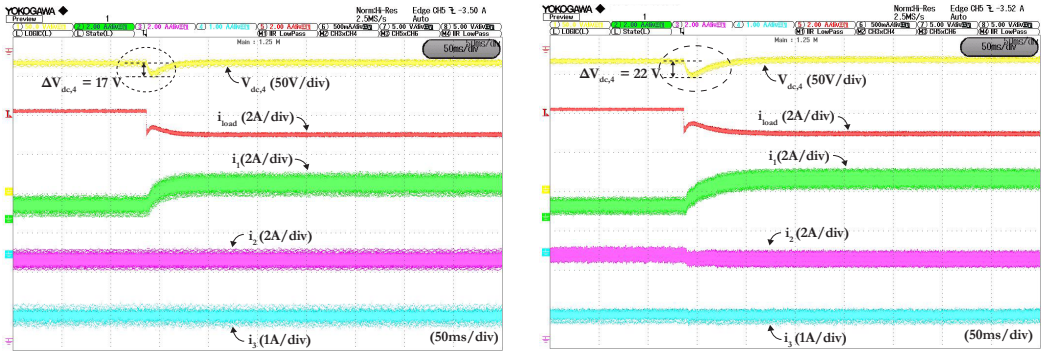

Figure 3.28: Transient behavior of the control currents and voltage during a load step of QAB system configuration with: (a) $L_{\sigma 1}$ = 0 pu, (b) $L_{\sigma 1}$ = 0.6 pu.

similar to the simulations in Section 3.5.2:

1. a step load in the load port #4 to investigate the effect of the relatively slower voltage loop on the current loops in port #2 and port #3.
2. simultaneous step change of current set points in port #2 and port #3 to study the effect of the current loops on the efficacy of the voltage control loop in port #4.

In addition, two sets of experiments are carried out: (a) the conventional QAB configuration with an external inductor of $L_{\sigma 1}$ = 0.6 pu is connected to the slack port winding transformer, and (b) the proposed QAB configuration without an external inductor as a leakage inductance connected to the

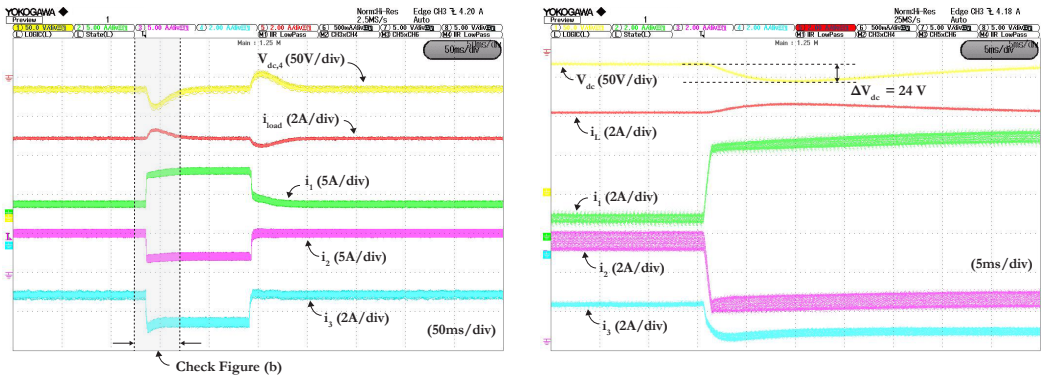

(a) (b)

Figure 3.29: Dynamic performance of the control currents and voltage during set-point alterations in port #2 and port #3 with QAB configuration with $L_{\sigma 1}$ = 0.6 pu. The current set point in port #2 is changed from 4A to 2A and back to 4A. The current set point in port #3 is changed from -2A to -4A and back to -2A. (a) overall transient waveforms, (b) transient waveforms during the first set-point change.

slack port winding transformer. The results obtained from the two configurations are compared to evaluate the effectiveness of the proposed configuration in terms of power flow decoupling.

Load step at port#4

The load step is realized on port #4 by switching a resistive load of 130 Ω in parallel with an existing load of 35 Ω. Figure 3.28a shows that the port currents of port #2 and port #3 are not affected by the load step change in port #4 when there is no external leakage inductance is added to the slack port transformer windings ($L_{\sigma 1}$ = 0 pu). In the modfied MAB configuration, the voltage dip at the load bus is 17 V compared to 22 V in the conventional QAB configuration as shown in Figure 3.28b. Simulation findings have also shown similar behavior as reported in Figure 3.16a. The cross-loop interference generated by the voltage loop is corrected by faster current loops regardless of the leakage inductance of the master port. In conclusion, the proposed QAB configuration has faster voltage restoration performance during load step compared to the conventional QAB configuration. However, in both the configurations the cross-coupling effect of the slower voltage loop on the current loops is negligible.

Current step at port#2 and port#3

The interference due to the current control loops on the voltage loop obtained from the experimental results is studied in this section. The current reference points at port #2 and port #3 are changed simultaneously ($I_{2,\text{set-point}}$ = 4A to 2A to 4A, $I_{3,\text{set-point}}$ = -2A to -4A to -2A). The transient response of the DC bus voltage during this event is observed for both the converter configurations with and without external leakage inductances. Figure 3.29 and Figure 3.30 show the transient behavior of the load DC bus voltage and the controlled currents of the proposed QAB configuration ($L_{\sigma 1}$ = 0.6 pu) and the conventional QAB configuration ($L_{\sigma 1}$ = 0 pu) respectively. The full decoupling of the control loops is observed from Figure 3.30a without any disruption to the DC bus voltage due to the current loop

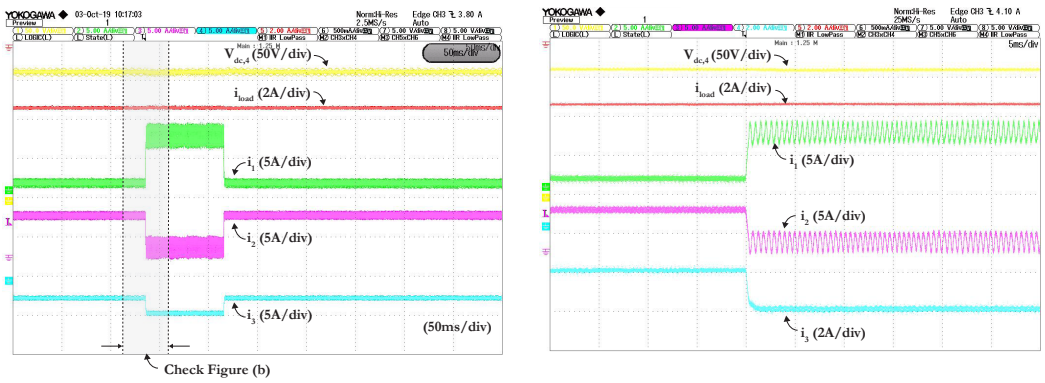

(a) (b)

Figure 3.30: Dynamic performance of the control currents and voltage during set-point alterations in port #2 and port #3 with QAB configuration with $L_{\sigma 1}$ = 0 pu. The current set point in port #2 is changed from 4A to 2A and back to 4A. The current set point in port #3 is changed from -2A to -4A and back to -2A. (a) overall transient waveforms, (b) transient waveforms during the first set-point change.

control operation. However, in case of the conventional converter configuration ($L_{\sigma 1}$ = 0.6 pu), the DC bus voltage is affected by the control action in the current control loops as shown on Figure 3.29. Figure 3.29b shows that the DC bus voltage drops approximately 24 V (15% of the nominal bus voltage) during the current set-point changes in port #2 and port #3 before the voltage control restores the DC bus nominal voltage.

In conclusion, the proposed MAB configuration with asymmetric leakage inductance distribution shows complete dynamic decoupling of the control loops independent of individual control bandwidths. Therefore, the experimental results validates the hardware approach towards power flow decoupling of MAB converters. In the upcoming section, the ADRC based software decoupling strategy is implemented on the QAB laboratory prototype.

3.6.5 Dynamic behavior: ADRC based decoupling

The dynamic decoupling performance of the ADRC based control strategy is validated by performing experiments on the prototype at the aforementioned operating point. Digital implementation of the ADRC controllers is detailed in Appendix A. The port #2 current is changed from 4A to 2A and the behavior of the current of port #3: i_3, and voltage of port #4: $v_{\mathrm{DC},4}$ are observed to evaluate the performance of the decoupling control strategies. Two sets of experiments are conducted: (a) only with PI controllers, and (b) with tuned ADRC decoupling control.

The individual port controllers are tuned by iteratively increasing the observer bandwidth (ω_o) and the controller gains until either the control signal becomes noisy and leads to oscillations or desired dynamic performance is achieved. After completion of the tuning strategy, an observer bandwidth of 35,000 rad/s is obtained for the second-order LADRC current controllers for ports #2 and #3. For the first order LADRC voltage controller of port #4, an observer bandwidth of 10,000 rad/s is obtained.

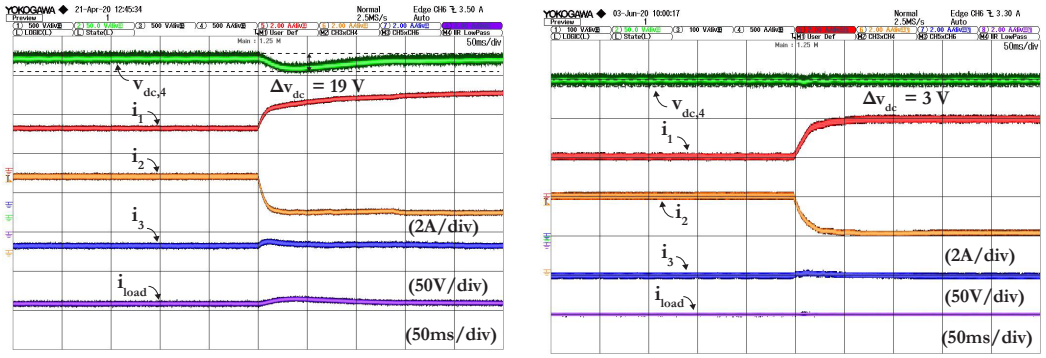

(a) (b)

Figure 3.31: Experimentally obtained dynamic performance of the QAB converter during set-point alteration in port #2: (a) only using PI controllers without ADRC decoupling, and (b) with ADRC decoupling control. ADRC controllers decouple the control loops of $v_{DC,4}$ and i_3 from the coupling disturbance from current loop of i_2. Further, ADRC control achieves zero-steady state error without using integral gain.

Figure 3.31a shows the transient waveforms of the relevant currents and voltage by only using PI controllers without active disturbance rejection. In this case, the load port voltage ($v_{DC,4}$) is disturbed and drops by 19 V (10% of nominal value) before recovering to its nominal value. Equivalently, the port #3 current (i_3) is also disturbed due to cross-coupling by 0.4 A (20% of nominal value). Figure 3.31b shows the transient waveforms of the QAB converter with the proposed ADRC based control. The improvement on the dynamic performance is evident in both the load port voltage $v_{DC,4}$ and port #3 current i_3. The load port current i_{load} is completely decoupled, while the voltage $v_{DC,4}$ only drops by 3 V (1.5% of nominal value). Finally, it must be noted that all the individual ADRC controllers achieve zero-steady state error without using integral gain. In conclusion, the experimental results validate the efficacy of proposed ADRC control for MAB converters in terms of dynamic decoupling performance.

3.6.6 Efficiency and loss distribution

The efficiency of the QAB converter prototype is experimentally measured using Yokogawa WT500 power analyzer. The QAB converter efficiency is measured with two sources (port #1 and #2) and two loads (port #3 and #4). The power of the load port #4 is kept constant at 730 W, whereas the load power at port #3 is varied from 200 W to 850 W. Two sets of experiment with the above power loading are conducted: (a) port #2 supplies constant power at 600 W, and (b) port #2 supplies constant power at 900 W. Figure 3.32a shows the measured efficiency curves obtained from the experiments. The QAB efficiency curve obtained during port #3 supplying power of 600 W is higher compared to the case when port #3 supplying power of 900 W by 1%-1.5%. Unequal sharing of the power between port #1 and #2 results in higher losses in the second case (P_2= -900 W).

The operating points in the first set of experiments (OP#1 - OP#5) are modelled to analyze the loss distribution within the QAB converter. Figure 3.32b shows the losses incurred at different ports of the QAB converter as the load power P_3 is increased. It can be observed from the loss distribution that the MOSFET conduction losses in both port #1 and port #3 increase as they process more power

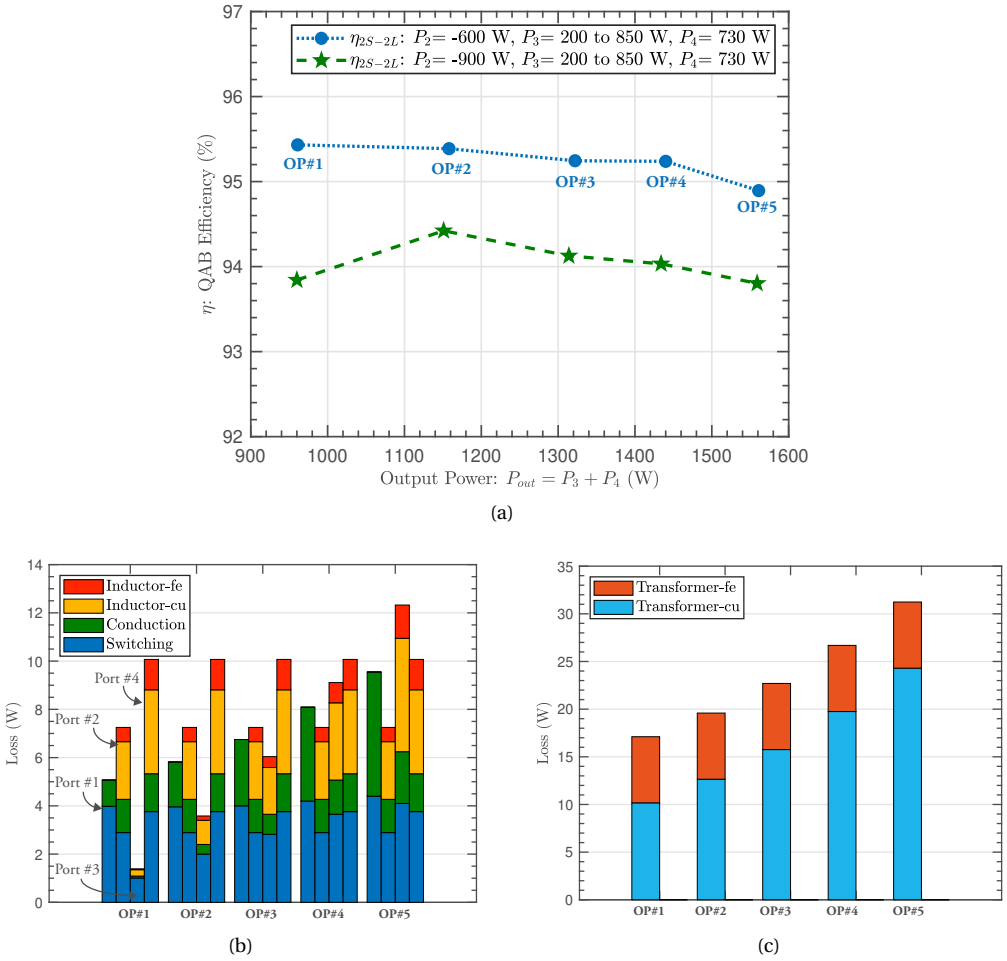

Figure 3.32: (a) QAB converter efficiency during 2S-2L mode of operation with two sources (port #1 and #2) and two loads (port #3 and #4). Port #3 acts as a variable load while port #1 acts as the slack port. Port #4 consumes a constant power of 730 W. Two sets of efficiency measurements are carried out with source port #2 supplying constant power of 600 W and 900 W, (b) loss distribution in different ports of the QAB converter at different operating points in 2S-2L mode with P_3: 200 W to 850 W (load), P_2: -600 W (source), and P_4: 730 W (load), and (c) loss distribution in the transformer of the QAB converter at different operating points.

from operating point 1 to 5. Similarly, the MOSFET switching losses in port #3 increases as the power increases. In all the operating points, port #3 MOSFETs are soft-switched. Therefore, they have zero turn-on losses. As the peak current during turning-off increases with increasing power, the turn-off losses of the port #3 MOSFETs increase. However, the MOSFET switching losses in port #1 almost remains constant even though the power delivered increases. Similar to port #3, the MOSFETs in port #1 are also soft-switched leading to zero turn-on losses. However, due to low leakage inductance of the master port, the peak current (i_{T1}) during the turn-off transition is high as seen in the steady-state transformer waveforms shown in Figure 3.26a. The master port inductor peak current value doesn't increase significantly as the power delivered by the master port increases. Therefore, the MOSFET switching losses in port #1 remain constant. The high peak transformer current of the master port

Table 3.5: Overview of MAB decoupling strategies

Category	Decoupling strategy	Performance metrics			
		Computational effort	Controller architecture	Design complexity	Additional component
Control	Band decoupling [31]	Low	Decentralized	Low	-
	Inverse matrix [14, 32]	High	Centralized	Low	-
	Pre-compensator [22]	Medium	Centralized	Low	-
	Time-sharing [11]	Low	Decentralized	Low	-
	Observer-based *[This thesis]*	Medium	Decentralized	Low	-
Hardware	Asymmetric leakage *[This thesis]*	Low	Decentralized	High	One less inductor
	Resonant capacitor [33]	Low	Decentralized	Medium	One extra capacitor

in the proposed MAB configuration results in high turn-off switching losses irrespective of operating point. This is a drawback of the proposed configuration compared to the conventional configuration.

The transformer loss distribution is presented in Figure 3.32c. The winding losses increase as the overall power processed by the QAB converter increases from operation point #1 to point #5. However, the core losses remain constant independent of the power processed by the transformer. Due to the zero leakage inductance, only the master-port volt-seconds determines the flux density swing in the transformer. Since the master-port volt-seconds remain constant throughout the operating points, the core losses also remain the same. Finally, Figure 3.26b shows the thermal performance of the QAB converter at operating point #5.

3.7 Conclusion

This chapter presented the development of the smart-power-router capable of integrating renewable sources, storages, and loads for future DC household nanogrids. Based on a qualitative evaluation of multi-port converters, a multi-winding transformer-coupled multi-active bridge converter (MAB) is selected due to the ease of bi-directional power flow management and port-to-port galvanic isolation. However, MAB converter design and control is challenging as the power flow between different sources connected via a multi-winding transformer is highly coupled. Therefore, from a control perspective, the MAB converter is a coupled multi-input multi-output (MIMO) system that requires sophisticated decoupling control strategies. Consequently, this hinders the scalability and reliability of the MAB converter.

In this thesis, two solutions to the MAB converter power flow coupling problem are presented. First, a new hardware configuration for a MAB converter with asymmetrical leakage inductance distribution is introduced. It is based on making a port as master with low leakage inductance (≤ 0.05 pu) act as a rigid-voltage source on the transformer magnetizing inductance while adding external inductors (1 pu) to the rest of the ports. The proposed MAB configuration has inherently magnetically decoupled power flows, enabling the regulation of power flows independently of the different port controller

bandwidths. However, the hardware approach increases the switching losses of the master port MOSFETs and makes the multi-winding transformer design challenging. To that end, a control-based solution to the MAB coupling problem is also presented in this thesis. Active-disturbance rejection control (ADRC) with high bandwidth extended state observer (ESO) is used to observe the cross-coupling disturbance, compensated in real-time. Thus, ADRC control decouples the power flows in a multi-active bridge (MAB) converter in a decentralized manner using minimal system information. The decoupling strategies decompose the MIMO system into independent single-input single-output (SISO) systems with no mutual interaction allowing power flow control regardless of controller bandwidth. Table 3.5 presents a comparative overview of the proposed decoupling strategies with existing state-of-the-art methods in literature.

The decoupling strategies are extensively validated using simulations and experiments conducted on a 2 kW, 100 kHz four-port MAB converter laboratory prototype. Further, an in-depth analysis of the losses incurred in the MAB converter is analyzed and experimentally validated. In summary, the proposed strategies solve the problem of power flow coupling inherent to MAB converters without losing any advantage of the MAB converter family. Thus, it allows an increase in the number of ports without increased control complexity leading to higher system reliability, scalability, and robustness. In conclusion, the developed MAB converter can be a promising candidate to be the smart-power router for future DC residential nanogrids.

References

[1] P. H. Nguyen, W. L. Kling, and P. F. Ribeiro, "Smart power router: A flexible agent-based converter interface in active distribution networks," *IEEE Transactions on Smart Grid*, vol. 2, no. 3, pp. 487–495, 2011.

[2] H. Wu, Y. Xing, Y. Xia, and K. Sun, "A family of non-isolated three-port converters for stand-alone renewable power system," in *IECON 2011-37th Annual Conference of the IEEE Industrial Electronics Society*, pp. 1030–1035, IEEE, 2011.

[3] H. Kim, B. Parkhideh, T. D. Bongers, and H. Gao, "Reconfigurable solar converter: A single-stage power conversion pv-battery system," *IEEE transactions on power electronics*, vol. 28, no. 8, pp. 3788–3797, 2012.

[4] Y.-M. Chen, A. Q. Huang, and X. Yu, "A high step-up three-port dc–dc converter for stand-alone pv/battery power systems," *IEEE Transactions on Power Electronics*, vol. 28, no. 11, pp. 5049–5062, 2013.

[5] G. R. C. Mouli, J. Schijffelen, M. van den Heuvel, M. Kardolus, and P. Bauer, "A 10 kw solar-powered bidirectional ev charger compatible with chademo and combo," *IEEE Transactions on Power Electronics*, vol. 34, no. 2, pp. 1082–1098, 2018.

[6] A. K. Bhattacharjee, N. Kutkut, and I. Batarseh, "Review of multiport converters for solar and energy storage integration," *IEEE Transactions on Power Electronics*, vol. 34, no. 2, pp. 1431–1445, 2018.

[7] C. Zhao and J. W. Kolar, "A novel three-phase three-port ups employing a single high-frequency isolation transformer," in *Power Electronics Specialists Conference*, vol. 6, pp. 4135–4141, IEEE, 2004.

[8] H. Krishnaswami and N. Mohan, "Three-port series-resonant dc–dc converter to interface renewable energy sources with bidirectional load and energy storage ports," *IEEE Transactions on Power Electronics*, vol. 24, no. 10, pp. 2289–2297, 2009.

[9] E. Asa, K. Colak, M. Bojarski, and D. Czarkowski, "Asymmetrical duty-cycle and phase-shift control of a novel multiport cll resonant converter," *IEEE Journal of Emerging and Selected Topics in Power Electronics*, vol. 3, no. 4, pp. 1122–1131, 2015.

[10] S. Falcones, R. Ayyanar, and X. Mao, "A dc–dc multiport-converter-based solid-state transformer integrating distributed generation and storage," *IEEE Transactions on Power electronics*, vol. 28, no. 5, pp. 2192–2203, 2012.

[11] Y. Chen, P. Wang, H. Li, and M. Chen, "Power flow control in multi-active-bridge converters: Theories and applications," in *2019 IEEE Applied Power Electronics Conference and Exposition (APEC)*, pp. 1500–1507, IEEE, 2019.

[12] R. W. De Doncker, D. M. Divan, and M. H. Kheraluwala, "A three-phase soft-switched high-power-density dc/dc converter for high-power applications," *IEEE transactions on industry applications*, vol. 27, no. 1, pp. 63–73, 1991.

[13] L. F. Costa, G. Buticchi, and M. Liserre, "Quad-active-bridge dc–dc converter as cross-link for medium-voltage modular inverters," *IEEE Transactions on Industry Applications*, vol. 53, pp. 1243–1253, 2016.

[14] C. Zhao, S. D. Round, and J. W. Kolar, "An isolated three-port bidirectional dc-dc converter with decoupled power flow management," *IEEE transactions on power electronics*, vol. 23, pp. 2443–2453, 2008.

[15] R. W. Erickson and D. Maksimovic, *Fundamentals of power electronics*. Springer Science & Business Media, 2007.

[16] R. D. Middlebrook and S. Cuk, "A general unified approach to modelling switching-converter power stages," in *1976 IEEE Power Electronics Specialists Conference*, pp. 18–34, IEEE, 1976.

[17] H. Bai, C. Mi, C. Wang, and S. Gargies, "The dynamic model and hybrid phase-shift control of a dual-active-bridge converter," in *Annual Conference of IEEE Industrial Electronics*, pp. 2840–2845, IEEE, 2008.

[18] K. Zhang, Z. Shan, and J. Jatskevich, "Large-and small-signal average-value modeling of dual-active-bridge dc–dc converter considering power losses," *IEEE Transactions on Power Electronics*, vol. 32, no. 3, pp. 1964–1974, 2016.

[19] V. Vorpérian, "Simplified analysis of pwm converters using model of pwm switch. ii. discontinuous conduction mode," *IEEE Transactions on aerospace and electronic systems*, vol. 26, no. 3, pp. 497–505, 1990.

[20] P. Wang, Y. Chen, Y. Elasser, and M. Chen, "Small signal model for very-large-scale multi-active-bridge differential power processing (mab-dpp) architecture," in *2019 20th Workshop on Control and Modeling for Power Electronics (COMPEL)*, pp. 1–8, IEEE, 2019.

[21] Q.-G. Wang, *Decoupling control*, vol. 285. Springer Science & Business Media, 2002.

[22] L. Wang, Z. Wang, and H. Li, "Asymmetrical duty cycle control and decoupled power flow design of a three-port bidirectional dc-dc converter for fuel cell vehicle application," *IEEE Transactions on Power Electronics*, vol. 27, no. 2, pp. 891–904, 2011.

[23] G. Herbst, "Practical active disturbance rejection control: Bumpless transfer, rate limitation, and incremental algorithm," *IEEE Transactions on Industrial Electronics*, vol. 63, no. 3, pp. 1754–1762, 2015.

[24] W.-H. Chen, J. Yang, L. Guo, and S. Li, "Disturbance-observer-based control and related methods—an overview," *IEEE Transactions on Industrial Electronics*, vol. 63, no. 2, pp. 1083–1095, 2015.

[25] W. Xue, W. Bai, S. Yang, K. Song, Y. Huang, and H. Xie, "Adrc with adaptive extended state observer and its application to air–fuel ratio control in gasoline engines," *IEEE Transactions on Industrial Electronics*, vol. 62, no. 9, pp. 5847–5857, 2015.

[26] Y. Zuo, X. Zhu, L. Quan, C. Zhang, Y. Du, and Z. Xiang, "Active disturbance rejection controller for speed control of electrical drives using phase-locking loop observer," *IEEE Transactions on Industrial Electronics*, vol. 66, no. 3, pp. 1748–1759, 2018.

[27] D. Wu and K. Chen, "Design and analysis of precision active disturbance rejection control for noncircular turning process," *IEEE Transactions on Industrial Electronics*, vol. 56, no. 7, pp. 2746–2753, 2009.

[28] J. Su, W. Qiu, H. Ma, and P.-Y. Woo, "Calibration-free robotic eye-hand coordination based on an auto disturbance-rejection controller," *IEEE Transactions on Robotics*, vol. 20, no. 5, pp. 899–907, 2004.

[29] J. Vincent, D. Morris, N. Usher, Z. Gao, S. Zhao, A. Nicoletti, and Q. Zheng, "On active disturbance rejection based control design for superconducting rf cavities," *Nuclear Instruments and Methods in Physics Research Section A: Accelerators, Spectrometers, Detectors and Associated Equipment*, vol. 643, no. 1, pp. 11–16, 2011.

[30] Z. Gao, "Scaling and bandwidth-parameterization based controller tuning," in *Proceedings of the American control conference*, vol. 6, pp. 4989–4996, 2006.

[31] H. Tao, A. Kotsopoulos, J. Duarte, and M. Hendrix, "A soft-switched three-port bidirectional converter for fuel cell and supercapacitor applications," in *PESC'05. 36th*, pp. 2487–2493, IEEE, 2005.

[32] G. Buticchi, L. F. Costa, D. Barater, M. Liserre, and E. D. Amarillo, "A quadruple active bridge converter for the storage integration on the more electric aircraft," *IEEE Transactions on Power Electronics*, vol. 33, no. 9, pp. 8174–8186, 2017.

[33] P. Wang, X. Lu, W. Wang, and D. Xu, "Hardware decoupling and autonomous control of series-resonance-based three-port converters in dc microgrids," *IEEE Transactions on Industry Applications*, vol. 55, no. 4, pp. 3901–3914, 2019.

4 Wireless Residential EV charging

Electric vehicles (EV) will be an integral part of future smart homes. Therefore, efficient charging infrastructure is needed for integration of EVs in the DC house. Inductive power transfer (IPT) based charging system is a promising candidate for household EV charging applications. IPT technology is more user-friendly and safer than conventional wired charging due to absence of electrical or mechanical contacts. Additionally, IPT systems can be bi-directional which will allow implementation of vehicle-to-home (V2H) and/or vehicle-to-grid (V2G) charging.

Based on:

1. "*Comparison of Magnetic Couplers for IPT EV Charging using Multi-Objective Optimization*" **IEEE Transactions on Vehicular Technology**, vol. 68, no. 6, pp. 5416-5429, June 2019, doi: 10.1109/TVT.2019.2909566.
2. *"Multi-objective optimisation of a 1-kW wireless IPT systems for charging of electric vehicles,"* IEEE Transportation Electrification Conference and Expo (ITEC), Dearborn, MI, 2016, pp. 1-7.
3. "*Comparison of Optimized Chargepads for Wireless EV Charging Application*" 10th International Conference on Power Electronics and ECCE Asia (ICPE 2019 - ECCE Asia), Busan, Korea (South), 2019, pp. 1-8.
4. "*Design considerations for a misalignment tolerant wireless inductive power system for electric vehicle (EV) charging*," 19th European Conference on Power Electronics and Applications (EPE'17 ECCE Europe), Warsaw, 2017, pp. P.1-P.10.

4.1 Introduction

Electric vehicles (EVs) are a critical element in the transition towards a green future. With the impending ban on diesel or petrol cars within the next decade, it is safe to assume that EVs will replace conventional cars in every household [1]. Therefore, it is necessary to integrate EV charging in future smart homes safely and efficiently. To that end, this chapter focuses on designing an EV charging infrastructure for smart home or building applications. In the proposed smart power router-based DC architecture, the EV charging can be integrated with two methods: (a) connecting directly to a smart power router port, and (b) connecting to the DC bus along with the household loads. The advantage of connecting directly to a smart power router is that it obviates the need for isolation. Thus, the homeowner can implement DC charging by merely connecting the EV battery to a smart power router port. On the other hand, the second method of EV charging integration via the smart home's DC bus requires galvanic isolation according to EU standards. But this solution is more generic and therefore, more applicable to future smart homes with or without a smart power router. Hence, this thesis focuses on the method of integrating EV charging in the smart home's DC bus.

Inductive wireless EV charging

Inductive power transfer (IPT) is a promising solution for EV charging integration in DC smart homes. IPT is already a popular solution for a wide range of battery charging applications, such as low power bio-medical implants, industrial automation, consumer electronics and electric vehicles (EVs) [2, 3]. IPT technology for EV charging is more user-friendly and safe than conventional wired charging due to the absence of electrical or mechanical contacts. Additionally, it opens up the possibility of dynamically charging the EV battery while they are running [4, 5]. Due to these advantages as mentioned above, IPT technology is a crucial enabling factor for a further increase in the popularity of EVs, especially in the in-house charging market which requires safety, comfort and convenience of charging.

A general scheme of an IPT system for EV charging from a utility grid consists of the following power conversion stages: a power factor corrector (PFC), a high-frequency inverter (HFI), magnetically coupled coils and a pickup circuitry comprised of a rectifier followed by a DC-DC converter to match the battery voltage. It has similar functional elements as that of a plug-in charger [6]. The high frequency isolating transformer in the onboard charger (OBC) of an EV is functionally identical to the magnetic couplers in an IPT system. The difference is the large air-gap and associated significant leakage of IPT couplers.

IPT designs require highly efficient magnetic couplers to match the plug-in EV charging efficiencies. Operational air-gap in a typical EV charging IPT system ranges from 5 cm to 40 cm. This poses a significant design challenge since coupling co-efficients (k) due to such large air-gaps typically vary between 0.01 and 0.5. Compared with conventional iron cored transformers (k ≈ 0.95 - 0.99), they are low [7]. Furthermore, there are other design challenges in magnetic couplers which include: limited allowable space and weight of the charge pads, misalignment tolerance and strict guidelines on EMF emissions. To that end, the goal of this thesis is on the design of the magnetic power conversion stage of the IPT system focusing on the comparative analysis of different coupler types.

Literature review

A large number of coupler topologies for IPT based EV charging is reported in literature [8–11]. Figure 4.1 shows all the popular magnetic couplers reported in literature. Based on coil winding strategy, there can be two types of lumped IPT charge pads: a) Solenoid or double sided flux couplers [10, 12] and b) planar or single-sided flux couplers [8]. Planar couplers can be further classified into two families based on fundamental flux path: a) non-polarized couplers like circular and rectangular geometries [13–15] and b) multi-coil polarized couplers like double D (DD) [7, 9], bi-polar pad (BPP) [16], and double D-Quadrature (DDQ) [8, 11, 17]. Comparisons between different concepts are found in several publications [18–21]. Several coil topologies are compared using numerical methods and statistical methods in [18, 19]. However, in those studies different loss mechanisms in the charge pads are not considered. Also, the advantages of the various coil topologies of primary performance factors like power transfer efficiency, power densities, misalignment tolerance, and stray field exposure are not clear. To ensure a fair quantitative comparison, the IPT couplers considered should be optimized under given constraints. A multi-objective optimization approach is introduced in [22, 23], where design tradeoffs between efficiency (η), area power density (α) and gravimetric power density (γ) in the form of Pareto fronts are presented. However, the study was limited to only two coupler geometries and didn't consider the trade-offs between misalignment tolerance and power densities of the couplers.

Contributions

This thesis extends the above studies to include all major topologies and performance parameters. The objective of this thesis is to compare the following coupler geometries:

1. Circular (Transmitter + Receiver)

2. Rectangular (Transmitter + Receiver)

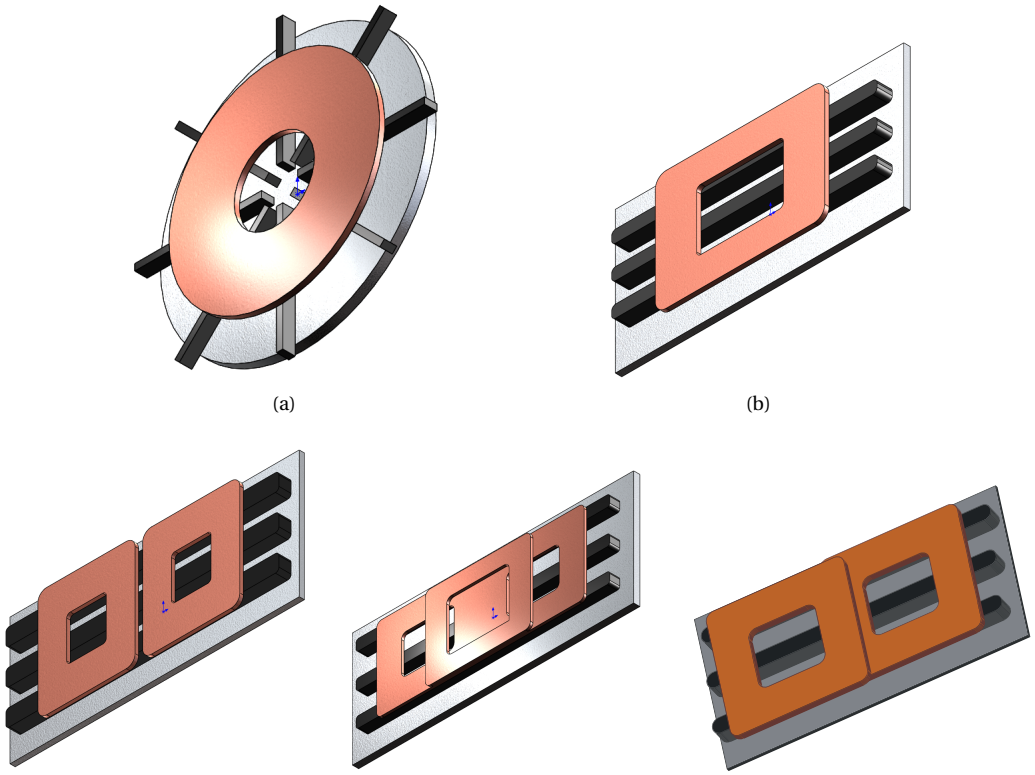

Figure 4.1: Popular magnetic couplers for inductive power transfer (IPT) based EV charging: (a) Circular, (b) Rectangular, (c) DD, (d) DDQ, and (e) BPP.

3. DD (Transmitter + Receiver)
4. DD (Transmitter) - DDQ (Receiver)
5. DD (Transmitter) - BPP (Receiver)

To ensure a fair comparison, the chosen coupler geometries as shown in Figure 4.1 are optimized with the goal of maximizing efficiency, vehicle pad area power density, gravimetric power density, and misalignment tolerance.

To that end, the main contributions of this chapter are:

1. Developing computationally efficient numerical modelling methodology of IPT couplers suitable for optimization.
2. Validating the developed numerical modelling methodology with experimental tests.
3. Developing a generalized multi-objective optimization (MOO) framework for design of IPT coupler.

4. The developed and validated modelling methodology is combined with the MOO framework to assess the performance of the five popular coupler topologies (see Figure 4.1) and presents the merits and demerits of individual concepts.

5. Highlighting trade-offs and trends among the performance parameters (efficiency, power density, misalignment tolerance and stray field) for all the coupler geometries.

Chapter outline

This chapter is organized into six parts. First, a brief overview of the magnetic couplers and their classification are provided in Section 4.3. In Section 4.4, the numerical modelling methodology of the magnetic couplers is discussed briefly. Section 4.5 validates the numerical modelling methodology with experimental results on a laboratory prototype. Section 4.6 develops a multi-objective optimization (MOO) framework to optimize the selected couplers and compare them. Based on the optimization results, a detailed comparative analysis of the coupler topologies is presented in Section 4.7. Finally, general conclusions are summarized based on the results.

4.2 Fundamentals of IPT system

A generic lumped IPT system is comprised of the three fundamental components: power supply, magnetic coils or chargepads, and a pick up circuit as shown in Figure 4.2. A DC power supply is followed by a single-phase square wave inverter. The IPT system consists of resonant compensation networks for the transmitter and receiver coils along with a rectifier (sometimes followed by an additional DC/DC converter) in the pick up side. A brief overview of the fundamentals of the above components is presented in this section.

4.2.1 Principle of operation

The principle of operation of inductive power transfer is based on near-field magnetics which can be explained by applying Ampere's law and Faraday's law. On the primary side as depicted in Figure 4.2, according to Ampere's law, an AC current i_1 generates a time-varying magnetic flux ϕ around the

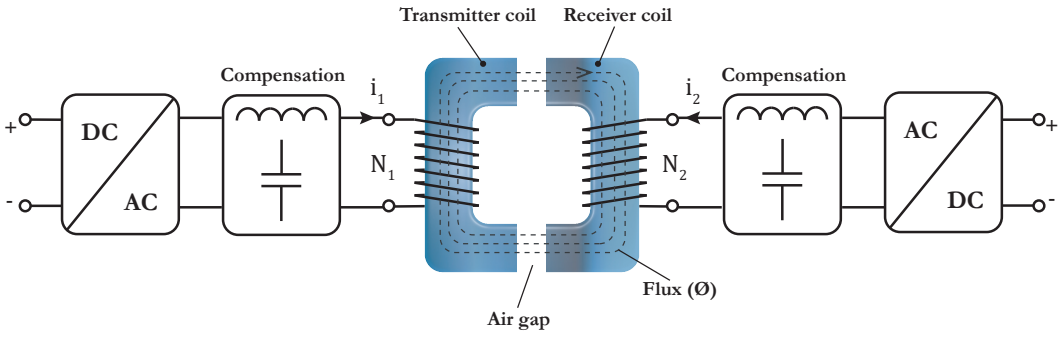

Figure 4.2: Architecture of a general inductive power transfer (IPT) system.

transmitter coil. Subsequently, the generated flux ϕ is linked to the receiver-side coil and induces a voltage across it. The amplitude of the induced voltage on the receiver coil is proportional to the coupled flux and the number of turns in the coil, as governed by Faraday's Law:

$$\oint_{\mathrm{c}} \vec{B} \cdot dl = \mu_0 N_1 i_1 \tag{4.1}$$

$$\phi = \oint_{\mathrm{s}} \vec{B} \cdot dS \tag{4.2}$$

$$v = -N_2 \frac{\mathrm{d}\phi}{\mathrm{d}t} \tag{4.3}$$

where $\vec{B}$ is the magnetic flux density, c is the contour for line integration, s is the contour for surface integration, N_1 and N_2 are the number of turns in the transmitter and receiver coil respectively, μ_0 is the permeability of air, and v is the voltage induced in the receiver side.

Compared to traditional transformers, IPT transmitter and receiver coils have a much larger air gap between them. Therefore, only a fraction of the transmitter's magnetic flux is coupled with the receiver coil, which leads to high leakage and low magnetizing coil inductances. Consequently, there is significant reactive power circulating in the system, which increases losses and reduces power transfer efficiency. Therefore, one or more passive elements, also called compensation networks are added to the system to provide a local path to the reactive power and improve efficiency. The compensation network cancels the high inductive reactance of the coils at the resonant frequency, reduces the coil's impedance, and allows high current to be injected into the winding.

In conclusion, in a generic IPT system, a single-phase inverter generates a high-frequency magnetic field transmitted and received by coils with impedance compensation, and rectified into DC, filtered, and fed to the load.

4.2.2 Mutual inductance model and power transfer

A mutual inductance model [24] is used to develop an equivalent circuit of the IPT system. In this model, the loosely coupled transformer is represented as a two port network, and the coupling between the primary and secondary sides is represented by the mutual inductance M, as shown in Figure 4.3. The mutual inductance model is popular for its simplicity as the leakage inductance is removed reducing the number of variables.

The mutual inductance model is also represented by the co-efficient of coupling k as represented in the following:

$$k = \frac{M}{\sqrt{L_1 L_2}} \tag{4.4}$$

where L_1, L_2 are the self inductances of the transmitter and receiver coils. The following circuit equations describing the IPT system can be expressed using the mutual inductance model:

$$\begin{bmatrix} v_{\mathrm{ac}} \\ 0 \end{bmatrix} = \begin{bmatrix} r_1 + j\omega L_1 & -j\omega M \\ -j\omega M & r_2 + R_{\mathrm{L,eq}} + j\omega L_2 \end{bmatrix} \tag{4.5}$$

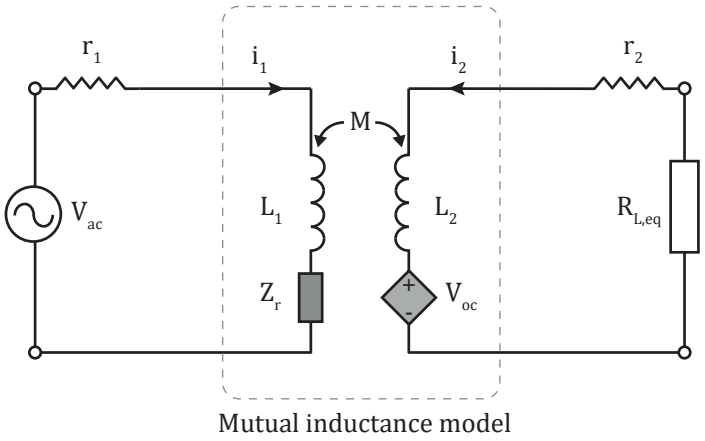

Figure 4.3: Circuit diagram of the mutual inductance model of IPT system.

Therefore, the input impedance as seen by the inverter can be solved and expressed as:

$$Z_{\text{in}} = \frac{v_{\text{ac}}}{i_1} = Z_1 + Z_{\text{r}} = Z_1 + \frac{(\omega M)^2}{Z_2} \tag{4.6}$$

where Z_1,Z_2 are the transmitter and receiver impedances, and Z_{r} is the reflected impedance of the receiver on the transmitter. The reflected impedance Z_{r} and the receiver open-circuit voltage V_{oc} represent the coupling between the transmitter and receiver sides. Based on this, the input and output power of the system can be expressed as following respectively:

$$P_{\text{in}} = \text{Re}\left(\frac{V_{\text{ac}}^2}{Z_{\text{in}}}\right) = \text{Re}\left(\frac{V_{\text{ac}}^2 Z_2}{Z_1 Z_2 + (\omega M)^2}\right) \tag{4.7}$$

$$P_{\text{out}} = |i_2|^2 R_{\text{L,eq}} = \frac{V_{\text{ac}}^2 \omega^2 M^2 R_{\text{L,eq}}}{\left|Z_1 Z_2 + (\omega M)^2\right|^2} \tag{4.8}$$

Further, the apparent power S that can be transferred from the transmitter to the receiver can be written as [25]:

$$S = |V_{\text{oc}} \times i_2| = \left|j\omega i_1 i_2\right| = \left|\frac{V_{\text{ac}}^2 \omega^2 M^2 Z_2}{[Z_1 Z_2 + (\omega M)^2]^2}\right| = P_{\text{out}} \frac{Z_2}{R_{\text{L,eq}}} \tag{4.9}$$

It is evident from (4.9), that purely active power can be transferred if the receiver side is fully compensated; i.e, $Z_2 = R_{\text{L,eq}} + r_2$. Additionally, (4.7) shows that the transmitter supplies active power if both the transmitter and the receiver side are fully compensated. Therefore, (4.7), (4.8) and (4.9) present the analytical tool to evaluate the power transfer characteristics and efficiency of IPT systems. A series-series compensation network to improve power transfer capability and efficiency is discussed in the next section.

4.2.3 Series-series compensation network

The compensation network is an integral part of the IPT system. It needs to provide multiple functionalities to ensure the high performance of any IPT system. Primarily, it needs to compensate for reactive power due to increased leakage inductances associated with loosely coupled coils. In EV charging applications, another compensation network performance requirement comes from the load change and coupling variation related to coils' position. Therefore, the resonant network needs to compensate for output fluctuations due to a wide range of parameter drift and reduce the sensitivity to load and coupling variation [26]. Finally, the current and voltage stresses on the compensation network elements are exceptionally high at high power ratings, leading to significant losses [27]. To that end, the simplicity of the compensation network is critical in maintaining overall high system efficiency.

Several compensation networks reported in the literature perform the functionalities as mentioned earlier to varying degrees. They can be divided into two main categories: (a) single-element compensations like series-series (SS), series-parallel (SP), parallel-series (PS), parallel-parallel (PP), and (b) multi-element compensations like LCL, LCC etc. A detailed comparison of various compensation networks' advantages and disadvantages is out of scope for this thesis. Comparisons between different compensation networks can be found in literature [28, 29]. In this thesis, a series-series (SS) compensation is selected as the compensation topology for its simplicity, load-independence, and position tolerance.

Figure 4.4a shows the converter topology for an IPT system with series compensation capacitors on both sides of the contactless transformer. The transformer model of the IPT system is built with a transformation ratio of $n = 1$ to simplify the circuit for better understanding. A fundamental frequency model of the IPT system is used to simplify the analysis of the power transfer and losses without losing accuracy [30]. The fundamental frequency model including the transformer equivalent circuit is shown in Figure 4.4b described by the leakage inductances $L_1 - M$ and $L_2 - M$ on both sides of the the magnetizing inductance M. Further, the receiver side is modelled as an equivalent resistance as the following:

$$R_{\mathrm{L,eq}} = \frac{8}{\pi^2} \frac{U_{2,\mathrm{dc}}^2}{\eta_{\mathrm{R}} P_{\mathrm{out}}} \tag{4.10}$$

where P_{out} is the output power of the converter, and η_{R} is the efficiency of the rectifier.

The values of the series compensator capacitors are selected such that the resonance frequency f_0 defined by the capacitors and the self-inductances of the transformer windings is equal to the switching frequency of the inverter:

$$f_{\mathrm{sw}} = f_0 = \frac{1}{2\pi\sqrt{L_1 C_1}} = \frac{1}{2\pi\sqrt{L_2 C_2}} \tag{4.11}$$

Figure 4.4c shows the equivalent circuit of the IPT system when the switching frequency of the inverter is equal to the resonant frequency of the passive elements. At this condition, the input impedance as seen by the inverter on the transmitter side can be expressed as:

$$Z_{\mathrm{in}} = \frac{\omega_{\mathrm{o}}^2 M^2}{R_{\mathrm{L,eq}}} \tag{4.12}$$

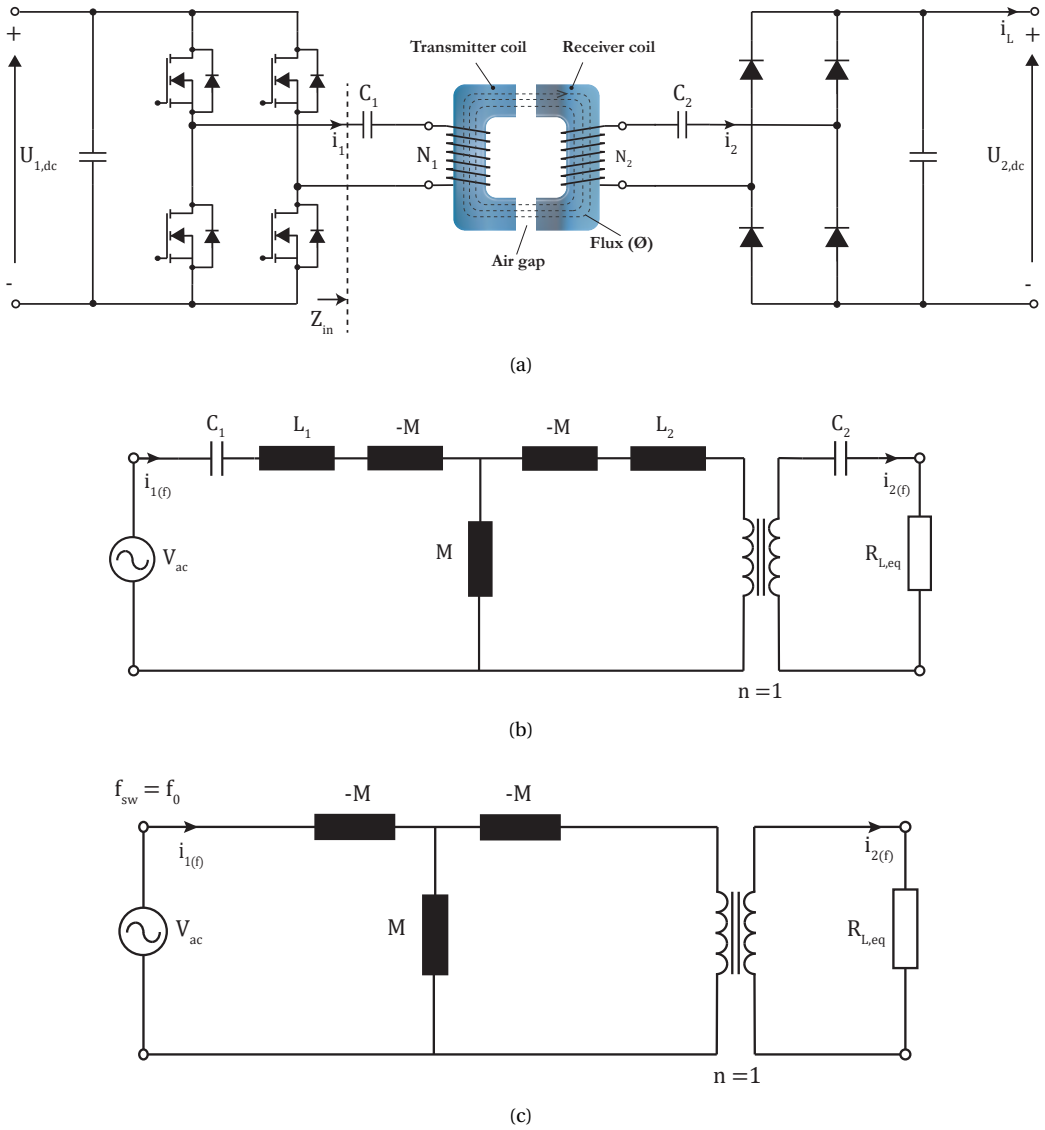

Figure 4.4: (a) Topology of the series-series compensated IPT system, (b) Fundamental frequency model of the IPT converter system including the transformer T-model, and (c) Equivalent circuit when the switching frequency f_{sw} is equal to the resonant frequency f_0 of the reactive elements L_1, C_1 and L_1, C_2.

which is purely real, independently of the magnetic coupling or the load. The transmitter and receiver currents can be expressed as the following:

$$i_1 = \frac{V_{\text{ac}}}{Z_{\text{in}}} = \frac{V_{\text{ac}} R_{\text{L,eq}}}{\omega_{\text{o}}^2 M^2} \tag{4.13}$$

$$i_2 = \frac{j\omega_{\text{o}} M i_1}{R_{\text{L,eq}}} = \frac{j\omega_{\text{o}} M V_{\text{ac}}}{\omega_{\text{o}}^2 M^2} \tag{4.14}$$

It is evident from (4.14) that an SS compensated IPT system behaves as a load-independent current source. Further, (4.12) shows that the Thevenin impedance as seen by the primary side inverter is always real independent of magnetic coupling or load. Therefore, series-series compensation is perfectly suited for EV charging applications for its simplicity, misalignment tolerance, and load-independent current source behaviour.

4.2.4 Efficiency optimal system operation

In this section, the efficiency limit of a series-series (SS) compensated IPT system is discussed. The equivalent circuit model highlighting the losses in an IPT system is shown in Figure 4.5. The power losses of the IPT coils are modeled as parasitic ac resistances $r_{\mathrm{ac},1}$ and $r_{\mathrm{ac},2}$ in series with the leakage inductances. During resonance operation, the transmitter and the receiver currents have only active components. Therefore, the efficiency of power transfer can be expressed as the following:

$$\eta = \frac{P_{\mathrm{out}}}{P_{\mathrm{in}}} = \frac{i_2^2 R_{\mathrm{L,eq}}}{i_2^2 R_{\mathrm{L,eq}} + i_2^2 r_{\mathrm{ac},2} + i_1^2 r_{\mathrm{ac},1}} \tag{4.15}$$

where the transmitter and the receiver currents are expressed as the following:

$$i_1 = \frac{V_{\mathrm{ac}}(R_{\mathrm{L,eq}} + r_{\mathrm{ac},2})}{\omega^2 M^2 + R_{\mathrm{L,eq}} r_{\mathrm{ac},1} + r_{\mathrm{ac},2} r_{\mathrm{ac},1}} \tag{4.16}$$

$$i_2 = \frac{\omega M V_{\mathrm{ac}}}{\omega^2 M^2 + R_{\mathrm{L,eq}} r_{\mathrm{ac},1} + r_{\mathrm{ac},2} r_{\mathrm{ac},1}} \tag{4.17}$$

Combining equations (4.15), (4.16), (4.17), the power transfer efficiency can be expressed as the following:

$$\eta = \frac{\omega^2 M^2 R_{\mathrm{L,eq}}}{(R_{\mathrm{L,eq}} + r_{\mathrm{ac},2})(\omega^2 M^2 + R_{\mathrm{L,eq}} r_{\mathrm{ac},1} + r_{\mathrm{ac},2} r_{\mathrm{ac},1})} \tag{4.18}$$

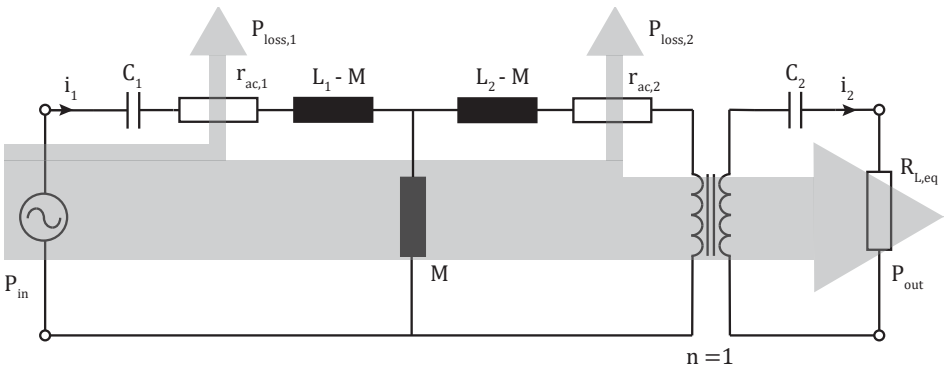

Figure 4.5: Equvalent circuit model of IPT system for loss and efficiency calculation.

The design condition for maximum efficiency at any operating point is achieved when:

$$\frac{\partial \eta}{\partial R_{\mathrm{L,eq}}} = \frac{\omega^2 M^2 (\omega^2 M^2 r_{\mathrm{ac,2}} - r_{\mathrm{ac,1}} R_{\mathrm{L,eq}}^2 - r_{\mathrm{ac,1}} r_{\mathrm{ac,2}}^2)}{(R_{\mathrm{L,eq}} + r_{\mathrm{ac,2}})^2 (\omega^2 M^2 + R_{\mathrm{L,eq}} r_{\mathrm{ac,1}} + r_{\mathrm{ac,2}} r_{\mathrm{ac,1}})^2} = 0 \tag{4.19}$$

Solving the above equation, it can be concluded that the following condition needs to be satisfied to acheive maximum IPT efficiency:

$$R_{\mathrm{L,opt}} = \sqrt{\omega^2 M^2 \frac{r_{\mathrm{ac,2}}}{r_{\mathrm{ac,1}}} + r_{\mathrm{ac,2}}^2} \approx \omega M \sqrt{\frac{r_{\mathrm{ac,2}}}{r_{\mathrm{ac,1}}}} \tag{4.20}$$

The above condition to achieve maximum operating efficiency is also known as load or impedance matching technique [22]. Theoretically, the above condition can be met at different load or coupling by altering the value of the equivalent load impedance $R_{\mathrm{L,eq}}$ by changing the receiver side DC voltage $U_{2,\mathrm{dc}}$ according to (4.10). More details about the implementation of this condition in the control strategy are discussed in the IPT control model in Section 4.4.3.

This concludes a brief overview of the fundamental aspects of an IPT system. It is evident from the above analysis that the magnetic coils' design is crucial in the development of an efficient IPT system for EV charging. In the next section, a review of the popular coil topologies in literature is presented.

4.3 Review of magnetic couplers

As previously highlighted, a significant number of IPT coil topologies are reported in the literature. Before the construction of a framework for comparative analysis, a classification strategy which includes most coil topologies is necessary to make the comparison insightful.

4.3.1 Single-sided and double-sided couplers

IPT coils typically use ferrite bars to enhance coupling coefficient by shaping the magnetic field produced by the coils. The focus of this work is on planar couplers. Spiral planar coils can be placed on the ferrite material to produce magneto-motive force (MMF) only in one side, resulting in a single-sided

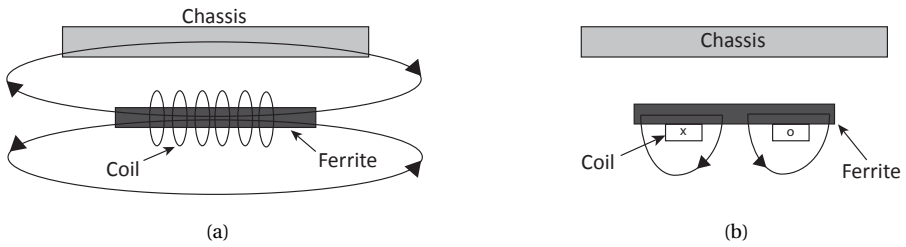

Figure 4.6: Classification of coupler topologies based on the strategy of coil winding: (a) double-sided winding, (b) single-sided winding.

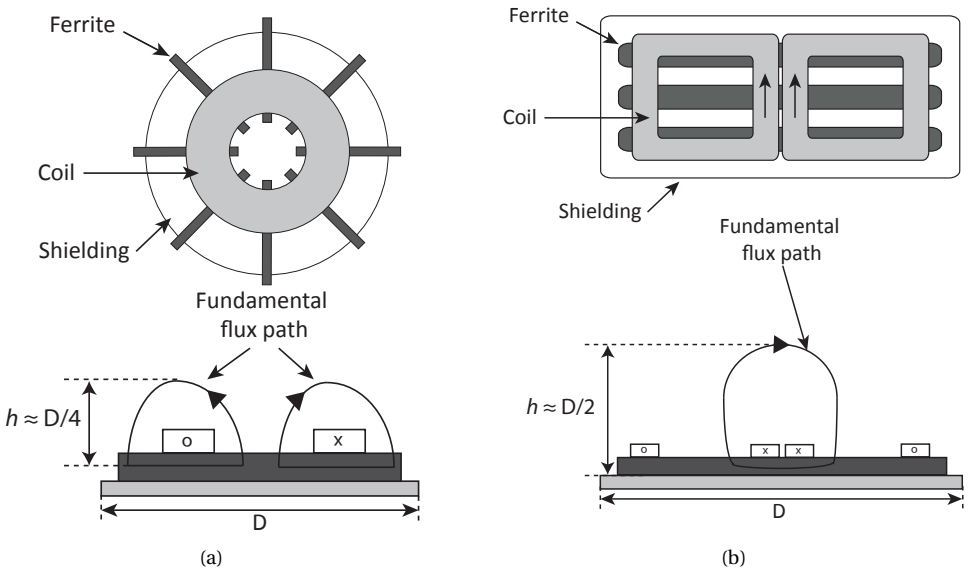

Figure 4.7: Classification of coupler topologies based on fundamental flux path:(a) Non-polarized coupler has a symmetric magnetic field around its center point, the fundamental flux height (h) is roughly proportional to a quarter of pad diameter ($h \approx \frac{D}{4}$), and (b) Polarized coupler has magnetic flux travelling along the length of the pad, the the fundamental flux height (h) is roughly proportional to half of the pad length ($h \approx \frac{D}{2}$).

winding or planar couplers. Comparative studies between solenoid couplers and planar couplers can be found in literature [8, 12]. When a double-sided winding is used, the magnetic coupler can be made smaller than a transformer with a single-sided winding. However, double-sided winding transformers have a leakage flux at the back of the core, and consequently, they have low coupling factors. Therefore, this thesis focuses on planar or single-sided flux couplers.

4.3.2 Unipolar and bi-polar couplers

Single-sided couplers can be further classified into two types: polarized couplers and non-polarized couplers. Popular polarized and non-polarized couplers reported in the literature are namely the double-D (DD) and circular topologies [13, 22] respectively. Other than circular topology, there also can be rectangular coils and square coil topologies (can be considered as a particular case of rectangular coils). The fundamental difference between polarized and non-polarized couplers is the nature of the magnetic flux path. To illustrate the difference between the couplers, the fundamental flux paths of both coupler types are shown and explained in Figure 4.7.

Polarized couplers can be further classified into three types depending on the receiver coil topology: (a) double-D planar (DD) receiver, (b) double-D-quadrature planar (DDQ) receiver, and (c) bi-polar pad (BPP) receiver. DD receiver has same structure as the DD primary (see Figure 4.7). Both DDQ and BPP coil topologies improve misalignment performance of a DD receiver. DDQ receiver (Figure 4.1d) has a Q coil symmetrically placed on the DD structure. The Q coil is magnetically decoupled from the

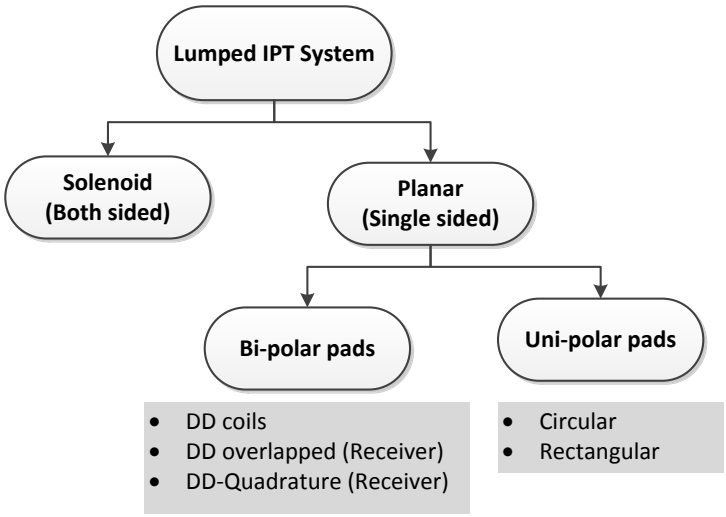

Figure 4.8: Classification of coupler topologies for IPT system.

DD structure due to its inherent spatial positioning. This enables individual tuning and control of the DD coils and the Q coil depending on alignment conditions. Therefore, DDQ topology is interoperable with both unipolar and bipolar pads. A similar decoupling strategy is exploited in BPP receivers. The overlap between the two coils is designed to ensure zero (as close to zero as practically possible) mutual coupling between them. The extent of overlap needed between the coils to ensure decoupling depends on the overall charge pad structure [9, 16]. Similar to DDQ pad, the BPP pad is interoperable with all the other pads and offers good misalignment tolerance. Based on the analysis above, a classification of the lumped magnetic couplers is shown in Figure 4.8.

4.4 Modelling the IPT system

The couplers selected for comparative analysis are be modeled and analyzed in this section. Finite element (FE) analysis is used to model the coupler electromagnetics. The resulting data is post-processed to extract the losses in the coupler along with other performance metrics.

4.4.1 3D coil model simplification and assumptions

COMSOL, a commercially available FE software is used to model the couplers. The considered couplers consist of distributed ferrite strips as shown in Figure 4.1. Hence, 3D finite element (FE) models are necessary to compute their electromagnetic behavior. However, this leads to the longer computation time for individual models. To make the 3D models suitable for optimization purposes, geometrical symmetries of the couplers are exploited to reduce the model. A combination of symmetry boundary

conditions like the parallel flux, normal flux, and periodic boundary conditions [31] are used to reduce the computational loads of the 3D models by several orders as depicted in Figure 4.9.

Automated physics based meshing is used in the 3D models which leads to optimal mesh sizes for different materials based on their skin depths. The litz wire winding is a 3D lumped model for a bundle of tiny wires tightly wound together with uniform current density, separated by an electrical insulator. This prevents the intensive computation load associated with the calculation of the eddy currents in the winding. This approximation is valid since: (1) since litz wire is composed of sinusoidally woven insulated strands of copper, the equal current distribution is a good assumption given they have symmetric impedances, (2) the litz wire strand diameter is chosen accordingly to render the high-frequency effects to a minimum, (3) the current distribution in the windings have small effect on the computation of the inductance of the coupler geometries, and (4) the losses in the windings

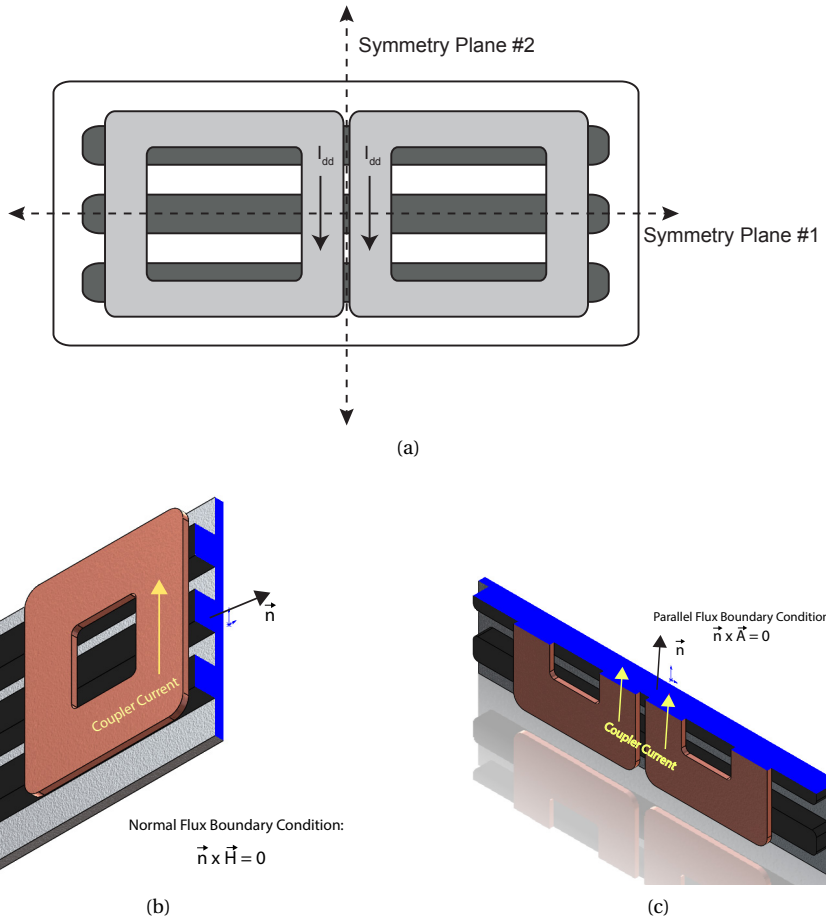

Figure 4.9: (a) Axes of symmetries in a polarized DD coupler, (b) Symmetry Plane #1: Normal flux boundary condition is applied along the axial plane between the two D coils, and (c) Symmetry Plane #2: Parallel flux boundary condition is applied along the axis of the central core strip. Since the coil currents are perpendicular to this boundary, the magnetic flux is parallel, and therefore no magnetic flux penetrates this plane. $\vec{A}$ is the magnetic vector potential.

are computed using analytical equations combined with field values derived separately from a 2D FE model. To further reduce the computation time, linear ferrites are considered with fixed relative permeability (μ_r = 2500). This approximation is valid since a hard constraint is placed on the maximum flux density (B_{max}) of the cores during optimization. B_{max} is strategically chosen well below the saturation flux density of the core material used.

4.4.2 Loss modelling

Coupler losses are computed by analytical post-processing in MATLAB by extracting magnetic field data from the FE models. The IPT system losses consist of: (a) coupler (litz wire, ferrite, aluminium), (b) compensation capacitors, and (c) power electronics. They are briefly discussed in this section.

The litz copper loss (P_{cu}) is comprised of DC ohmic losses (P_{dc}) and AC losses (P_{ac}) due to skin effect and proximity effect (internal and external). They are computed using the following equations [32]:

$$P_{skin} + P_{dc} = n_{str} r_{dc} F_R(f_0) \left(\frac{\hat{I}}{n_{str}} \right)^2 L_{coil} \tag{4.21}$$

$$\begin{aligned} P_{prox,tot} &= P_{prox,int} + P_{prox,ext} \\ &= n_{str} r_{dc} G_R(f_0) \frac{\hat{I}^2}{2\pi^2 d_a^2} L_{coil} + \\ &\sum_{i=i}^{N} n_{str} r_{dc} G_R(f_0) \int_{l_i} \hat{H_{ext}}(l)^2 \mathrm{dl} \end{aligned} \tag{4.22}$$

where n_{str} denotes the number of strands in the litz wire, r_{dc} is the DC resistance per unit length of unit strand of the litz wire, $\hat{H_{ext}}$ is the external magnetic field penetrating the individual coil turns, $F_R(f_0)$ and $G_R(f_0)$ are frequency dependent factors. For accurate loss estimation, $\hat{H_{ext}}$ is extracted from a 2D FE model data separately as shown in Figure 4.10 for each turn and summed. The ferrite core losses (P_{fe}) are determined using the Steinmetz equation and integrating it over the core volumes [33]:

$$P_{fe} = \iiint_V \kappa f_0^{\alpha} \hat{B}^{\beta} dV \tag{4.23}$$

where the Steinmetz parameters of the core material 3C-90 are κ = 3.2E-3, α = 1.46 and β = 2.75. The peak AC flux density ($\hat{B}$) is extracted from the 3D FE models as highlighted in Figure 4.11. Loss due to eddy currents induced in the aluminium (P_{al}) is computed using the surface current density equation [34]:

$$P_{al} = \iint_A \frac{1}{2} (J_S . E^*) dA \tag{4.24}$$

where J_S is the induced surface current density on the aluminium sheets and E is the electric field at the surface boundary.

Polypropylene film capacitors from KEMET are considered for resonant compensation due to their relatively low dielectric losses. The capacitor dielectric loss is calculated according to the following

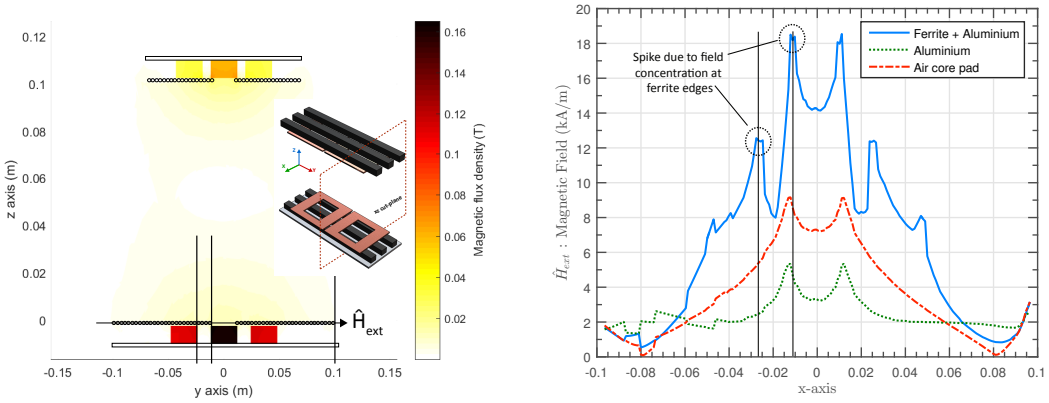

(a) (b)

Figure 4.10: Example of proximity loss computation in a DD coupler with 30 turns and 10 A peak current: (a) Surface magnetic flux density plot of a DD coupler in the xz plane for extraction of external magnetic field intensity ($\vec{H}_{\text{ext}}$) penetrating the turns in the coupler, (b) plot of magnetic field intensity ($\vec{H}_{\text{ext}}$) penetrating the transmitter coil turns. Presence of ferrite increases the H-field penetrating the coil turns while compared to an air core coil, especially for turns located at the edge of the ferrites. In the absence of ferrites, eddy currents induced in the aluminum shield reduces the H-field penetration since they oppose the magnetic field produced by the coil turns in accordance with Lenz's law.

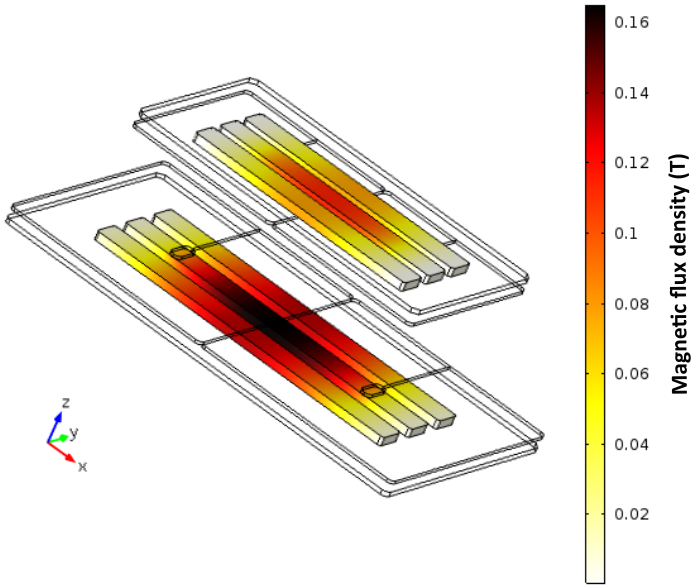

Figure 4.11: Example of peak AC magnetic flux density distribution (T) in the ferrite cores of a DD coupler. The design of DD couplers is limited by the central region of the ferrites which carries the maximum flux.

equation [35]:

$$P_{\text{cap}} = \frac{\tan\delta}{\omega C} I_{\text{rms}}^2 \tag{4.25}$$

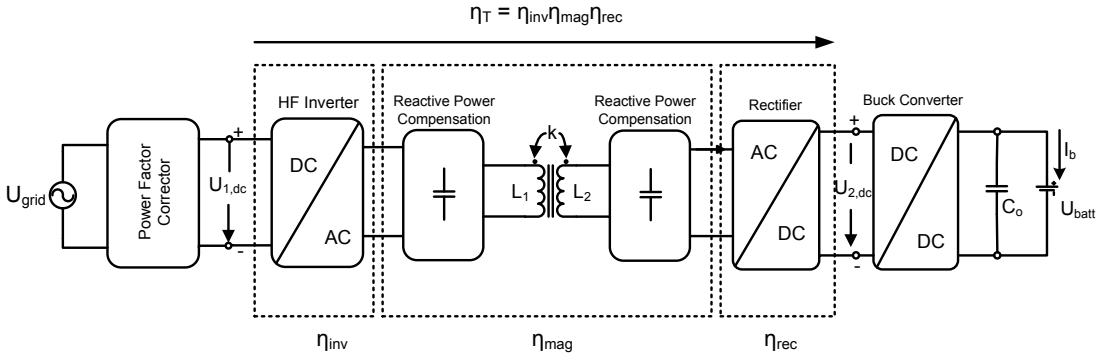

Figure 4.12: The overall IPT system for EV charging from the grid to the battery is presented. In this thesis, the efficiency of power transfer from the transmission side DC link ($U_{1,\mathrm{dc}}$) to the receiver side DC link ($U_{2,\mathrm{dc}}$). There are three power conversion stages in between: (1) the DC-AC stage of the high frequency inverter with efficiency η_{inv}, (2) the AC-AC stage of the magnetic couplers with efficiency η_{mag}, and (3) the AC-DC stage of the rectifier with efficiency η_{rec}. This leads to a total system power trnasmission efficiency of $\eta_{\mathrm{T}} = \eta_{\mathrm{inv}}\eta_{\mathrm{mag}}\eta_{\mathrm{rec}}$.

The dielectric loss factor $\tan\delta$ is chosen to be 0.1% at 100 kHz [36]. The power electronic losses include the losses in the inverter and the rectifier ($P_{\mathrm{inv}}, P_{\mathrm{rec}}$). SiC Schottky diodes (C4D40120D) and MOSFET (C2M0025120D) by Cree are considered for the device loss models. The switching and conduction losses are computed using the data provided in the manufacturer's datasheet and equations presented in [37].

Once all the losses in the couplers are computed resulting in total loss P_{tot}, the ac resistance (r_{ac}) of the individual couplers is given by the following equation:

$$r_{\mathrm{ac}} = \frac{P_{\mathrm{tot}}}{I^2} = \frac{P_{\mathrm{al}} + P_{\mathrm{fe}} + P_{\mathrm{cu}}}{I^2} \tag{4.26}$$

where I is the driving current through a coupler. The total system transmission efficiency η_{T} is then determined by the following equation:

$$\eta_T = \eta_{\mathrm{inv}}\eta_{\mathrm{mag}}\eta_{\mathrm{rec}} = \frac{P_{\mathrm{out}}}{P_{\mathrm{out}} + P_{\mathrm{tot}} + P_{\mathrm{inv}} + P_{\mathrm{rec}}} \tag{4.27}$$

where P_{out} is the power ouput computed at the terminals of the rectifier, η_{inv} , η_{rec} , η_{mag} are the efficiencies of the inverter, rectifier, and couplers respectively (see Figure 4.12).

To improve efficiency performance during both aligned and mis-aligned conditions, the optimal load impedance matching algorithm with dual side control [22] is used which is briefly explained in the upcoming section.

4.4.3 Optimal load matching with dual-side control

A dual sided control strategy [38] with optimal load matching algorithm is considered in this thesis. Figure 4.12 depicts the overall IPT system with different conversion stages. The power is controlled

by varying the transmitter side DC voltage $U_{1,dc}$ and the receiver side DC voltage $U_{2,dc}$ based on the following:

$$P_{out} = \frac{8}{\pi^2} \frac{U_{1,dc} U_{2,dc}}{\omega M} \tag{4.28}$$

where P_{out} is the reference power requested by the battery, ω is the angular frequency of the system, M is the mutual inductance between the couplers. The DC link voltage ($U_{2,dc}$) in the pickup circuit is controlled by a DC-DC converter before the battery. Optimal load impedance matching algorithm as depicted in (4.20) is used in conjunction with dual-side control which results in maximum power transfer efficiency for a certain operating condition. Accordingly, the reference value of the receiver DC link voltage $U^*_{2,dc}$ (see Figure 4.12) using load impedance matching is determined using the following equation:

$$U^{*2}_{2,dc} \approx \frac{\pi^2}{8} \eta_R \omega M P_{out} \sqrt{\frac{r_{ac,2}}{r_{ac,1}}} \tag{4.29}$$

Therefore, $U^*_{2,dc}$ is used as a set point to ensure maximum power transfer efficiency. To ensure power regulation, the set point value of the transmitter side DC link voltage $U^*_{1,dc}$ is calculated based on the set point $U^*_{2,dc}$.

During misalignment, the value of M changes which will lead to the change of set point value of $U^*_{2,dc}$. Active impedance matching can still be executed on real time with a new estimate of coupling (k′) and the new set point for the secondary DC link voltage will then be:

$$U^{'*}_{2,dc} = U^*_{2,dc} \sqrt{\frac{k'}{k}} \tag{4.30}$$

During operation, the coupling co-efficient or the mutual inductance can be estimated online by measuring the voltages and currents of the transmitter and receiver pads [39].

This concludes the numerical modelling strategy of the coupler concepts along with the system control strategy. Before utilizing the models to optimize and compare different coupler geometries, they need to be validated to establish confidence of trends derived from the optimization results. In the upcoming section, the modelling strategy is validated with experimental results.

4.5 Experimental validation of modelling approach

The goal of this thesis is to compare different coupler geometries by multi-objective optimization which is computationally intensive. Hence, a computationally efficient and reasonably accurate modelling approach is necessary. Section 4.4 introduces a computational-friendly axi-symmetric 3D FE based modelling strategy. To establish confidence in the modelling approach, time should be spent to examine the integrity of the results obtained before using the modelling strategy for optimization. Thus, this section will validate the accuracy of the developed modelling approach by experiments on a laboratory prototype. Since the same modelling strategy is utilized for the different coupler geometries, validating the modelling approach is sufficient. The accuracy of the modelling approach will be validated on three

Table 4.1: Experimental component details

Part	Property
Semiconductors	SiC Cree: C2M008012D $R_{DS(on)}$ = 80 mΩ (25^o C)
Ferrite	Material type: P n_{fe} = 3
Litze	AWG 41 n_{str} = 525
Coils	DD-DD $N_T = N_R = 30$
Capacitor	Polypropylene film/foil tan δ = 0.2 [EPCOS]

essential aspects: (a) magnetic and electrical parameters of the couplers, (b) loss prediction, and (c) stray field estimation. To that end, the experimental setup built for this purpose is discussed in the following section followed by comparing model generated results and experimentally obtained data.

In this thesis, an IPT system with DD coils will be utilized to validate the modelling strategy. This system was initially designed for a power transfer rating of 2.5 kW across an air gap of 10.2 cm. The experimental IPT schematic and the laboratory setup is presented in Figure 4.13a. It is comprised of 3-ϕ AC supply, a DC power supply, an 85 kHz square wave SiC-based H-bridge inverter, resonant capacitor banks, DD coils and a resistive load. To simplify the experiments, a resistor is used instead of the battery. The resistive load is realized using low parasitic thick film power resistors (TAP1000 series) manufactured by OHMITE. Other details of the components used are presented in Table 4.1. The SiC switch used to build the inverter (Figure 4.13c) is C2M0025120D ($R_{ds,on}$ = 25mΩ) manufactured by CREE. The DD transmitter and receiver coils have similar designs with the number of turns equal to 30. The external diameter of the litz wire (AWG 41) is 2.6 mm. The number of strands is 525 with an individual strand radius of 71 μm. Three ferrite strips are used in the coil with dimensions: 230 mm × 6.5 mm × 6.5 mm. The ferrite material used is P manufactured by MAGNETICS. The resonant capacitor banks are comprised of metalized polypropylene capacitors manufactured by KEMET and EPCOS.

4.5.1 Self-inductance, coupling, and misalignment

The magnetic properties of the coils will be validated in this section. Table 4.2 shows the measured parameters at a nominal air gap of 10.2 cm and those obtained from the FE method along with the calculation error relative to the measured values. It can be observed that the self-inductances are calculated accurately by the used FE tool. The mutual inductance and magnetic coupling are also accurate with all absolute errors less than 10%. The negative error appears for the magnetic coupling, because in its calculation according to k = $\frac{M}{\sqrt{L_1 L_2}}$, the calculation errors in the self-inductance and the mutual inductance are combined. To validate the FE model over a wider operating range, the magnetic coupling is measured during misaligned conditions in all three axes. The results are compared to those obtained by the FE model and presented in Figure 4.14. It can be observed that the misalignment behavior of the coil system is calculated accurately by the FE model.

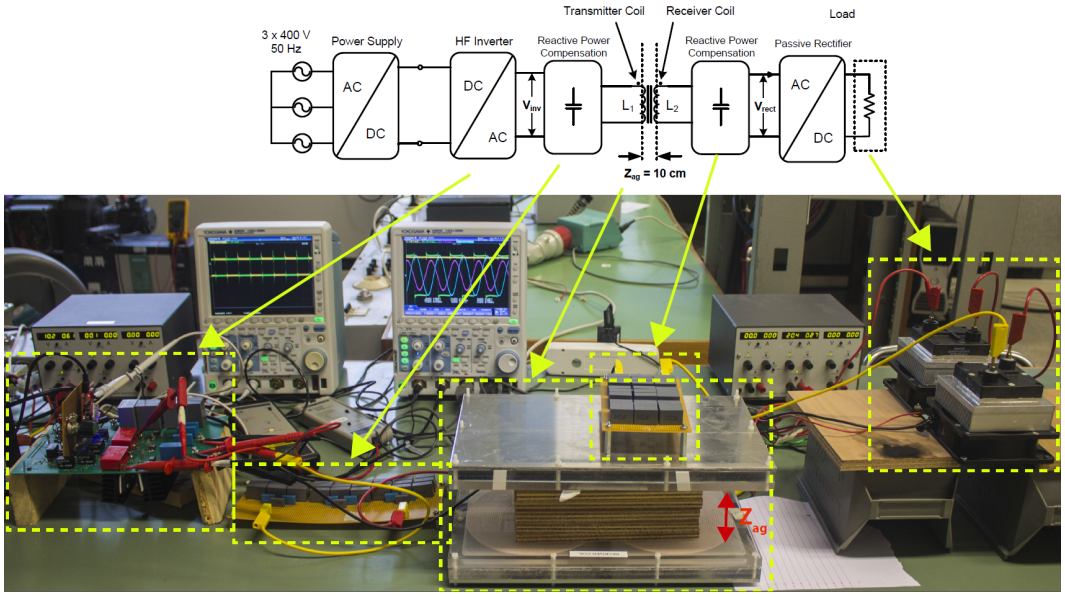

(a)

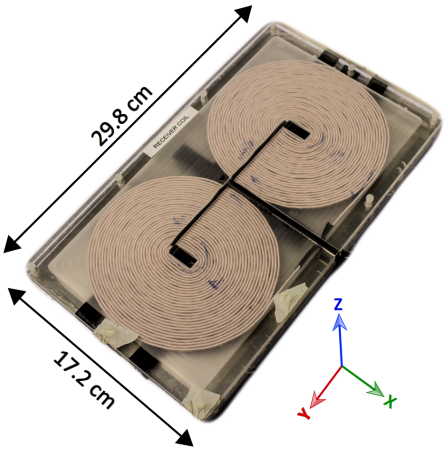

(b)

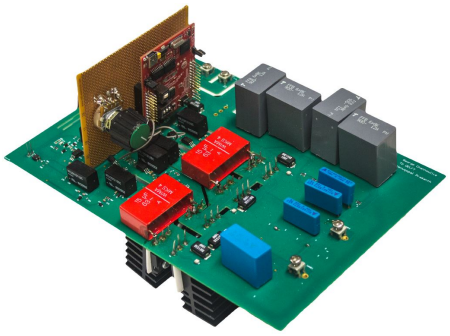

(c)

Figure 4.13: (a) The overall experimental setup is shown along with the circuit schematic, (b) The dd coil setup is shown along with the dimensions. The receiver coil and the transmitter coil have similar design, (c) the SiC based H-bridge inverter is presented in this picture.

4.5.2 System power losses

Experiments are conducted to validate the loss models of the coils including the resonant capacitors and the power electronic devices. The total system loss is determined by post-processing the data extracted from waveforms at different operating points. The experimentally obtained losses are compared with the model generated losses at different power levels. The collected data is presented with the aid of bar charts as shown in Figure 4.15. The data show good agreement between the experimental results and

Table 4.2: Comparison of FE computed and experimentally obtained circuit parameters

Variable	FE Model	Experiment	Error
L_1	211.2 µH	205.1 µH	+2.9 %
L_2	211.2 µH	198.7 µH	+6.2 %
M	31.4 µH	30.5 µH	+2.9 %
k	0.149	0.151	-1.5 %

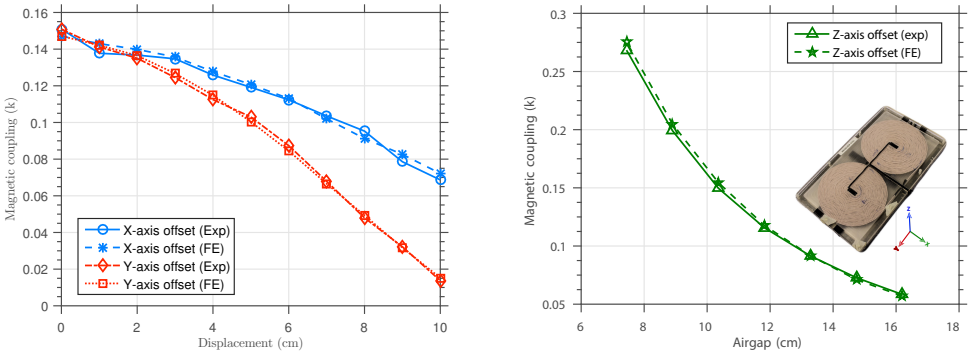

(a) (b)

Figure 4.14: Comparison of FE calculated magnetic coupling during misalignment with experiments. Variation of k with, (a) x-y misalignment with constant z-gap of 10 cm, (b) z-axis misalignment with perfect alignment in x-y axis.

the model generated loss values with percentage error varying between 10% - 15%. The percentage error in loss estimation is 2-3 times compared to the percentage errors in parameter estimation (see Table 4.2). This basically is due to error propagation as losses which depend on multiple parameters which in turn adds up to the error. Additionally, the model ignores the temperature dependence of copper resistivity. It uses the DC-resistance per unit length data provided by the litz wire manufacturer at 20^oC. In addition to that, the resonant capacitor banks consist of capacitors from different manufacturers with different tan δ values.

The distribution of the computed losses is also presented in the same plot. It is evident from the loss distribution bar charts that the capacitor dielectric is the dominant source of loss followed by ferrite core loss and copper losses. Shielding loss is almost negligible compared to other loss mechanisms which are in line with results reported in [15]. High capacitor dielectric losses can be attributed to the series-series compensation strategy which results in the capacitors carrying the full coupler driving currents.

4.5.3 Stray field measurement

Field measurements were taken with a field probe to validate the accuracy of the stray field calculation. The field probe used is EHP 50A manufactured by Narda. The comparison between rms stray field measurements and FE computed fields is presented in Figure 4.16 which shows reasonably good

accuracy.

This concludes the experimental validtaion of the modelling strategy presented in Section 4.4. The differences of the results obtained from the modelling approach are in good agreement with the experimentally obtained results (error of 3-5% in estimating the electro-magnetic parameters, 6-10%

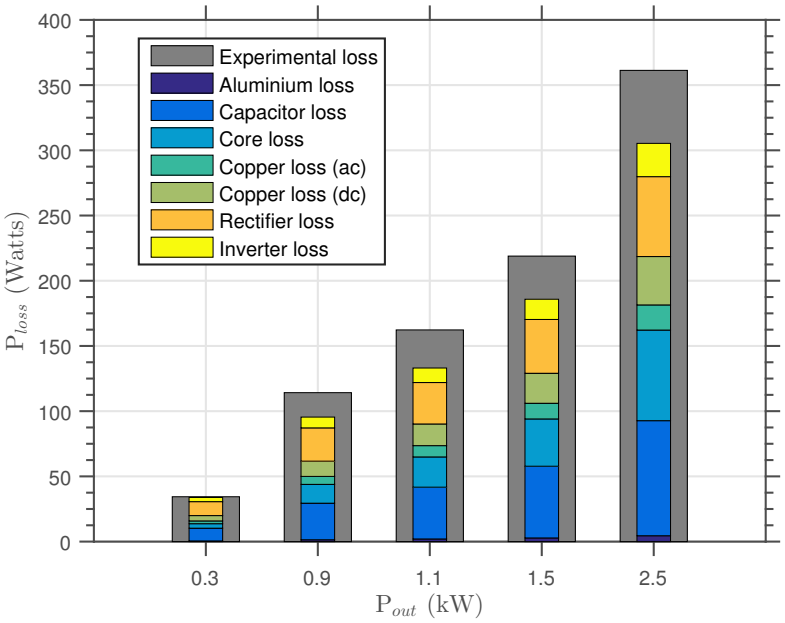

Figure 4.15: Comparison of model computed losses with experimental loss data at different operating power at an airgap of 10 cm. The distribution of computed losses is also highlighted at different power levels. Computed losses are lower than experimentally determined losses with absolute average relative error of 15.2 %.

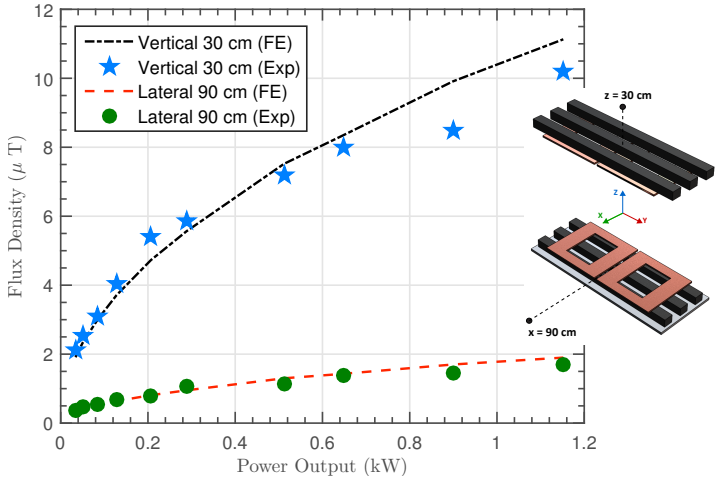

Figure 4.16: Comparison of calculated and measured rms stray field of the IPT system at two different spots, namely 30 cm from the receiver coil center in the z-direction and 90 cm from the transmitter coil center in the x-direction. The average absolute value of the relative error with respect to the experimental values is 8.1 %.

in stray field estimation, and 10-15% in predicting the overall system losses). Therefore, it can be conluded that couplers optimized using this simulator will perform as expected in practice. Next, this validated modelling strategy is utilized in a multi-objective optimization framework to fairly compare the different coupler concepts.

4.6 Multi-objective optimization framework

A multi-objective optimization framework is developed in this section to compare the chosen coupler concepts. It utilizes the numerical modelling strategy developed in Section 4.4 and experimentally validated in Section 4.5 to evaluate the performance of the couplers. Initially, the system analysis flowchart is described followed by discussion on the optimization targets, variables, and constraints. Finally, the results of the optimization are presented and analyzed to compare among the coupler concepts.

4.6.1 System analysis and performance parameters

The IPT system analysis is performed broadly in three stages. First, MATLAB is used to create the FE models. Second, COMSOL multiphysics is used to solve the FE models. Finally, the solved FE model generated data is post-processed in MATLAB to obtain primary and secondary system performances.

Figure 4.17 shows the steps required to analyze a single IPT design in the optimization procedure. The system active mass (m_{sys}) includes the mass of the ferrite cores, litz wire winding, and the aluminum shielding. The gravimetric power density of the system is computed as : $\gamma = P_{\text{out}}/m_{\text{sys}}$. The area power density of the receiver coupler is calculated as: $\alpha = P_{\text{out}}/A_{\text{rec}}$ where A_{rec} is the receiver coupler area. The system losses are re-computed during misalignment to determine the misalignment efficiency (η_{mis}).

This concludes the modelling strategy of the coupler concepts along with the overall analysis of a single IPT design. Not all the steps are needed, depending on the objectives. The time required to evaluate a complete design varies between 3 mins - 6 mins[1].

[1] Intel Xeon CPU E5-1620 *v2* @ 3.70 GHz, 16 GB RAM.

Table 4.3: IPT system specfications

Symbol	Description	Value
δ	Operational air-gap	15 cm
P_{out}	Battery power requirement	5 kW
f	Operational frequency	85 kHz
U_{batt}	Nominal battery voltage	400 V
$U_{1,\text{dc}}$	Input DC link voltage	850 V
$U_{2,\text{dc}}$	Pick up DC link voltage	400-850 V
Δx	Lateral misalignment	± 15 cm
Δy	Longitudinal misalignment	± 15 cm

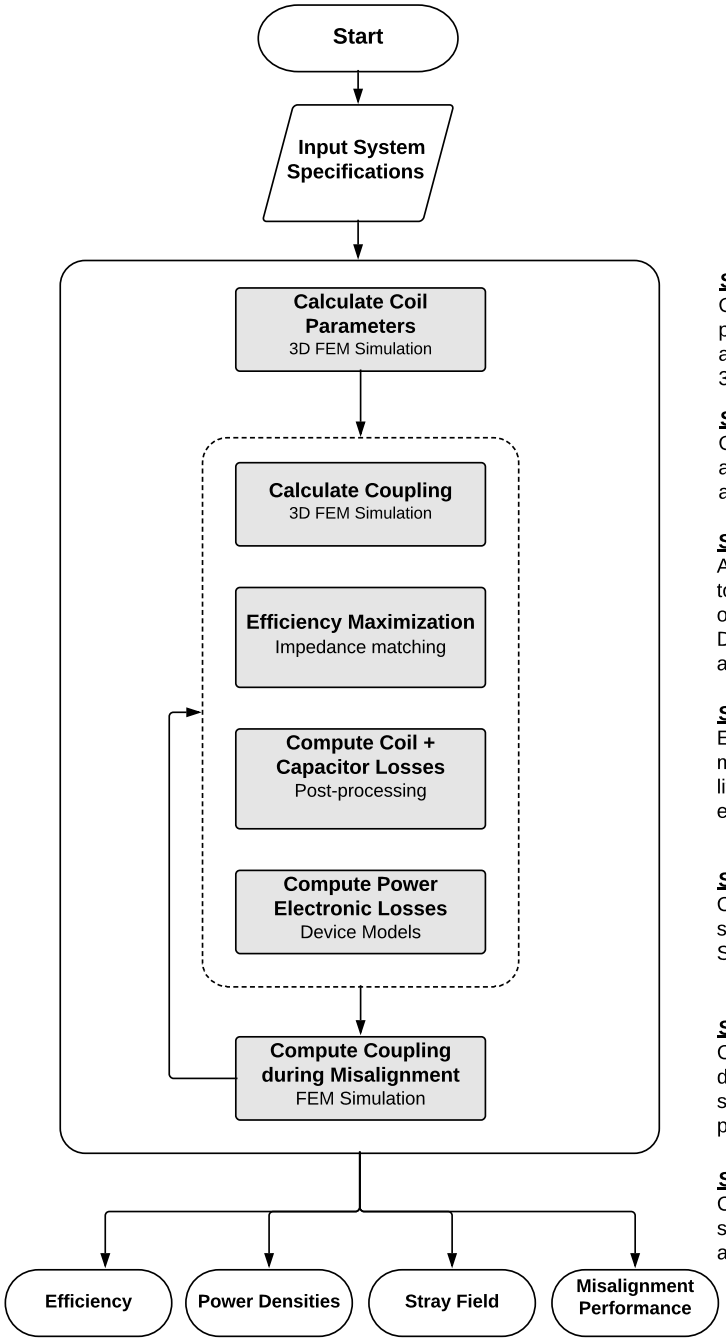

Figure 4.17: System analysis flowchart for individual IPT designs during the optimization process

4.6.2 Optimization targets, and system specifications

The coupler concepts are compared on the primary performance factors like efficiency, power densities, and misalignment performance. Based on that, the targets of the optimization are:

1. Maximize power transmission efficiency (η_T)
2. Maximize gravimetric power density (γ)
3. Maximize receiver pad area power density (α)
4. Maximize efficiency during misalignment (η_{mis})

The objectives mentioned above are selected strategically to ensure that the optimization progresses towards designs with acceptable power densities and efficiency performance during both aligned and misaligned conditions. Table 4.3 shows the IPT system specifications. The optimization algorithm used for this problem is particle swarm optimization (PSO). PSO is an evolutionary gradient free algorithm inspired by the movement of birds or insects in swarm which is gradient free and potentially requires fewer function calls. In this paper, an approach based on placing particles on the border of the search space using a combination of variable clipping and reflecting [40].

4.6.3 Optimization variables, and constraints

The design variables of the optimization problem are all geometrical parameters of different coupler structures as shown in Figure 4.18. Ten geometrical parameters per coupler pad (transmitter and receiver) are optimized to ensure high design flexibility and exhaustive design space exploitation. The optimization variables and their range are presented in Table 4.4.

To ensure feasible designs, specific constraints are put on the optimization solution space as highlighted in Table 4.5. A hard limit of 5A/mm^2 is placed on the litz wire current density to ensure thermal stability. To avoid bifurcation phenomena (multiple operating modes), limits on coil quality factors are placed by following bifurcation criterion proposed in [41]. The maximum flux density and the average flux density in the ferrite cores during misalignment operation is set to be 0.35 T and 0.2 T respectively

[2] 100% means the outermost ferrite strips are at the edge of the coupler and 0% represents that all the ferrites are together forming a block in the center.
[3] Represented as a percentage of the total coil length.

Table 4.4: Optimization variables and their range

Variable	Symbol	Unit	Range				
			DD-DD	DD-BPP	DD-DDQ	Rect	Circ
Number of turns	N_T, N_R	-	15-60	15-60	15-60	20-65	20-65
Number of turns in Q coil	N_Q	-	-	-	15-60	-	-
Diameter of litz wire	d_{litz}	mm	2.4 - 4.8	2.4 - 4.8	2.4 - 4.8	2.4 - 4.8	2.4 - 4.8
Inner length	l_i , r_i	mm	10-35	10-35	10-35	10-75	10-75
Inner width	w_i	mm	10-35	10-35	10-35	10-75	-
Ferrite thickness	h_{fe}	mm	5-35	5-35	5-35	5-35	5-35
Ferrite width	w_{fe}	mm	15-45	15-45	15-45	15-45	15-45
Gap between ferrites[2]	w_{ag}	%	20-100	20-100	20-100	20-100	-
Length of ferrite [3]	l_{fe}	%	50-120	50-120	50-120	50-120	50-120
Number of ferrites	n_{fe}	-	1-7	1-7	1-7	1-7	2-12

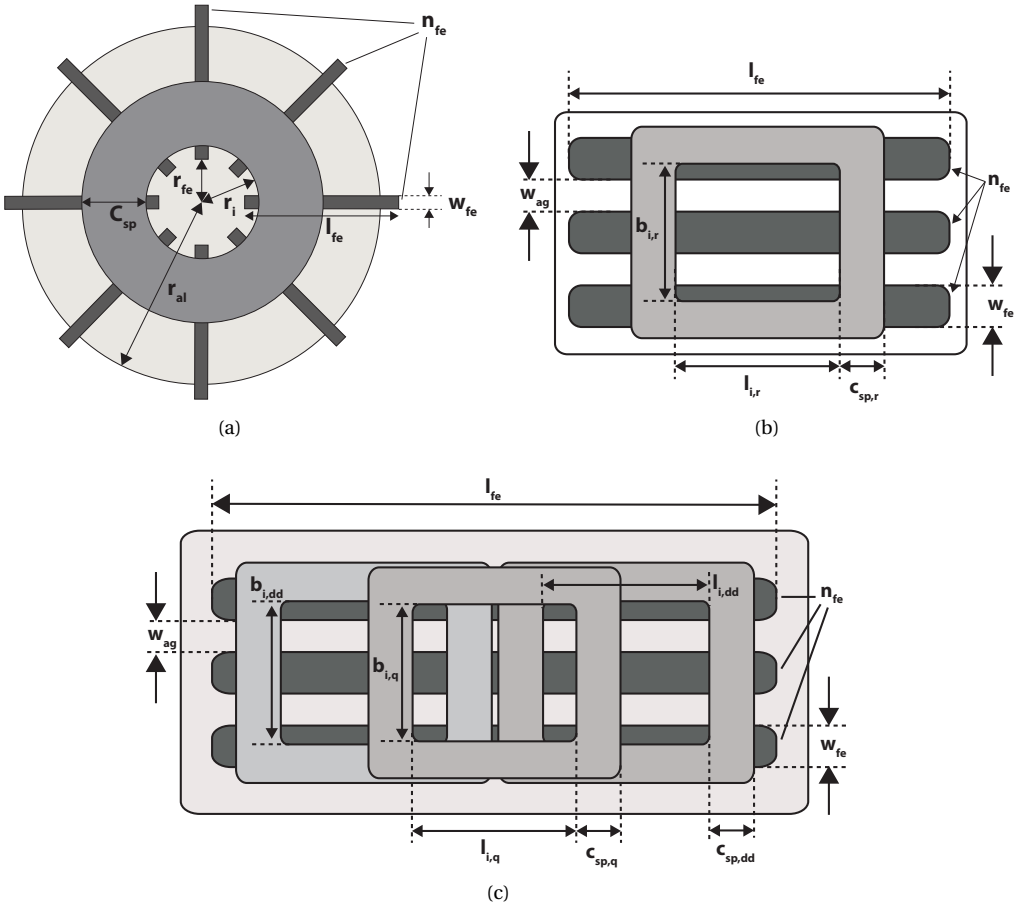

Figure 4.18: Design variables for (a) Circular coupler, (b) rectangular coupler and (c) DDQ receiver pad topology. In the figures, the ferrite thickness (h_{fe}) is a variable which is not shown. The optimization variables of DD-DD and DD-BPP are similar to that of DDQ with the exception of the extra variables due to the Q coil. The coil spread parameter (C_{sp}) is defined as: $C_{\text{sp}} = N \times d$, where N is the number of turns and d is the external diameter of the litz wire which depends on the number of strands (n_{str}).

(saturation flux density for 3C-90 core material is 0.45 T). In addition to that, a constraint is placed on the maximum core loss density at 800 kW/m^3 to ensure that the cores don't get overheated. To avoid

Table 4.5: Optimization constraints

Symbol	Limit	Unit	Description
J	≤ 5	A/mm^2	Current density limit
k_{bi}	≥ 1.5	-	Bifurcation factor[41]
$B_{\text{fe,max}}$	≤ 35	mT	Maximum core flux density
$B_{\text{fe,avg}}$	≤ 20	mT	Average core flux density
$p_{\text{fe,density}}$	≤ 800	kW/m^3	Core loss density
η_{T}	≥ 93	%	Power transfer efficiency

wasting computational cycles on those designs, the global target in the PSO algorithm was selected from particles with at least 93 % efficiency. Coil designs which violate the above constraints are removed from the repository. Coil designs which violate the above constraints are removed from the repository.

This concludes the development of the MOO framework consisting of 20 design variables, 4 performance targets, and 6 constraints. The overall optimization is computationally expensive and requires solving 3000-4000 designs to arrive at stable Pareto fronts. The optimization results are discussed in the next section.

4.7 Optimization results

The optimization returns a 4D Pareto optimal front. A detailed analysis is conducted in three steps to aid visualization and insight into the results. First, higher-level results are analyzed using sub-fronts of two targets. At a second level, complete fronts are shown to aid explanation of underlying trends. Finally, selected optimal designs are compared in depth. Figure 4.19 and Figure 4.23 show the side views of the 4D Pareto optimal front which highlight the trade-offs between efficiency at alignment, efficiency at misalignment, and power densities. To distinguish between the coupler shapes, only the sub-fronts are shown. These plots show the maximum achievable performance in one parameter only, disregarding the performance on other parameters. It means that the designs located on, e.g., the $\eta - \gamma$ sub-front do not necessarily lie on the $\eta_{\text{mis}} - \alpha$. However, this representation can reveal strong or weak coupler shapes based on the goals and provide insight into the limits of the performance goals individually.

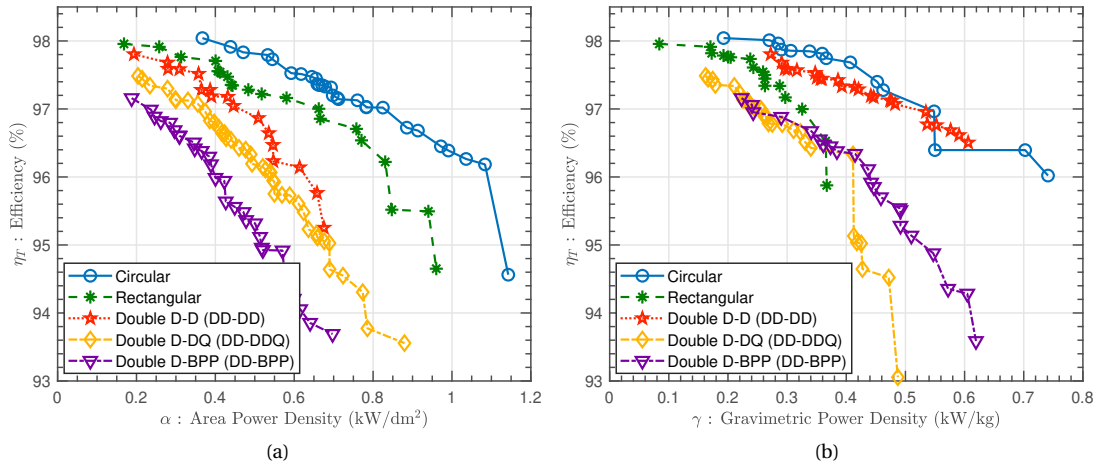

Figure 4.19: Results of multi-objective optimization during perfect alignment operating conditions: (a) $\eta - \alpha$: pareto fronts of trade off between efficiency and receiver area power density, (b) $\eta - \gamma$: pareto fronts of trade off between efficiency and gravimetric power density.

4.7.1 Pareto front analysis of designs during alignment

The trade-offs between IPT power transfer efficiency and power densities during alignment are shown in Figure 4.19. Figure 4.19a show the Pareto fronts of efficiency during perfect alignment versus receiver area power density of the couplers while Figure 4.19b show the Pareto fronts of efficiency versus gravimetric power density of the couplers. A detailed analysis of the individual couplers is discussed in the following.

The circular coupler is the best performer as it achieves higher efficiency of power transfer for both the power densities than other couplers. IPT designs using circular couplers have higher coupling factors for the same receiver area and material usage, as shown in Figure 4.20. Therefore, the pad driving currents are lower for the same power transfers according to equations (4.16), and (4.17) leading to lower copper losses as shown in Figure 4.21a. Further, circular couplers also have the lowest ferrite losses (see Figure 4.21b). It utilizes more ferrite material for the same gravimetric power density than other coils, as highlighted in Figure 4.22a. It leads to comparatively lower average flux density (B_{avg}) in the ferrite strips (see Figure 4.22b), thus leading to lower ferrite core losses.

Rectangular couplers perform very close to circular couplers in the η - α front due to its superior coupling characteristics leading to lower copper and iron losses. However, rectangular couplers perform comparatively poorly compared to different coils in the η - γ front, due to the mismatch between the linear alignment of the ferrite strips and the fundamental flux pattern associated with a unipolar rectangular coil. Therefore, it has lower coupling co-efficient for the same gravimetric power density compared to other coil geometries. This leads to higher driving currents increasing both copper losses and core losses.

The uni-polar couplers perform much better than the polarized family in the η - α front. Higher coupling coefficients associated with uni-polar couplers for the same receiver pad area compared to their polarized counterpart (see Figure 4.20a) results in lower driving currents for the same power

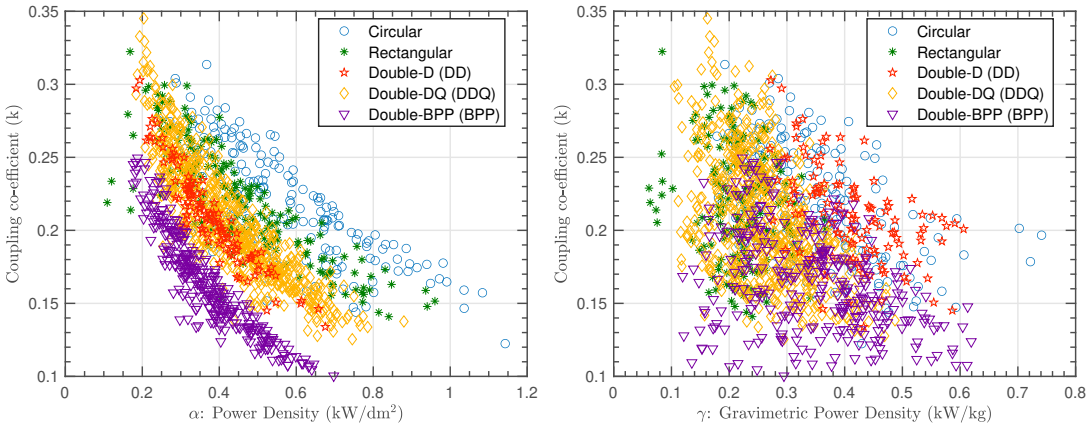

Figure 4.20: Variation of coupling coefficient (k) of Pareto optimal designs with: (a) receiver pad area power density, (b) gravimetric power density.

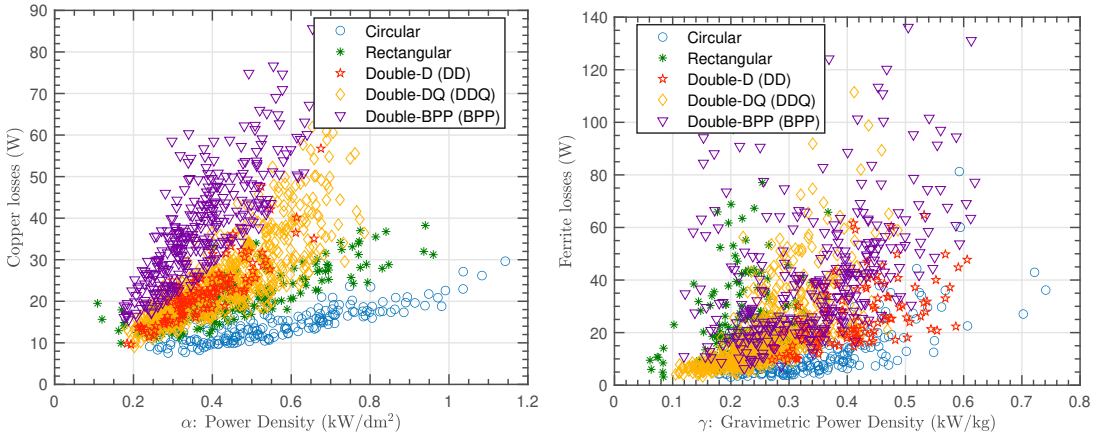

(a) (b)

Figure 4.21: Loss incurred in the Pareto optimal designs during perfect alignment: (a) copper losses, (b) ferrite losses.

transfer. Within the polar couplers, the DD-DD coils perform the best in the η - α front followed by the DD-DDQ. However, an interesting observation is that even though DD-DD couplers perform better than DD-DDQ, the coupling coefficient of DD-DD coils is slightly lower than DD-DDQ. But DD-DDQ has more losses in the rectification stages due to its multi-coil nature which needs independent rectifiers. Finally, the DD-BPP coupler is the worst performer in the η - α front. Due to the overlapping nature of DD-BPP couplers, it inherently utilizes more material to achieve the same area power leading to higher self-inductances. Therefore, they have similar mutual inductance for higher self-inductances leading to lower coupling co-efficient as seen in Figure 4.20a. In the $\eta - \gamma$ Pareto front, the DD-DD coupler performs as good as circular couplers. DD-DD couplers utilize material very efficiently and have high coupling factors for the same gravimetric power density. However, other polarized couplers do not perform similar to DD-DD in this front. The DD-DDQ coils perform comparatively worse than DD-BPP coils in the $\eta - \gamma$ sub-fronts. This is expected since these performance parameters are computed during perfect alignment, and DD-DDQ couplers have added weight and area due to the Q-coil. As shown by the above analysis, that circular and rectangular couplers show higher attainable coupling k during aligned conditions for the same area power density (α) than bi-polar couplers like DD-DD, DD-BPP and DD-DDQ which is following the results reported in [15, 18, 19]. However, several publications report that bi-polar pads like DD-DD have better coupling than circular couplers [7–9, 16]. It must be noted that the comparative analysis presented in those papers is based on conceptual arguments like fundamental flux height which depend on the specific parameters of each coupler design. In this thesis, the couplers are optimized within specific design constraints which are not considered in the previous papers. The results obtained from this section show that using fundamental flux height as a metric to predict coupling of different coupler types is inaccurate.

However, it must be noted that the comparison trends derived from the presented optimization results are only applicable to circular couplers with radial ferrite distribution and rectangular, DD-DD, DD-DDQ couplers with longitudinal ferrite distribution. The general conclusions based on these trends might not be the same if only air-cored couplers are considered.

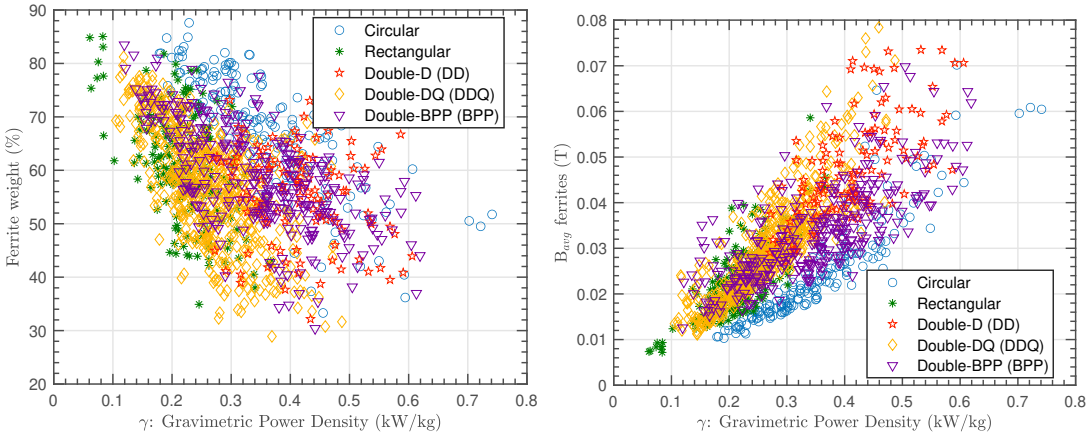

Figure 4.22: (a) Ferrite weight as a percentage of total coupler system weight in the pareto optimal designs, (b) average flux density in the ferrite strips in the pareto optimal designs.

4.7.2 Pareto front analysis of designs during misalignment

The trade-offs between IPT power transfer efficiency during misalignment and power densities discussed in this section. The Pareto sub-fronts of η_{mis}-α and η_{mis}-γ are presented in Figure 4.23a, 4.23b respectively.

The polarized DD-BPP coupler is the standout performer in both the sub-fronts especially in the η_{mis}-γ front. The dominance of DD-BPP coupler in all Pareto fronts regarding misalignment performance can be explained by the complementary flux capturing of the BPP coils, leading to high coupling coefficients even during misalignment (Figure 4.23c). Interestingly, circular coils show good misalignment efficiencies just second to DD-BPP. In the $\eta_{\text{mis}} - \alpha$ sub-front, circular couplers perform similar or slightly better than DD-BPP at higher area power densities. Rectangular couplers also perform well in the $\eta_{\text{mis}} - \alpha$ sub-front, but its performance in the $\eta_{\text{mis}} - \gamma$ sub-front is the worst in the selected coupler topologies. This highlights the inherent mismatch between the linear alignment of the ferrite strips and the fundamental flux pattern associated with a unipolar rectangular coil, which is a disadvantage. The DD-DD coil fails to replicate its performance during alignment in both the sub-fronts during misalignment. It is the worst performer in the $\eta_{\text{mis}} - \alpha$ sub-front, while being better than DD-DDQ and rectangular couplers in the $\eta_{\text{mis}} - \alpha$ sub-front. DD-DD couplers show poor coupling co-efficient for the same area power density when designed for misalignment, as shown in Figure 4.23c. Finally, the performance of DD-DDQ during misalignment is not very promising from a power density point of view. During misalignment condition, the Q-coil captures additional flux leading to higher values of mutual inductance. Although DD-DDQ couplers have significantly higher mutual inductances during misalignment, their power transfer efficiency doesn't show similar improvement due to additional losses incurred in the Q-coil and associated rectification circuit. It is penalized for higher coil area due to the Q-coil since the Q-coil tends to be larger than the individual DD coils due to high misalignment. Additionally, the DD-DDQ coil is only advantageous if misalignment occurs in the longitudinal direction (Y-axis) [8]. Therefore, the DD-DDQ coil performance is inferior to circular and rectangular

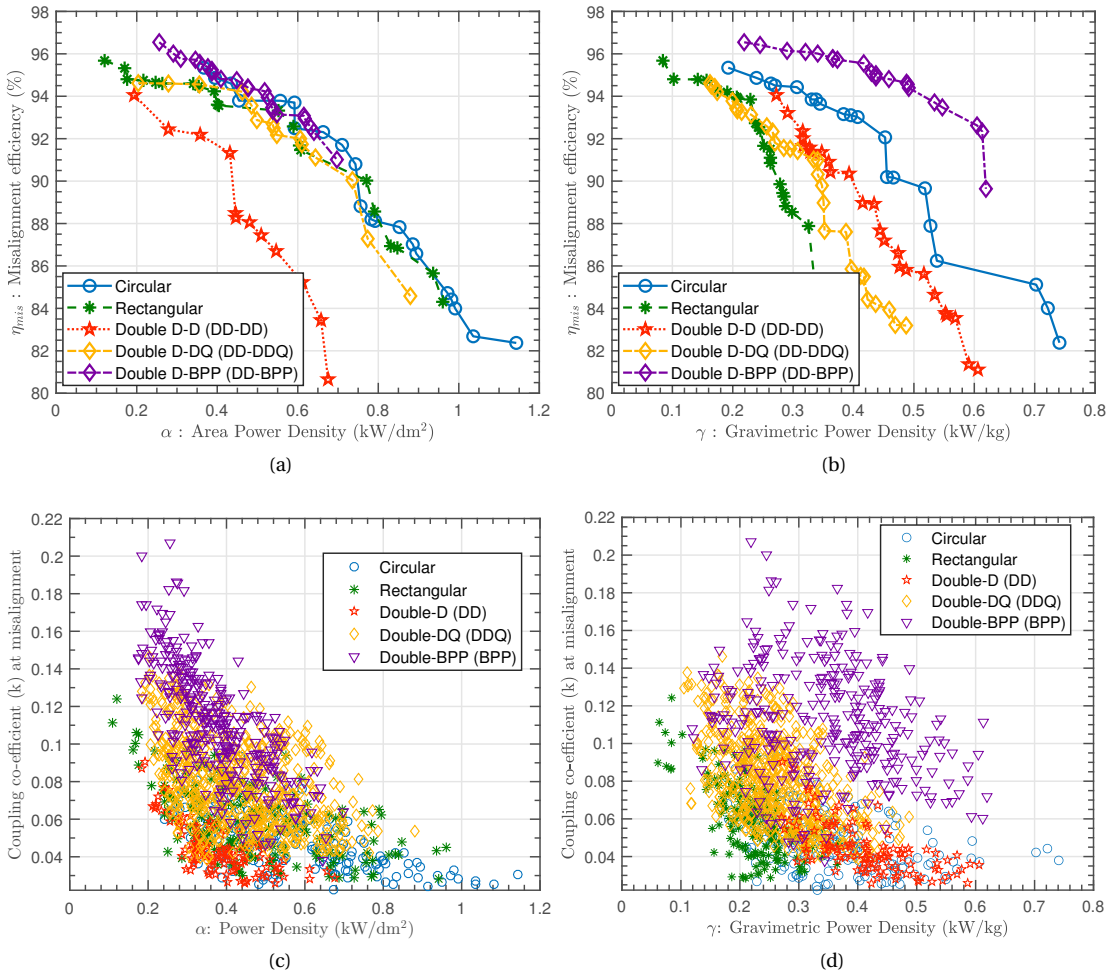

Figure 4.23: Results of multi-objective optimization during misaligned operating conditions: (a) $\eta_{\text{mis}} - \alpha$: pareto fronts of trade off between misaligned efficiency and receiver area power density, (b) $\eta_{\text{mis}} - \gamma$: pareto fronts of trade off between misaligned efficiency and gravimetric power density, (c) coupling coefficient of pareto designs vs receiver area power density during misaligned conditions, and (d) coupling coefficient of pareto designs vs gravimetric power density during misaligned conditions.

coils since the design specifications (see Table 4.3) also include significant misalignment in the lateral direction.

4.7.3 Stray magnetic field performance

The stray magnetic field generated by IPT couplers should comply with the guidelines set by ICNIRP [42]. It stipulates that the general public should not be exposed to RMS magnetic flux densities greater than 27 µT (100 µT for occupational exposure). In literature, authors have chosen different spatial points for spot measurements. Some examples are, 10 cm from the edge of a (1.5×1.5 m^2)

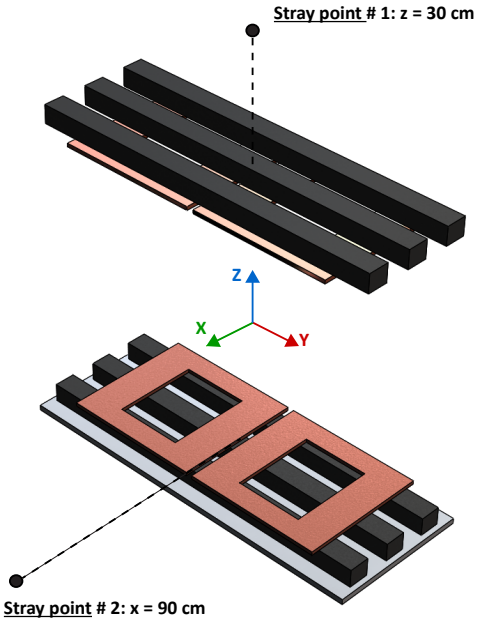

Figure 4.24: Spot stray field measurements according to ICNIRP guidelines.The aluminum shielding on the receiver pad is not shown but considered.

vehicle [43], 110 cm from the airgap center point on the lateral direction [15], 30 cm from the receiver coil center in the vertical direction [22] etc. In this thesis, two points are taken for spot flux density computation: (a) 30 cm from the receiver coil center in the vertical direction (z) and, (b) 90 cm from the transmitter coil center on the lateral direction (x) as shown in Figure 4.24. The stray flux densities of the Pareto designs for the different coils with coupling coefficient are shown in Figure 4.25.

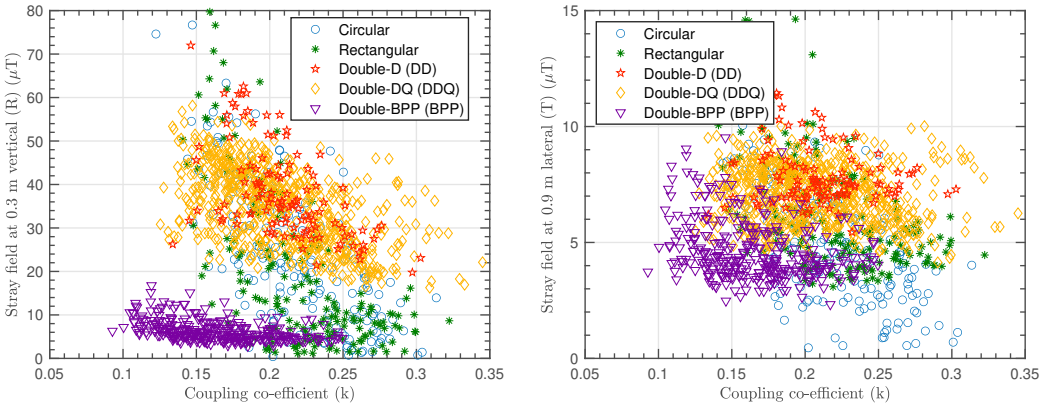

(a) (b)

Figure 4.25: Stray field behavior of different coil concepts during perfectly aligned operation with coupling coefficient: (a) Stray field computed at 0.3 m vertical (z-direction) from the receiver coil center, and (b) Stray field computed at 0.9 m lateral (x-direction) from the transmitter coil center.

DD-BPP couplers show the lowest stray field in the vertical direction. Due to its overlapping nature, the fields generated by the individual coils cancel out each other in the overlap region leading to very low stray fields. DD-BPP also has low stray fields in the lateral direction. The uni-polar coils have significantly lower stray fields compared to the polarized family apart from DD-BP in the both directions. In practical EV charging applications, there will be an aluminium vehicle body which will further reduce this stray field value.

4.7.4 Comparison of selected Pareto optimal designs

In this section, detailed analysis on selected designs is conducted to gain deeper insights into the performance trends discussed in the previous results. Since the couplers are optimized with different conflicting objectives, it is difficult to select a single optimized design from each coupler family. To ensure a fair comparison, optimized couplers of similar power densities are selected and compared in detail. Figure 4.26 shows the selected particles in the 2D power denisty plot of all the Pareto dominant designs. All the selected coupler designs have a receiver power density of 0.5 kW/dm^2 and system gravimetric power density of 0.3 kW/kg.

Table 4.6 shows in-depth performance of the selected optimized designs of different coupler concepts. The circular design performs the best in terms of both efficiencies during alignment and efficiency during misalignment. The circular coupler design uses minimum copper material, whereas DD-DDQ and rectangular design use the highest amount of copper. As shown in the Pareto-front analysis, the efficiency and losses trends are similar to the data presented for the Table 4.6. Further, the stray field behaviour is also in line with expectations with unipolar couplers being better performers. However,

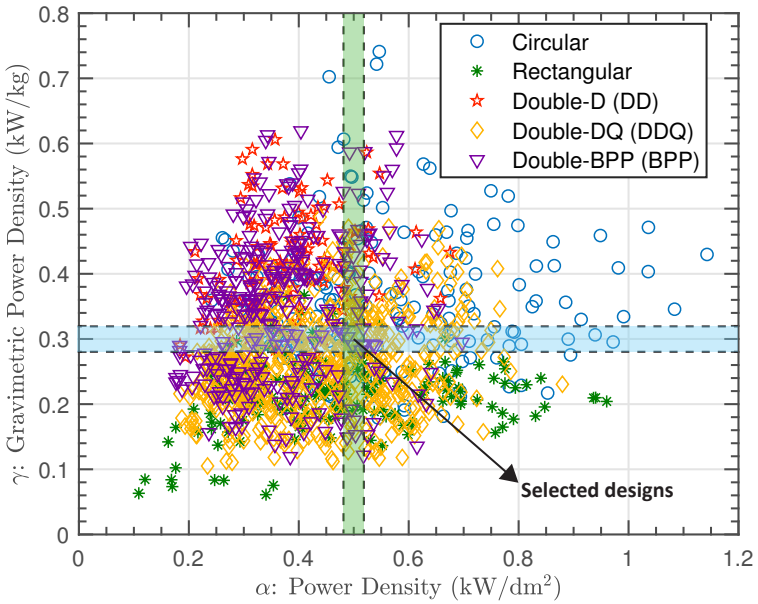

Figure 4.26: Selected Pareto optimal designs of all the coupler families based on similar gravimetric and area power densities to ensure a fair comparison.

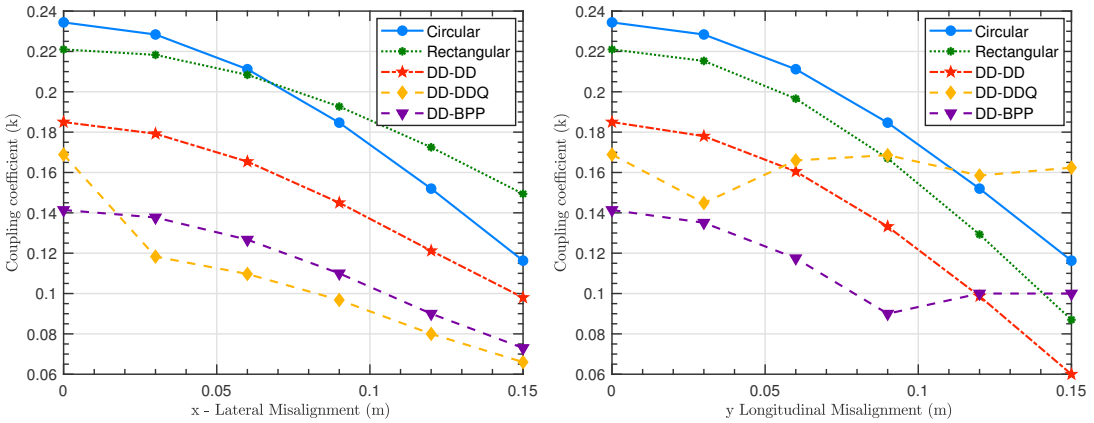

Figure 4.27: Variation of coupling coefficient during: (a) misalignment in the lateral direction, (b) misalignment in the longitudinal direction

DD-BPP shows promising stray field performance with the lowest fields in the vertical direction and comparable field to unipolar couplers in the lateral direction.

The coupling coefficient of the selected coupler designs due to misalignment in longitudinal and lateral direction are shown in Figure 4.27. In case of lateral misalignment in the x-direction, the unipolar rectangular coupler show better tolerance than circular and other polarized couplers. The advantage of the unipolar couplers is that they have inherently high coupling coefficients. Therefore, even if the drop in coupling is significant compared to polarized couplers, the absolute value of coupling coefficient remains high. Among the polarized couplers, the DD-DDQ performs poorly as the quadrature coil Q is only activated during longitudinal misalignment. However, the polarized couplers perform much better in longitudinal misalignment as shown in Figure 4.27b. The DD-DDQ shows high misalignment tolerance due to the presence of the Quadrature coil (Q) with the coupling coefficient almost remaining constant. DD-BPP couplers also show good misalignment tolerance in the y-direction. The unipolar couplers along with DD-DD are not as misalignment tolerant in the longitudinal direction.

Table 4.6: Comparison of selected Pareto Optimal Couplers

Performance Group	Performance Metrics	Symbol	Unit	Circular	Rectangular	DD-DD	DD-DDQ	DD-BPP
Coupler Sizing	Receiver area power density	α	kW/dm^2	0.5	0.48	0.5	0.5	0.5
	Gravimetric power density	γ	kW/kg	0.28	0.3	0.322	0.29	0.29
	Copper weight	W_{cu}	kg	1.7	4.3	2.4	4.8	2.2
	Ferrite weight	W_{fe}	kg	13.3	7.8	10.6	9.7	12
	Receiver weight	W_{rec}	kg	9	5.8	2.7	5	6.1
	Transmitter weight	W_{tr}	kg	8.8	11	13	12	11.3
Performance during alignment	Magnetic link Efficiency	η_{mag}	%	98.6	97.7	98	97.8	97
	Coupling co-efficient	k	-	0.23	0.22	0.18	0.17	0.15
	Ferrite average flux density	B_{avg}	mT	75	120	90	80	120
	Ferrite loss	P_{fe}	W	7	46	17	22	31
	Copper loss	P_{cu}	W	13	19	26	26	43
	Capacitor loss	W_{cap}	W	46	46	57	64	74
	Shielding loss	W_{al}	W	5	4	4	5	3
	Stray Vertical	B_{vert}	µT	16	17	57	43	13
	Stray Lateral	B_{lat}	µT	4	6	9	9	7
Performance during misalignment	Magnetic link Efficiency	η_{mag}	%	93.4	90.7	89.9	93.1	91.1
	Coupling co-efficient	k_{mis}	-	0.05	0.06	0.04	0.08	0.05
	Ferrite loss	P_{fe}	W	55	238	148	107	133
	Copper loss	P_{cu}	W	64	72	130	130	124
	Capacitor loss	W_{cap}	W	217	174	270	124	227
	Shielding loss	W_{al}	W	20	27	16	20	12

To summarize the detailed comparative evaluation of the selected IPT couplers, a radar chart highlighting the relative advantages and disadvantages of each coupler types in terms of efficiency, power densities, material effort, stray field and misalignment performance is shown in Figure 4.28. It must be noted that the performance factors analysed in IPT systems are mutually conflicting in nature. Therefore, the relative grades assigned to individual coupler shapes represent the absolute maximum performance in only that category. This concludes a detailed comparative analysis of the primary and secondary performance parameters of the considered coil topologies.

4.8 Conclusion

In this thesis, inductive power transfer (IPT) is proposed as a solution to EV charging integration for DC smart homes. Selecting the right magnetic coupler is crucial to ensure a high-performance IPT system. To that end, this chapter presents a holistic comparison of five coupler concepts: circular, rectangular, DD-DD, DD-DDQ, and DD-BPP. The main advantages and disadvantages of the five IPT coupler concepts are discussed with multi-objective Pareto analysis. Detailed experiments are conducted on a laboratory prototype to validate the models. Thus, the analysis is accurate. Some important results obtained are:

1. Circular couplers have the best efficiencies and coupling coefficients for the same power den-

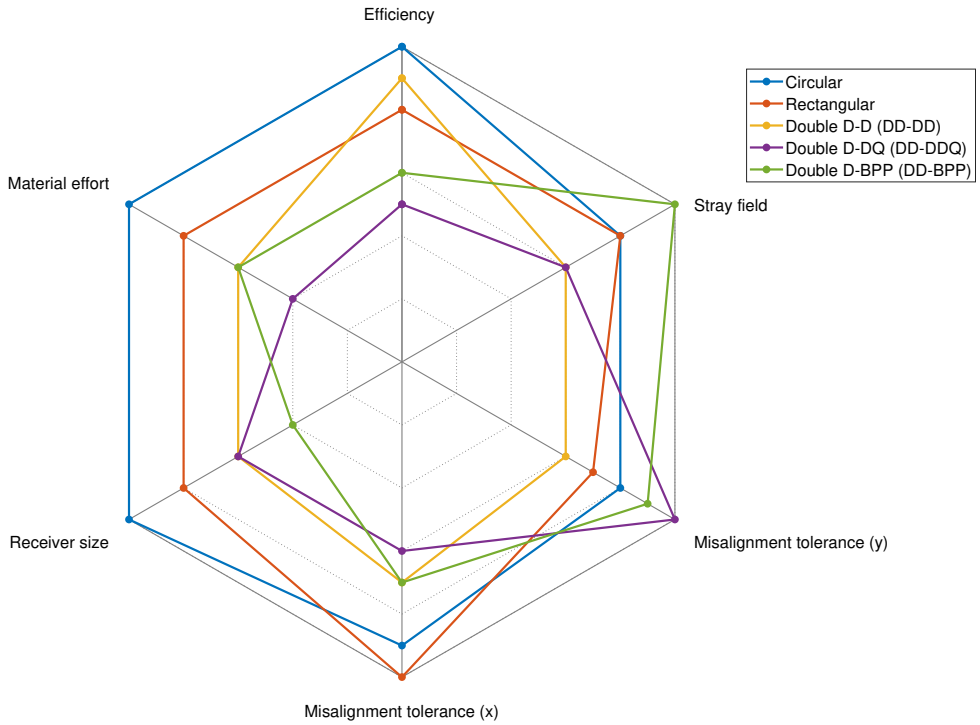

Figure 4.28: Comparative qualitative evaluation of different IPT coupler topologies for various performance metrics.

sities among all concepts during perfectly aligned conditions. Circular couplers use the most ferrite material and the least copper material among all the coupler topologies for the same performance.

2. The unipolar couplers outperform the polarized couplers for the same receiver area power density (α), with higher power transmission efficiency by 1%-4%. This is caused by higher average core flux densities and lower absolute coupling k in the polarized couplers.

3. Rectangular couplers perform poorly in the $\eta - \gamma$ metric and thus lead to heavier designs for the same efficiency. However, rectangular couplers show good misalignment tolerance in the lateral direction (x) perpendicular to the direction of driving.

4. DD-DD coupler shows high efficiency for the same material effort or gravimetric power density.

5. While designing for high efficiency during misalignment, DD-BPP is the best coupler topology. However, the misalignment tolerance of DD-DDQ is better than the rest with low fluctuations of coupling co-efficient, especially in the direction of driving (longitudinal or y-direction).

6. In terms of stray fields, DD-BPP shows good performance with very low stray fields in the vertical direction. The circular and rectangular couplers have lower stray flux densities in the lateral direction compared to polarized couplers.

In conclusion, the presented multi-objective IPT optimization process provides a platform for a systematic comparison of all the popular coupler concepts that allow Pareto tradeoffs to be taken into account during the initial design phase. In IPT applications without misalignment, circular coupler provides the best performance. Optimized circular couplers are more efficient, lighter, and smaller compared to all other topologies. Besides, they have lower leakage flux in both vertical and lateral direction. However, in IPT applications requiring misalignment operation, DD-DDQ provides the best misalignment tolerance, and DD-BPP shows the maximum achievable efficiency.

References

[1] J. Ekblom, "Denmark calls for eu strategy to phase out diesel and petrol cars from 2030." https://www.reuters.com/article/us-eu-autos-denmark-idUSKBN1WJ1YW, October 2019.

[2] K. Van Schuylenbergh and R. Puers, *Inductive powering: basic theory and application to biomedical systems*. Springer Science & Business Media, 2009.

[3] D. Patil, M. K. McDonough, J. M. Miller, B. Fahimi, and P. T. Balsara, "Wireless power transfer for vehicular applications: Overview and challenges," *IEEE Transactions on Transportation Electrification*, vol. 4, no. 1, pp. 3–37, 2018.

[4] G. A. Covic and J. T. Boys, "Modern trends in inductive power transfer for transportation applications," *IEEE Journal of Emerging and Selected topics in power electronics*, vol. 1, no. 1, pp. 28–41, 2013.

[5] S. Jeong, Y. J. Jang, and D. Kum, "Economic analysis of the dynamic charging electric vehicle," *IEEE Transactions on Power Electronics*, vol. 30, no. 11, pp. 6368–6377, 2015.

[6] M. Yilmaz and P. Krein, "Review of charging power levels and infrastructure for plug-in electric and hybrid vehicles and commentary on unidirectional charging," in *International Electrical Vehicle Conference (IEVC'12)*, pp. 1–34, 2012.

[7] G. R. Nagendra, G. A. Covic, and J. T. Boys, "Determining the physical size of inductive couplers for ipt ev systems," *IEEE Journal of Emerging and Selected Topics in Power Electronics*, vol. 2, no. 3, pp. 571–583, 2014.

[8] M. Budhia, J. T. Boys, G. A. Covic, and C.-Y. Huang, "Development of a single-sided flux magnetic coupler for electric vehicle ipt charging systems," *IEEE Transactions on Industrial Electronics*, vol. 60, no. 1, pp. 318–328, 2013.

[9] G. A. Covic, M. L. Kissin, D. Kacprzak, N. Clausen, and H. Hao, "A bipolar primary pad topology for ev stationary charging and highway power by inductive coupling," in *Energy Conversion Congress and Exposition (ECCE)*, pp. 1832–1838, IEEE, 2011.

[10] S. Raabe, G. Elliott, G. Covic, and J. Boys, "A quadrature pickup for inductive power transfer systems," in *Industrial Electronics and Applications,ICIEA*, pp. 68–73, IEEE, 2007.

[11] S. Y. Jeong, S. Y. Choi, M. Sonapreetha, and C. T. Rim, "Dq-quadrature power supply coil sets with large tolerances for wireless stationary ev chargers," in *Emerging Technologies: Wireless Power (WoW), IEEE PELS*, pp. 1–6, IEEE, 2015.

[12] Y. Nagatsuka, N. Ehara, Y. Kaneko, S. Abe, and T. Yasuda, "Compact contactless power transfer system for electric vehicles," in *Power Electronics Conference (IPEC)*, pp. 807–813, IEEE, 2010.

[13] M. Budhia, G. A. Covic, and J. T. Boys, "Design and optimization of circular magnetic structures for lumped inductive power transfer systems," *IEEE Transactions on Power Electronics*, vol. 26, no. 11, pp. 3096–3108, 2011.

[14] G. Buja, M. Bertoluzzo, and K. N. Mude, "Design and experimentation of wpt charger for electric city car," *IEEE Transactions on Industrial Electronics*, vol. 62, no. 12, pp. 7436–7447, 2015.

[15] R. Bosshard and J. W. Kolar, "Multi-objective optimization of 50 kw/85 khz ipt system for public transport," *IEEE Journal of Emerging and Selected Topics in Power Electronics*, vol. 4, no. 4, pp. 1370–1382, 2016.

[16] A. Zaheer, D. Kacprzak, and G. A. Covic, "A bipolar receiver pad in a lumped ipt system for electric vehicle charging applications," in *Energy Conversion Congress and Exposition (ECCE)*, pp. 283–290, IEEE, 2012.

[17] S. Bandyopadhyay, V. Prasanth, L. R. Elizondo, and P. Bauer, "Design considerations for a misalignment tolerant wireless inductive power system for electric vehicle (ev) charging," in *Energy Conversion Congress and Exposition (ECCE)*, pp. 1–10, IEEE, 2017.

[18] K. Knaisch and P. Gratzfeld, "Comparison of magnetic couplers for inductive electric vehicle charging using accurate numerical simulation and statistical methods," in *Electric Drives Production Conference (EDPC)*, pp. 1–10, IEEE, 2015.

[19] K. Knaisch, M. Springmann, and P. Gratzfeld, "Comparison of coil topologies for inductive power transfer under the influence of ferrite and aluminum," in *Ecological Vehicles and Renewable Energies (EVER)*, pp. 1–9, IEEE, 2016.

[20] V. Prasanth, S. Bandyopadhyay, P. Bauer, and J. A. Ferreira, "Analysis and comparison of multi-coil inductive power transfer systems," in *Power Electronics and Motion Control Conference (PEMC)*, pp. 993–999, IEEE, 2016.

[21] R. Bosshard, U. Iruretagoyena, and J. W. Kolar, "Comprehensive evaluation of rectangular and double-d coil geometry for 50 kw/85 khz ipt system," *IEEE Journal of Emerging and Selected Topics in Power Electronics*, vol. 4, no. 4, pp. 1406–1415, 2016.

[22] R. Bosshard, J. W. Kolar, J. Mühlethaler, I. Stevanović, B. Wunsch, and F. Canales, "Modeling and pareto optimization of inductive power transfer coils for electric vehicles," *IEEE Journal of Emerging and Selected Topics in Power Electronics*, vol. 3, no. 1, pp. 50–64, 2015.

[23] S. Bandyopadhyay, V. Prasanth, P. Bauer, and J. Ferreira, "Multi-objective optimisation of a 1-kw wireless ipt systems for charging of electric vehicles," in *Transportation Electrification Conference and Expo (ITEC)*, pp. 1–7, IEEE, 2016.

[24] H. Feng, R. Tavakoli, O. C. Onar, and Z. Pantic, "Advances in high-power wireless charging systems: Overview and design considerations," *IEEE Transactions on Transportation Electrification*, vol. 6, no. 3, pp. 886–919, 2020.

[25] R. Bosshard, *Multi-objective optimization of inductive power transfer systems for EV charging*. PhD thesis, ETH Zurich, 2015.

[26] I. Nam, R. Dougal, and E. Santi, "General optimal design method for series-series resonant tank in loosely-coupled wireless power transfer applications," in *2014 IEEE Applied Power Electronics Conference and Exposition-APEC 2014*, pp. 857–866, IEEE, 2014.

[27] J. Deng, F. Lu, S. Li, T.-D. Nguyen, and C. Mi, "Development of a high efficiency primary side controlled 7kw wireless power charger," in *2014 IEEE International Electric Vehicle Conference (IEVC)*, pp. 1–6, IEEE, 2014.

[28] B. Esteban, M. Sid-Ahmed, and N. C. Kar, "A comparative study of power supply architectures in wireless ev charging systems," *IEEE Transactions on Power Electronics*, vol. 30, no. 11, pp. 6408–6422, 2015.

[29] J. Hou, Q. Chen, Z. Zhang, S.-C. Wong, and K. T. Chi, "Analysis of output current characteristics for higher order primary compensation in inductive power transfer systems," *IEEE Transactions on Power Electronics*, vol. 33, no. 8, pp. 6807–6821, 2017.

[30] R. L. Steigerwald, "A comparison of half-bridge resonant converter topologies," *IEEE transactions on Power Electronics*, vol. 3, no. 2, pp. 174–182, 1988.

[31] T. Nakata, N. Takahashi, K. Fujiwara, and A. Ahagon, "Periodic boundary condition for 3-d magnetic field analysis and its applications to electrical machines," *IEEE Transactions on Magnetics*, vol. 24, no. 6, pp. 2694–2696, 1988.

[32] J. Mühlethaler, "Modeling and multi-objective optimization of inductive power components," 2012.

[33] C. P. Steinmetz, "On the law of hysteresis," *Proceedings of the IEEE*, vol. 72, no. 2, pp. 197–221, 1984.

[34] C. Multiphysics, "v. 5.2," *COMSOL AB, Stockholm, Sweden*, 2015.

[35] M. Brubaker, H. Kirbie, T. Hosking, and T. Von Kampen, "System level considerations for integration of resonant capacitors in high power wireless charging," in *Conference on Eletric Roads and Vehicles (CERV)*, 2012.

[36] T. Diekhans, F. Stewing, G. Engelmann, H. van Hoek, and R. W. De Doncker, "A systematic comparison of hard-and soft-switching topologies for inductive power transfer systems," in *Electric Drives Production Conference (EDPC)*, pp. 1–8, IEEE, 2014.

[37] K. Peng and E. Santi, "Performance projection and scalable loss model of sic mosfets and sic schottky diodes," in *Electric Ship Technologies Symposium (ESTS)*, pp. 281–286, IEEE, 2015.

[38] T. Diekhans and R. W. De Doncker, "A dual-side controlled inductive power transfer system optimized for large coupling factor variations and partial load," *IEEE Transactions on Power Electronics*, vol. 30, no. 11, pp. 6320–6328, 2015.

[39] D. Kobayashi, T. Imura, and Y. Hori, "Real-time coupling coefficient estimation and maximum efficiency control on dynamic wireless power transfer for electric vehicles," in *Emerging Technologies: Wireless Power (WoW), 2015 IEEE PELS Workshop on*, pp. 1–6, IEEE, 2015.

[40] Y. Del Valle, G. K. Venayagamoorthy, S. Mohagheghi, J.-C. Hernandez, and R. G. Harley, "Particle swarm optimization: basic concepts, variants and applications in power systems," *IEEE Transactions on evolutionary computation*, vol. 12, no. 2, pp. 171–195, 2008.

[41] C.-S. Wang, G. A. Covic, and O. H. Stielau, "Power transfer capability and bifurcation phenomena of loosely coupled inductive power transfer systems," *IEEE transactions on industrial electronics*, vol. 51, no. 1, pp. 148–157, 2004.

[42] J. Lin, R. Saunders, K. Schulmeister, P. Söderberg, A. Swerdlow, M. Taki, B. Veyret, G. Ziegelberger, M. H. Repacholi, R. Matthes, *et al.*, "Icnirp guidelines for limiting exposure to time-varying electric and magnetic fields (1 hz to 100 khz).," *Health Physics*, vol. 99, pp. 818–836, 2010.

[43] F. Y. Lin, G. A. Covic, and J. T. Boys, "Evaluation of magnetic pad sizes and topologies for electric vehicle charging," *IEEE Transactions on Power Electronics*, vol. 30, no. 11, pp. 6391–6407, 2015.

5 Optimal System Sizing of DC Homes

In residential houses, there is a temporal mismatch between the PV profile and the house load profile. This is due to a combination of seasonal nature of PV power generation and user behaviour. To mitigate this, an energy storage systemlike battery is used in conjunction with the PV system to compensate for the long-term and short-term imbalance between power generation and demand. To that end, it is necessary to optimally size PV and battery systems for reducing grid dependency in terms of both energy and power.

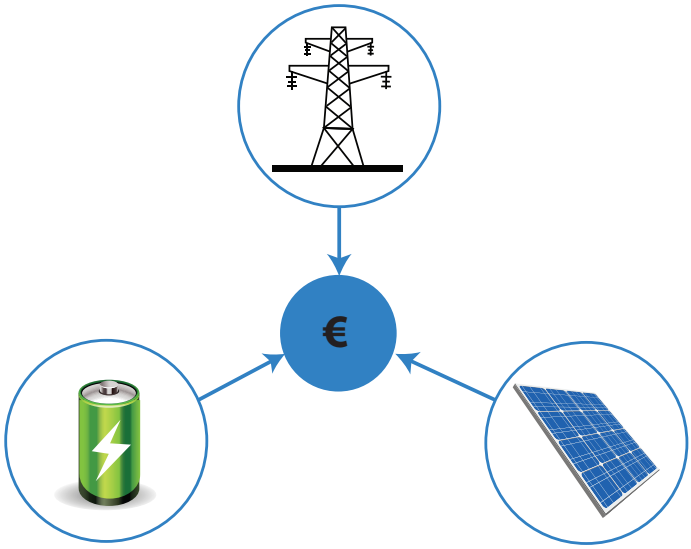

Based on:

1. "*Techno-economical Model based Optimal Sizing of PV-Battery Systems for Microgrids*", **IEEE Transactions on Sustainable Energy**, vol. 11, no. 3, pp. 1657-1668, July 2020, doi: 10.1109/TSTE.2019.2936129.
2. *"Comparison of Battery Technologies for DC Microgrids with Integrated PV,"* IEEE Third International Conference on DC Microgrids (ICDCM), Matsue, Japan, 2019, pp. 1-9, doi: 10.1109/ICDCM45535.2019.9232746.

5.1 Introduction

Increasing energy consumption of buildings (both residential and commercial) has led to 40% of total energy consumption in developed countries [1]. The rise of energy demand in buildings will continue in the near future because of population growth, urbanization, increasing penetration of electric vehicles (EVs) [2], and electrification of household heating [3, 4]. To that end, a centralized nanogrid with integrated rooftop solar and battery-based energy is proposed in this thesis to make future households and buildings more efficient and energy-independent to reduce the burden on the overhead grid.

However, a significant investment cost is associated with battery and PV systems. In addition to battery and PV, the grid-interfacing converter's sizing connecting the nanogrid to the utility grid needs to be considered in the optimization. Since there are numerous design degrees of freedom like PV design variables, storage sizes, the converter rating and battery technologies, a fundamental question arises: What is the optimal and cost-effective PV installed power, converter rating and storage capacity mix that minimizes the annual cost of electricity, maximizes self-sufficiency while considering battery degradation? This problem complexity demands a multi-objective optimization based solution where the underlying trends can be visualized by analyzing trade-offs between mutually conflicting objectives. Compared to AC nanogrids for buildings or households, the system sizing problem in DC nanogrid has an additional design variable: the front-end converter's rating. Therefore, existing literature on optimal sizing strategies of PV-battery systems for AC residential application can be utilized in the DC application as well.

Literature review

Several publications have proposed optimal sizing of PV-battery systems by maximizing the economic value created by using battery and PV system, focusing on improving self-consumption or energy autonomy [5, 6]. Other studies have focused on the optimal sizing of only the battery to maximize peak-shaving [7–9]. A MILP based optimization model for system sizing for grid-connected and off-grid nanogrids is presented in [10–12]. However, there are several limitations in current literature regarding the optimal sizing of PV-battery systems for nanogrids. First, most studies focus on a single objective like increasing self-consumption, or reduce demand peaks or maximize economic benefits [8, 10, 11].

Due to the mutually conflicting nature of the targets, the single objective optimization approach cannot provide valuable insights regarding the trade-offs between these objectives. Additionally, the inherent simplification associated with formulating a complex multi-objective problem into a weighted single objective problem fails to capture underlying trends. Second, in PV system modelling, most studies use solar irradiation as the only input [13], occasionally combined with temperature [10]. Some studies utilize more accurate PV models that consider the tilt and azimuth angle of the panel orientations. However, during the design process, they select fixed values of tilt and azimuth angle [9, 14] for maximum solar generation. This approach may not result in optimal PV and storage sizes as they do not consider the degree of temporal match of the PV profile and the load profile. Third, many studies do not take into account the effect of load profiles and power management strategy on battery lifetime [6, 8, 12]. Fourth, the impact of incentives given by real-life electricity tariffs on the optimal sizing is not investigated in the literature [9, 10]. Another drawback of most studies is that they use load profiles with a resolution of 15 min to one hour, which in substantial errors (>5%) in determining self-consumption [5].

Contributions

This chapter aims to develop a multi-objective optimisation (MOO) framework to solve the system sizing problem for a grid-connected residential microgrid system to incorporate multiple mutually opposing objectives while taking into account the effect of battery degradation, incentives like feed-in tariffs, and PV system orientation. The developed MOO framework is applied to optimally size the PV-battery-converter system in two residential load profiles in Cabauw, Netherlands (NL), and in Austin, United States (US). Additionally, three battery technologies, lithium-ion, lead-acid, and vanadium redox flow batteries, are compared in their techno-economic feasibility. The main contributions of this paper compared to previous works are:

1. Develop a multi-objective optimisation framework to size PV system, grid converter, and battery storage capacity resulting in Pareto fronts of trade-offs between multiple objectives like lifetime capital cost, self-sufficiency, power autonomy and simple payback period.

2. Investigating the performance of three different battery technologies in residential grids, namely: lithium-ion, lead-acid and vanadium redox flow.

3. Study the effect of solar meteorological potential on optimal PV and battery sizing by comparing results on two different geographical locations: Cabauw, NL and Austin, US.

4. Investigate the effect of electricity pricing tariffs and feed-in tariffs on optimal sizing of PV and battery system.

5. Draw guidelines for selecting the optimal azimuth angle for a residential PV system.

6. Derive sizing equations and thumb rules to optimally size PV-battery-converter systems for microgrids based on solar potential and specific load profile.

Chapter outline

The chapter is structured into five parts. In Section 5.2, the techno-economical model of the microgrid is presented. Section 5.3 develops the multi-objective optimization (MOO) framework and optimizes the sizing of PV-battery based microgrid for two residential load profiles in NL and US. Further, the effect of battery chemistry on relative sizing is also considered. The results of the multi-objective optimization are presented and analyzed in two different sections. Section 5.4 derives insights into optimal design and thumb rules for optimal system sizing looking at the effect of solar potential, and section 5.5 presents a detailed comparison of the techno-economical performances of three battery technologies. Finally, general conclusions are summarised based on the results.

5.2 Techno-economical model of a nanogrid

A techno-economical model of PV-battery based nanogrids are developed in this section. The technical model comprises the PV system model, the battery lifetime model, and the power management model. The economic model presents the methodology to compute the lifetime cost, which consists of the capital cost and the operational cost. Finally, the figure of merits (FoMs) of a grid-connected PV-battery based residential nanogrid are highlighted based on the different metrics produced by the two models.

The technical model is presented in three sub-sections. First, the power and energy output of a rooftop PV system is modelled considering azimuth and tilt angle of the PV panels. Second, the power management strategy to control battery bank power is presented. Finally, the methodology of estimating the battery lifetime of the selected battery technologies is discussed briefly.

Power flow equations

The power required by different loads in a household (P_{load}) at a certain instant can be provided by one or different combinations of three sources: the grid (P_{grid}), PV system (P_{pv}) and the battery energy storage (P_{bess}). Therefore, the main power flow equation can be written as:

$$P_{\text{load}}(t) + P_{\text{pv}}(t) + P_{\text{grid}}(t) + P_{\text{bess}}(t) = 0, \qquad \forall\, t \in T \tag{5.1}$$

subjected to the following constraints:

$$0 \leq P_{\text{pv}}(t) \leq PV^{\max}(t), \qquad \forall\, t \in T \tag{5.2}$$

$$-\mathrm{P}_{\text{bess}}^{\max} \leq P_{\text{bess}}(t) \leq \mathrm{P}_{\text{bess}}^{\max}, \qquad \forall\, t \in T \tag{5.3}$$

$$-\mathrm{P}_{\text{grid}}^{\max} \leq P_{\text{grid}}(t) \leq \mathrm{P}_{\text{grid}}^{\max}, \qquad \forall\, t \in T \tag{5.4}$$

where $PV^{\max}(t)$ is the maximum PV production at any time instant, $\mathrm{P}_{\text{bess}}^{\max}$ is the maximum power that can be supplied by the battery converter and $\mathrm{P}_{\text{grid}}^{\max}$ is the rating of the bi-directional front-end converter interfacing the utility grid and the DC house.

Figure 5.1 depicts the power flow equation (5.1) at the point of common coupling (PCC) of all the different loads and the sources interfaced with power converters. Therefore, to model the power dispatched by different sources, these interfacing power converters' efficiency needs to be considered.

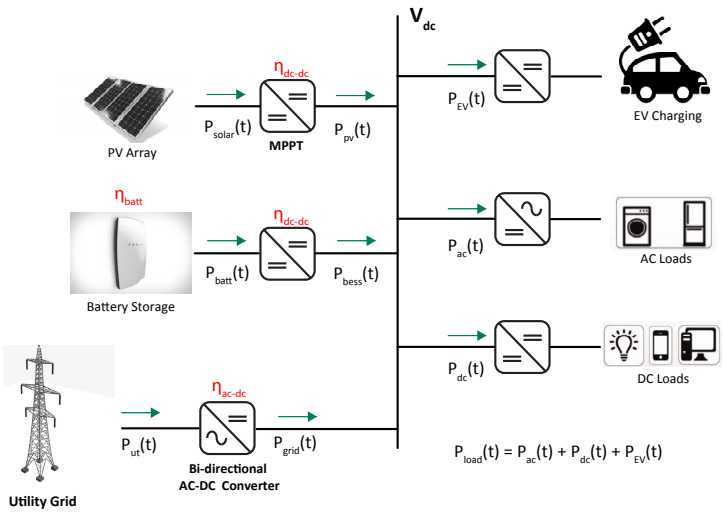

Figure 5.1: Power flow between different sources and loads in the DC nanogrid

To that end, different sources are modelled in the following.

Depending on the direction of the power flow, the power processed and the State of Charge (SoC) of the battery bank can be presented by the following:

$$P_{\text{batt}}(t) = \frac{P_{\text{bess}}(t)}{\eta_{\text{conv-batt}}\sqrt{\eta_{\text{batt}}}} \qquad \forall P_{\text{bess}}(t) < 0 \tag{5.5}$$

$$P_{\text{batt}}(t) = \eta_{\text{conv-batt}}\sqrt{\eta_{\text{batt}}}P_{\text{bess}}(t) \qquad \forall P_{\text{bess}}(t) \geq 0 \tag{5.6}$$

$$\text{SoC}(t) = \text{SoC}(t-\Delta t) + \frac{P_{\text{batt}}(t)}{C_{\text{batt}}}.\Delta t \tag{5.7}$$

where $\eta_{\text{conv-batt}}$ is the efficiency of the DC-DC converter, C_{batt} is the nominal capacity, and η_{batt} is the round-trip efficiency of the battery. The DC house is interfaced with the utility grid with a converter capable of bi-directional power flow. Therefore, depending on the direction of power flow, the power delivered/fed into the grid is modelled using the following:

$$P_{\text{ut}}(t) = \frac{P_{\text{grid}}(t)}{\eta_{\text{grid}}} \qquad \forall P_{\text{grid}}(t) > 0 \tag{5.8}$$

$$P_{\text{ut}}(t) = \eta_{\text{grid}}P_{\text{grid}}(t) \qquad \forall P_{\text{grid}}(t) \leq 0 \tag{5.9}$$

where η_{grid} is the grid-tied converter efficiency whcih can be obtained from manufacturer's datasheet. The value of η_{grid} is dependent on the power processed by the converter $P_{\text{grid}}(t)$. Since this study does not focus on system losses, we will ignore the dependence of converter efficiency on $P_{\text{grid}}(t)$ and assume a constant value.

The PV panel array is interfaced to the common DC bus with a DC-DC converter which tracks the maximum power point (MPPT) of the PV array. Since power flows only in one direction, the PV

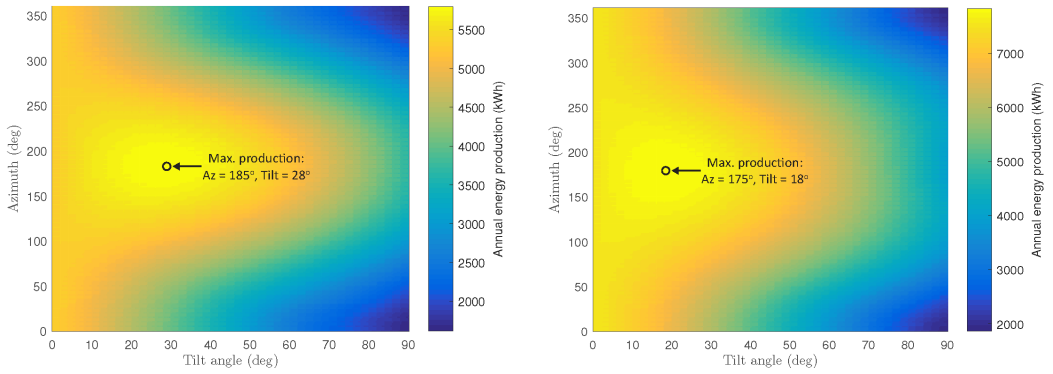

(a) (b)

Figure 5.2: (a) Annual energy yield of a 5kW PV system in: Cabauw, Netherlands, (b) Annual energy yield of a 5 kW PV system in: Austin, Texas.

power (P_{pv}) supplied at the point of common coupling (PCC) can be presented as :

$$P_{\text{pv}}(t) = \eta_{\text{conv-pv}} P_{\text{solar}}(t) \qquad \forall P_{\text{grid}}(t) > 0 \tag{5.10}$$

where $\eta_{\text{conv-pv}}$ is the efficiency of the solar MPPT converter and $P_{\text{solar}}(t)$ is the energy generated by the PV panels at a particular time instant.

5.2.1 PV system modelling

An accurate PV system model is built in this paper to estimate the energy and power generated by the rooftop PV array. Based on meteorological data of Netherlands and Texas, US, Global Horizontal Irradiance (S^{GHI}), Diffuse Horizontal Irradiance (S^{DHI}), Direct Normal Irradiance (S^{DNI}) and ambient temperature (T_{a}) are obtained. The PV array is modelled in MATLAB using Sun power E20-327 modules rated at 327 W. To compute the power generated by a PV module with an azimuth (A_{m}) and tilt angle (θ_{m}), an estimate of the solar irradiance (S_{m}) on the module is required. To that end, a solar position calculator is built by which the azimuth (A_{S}) and the altitude (a_{S}) of the sun throughout the year at any location can be estimated.

At a certain sun position, the irradiance on a panel with a specific orientation ($A_{\text{m}}, \theta_{\text{m}}$) can be computed using the geometric models and the isotropic sky diffused model:

$$S_{\text{m}}^{\text{DNI}} = S^{\text{DNI}} [\sin\theta_{\text{m}} \cos a_{\text{s}} \cos(A_{\text{m}} - A_{\text{s}}) + \cos\theta_{\text{m}} \sin a_{\text{s}}] \tag{5.11}$$

$$S_{\text{m}}^{\text{DHI}} = S^{\text{DHI}} \frac{1 + \cos\theta_{\text{m}}}{2} \tag{5.12}$$

$$S_{\text{m}} = S_{\text{m}}^{\text{DNI}} + S_{\text{m}}^{\text{DHI}} \tag{5.13}$$

where $S_{\text{m}}^{\text{DHI}}$, $S_{\text{m}}^{\text{DNI}}$ are the components of DHI and DNI which are incident on the panel. The above equations show that the solar energy generation by a panel can be controlled by changing the module azimuth (A_{m}) and the tilt angle (θ_{m}).

To improve the PV model accuracy, the effect of the ambient temperature on solar power generation is also taken into consideration. The E20-327 PV module is rated for 327 W at the ambient temperature of 25^o. For other ambient temperatures, the PV array output power $P_{\text{solar}}(t)$ at a certain time instant can be computed using [15]:

$$T_{\text{cell}} = T_{\text{a}} + \frac{S_{\text{m}}(T_{\text{NOCT}} - 20)}{800} \tag{5.14}$$

$$P_{\text{solar}}(t) = \frac{N_{\text{p}} P_{\text{r}} S_{\text{m}}[1 - \gamma(T_{\text{cell}} - 25)]}{1000} \tag{5.15}$$

Figure 5.2 shows the annual energy yield for a 5kWp PV array for different azimuth angle and module tilt is estimated for the case of Netherlands (NL) and Texas (TX) based on equations (5.11)-(5.15). In case of Netherlands, the maximum annual yield is 5800 kWh obtained for south-facing panels with A_{m}= 185^o, θ_{m}= 28^o. The maximum energy yield of 7830 kWh for Austin, Texas is obtained for panels with A_{m}= 175^o, θ_{m}= 18^o.

The lower tilt angle in Austin, Texas, is since Texas is at a lower latitude than the Netherlands. However, the maximum annual energy yield in Austin, Texas, is 35% higher than that of the Netherlands. To elaborate the effect of module azimuth orientation, Figure 5.3 shows the power output profile of a 5 kW PV system during a summer day in the Netherlands with different azimuth (A_{m}) angles at an optimal tilt angle of $\theta_{\text{m}} = 28^o$. By changing the azimuth, the time of the day when maximum PV power is available can be controlled at the cost of a lower energy yield. To investigate the effect of module azimuth on optimal storage size sizing, the azimuth angle (A_{m}) is considered as a design variable in the optimization framework.

5.2.2 Battery lifetime modelling

The battery cost plays a key role in the overall system cost. Therefore, their lifetime may have significant implications on total operational costs over the long-term and should not be neglected. The usable capacity of a battery reduces over time with each charge-discharge cycle. This is called cyclic ageing [16]. The battery capacity can also fade even when it is not used, i.e. held at a constant state of charge (SoC) level. This is known as calendar ageing [17]. Therefore, an additional cost of battery replacements during the system service life should be considered during PV and battery system sizing optimization.

Table 5.1: Parameters of Sun power E20-327 module

Parameter	Symbol	Value
Area of module (m^2)	A_{pv}	1.63
Nominal Power (W)	P_{r}	327
Avg. Panel Efficiency (%)	η	20.4
Rated Voltage (V)	V_{mpp}	54.7
Rated Current (A)	I_{mpp}	5.98
Open-circuit Voltage (V)	V_{oc}	64.9
Short-circuit Current (A)	I_{sc}	6.46
Nominal Operating Cell Temperature (^{o}C)	T_{NOCT}	45±2
Power Temp Coefficient (%/^{o}C)	γ	-0.38

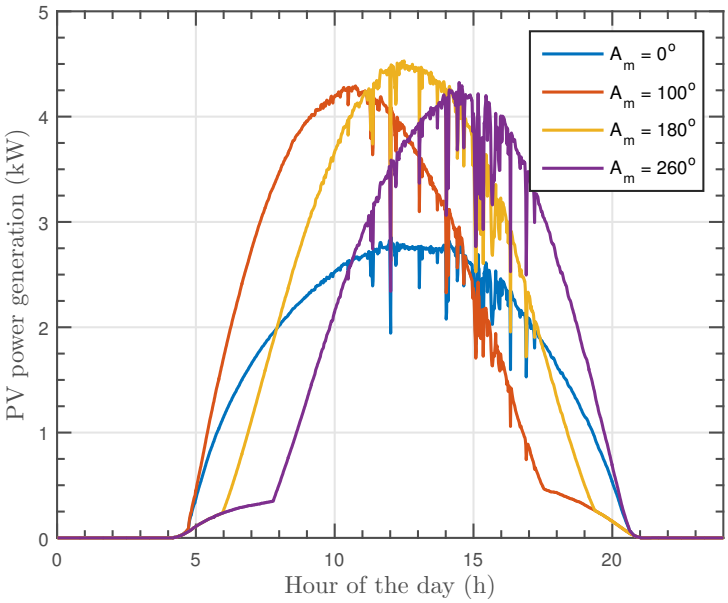

Figure 5.3: Power generated by 5 kW PV system for a summer day (Day 165 of year 2017) in Netherlands for different azimuth angles = 0^o, 100^o, 180^o, and 260^o with constant tilt angle of 28^o.

Rechargeable batteries, regardless of the choice of technology, show a decreasing performance with usage/time. This reduction of battery performance is termed battery ageing. SoH is a subjective term, and researchers interpret it depending on the type of applications. For applications that use a battery as a primary energy source, such as consumer electronics, electric vehicles, and grid storage, they are more susceptible to capacity fade than power fade. In literature, battery ageing is characterised and quantified by the term state of health (SoH). For residential based grid storage application, capacity fading (permanent capacity loss) is used as the primary indicator for the battery's SoH. By convention, in EV batteries, the end-of-life (EOL) condition is reached when the battery capacity has dropped to 80% of its nominal capacity [18]. The same convention is used in this analysis for residential applications. Therefore, the SoH of the battery becomes:

$$\text{SoH} = (1 - \frac{\xi}{Q_0}).100\% \tag{5.16}$$

where ξ is the total capacity fade of the battery during operation and Q_0 is the battery's nominal capacity. It can be seen that when 20% of the nominal battery capacity has faded, the SoH of the battery becomes 80% based on (5.16), and thus the battery system has reached the end-of-life (EOL) condition.

However, different battery technologies age at different rates and have different round-trip efficiency. To that end, battery lifetime models for the three battery technologies considered, namely: lead-acid, lithium-ion and vanadium redox flow, are discussed next.

Lithium-ion battery

The capacity fading of Li-ion battery cells is a complex process depending on multiple degradation mechanisms, which can be even further accelerated by different external and internal stress factors based on operating conditions [16]. As already mentioned, capacity fading can be further divided into the two categories: (a) Calendar aging [19], and (b) Cyclic aging [16]. However, it has been reported that cycling losses have a more dominant effect on capacity fading than calendar losses [20]. To that end, in this research, the effect of calendar ageing on capacity fading in lithium-ion batteries is neglected. As already highlighted, the capacity fading of a battery is a function of the battery's operating conditions. A brief literature review on the effects of different operating conditions on a lithium-ion battery lifetime is presented in Table 5.2. Definitions of SoC and DoD are based on [25] and they are presented below :

$$SoC = \frac{Q}{Q_0} \tag{5.17}$$

$$DoD = \frac{1}{Q_0} \int I(t)dt \tag{5.18}$$

where Q is the instantaneous amount of charge, Q_0 is the nominal capacity of the battery, and I is the discharge current. From Table 5.2, it is clear that DoD, SoC and temperature are critical to the battery lifetime. In this research, the effect of temperature on battery life is not considered since this study's primary focus is system-level storage optimization. Based on the literature review presented above, a battery lifetime predicting model is developed in the next section. There is extensive research on battery lifetime modelling reported in the literature. Majority of the studies are on empirical modelling approach based on experimental data [21, 24–26]. Electrochemical based battery models are also reported in literature [27]. Models based on advanced mathematics and machine learning algorithms can also be found in literature [28, 29].

The main challenge is to find an optimal trade-off between model accuracy and complexity. Generally, in storage optimization literature, the battery life is determined from models based on the number

Table 5.2: Effect of different operating conditions on battery lifetime

Parameter	Description	Effect on Lifetime
DoD	Depth of discharge	[21] reports battery cycle life as an exponential function of DoD
SoC	State of charge	High average SoC of a battery increases capacity fading. SoCs below 20% lead to mechanical stress with lithium intercalation [22]
C_{rate}	Charging/ discharging current	C_{rate} have no direct effect on capacity fading, only indirectly in form of temperature rise due to ohmic heating [**?**]
$T_{batt,cell}$	Battery cell temperature	High temperatures leads to stress and reduces lifetime [16, 24**?**]

of battery cycles and their corresponding depth of discharge (DoD) [11, 30]. However, in the case of lithium-ion batteries, researchers have shown that in addition to the depth of discharge, other stress factors like average SoC also affect the cyclic capacity fading rate [26**?**]. Therefore, in residential applications associated with diverse battery cycles modelling, battery life with only DoD is not enough. To that end, in this research, an empirical model based on [26] is used to model the capacity fading in lithium-ion batteries, which takes into account the effect of stress associated with average SoC in addition to cycling DoD. A brief description of the methodology is presented in Appendix B.

Lead acid battery

The Schiffer weighted Ah-throughput model [31] is used in this study to model the lifetime of the lead-acid battery. Like the lifetime model of lithium-ion battery presented in the previous section, the Schiffer model for lead-acid batteries assumes that real-life applications' operating conditions are more severe than those used in cyclic standard tests. Therefore, the actual Ah throughput is multiplied by several weight factors associated with different operating conditions like battery SoC, charge/discharge current etc. A detailed description of the Schiffer modelling approach is not in the scope of this thesis. However, interested readers can refer to [32], which experimentally validates the battery lifetime modelling approach for household applications.

Vanadium redox flow battery (VRFB)

The Vanadium redox flow battery differs from conventional battery storage in that the amount of energy it can store is independent of its power rating, which allows better flexibility in sizing the battery energy storage for microgrid systems [33]. The initial capital and maintenance costs for the VRB are still relatively high in comparison to other ESS. One of the crucial advantages of VRFB is the long calendar and cycle life with more than 200,000 cycles [34]. Therefore, replacing the entire battery for the VRFB system during the system lifetime for residential applications is not required, like Lithium-ion and lead-acid battery. The VRFB system requires timely replacement of the membrane and annual preventive overhaul [35], which are accounted for in the economic model.

This concludes the battery degradation modelling for different battery technologies. The models presented are derived from battery models in the literature, which consider the stressing factors associated with real-life applications. However, real-life applications like household do not have well-defined battery cycles, making it challenging to estimate capacity fading since the equations are based on well-defined cycle parameters like SoC_{avg}, and DoD. To that end, the next section discusses the methodology of estimating capacity fading and battery lifetime from real-life battery SoC profiles.

Rainflow counting algorithm

Traditionally, to calculate the total capacity loss of a battery over a given time horizon, the capacity degradation is computed for every cycle that occurs. To that end, the total number of cycles and their respective SoC_{avg}, DoD, and SoC_{dev} need to be computed. A modified fast rainflow algorithm [36] is used on annual SoC profiles of the battery to extract the number of cycles along with their characteristic

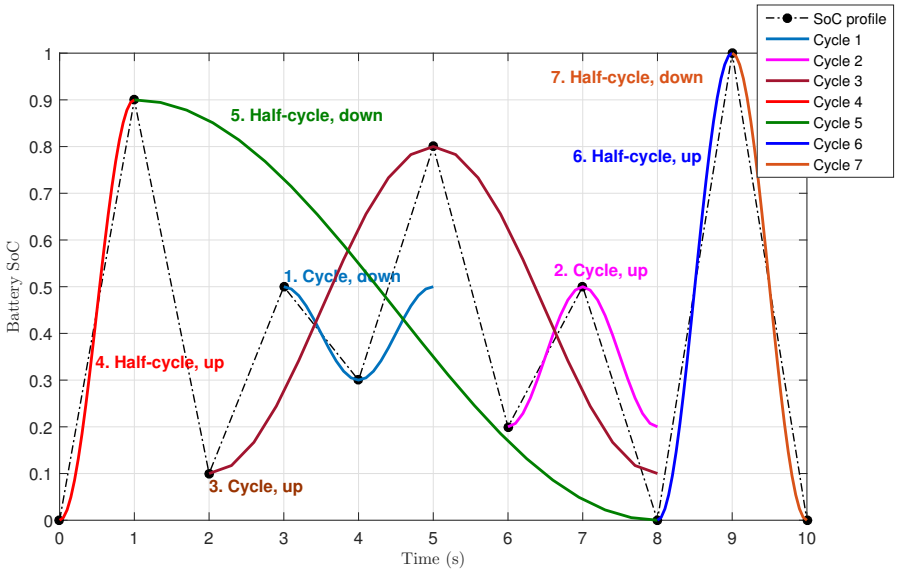

Figure 5.4: Cycle extraction based on Rainflow algorithm on an SoC profile.

data. An example of the extraction of cycle data is on a synthetic SoC profile is shown in Figure 5.4. Therefore, the annual capacity fade (ξ_y) of a battery for a given annual SoC profile can be computed using the per cycle capacity fading model along with the cycles extracted by the rainflow algorithm. Then, the battery lifetime (τ_{Batt}) becomes:

$$\tau_{Batt} = \frac{0.2Q_0}{\xi_y} \tag{5.19}$$

In the next section, the power management strategy of the different sources and loads of the DC house is presented. Finally, the effect of varying power management strategies on battery degradation is shown.

5.2.3 Power management strategy

The goal of the power management strategy is to determine the charging/discharging power of the battery $P_{bess}(t)$ and grid power $P_{grid}(t)$ at a certain time instant based on the load power $P_{load}(t)$ and PV power generation $P_{pv}(t)$ at that particular instant. Multiple solution pairs $[P_{grid}(t), P_{bess}(t)]$ exist for the power flow equation (5.1). In literature, several studies on power management algorithms can be found ranging from simple state diagram based approach [15] to more complex optimization based algorithms like mixed integer linear programming (MILP) [37, 38], mixed integer nonlinear programming (MINLP) [39], dynamic programming [40, 41] and multipass iteration optimization approach based on evolutionary algorithms [42].

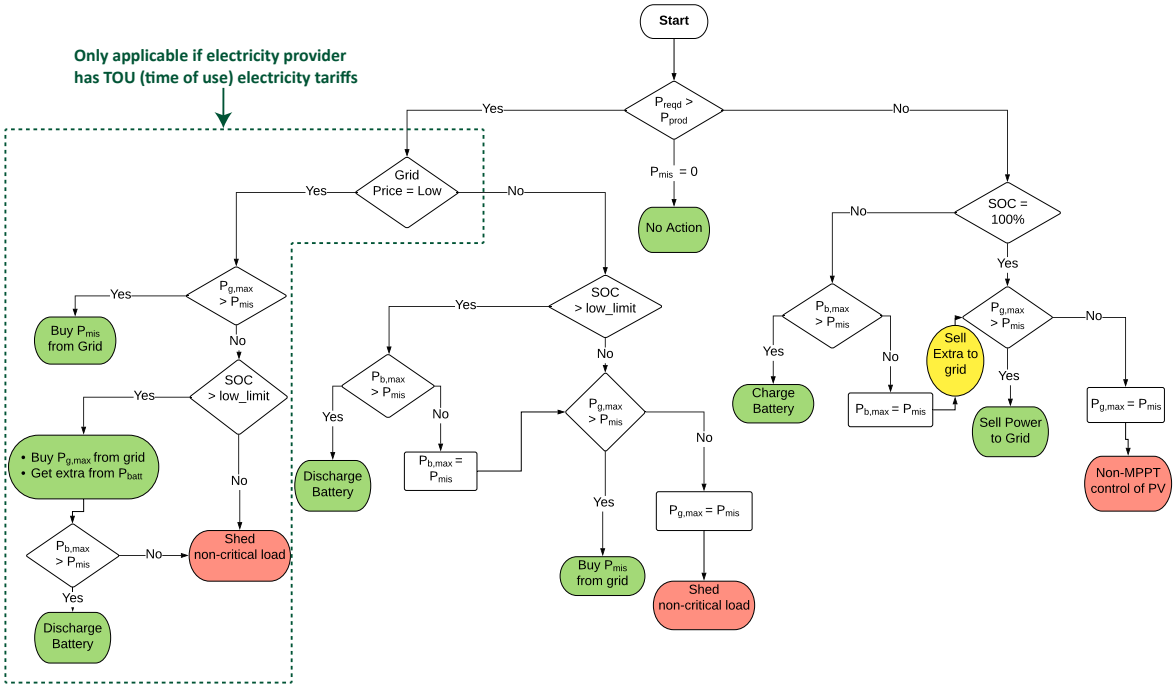

Figure 5.5: State diagram for operation of PV-Battery based grid connected DC households. The highlighted box part of the algorithm is only applicable to households whose eletricity providers offer time-of-use (TOU) rates for energy. For electricity providers with flat rates, that part of the algorithm is not considered.

Different power management algorithms will lead to other solutions to the optimal storage and PV sizing problem. In this study, a state-machine based power management algorithm approach is considered due to its simplicity, low computational requirement and ease of real-life implementation. Figure 5.5 shows the state diagram for the operation of the grid-connected DC house with integrated local storage and PV system. As highlighted in the figure, there can be two variants of the power management strategy: (a) a time-of-use (TOU) algorithm which uses the grid as the primary source for the excess power required if grid prices are off peak (NL Eneco price structure), (b) battery as primary source (BP) algorithm which uses the battery as the primary source of power all the time. The TOU algorithm is only applicable for Netherlands (NL), where the electricity tariffs have on-peak and off-peak prices whereas, the BP algorithm applies to both NL and US. Since both the algorithms can be used for the NL DC house, the optimal sizing solutions will differ.

Figure 5.6 shows the power profiles of the grid, battery, PV and load along with the SoC of the battery on a summer day in NL using the TOU algorithm and the BP algorithm. It is evident from the figure that the BP algorithm will reduce the grid dependency and electricity bill compared to the TOU algorithm. However, the BP algorithm results in a deeper depth of discharge (DoD), which may accelerate the battery's accelerated degradation. Figure 5.7 and 5.8 show the effect of different power management algorithms on battery degradation for different battery technologies in case of Netherlands and the US.

This concludes the details of the technical model of the grid-connected DC house. The economic modelling approach is presented in the next section. The goal is to combine the technical and financial models to form a holistic model to be used in the optimization framework.

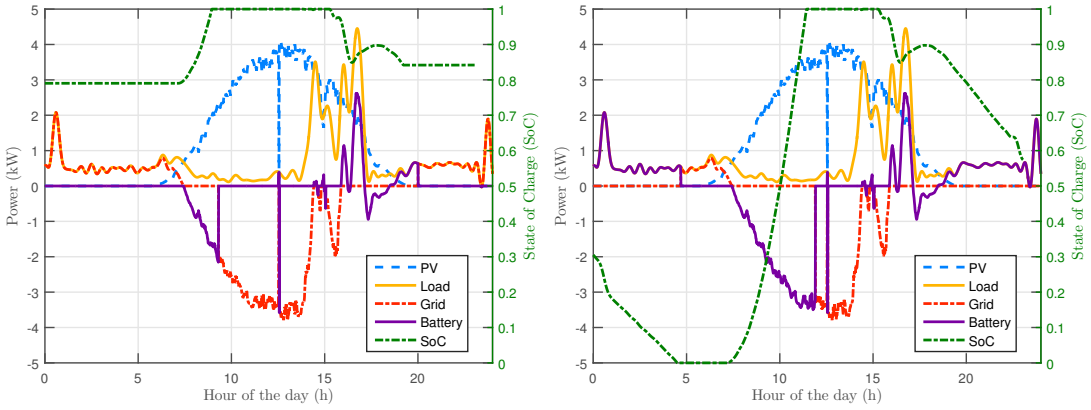

Figure 5.6: Power profiles (1 minute resolution) of different sources and overall load along with battery SoC profile on a summer day (day = 240) in Netherlands with: (a) Time of Use (TOU) algorithm , (b) battery as primary source algorithm. The simulated house has installed PV power is 5 kW, a lithium ion battery of 10 kWh capacity with C_{rate} of 1 and a 5 kW front-end converter.

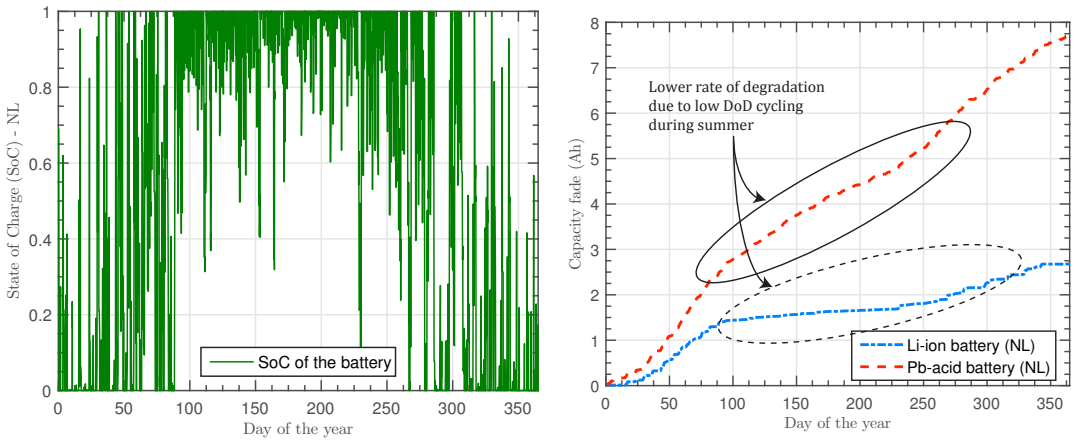

(a) (b)

Figure 5.7: Power management strategy and battery degradation in the Netherlands: (a) Annual SoC profile of a 10 kWh battery used for the NL load profile in conjunction with 5 kW PV with the time-of-use (TOU) power managmenet algorithm, and (b) Comparison of annual capacity fading between a Li-ion and lead-acid battery. It is evident that the battery degradation rate is lower for both battery technologies during summer in NL due to low loads and therefore low DoD cycling of the battery.

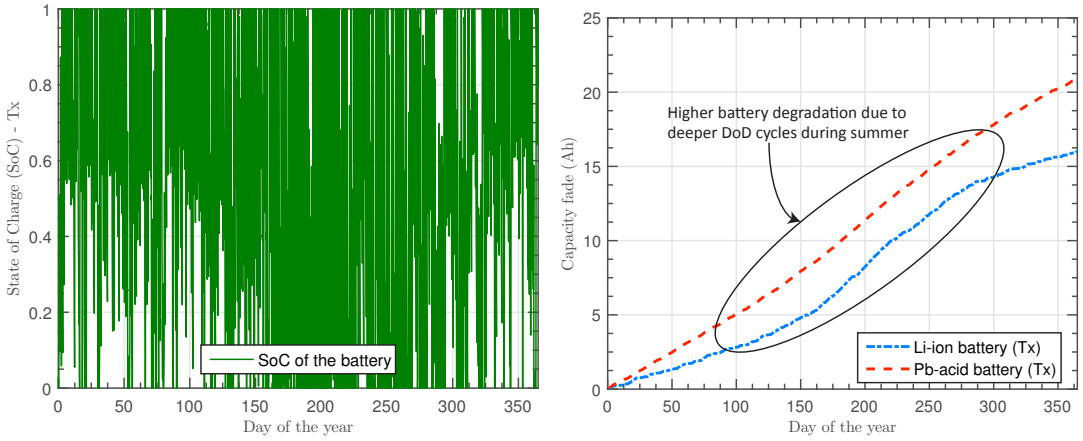

(a) (b)

Figure 5.8: Power management strategy and battery degradation in Texas, US: (a) Annual SoC profile of a 10 kWh battery used for the US load profile in conjunction with 5 kW PV with the battery as primary source (BP) algorithm, and (b) Comparison of annual capacity fading between a Li-ion and lead-acid battery. It is evident that the battery degradation rate is higher for both battery technologies during summer in the US due to higher load demandleading to deeper DoD cycling of the battery.

5.2.4 Economic model

An economic model of the nanogrid is required to quantify the benefits of installing a PV and battery system in grid-connected nanogrids. The economic benefit comes from savings in the electricity bill

due to: (a) using PV energy and battery stored energy for household loads, thereby reducing grid dependency, and (b) selling unused PV power to the grid.

During the system lifetime, the system's total cost can be divided into two parts: (a) capital cost and (b) operational costs, which include the cost of electricity. The cost of battery replacements and maintenance is considered within the capital costs. Thus, the total capital cost (κ_{total}) of a PV-battery integrated grid-connected DC house can be formulated as the following:

$$\kappa_{\text{total}} = \kappa_{\text{batt}} + \kappa_{\text{pv}} + \kappa_{\text{grid-conv}} \tag{5.20}$$

where, κ_{Batt}, κ_{pv}, and $\kappa_{\text{grid-conv}}$ are the capital cost associated with the battery storage system, PV system, and the front end grid converter. The three cost categories are further explained by the following equations:

$$\kappa_{\text{Batt}} = \pi_{\text{batt}} C_{\text{batt}} (n_{\text{replace}} + 1) \tag{5.21}$$

$$\kappa_{\text{pv}} = \pi_{\text{pv}} P_{\text{pv,r}} \tag{5.22}$$

$$\kappa_{\text{grid-conv}} = \pi_{\text{conv}} P_{\text{grid-conv,r}} \tag{5.23}$$

where π_{batt}, π_{pv}, and π_{conv} are unit-price for the battery system, the PV system, and the grid interfacing converter. n_{replace} denotes the number of battery replacements needed during the total system lifetime. Table 5.3 shows the values of the constants used in the economic model along with their sources. π_{batt}, π_{pv}, and π_{conv} are unit-price for the battery system, the PV system, and the grid interfacing converter. n_{replace} denotes the number of battery replacements needed during the total system lifetime. Table 5.3 shows the values of the constants used in the economic model along with their sources. Equation (5.21) is only applicable to lithium-ion and lead-acid based ESS system. The cost structure of Vanadium redox flow batteries (VRFB) is different from other ESS like Li-ion or lead-acid due to its unique characteristic of independent scalability of power and energy storage capacity. The power is defined by the energy converter's size (the cell stack), whereas the energy is defined by the amount of positive and negative charged electrolyte stored in two tanks. To that end, the VRFB cost structure used in this study is based on the model detailed in [35], which is based on the power rating and the energy rating of the VRFB system. The model computes the total lifetime cost of a VRFB based system, including initial investment cost, converter cost and maintenance/replacement cost. Next, the electricity tariffs associated with NL and the US are discussed in detail.

Table 5.3: Overview of Economic Parameters

Parameter	Symbol	Unit	Value
Converter	π_{conv}	\$/kW	100
PV system [43]	π_{pv}	\$/kWp	1350
Lithium-ion BESS [44]	π_{batt}	\$/kWh	500
Lead-acid BESS [45]			200
Vanadium redox BESS [35]			-

NL tariff

The electricity tariff in the Netherlands chosen for this study is based on Eneco residential rates [46]. Eneco tariff is based on time-of-use (TOU) prices with peak and off-peak rates as shown in Table 5.4. Based on the data provided, the total electricity bill (κ_{elec}) can be computed based on the following:

Table 5.4: Netherlands Eneco Electricity tariffs

Tariff Type	Symbol	Time (hours)	Value (€/kWh)
Peak	c_{p}	9 - 20	0.2202
Off-peak	c_{off}	0-9, 20-24	0.2062
Feed-in	c_{fed}	0-24	0.092

$$\kappa_{\text{elec}} = \kappa_{\text{peak}} + \kappa_{\text{off-peak}} \tag{5.24}$$

$$\begin{aligned} \kappa_{\text{peak}} &= E_{\text{net,p}}\, c_{\text{p}} \quad \text{if} \quad E_{\text{net,p}} > 0 \\ &= E_{\text{net,p}}\, c_{\text{fed}} \quad \text{if} \quad E_{\text{net,p}} < 0 \end{aligned} \tag{5.25}$$

$$\begin{aligned} \kappa_{\text{off-peak}} &= E_{\text{net,off}}\, c_{\text{off}} \quad \text{if} \quad E_{\text{net,off}} > 0 \\ &= E_{\text{net,off}}\, c_{\text{fed}} \quad \text{if} \quad E_{\text{net,off}} < 0 \end{aligned} \tag{5.26}$$

where $E_{\text{net,i}}$ is the net energy exchanged between the grid and the house for the period i={p,off}:

$$E_{\text{net,i}} = E_{\text{grid-drawn,i}} - E_{\text{grid-fed,i}} \tag{5.27}$$

Texas tariff

The electricity tariff system for Texas considered in this study is based on Austin energy residential rates [47]. Austin Energy has a five-tier rate structure that incentivises customers on lowering their electric usage resulting in lower bills. Details of the electricity bill are presented in Table 5.5.

Based on the rate structure, the annual electricity bill of a household in Austin, Texas, is computed using the following equation:

$$\kappa_{\text{elec}} = c_{\text{fixed}} + E_{\text{total}} c_{\text{rc}} + E_{\text{sum}}\, c_{\text{psa,s}} + E_{\text{win}}\, c_{\text{psa,w}} + \sum_{i=1}^{5} E_{\text{tier,i}}\, c_{\text{tier,i}} - E_{\text{fed}}\, c_{\text{fed}} \tag{5.28}$$

where E_{total} is the total energy exchanged with the grid (drawn and fed), E_{sum} and E_{win} are the energy exchanged with the grid during the summer and the winter months. $E_{\text{tier,i}}$ for i =1-5 are obtained from the net drawn energy from the grid. E_{fed} is the net energy fed into the grid.

The tariff equation (5.28) shows that self-consumption by consumers is encouraged as the electricity tariff increases sharply between tiers. Additionally, consumers are encouraged to be producers and the Value of Solar (VOS) tariff. Austin Energy credits solar customers for the solar energy produced by their on-site solar energy system. However, it must be noted that the regulatory charge and the power supply adjustment charges discourage consumers from being dependent on the grid in terms of both drawing and feeding in power. In conclusion, multiple objectives like self-consumption of energy autonomy,

Table 5.5: Austin Energy Electricity Tariff Structure

Type	Bill Components	Symbol	$/kWh
Administrative Charge	Regulatory charge	c_{rc}	0.013
	Customer charge ($/month)	c_{fixed}	10
Energy charge	Tier 1: 0-500 kWh	$c_{tier,1}$	0.028
	Tier 2: 501-1000 kWh	$c_{tier,2}$	0.058
	Tier 3: 1001-1500 kWh	$c_{tier,3}$	0.078
	Tier 4: 1501-2500 kWh	$c_{tier,4}$	0.093
	Tier 5: >2500 kWh	$c_{tier,5}$	0.11
Power supply adjustment	Summer	$c_{psa,s}$	0.029
	Winter	$c_{psa,w}$	0.031
Feed-in tariff	Value of Solar (VOS)	c_{fed}	0.097

peak shaving or power autonomy need to be considered while optimally sizing PV and battery systems to lower electricity bills in the Austin Energy tariff structure.

5.2.5 Figure of merits (FoMs)

A detailed description of the modelling methodology of the technical and economic aspects of the PV-battery system integrated nanogrid is presented in the previous section. However, to optimally size the PV system, battery storage and the converters, specific performance metrics or figure of merits (FoMs) need to be defined to evaluate and differentiate between designs objectively. To that end, the following four FoMs are introduced:

Energy autonomy factor (α): The grid energy autonomy factor is a metric to measure self-sufficiency or energy independence of the nanogrid design. It is calculated as:

$$\gamma = \frac{E_{load} - E_{grid,buy}}{E_{load}} \times 100 \quad (\%) \tag{5.29}$$

Power autonomy (ρ): Power autonomy factor is a metric to quantify the power independence of the nanogrid from the utility grid. It is computed as the following:

$$\rho = \left(1 - \frac{1}{N}\sum_{i=1}^{N}\frac{|P_{grid,i}|}{|P_{load,i}|}\right) \times 100 \quad (\%) \tag{5.30}$$

where N depends on the resolution of the power profiles used. In this study, 1 min resolution is chosen.

Therefore, to compute the power autonomy factor for an annual load profile, N is = $24 \times 60 \times 365$. As the energy autonomy factor (α) measures the energy independence of the nanogrid, the power autonomy factor (ρ) measures the power independence, which includes both drawn and fed power. For example, the Texas electricity bill, as shown in equation (5.28), incentivises customers to regulate their peak by charging the regulatory and the power supply adjustment costs. However, in the Netherlands

tariff structure, the customer is encouraged to be energy independent and not necessarily power independent.

Lifetime capital cost (κ_{total}): The capital cost of the entire system is an economic metric to quantify the total lifetime cost of the system, which includes the initial investment cost, maintenance, and the replacement costs during the system lifetime [48]. Detailed modelling of the capital cost is already shown in equation (5.20).

Simple payback period (T_{PB}): The simple payback period is a metric to measure the economic viability of the PV-battery based system [43, 49]. It is defined as the number of years needed to pay back the capital cost with the savings related to electricity bill (R_{savings}): the following four FoMs are introduced:

Energy autonomy factor (α): The grid energy autonomy factor is a metric to measure self-sufficiency or energy independence of the nanogrid design. It is calculated as:

$$T_{\text{PB}}\ (\text{year}) = \frac{\kappa_{\text{total}}}{R_{\text{savings}}} = \frac{\kappa_{\text{total}}}{\kappa_{\text{elec,o}} - \kappa_{\text{elec,pv-batt}}} \tag{5.31}$$

where $\kappa_{\text{elec,o}}$ and $\kappa_{\text{elec,pv-batt}}$ are the annual electricity bills without and with integrated pv-battery system in the house.

The choice of performance metrics is motivated to facilitate both the end-users and the distribution system operators (DSOs). Economic metrics like lifetime system cost and the simple payback period are useful to end-users to analyze the cost-effectiveness of the solutions. On the other hand, fundamental technical metrics like energy autonomy and power autonomy can be utilized by DSOs to design tariff schemes to incentivize users to achieve their higher system-level goals like reducing the operating costs, delay expensive grid upgrades [7], and solving network congestion [50, 51]. This concludes the techno-economical modelling of the PV-battery based nanogrid. Based on the model metrics, four FoMs are identified, which will be used for the optimization problem formulation.

5.3 Multi-objective optimization framework

A multi-objective optimization framework is developed in this section to optimally size the PV system, the grid converter, and the battery of a nanogrid. It utilizes the techno-economical model developed in the previous section. Initially, the optimization targets and variables are described, followed by a discussion on the system analysis flowchart. In the final part of this study, the developed multi-objective optimization framework is utilized to optimally size the PV-battery for a nanogrid in different operational scenarios. The results obtained are presented and analyzed in detail in the next section.

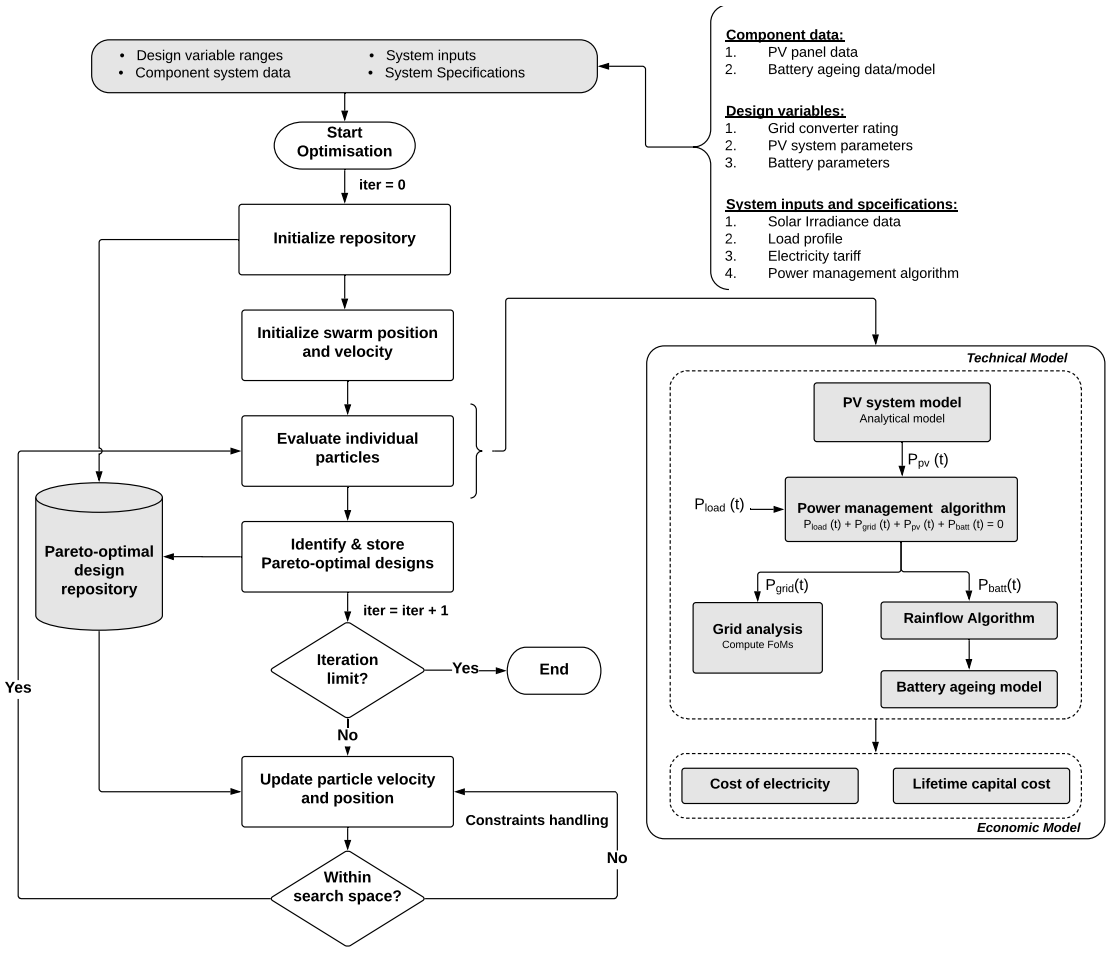

Figure 5.9: Flowchart of the proposed main multi-objective optimization routine for PV-battery sizing for nanogrids. The routine calculates and identifies the Pareto-optimal designs as a combination of the optimization design variables, which include the PV system parameters, battery management parameter, and grid converter ratings. The system analysis for individual designs evaluates the optimization targets based on the swarm algorithm-generated designs and feeds it back to the optimization routine to update the Pareto-optimal design repository.

5.3.1 Optimization targets and variables

Based on the FoMs introduced in the modelling section, the targets of the optimization are:

1. Maximize energy autonomy factor (α)
2. Maximize power autonomy factor (ρ)
3. Minimize lifetime capital cost (κ_{total})
4. Minimize simple payback period (T_{PB})

The objectives mentioned above are selected strategically to ensure that the optimization progresses towards designs with acceptable economic and technical performances.

Table 5.6 presents the optimization variables and their range. The optimization variables are mainly categorized into three groups: battery variables, PV system variables and grid converter variables. C_{rate} is chosen as an independent optimization variable which decides the rated power of the battery $P_{\text{batt,r}}$ based on the battery capacity E_{cap}. Specific constraints are put on the optimization solution space to ensure feasible designs. In the next part, the multi-objective optimization algorithm and sizing methodology are discussed in detail.

5.3.2 Optimization algorithm and methodology

Particle swarm optimization (PSO) algorithm is used for optimizing the proposed PV-battery sizing problem. PSO is an evolutionary gradient-free algorithm inspired by the movement of birds or insects in a swarm which potentially requires fewer function calls [52]. However, PSO is a single-objective optimization algorithm. To make it suitable for multi-objective optimization problems, the concept of Pareto dominance is combined [53] to generate non-dominated solutions or Pareto-optimal solutions, which results in Pareto fronts. A repository is used to store the Pareto-optimal solutions updated at the end of each iteration. Figure 5.9 presents the multi-objective optimization routine in a flowchart depicting the inputs, outputs, and system analysis of the PV-battery optimal sizing problem.

Table 5.6: Optimization variables and their range

Component	Variable	Symbol	Unit	Range		
				Li-ion	Pb-acid	VRFB
Battery System	Battery capacity	E_{cap}	kWh	1-30	1-30	1-30
	C-rate of the battery	C_{rate}	-	0.1-1	0.1-1	-
	Minimum SoC	SoC_{min}	(%)	0-30	0-30	-
	Depth of discharge	DoD	(%)	20-100	20-100	-
	Rated battery power	$P_{\text{batt,r}}$ [1]	kW	-	-	0.1-10
PV System	Azimuth angle	A_{z}	$^{\text{o}}$	100-300	100-300	100-300
	Rated pv power	$P_{\text{pv,r}}$	kW	0.3-15	0.3-15	0.3-15
Grid converter	Rated power	$P_{\text{grid,r}}$	kW	0-10	0-10	0-10

Thirty particles or designs per iteration and two-hundred iterations are evaluated to generate a stable Pareto front between two conflicting objectives. MATLAB is used to compute all the analytical equations presented in the previous section to model the performance parameters or figure of merits (FoMs) of the nanogrid design. The time required to evaluate a complete design varies between 15 s - 30 s[2]. In this paper, an approach based on placing particles on the border of the search space using a combination of variable clipping and reflecting [52]. The optimization results for two case studies (Netherlands and US) are discussed in the next section.

5.4 Optimization results I: effect of meteorology

The MOO framework developed in the previous section is utilised to optimally size the PV-battery-grid converter system in both the Netherlands and the US residential case studies. Figure 5.10 shows the real-life load profiles used for the analysis. The data for the NL residential load profile is obtained from a Dutch DSO company, and the US profile is obtained from Pecanstreet online database [54]. The load profiles of both the households at different days of the year are shown in Figure 5.10. Table 5.7 presents the details regarding the selected household load profiles.

It must be noted that the PV-battery sizing results obtained from the MOO framework for the two case studies are particular solutions for the specific combination of the load profile, solar irradiance profile, battery technology, power management strategy, and electricity tariff structure. Altering any of the above aspects will lead to different conclusions on the PV-battery sizing problem.

The optimization returns a 4-D Pareto optimal front. A detailed analysis is conducted in three steps to aid visualization and insight into the results. First, higher-level results are analyzed using sub-fronts of two targets. At a second level, complete fronts are shown to aid the explanation of underlying trends.

[2]Intel Xeon CPU E5-1620 v2 @ 3.70 GHz, 16 GB RAM.

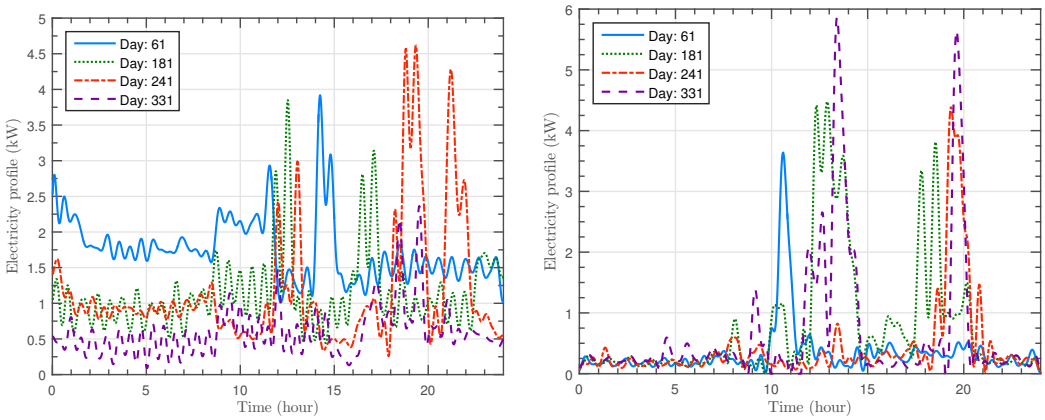

Figure 5.10: (a) NL house daily load profile for four days of the year with maximum load $P_{\text{load,max}}$ = 7 kW, , (b) Texas, US house daily load profile for four days of the year with maximum load$P_{\text{load,max}}$ = 9.8 kW.

Table 5.7: Load profile details

Description	Symbol	Units	Load profile	
			NL	US
Energy consumption per day	E_{daily}	kWh	18	17
Peak power annual	$P_{\text{load,max}}$	kW	7	9.8
Annual cost of electricity	$\kappa_{\text{elec,o}}$	$	1630	840

Finally, two optimal designs are selected and analyzed to verify the efficacy of the optimization process. Figure 5.11 shows the side views of the 4D Pareto optimal front, which highlight the trade-offs between lifetime system cost, energy autonomy, power autonomy, and payback period. Individual 2D Pareto fronts are discussed in the following:

Pareto Front Analysis

$\alpha - \kappa_{total}$ *Pareto front:* In the Texas load profile, it is evident from the fronts shown in Figure 5.11 that full energy autonomy is achievable after significant capital investment. However, in the NL residential profile, it isn't easy to achieve full energy autonomy, which asymptotes around 80%. It can be explained due to the low solar potential combined with the temporal mismatch between the yearly solar generation profile (Figure 5.12a) and daily energy usage profile (Figure 5.12b) of the Netherlands. Therefore, to achieve full energy autonomy in the case of NL load profiles, battery-based storage is not sufficient and seasonal storage is required.

$\rho - \kappa_{total}$ *Pareto front:* Figure 5.11b shows that full power autonomy is hard to achieve in both NL and US case studies with maximum possible values of 60% and 90% respectively. Additionally, power autonomy in the US case study decreases after 100% energy autonomy is achieved. The decreasing power autonomy is due to feeding more power into the grid than the actual in-house load power demand, leading to even lower electric bills.

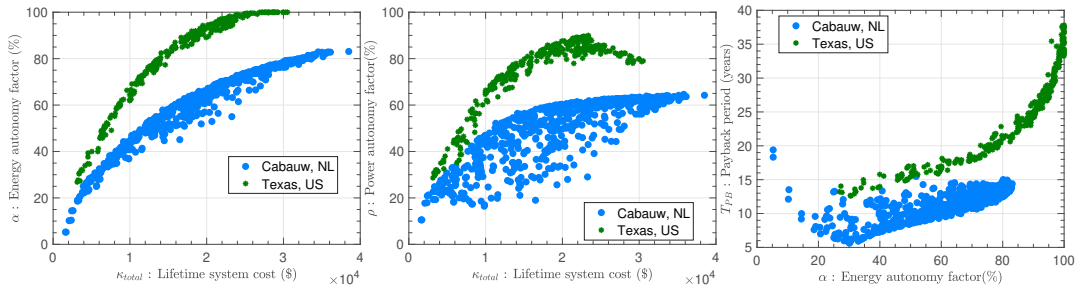

(a) (b) (c)

Figure 5.11: Results of multi-objective optimization for PV-battery sizing with NL and US houseload profile: (a) $\alpha - \kappa_{\text{total}}$: pareto fronts of trade off between energy autonomy factor and lifetime system cost, (b) $\rho - \kappa_{\text{total}}$: pareto fronts of trade off between power autonomy and lifetime system cost, and (c) $T_{\text{PB}} - \alpha$: pareto-fronts of simple payback period and energy autonomy factor.

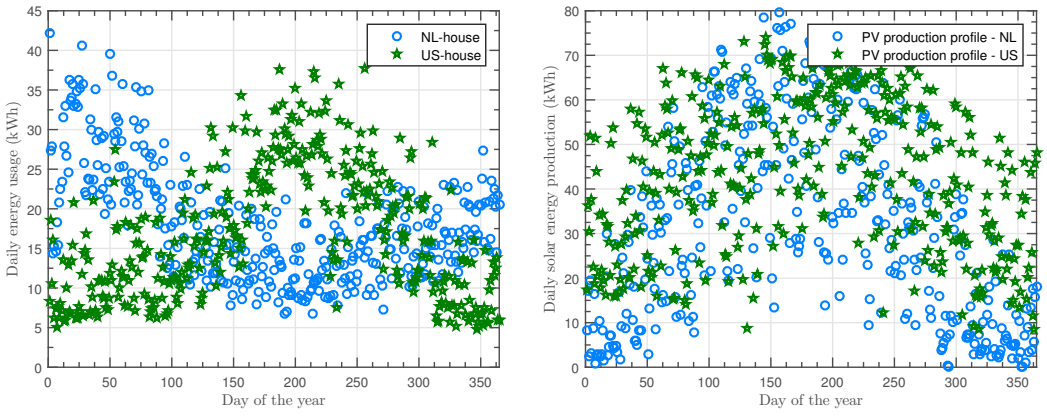

(a) (b)

Figure 5.12: (a) Annual daily energy usage profile for the NL with a daily average of 18 kWh and US load profile with a daily average of 17 kWh, (b) comparison of solar energy production throughout the year in Cabauw, Netherlands and Austin, Texas for a 5 kW PV system designed for maximum annual solar output.

$T_{PB} - \alpha$ *Pareto front:* The trade-off between simple payback period and energy autonomy is presented in Figure 5.11c. Previously it is shown that the US-based PV-battery system performs much better than the NL system in terms of both power autonomy and energy autonomy for the same capital investment. However, the NL based PV-battery system performs significantly better in the metric of simple payback period (T_{PB}) for certain energy autonomy. It can be explained due to the following reasons: (a) the annual electricity bill for the NL load profile without any PV and battery is 1630 $ compared to 840 $ in case of the US Austin load profile leading to higher savings potential for the NL case is much higher and therefore leads to lower payback period, and (b) the NL electricity tariff heavily incentivizes the end-user to be energy autonomous by installing PV with battery storage compared to the Austin tariff. This result underlines the importance of incorporating the cost of the electricity model in the optimization problem.

5.4.1 PV-battery system sizing guidelines

Underlying trends regarding the battery system design, PV system design and sizing are analysed in this section. Figure 5.13 presents the maximum allowable depth of discharge (DoD) of the Li-ion battery system of the optimised designs. The maximum allowable DoD of the Li-ion battery system increases with the increase of the battery capacity for both NL and US. Based on that, it is concluded that for optimal performance of a Li-ion based nanogrid, one should select a proper DoD range depending on the battery's size. For these particular case studies, a smaller capacity battery (≤5 kWh) has an optimal maximum DoD of 40% - 70%. The optimal maximum DoD is 65% - 90% for battery capacities ranging from 10 kWh to 20 kWh. 100% DoD of the battery can be utilised for battery sizes bigger than 20 kWh when the capacity fading due to daily cycles is insignificant compared to this particular application's nominal battery capacity.

Section 5.2.1 presented the potential of changing the azimuth angle A_{m} to improve the temporal match

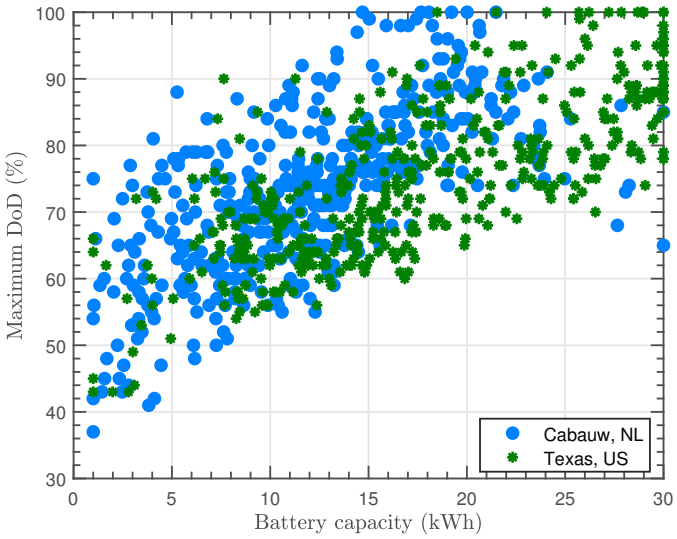

Figure 5.13: Maximum allowable DoD vs the battery capacity of the optimal Pareto system designs.

between the PV generation profile and the household profile. To that end, A_{m} was considered to be a design variable in the optimization framework (Table 5.6). Figure 5.14a and 5.14b presents the range of A_{m} for the optimal designs for the NL and US case studies respectively. In the case of the NL designs, the optimal range is between 180^o - 220^o whereas for the case of Austin, US, the optimal range is 240^o - 300^o. It is interesting to highlight that the optimal designs have significantly different A_{m} from the maximum energy generation $A_{\mathrm{m,max}}$ which is 185^o for NL and 175^o for the US case (Figure 5.2). A new metric based on the Pearson correlation coefficient is defined to quantify the temporal match between the PV power profile and load profile:

$$\gamma(P_{\mathrm{pv}}, P_{\mathrm{load}}) = \frac{1}{N-1}\sum_{i=1}^{N}\left(\frac{P_{\mathrm{pv,i}}-\mu_{\mathrm{pv}}}{\sigma_{\mathrm{pv}}}\right)\left(\frac{P_{\mathrm{load,i}}-\mu_{\mathrm{load}}}{\sigma_{\mathrm{load}}}\right) \tag{5.32}$$

where P_{j}, μ_{j}, and σ_{j} are the annual power profile, mean and the standard deviation of the power profile for the j^{th} system with j = {pv, load}. The correlation co-efficient γ represents the degree of temporal match between the PV profile and the load profile. γ ranges from 1 (complete temporal match) to -1 (complete temporal mismatch). Figure 5.14c shows the variation of correlation coefficient γ with the choice of azimuth angle for both the NL and the US case studies. It is evident from Figure 5.14 that the optimal choice of azimuth angle A_{m} for PV-battery system design is the one that results in the maximum temporal match between the PV profile and the load profile. Additionally, the correlation coefficient γ for the case of NL load profile and PV profile is almost ten times lower than the case of the US profile. It is expected since there is a significant mismatch between the annual solar profile and load profile for the NL case study. Figure 5.12a and Figure 5.12b show that there are high load demand and low solar generation during winter coupled with comparatively lower load demand and higher solar generation during the summer. However, in the US case study, the seasonal load demand variations match the seasonal PV profile variations leading to high correlation coefficient values γ.

Finally, it is important to derive design thumb rules to select PV system size and battery capacity to

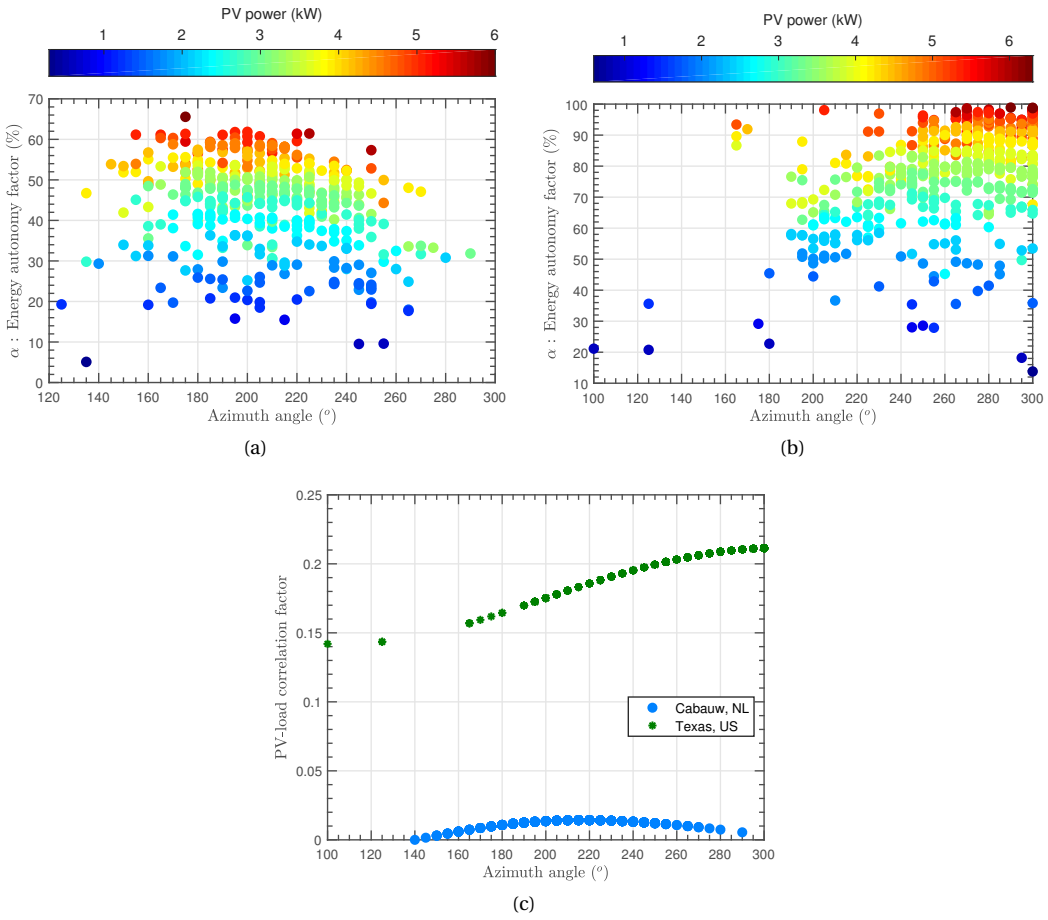

Figure 5.14: Effect of PV module azimuth angle on: (a) energy autonomy for different PV power for Cabauw, NL, (b) energy autonomy for different PV power for Texas, US, (c) correlation coefficient between annual pv generation profile and load profile for the case of NL and US.

achieve optimal performance for a certain capital investment. In this considered PV-battery system for grid-connected nanogrids there are four unknown variables: $P_{\text{pv,r}}$, $P_{\text{batt,r}}$, $P_{\text{grid,r}}$, and E_{cap}. For the relative sizing of PV power and battery capacity, a metric called storage hours (S_{h}) is defined as following:

$$S_{\text{h}} = \frac{E_{\text{cap}}}{P_{\text{pv,r}}} \tag{5.33}$$

Figure 5.15a shows the effect of storage hours on the energy autonomy of the PV-battery based nanogrid for the NL case study. It can be seen that the optimal range of S_{h} is 2 to 4, which also results in the minimum annual cost of electricity as shown in Figure 5.15b. Applying similar analysis to the case of US as shown in Figure 5.16a and 5.16b, the optimal range of S_{h} turns out to be 4 to 6. Since Texas, US has higher solar potential ($\approx$ 35%) compared to Cabauw, NL, it is intuitive that a bigger sized battery is needed to harness the excess solar potential properly. This ratio can be used as a thumb rule for sizing

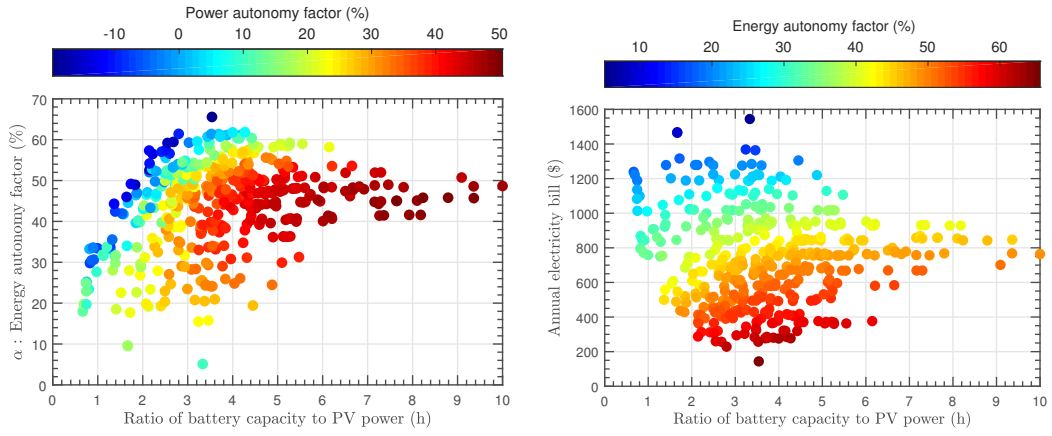

Figure 5.15: Results of multi-objective optimization for PV-battery sizing with NL and US houseload profile: (a) variation of energy autonomy factor with storage hours (S_h) or ratio of battery capacity to rated pv power in case of NL, (b) variation of annual cost of electricity with S_h in case of NL.

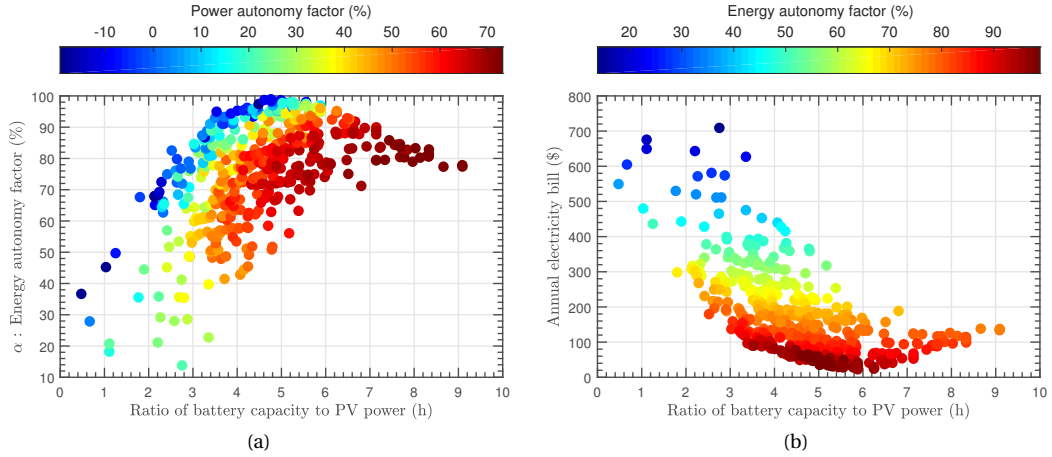

Figure 5.16: Results of multi-objective optimization for PV-battery sizing with NL and US houseload profile: (a) variation of energy autonomy factor with S_h in case of US, and (b) variation of annual cost of electricity with S_h in case of US.

PV and battery system for a nanogrid in the Netherlands and the US, Texas to ensure high performance for a fixed capital cost.

To optimally size the different converters associated with the grid, PV, and the storage, two additional

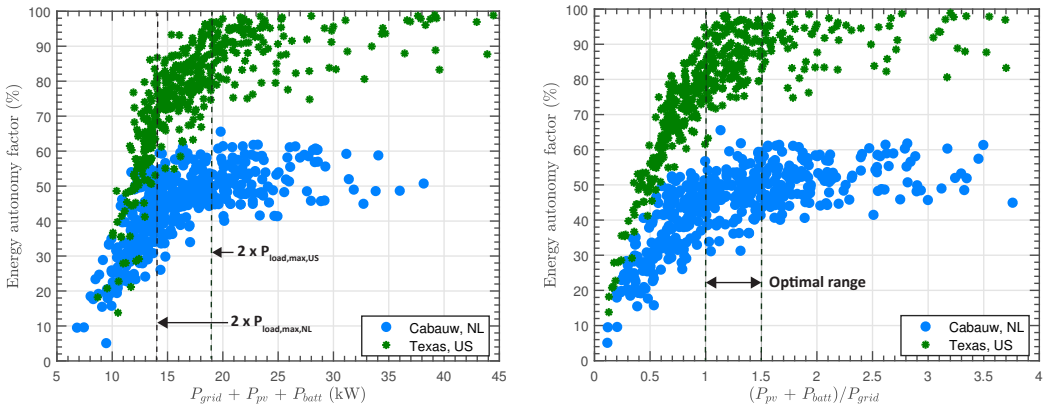

Figure 5.17: Variation of energy autonomy factor with (a) sum of all the source converter ratings $P_{\text{sum,total}}$, (b) ratio of the sum of pv-battery converter ratings to the grid converter rating P_{ratio}.

metrics or equations are introduced:

$$P_{\text{sum,total}} = P_{\text{grid,r}} + P_{\text{pv,r}} + P_{\text{batt,r}} \tag{5.34}$$

$$P_{\text{ratio}} = \frac{(P_{\text{pv,r}} + P_{\text{batt,r}})}{P_{\text{grid,r}}} \tag{5.35}$$

where $P_{\text{sum,total}}$ represents the sum of all the source/storage converter ratings, and P_{ratio} is the ratio of the sum of PV-battery converters to the grid converter rating. Figure 5.17 presents the effect of the two metrics mentioned above on the energy autonomy of the nanogrid optimal designs for both the case studies. In the case of the NL house, a $P_{\text{sum,total}}$ of 15 kW or above will result in high energy autonomy. Similarly, a $P_{\text{sum,total}}$ of 20 kW or above is required for high energy autonomy for the Austin, US house. Interestingly, the maximum load power in NL and US is 7 kW and 9.8 kW, respectively, which are approximately half of the thresholds required for high energy autonomy. Similarly, from analysing Figure 5.17b, the optimal converter ratio factor P_{ratio} lies somewhere around 1 - 1.5 for both the case studies of NL and US. As for sizing guidelines, one can select a certain rated power for the PV system depending on the available area for PV installation and use equations (5.33), (5.34), (5.35) as thumb rules to optimally size the battery capacity, and the converter sizes for a grid-connected nanogrid. Table 5.8 summarizes all the sizing equations derived from analyzing the data obtained from the optimization procedure.

Table 5.8: System sizing thumb rules

Sizing equation	**Cabauw, NL**	**Austin, US**
S_{h}	2 - 4	4 - 6
$P_{\text{grid,r}} + P_{\text{pv,r}} + P_{\text{batt,r}}$	$\geq 2P_{\text{load,max}}$	$\geq 2P_{\text{load,max}}$
$\frac{(P_{\text{pv,r}} + P_{\text{batt,r}})}{P_{\text{grid,r}}}$	1 - 1.5	1 - 1.5

5.4.2 Analysis of selected optimal designs

Higher-level design sizing trends are obtained in the previous section by analyzing the optimization results. To highlight the sizing optimization procedure's efficacy, we have selected two Pareto optimal nanogrid designs for more in-depth analysis. The designs are chosen with the same total lifetime cost of 13,000 $ to ensure a fair comparison.

Table 5.9 presents the critical design and performance metrics of the two selected design cases. In terms of PV-battery system sizing, the NL nanogrid has a higher power PV system and lower battery capacity than the US counterpart. Due to higher solar potential, the US nanogrid needs a slightly bigger battery to store the excess solar energy. Both the nanogrid designs under-utilize the battery capacity by selecting a maximum allowable DoD of 63 % (NL) and 70 % (US) to extend the lithium-ion battery lifetime.

In performance factors like energy autonomy and power autonomy, the NL nanogrid lags behind the US nanogrid. Still, the NL nanogrid performs much better economically with a simple payback period of almost half that of the US nanogrid design. This is mainly due to two reasons. First, the US house's annual cost of electricity is significantly lower than the NL house (see Table 5.7) for almost similar energy consumption, thereby limiting the savings margin. Second, the Dutch electricity provider incentivises high energy autonomy with a net-metering based tariff system. In contrast, the US tariff system incentivises high power autonomy, a comparatively more difficult metric to achieve. Figure 5.18 presents the annual grid power profiles of the two selected case studies. It is evident from the profile (Figure 5.18a) that the NL house nanogrid interacts heavily with the utility grid throughout the year, which results in weak power autonomy of 15%. During winter, when the solar generation is low and the load requirement is high, it depends solely on the grid to supply the load. However, during the summer days, when the load is comparatively lighter and solar power is higher, the nanogrid consistently dumps the excess solar energy to the utility grid. Therefore, the NL nanogrid is highly energy-positive during the winter days and highly energy-negative during the summer days, which

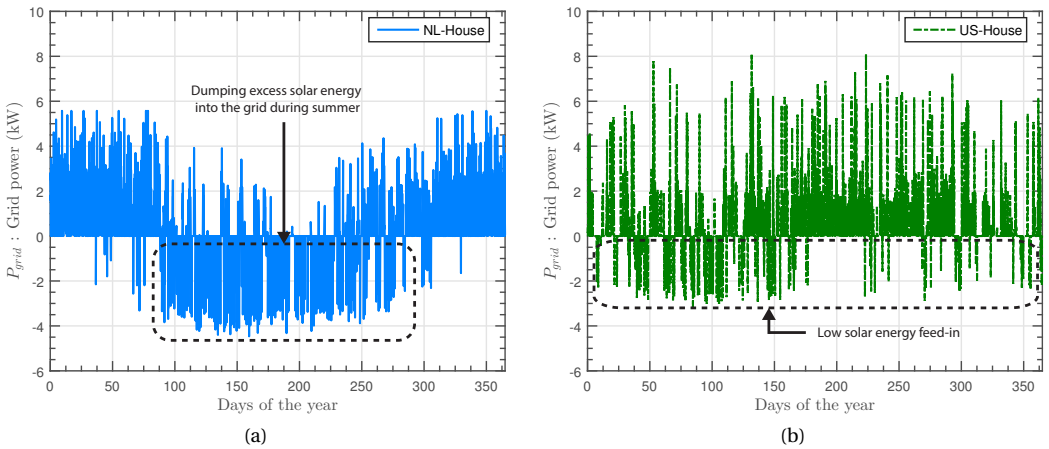

Figure 5.18: Annual profile of the power exchange of nanogrids with the utility grid (P_{grid}): (a) NL house nanogrid, (b) US house nanogrid.

Table 5.9: Results of selected optimized nanogrid designs

Performance Group	Performance Metrics	Symbol	Unit	Cabauw, NL	Texas, US
Design parameters	Rated PV power	$P_{\text{pv,r}}$	kW	4.2	3.3
	Battery capacity	E_{cap}	kWh	13	15
	Battery rated power	$P_{\text{batt,r}}$	kW	3.8	4.8
	Grid converter rating	$P_{\text{grid,r}}$	kW	5.6	8.1
	Azimuth angle	A_{m}	^{o}	205	250
	Battery DoD max	DoD	%	63	70
Sizing parameters	Storage hours	S_{h}	h	3.1	4.5
	Total converter ratings	$P_{\text{sum,total}}$	kW	13.6	16.2
	Converter ratings ratio	P_{ratio}	-	1.4	1
Microgrid Performance	Energy autonomy	α	%	54	74
	Power autonomy	ρ	%	15	57
	Payback period	T_{PB}	years	11	20
	Electricity bill	κ_{elec}	$	436	178
	PV Cost	κ_{pv}	$	5460	4290
	Battery cost	κ_{batt}	$	6520	7400
	Total lifetime cost	κ_{total}	$	13000	13000

eventually balances out due to the electricity tariff's sole dependence on energy autonomy rather than power autonomy. This leads to a low simple payback period for the NL nanogrid. However, unlike the NL nanogrid, the US nanogrid has weaker interaction with the grid as the Texas electricity tariff incentivises power autonomy, which leads to less dumping of solar power in the grid. Therefore, it is economically more viable to install PV and battery systems for the NL case study than the US case study. However, the solar potential of Texas, US is much higher than Cabauw, NL.

5.5 Optimization results II: comparison of battery technologies

The MOO framework developed in Section 5.3 is used to optimally design the PV-battery-grid system for the Netherlands load profile and compare the performance of the battery technologies. Figure 5.19 shows the side views of the 4D Pareto optimal front, highlighting the trade-offs between lifetime system cost, energy autonomy, and power autonomy and simple payback period. And Figure 5.19a and 5.19b show the energy autonomy factor vs lifetime system cost Pareto front and power autonomy factor vs lifetime system cost Pareto front for different battery technologies for the NL household profile and solar generation profile.

Pareto Front Analysis

$\alpha - \kappa_{total}$ *Pareto front:* Figure 5.19a presents the Pareto front showing the trade-off between energy autonomy and lifetime capital cost for the battery technologies. Lithium-ion performs the best in this metric, followed closely by Vanadium redox flow battery (VRFB). Lithium-ion performs much better at lower capital cost (less than 10,000 $) than VRFB. However, for designs with capital cost higher than 20,000 $, VRFB performs similar to Li-ion based PV-battery system. The performance of lead-acid is the

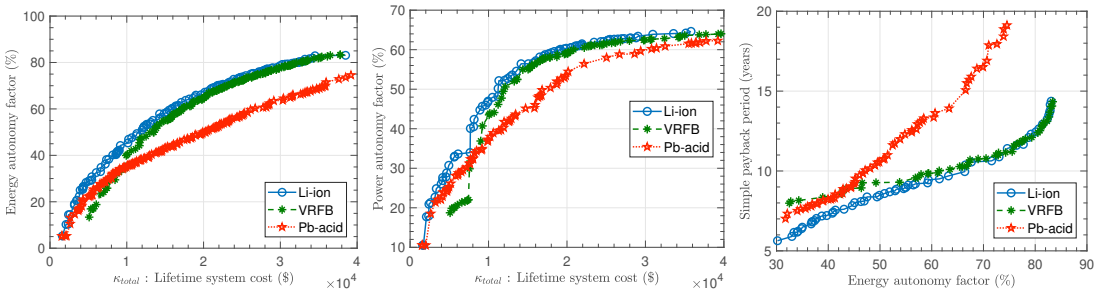

(a) (b) (c)

Figure 5.19: Results of multi-objective optimization for PV-battery sizing with NL houseload profile presenting Pareto fronts of trade off between: (a) $\alpha - \kappa_{\text{total}}$: energy autonomy vs lifetime cost, (b) $\rho - \kappa_{\text{total}}$: power autonomy vs lifetime cost, and (c) $T_{\text{PB}} - \alpha$: simple payback period vs energy autonomy.

worst among the selected battery technologies.

$\rho - \kappa_{total}$ *Pareto front:* The power autonomy and lifetime capital cost Pareto front is shown in Figure 5.19b. The relative performance of the battery technologies in this front is similar to the energy autonomy - lifetime cost Pareto front. The Li-ion based system performs the best closely followed by the VRFB based system. The performance of the lead-acid based system is still the worst among the battery technologies. Still, the difference between the performance is much lower, especially at the high capital cost.

$T_{PB} - \alpha$ *Pareto front:* The simple payback period - energy autonomy factor Pareto front is shown in Figure 5.11c for the battery technologies. For lower energy autonomy ($\leq$ 50 %), Li-ion based system performs the best with low simple payback periods while VRFB suffers from high initial investment cost. However, at high energy autonomy, VRFB based systems have similar payback periods as Li-ion based systems. However, from an economic perspective, lead-acid based systems is not an optimal choice for residential applications.

Based on the individual 2D Pareto fronts, a more in-depth analysis of the battery lifetime and optimal sizing guidelines for different battery technologies are discussed in the following sections.

5.5.1 Effect on battery lifetime

Among the battery technologies considered in this study, the lithium-ion battery-based PV household system performs the best closely followed by Vanadium redox flow battery (VRFB) in all the metrics. The lead-acid battery-based system performs poorly compared to VRFB and lithium-ion battery-based system due to a high number of battery replacements required during the system lifetime, as shown in Figure 5.20a. Thus, the high number of replacements in the lead-acid-based PV-battery system leads to the system's overall higher lifetime cost and, consequently, more extended simple payback period. VRFB based PV-battery system performs well due to its high inherent lifetime despite significant initial investment cost. Its performance is close to Li-ion battery-based system for bigger systems where the replacement cost of Li-ion batteries bridges the gap between the two systems.

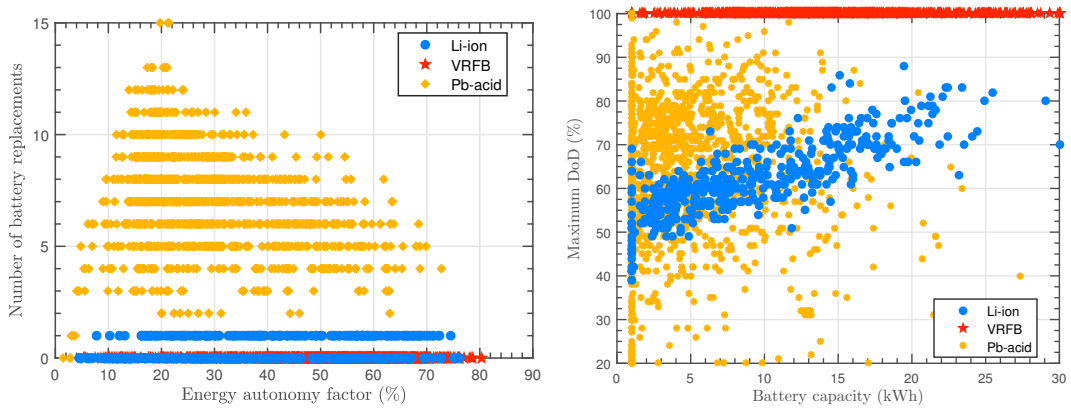

(a) (b)

Figure 5.20: (a) Number of battery replacements required for different battery technologies at different energy autonomy factor, (b) maximum depth of discharge (DoD) allowed by the optimized designs for different battery capacities.

5.5.2 Optimal PV-battery sizing guidelines

Based on the battery lifetime analysis, the optimal sizing for different battery technologies can be derived. The maximum allowable depth of discharge (DoD) was selected as a design variable during optimization to ensure a longer battery life for lithium-ion and lead-acid batteries. The variation of the maximum allowable DoD of the Pareto optimal designs with the battery capacity is shown in Figure 5.20b. Lithium-ion battery-based system prefers lower maximum DoDs to improve the lifetime of the battery as shown from Figure 5.20b. It is evident from the same figure that the maximum allowable DoD of the li-ion battery system increases with the battery capacity increase. In conclusion, the optimization results show that for optimal performance of a li-ion based household, one should select a proper DoD range depending on the battery's size. For a smaller capacity battery ($\leq$ 5 kWh), the optimal range of maximum DoD is 50% - 60%, whereas, for a bigger capacity battery ($\geq$ 10 kWh),

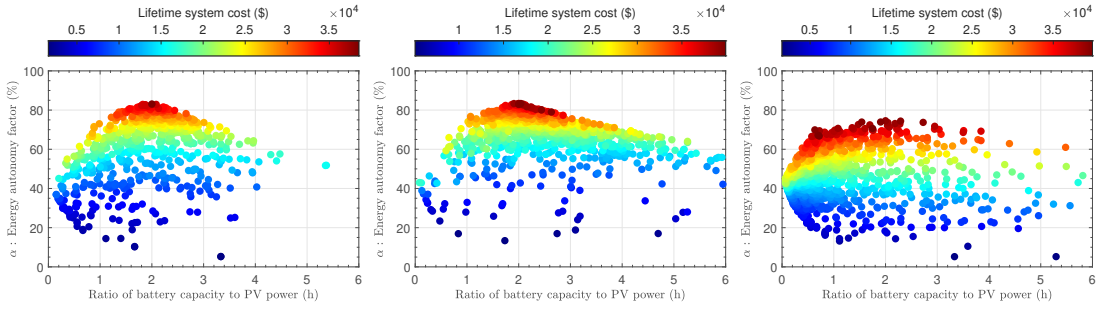

(a) (b) (c)

Figure 5.21: Results of multi-objective optimization for PV-battery sizing with NL houseload profile showing the variation of energy autonomy factor with storage hours (S_h) or ratio of battery capacity to rated pv power for: (a) lithium-ion based system, (b) vanadium redox flow (VRFB) based system, (c) lead-acid based system.

the optimal DoD range is 65% - 85%. It is interesting to point out that the optimization doesn't lead to a similar trend for the lead-acid battery-based system even though higher DoD results in lower battery life, similar to the Li-ion battery case. Due to the poor cycle lifetime behaviour of lead-acid batteries, it is economically more beneficial to select smaller capacity batteries (≤ 10 kWh) and replace them multiple times during the system lifetime than to go for bigger capacity batteries.

For the relative sizing of the PV-battery system, the storage-hour (S_h) metric, which is the ratio of the battery capacity to the rated PV power, is used here. The variation of energy autonomy with storage-hour for different battery technologies is presented in Figure 5.21. The optimal storage hour for lithium-ion battery and vanadium redox flow battery is around 2. However, for a lead-acid battery-based grid system, the optimal storage hour is approximately 1 - 1.5. Due to lower battery lifetimes, lead-acid based grid systems prefer lower battery capacity than Li-ion or VRFB batteries to reduce repeated battery replacement costs.

5.6 Conclusion

This chapter presents a multi-objective optimization (MOO) procedure to size the PV-battery-converter system for nanogrid applications. The MOO framework is applied to an optimal size PV-lithium-ion (Li-ion) battery-converter system for two residential case studies in Cabauw, Netherlands and Austin, US. An in-depth nanogrid model considering battery degradation for different battery technologies, PV design variables, and real-life electricity tariffs are coupled with the MOO framework to draw design guidelines for optimal system sizing. Some essential observations obtained from a detailed analysis of the optimization results are presented below:

1. To improve battery life of Li-ion battery system for household power profiles, it is recommended to select a low depth of discharge (DoD) (40%-70%) for smaller sized batteries (≤ 10 kWh). However, to improve battery capacity utilization, designers can select high DoD (60%-100%) for battery sizes above 15 kWh.
2. The local electricity tariffs in Cabauw, NL heavily incentivizes energy autonomy with significant feed-in tariffs leading to low payback periods for an initial investment. However, Austin electricity tariffs incentivize power autonomy by power-based tariffs, which lead to higher payback periods for an initial investment.
3. Solar potential of a location has a significant impact on the relative sizing of the battery capacity relative to the rated PV power. The optimal value of storage hour ($S_h = \frac{E_{cap}}{P_{pv,r}}$) for Cabauw is between 2 to 4, whereas for Austin it is between 4 to 6.
4. Optimal value of the azimuth angle (A_m) for the PV system is found to be the one that results in a maximum temporal match between the annual PV and load profile.
5. Thumb rules for optimal system sizing are derived to size the battery power rating, battery capacity, PV power rating, and the grid converter rating in equations in Table 5.8 for grid-connected nanogrid application.
6. Both technically and economically, Li-ion based PV-battery nanogrid performs the best with low payback periods. However, Vanadium redox flow battery based nanogrid performs close to Li-ion

in both metrics. Lead-acid based battery systems are not really suitable for PV-battery-based nanogrids to achieve high energy autonomy due to the high rate of battery degradation.

In conclusion, the presented multi-objective optimization process provides a platform to optimally size PV-battery systems during the initial design process taking into account many design variables and multiple objectives. For future work, this study can be extended to compare different battery technologies to select the most economical design. Additionally, the effect of intelligent power management algorithms with forecasting capability on the system sizing problem can be investigated with this framework.

References

[1] L. Pérez-Lombard, J. Ortiz, and C. Pout, "A review on buildings energy consumption information," *Energy and buildings*, vol. 40, no. 3, pp. 394–398, 2008.

[2] A. Dubey and S. Santoso, "Electric vehicle charging on residential distribution systems: Impacts and mitigations," *IEEE Access*, 2015.

[3] E. Veldman, M. Gibescu, H. Slootweg, and W. L. Kling, "Impact of electrification of residential heating on loading of distribution networks," in *PowerTech, 2011 IEEE Trondheim*, pp. 1–7, IEEE, 2011.

[4] A. Peacock and M. Newborough, "Controlling micro-chp systems to modulate electrical load profiles," *Energy*, vol. 32, no. 7, pp. 1093–1103, 2007.

[5] T. Beck, H. Kondziella, G. Huard, and T. Bruckner, "Assessing the influence of the temporal resolution of electrical load and pv generation profiles on self-consumption and sizing of pv-battery systems," *Applied energy*, vol. 173, pp. 331–342, 2016.

[6] E. Tervo, K. Agbim, F. DeAngelis, J. Hernandez, H. K. Kim, and A. Odukomaiya, "An economic analysis of residential photovoltaic systems with lithium ion battery storage in the united states," *Renewable and Sustainable Energy Reviews*, vol. 94, pp. 1057–1066, 2018.

[7] J. Tant, F. Geth, D. Six, P. Tant, and J. Driesen, "Multiobjective battery storage to improve pv integration in residential distribution grids," *IEEE Transactions on Sustainable Energy*, vol. 4, no. 1, pp. 182–191, 2013.

[8] W. L. Schram, I. Lampropoulos, and W. G. van Sark, "Photovoltaic systems coupled with batteries that are optimally sized for household self-consumption: Assessment of peak shaving potential," *Applied energy*, vol. 223, pp. 69–81, 2018.

[9] J. Moshövel, K.-P. Kairies, D. Magnor, M. Leuthold, M. Bost, S. Gährs, E. Szczechowicz, M. Cramer, and D. U. Sauer, "Analysis of the maximal possible grid relief from pv-peak-power impacts by using storage systems for increased self-consumption," *Applied Energy*, vol. 137, pp. 567–575, 2015.

[10] R. Atia and N. Yamada, "Sizing and analysis of renewable energy and battery systems in residential microgrids," *IEEE Transactions on Smart Grid*, vol. 7, no. 3, pp. 1204–1213, 2016.

[11] T. Dragičević, H. Pandžić, D. Škrlec, I. Kuzle, J. M. Guerrero, and D. S. Kirschen, "Capacity optimization of renewable energy sources and battery storage in an autonomous telecommunication facility," *IEEE Transactions on Sustainable Energy*, vol. 5, no. 4, pp. 1367–1378, 2014.

[12] S. Kahrobaee, S. Asgarpoor, and W. Qiao, "Optimum sizing of distributed generation and storage capacity in smart households," *IEEE Transactions on Smart Grid*, vol. 4, no. 4, pp. 1791–1801, 2013.

[13] M. Bortolini, M. Gamberi, and A. Graziani, "Technical and economic design of photovoltaic and battery energy storage system," *Energy Conversion and Management*, vol. 86, pp. 81–92, 2014.

[14] L. Xu, X. Ruan, C. Mao, B. Zhang, and Y. Luo, "An improved optimal sizing method for wind-solar-battery hybrid power system," *IEEE transactions on sustainable energy*, vol. 4, no. 3, 2013.

[15] G. C. Mouli, P. Bauer, and M. Zeman, "System design for a solar powered electric vehicle charging station for workplaces," *Applied Energy*, vol. 168, 2016.

[16] J. Vetter, P. Novák, M. Wagner, C. Veit, K.-C. Möller, J. Besenhard, M. Winter, M. Wohlfahrt-Mehrens, C. Vogler, and A. Hammouche, "Ageing mechanisms in lithium-ion batteries," *Journal of power sources*, vol. 147, no. 1, pp. 269–281, 2005.

[17] M. Broussely, S. Herreyre, P. Biensan, P. Kasztejna, K. Nechev, and R. Staniewicz, "Aging mechanism in li ion cells and calendar life predictions," *Journal of Power Sources*, vol. 97, pp. 13–21, 2001.

[18] M. O. Ramoni and H.-C. Zhang, "End-of-life (eol) issues and options for electric vehicle batteries," *Clean Technologies and Environmental Policy*, vol. 15, no. 6, pp. 881–891, 2013.

[19] K. L. Gering, S. V. Sazhin, D. K. Jamison, C. J. Michelbacher, B. Y. Liaw, M. Dubarry, and M. Cugnet, "Investigation of path dependence in commercial lithium-ion cells chosen for plug-in hybrid vehicle duty cycle protocols," *Journal of Power Sources*, vol. 196, no. 7, pp. 3395–3403, 2011.

[20] M. Broussely, P. Biensan, F. Bonhomme, P. Blanchard, S. Herreyre, K. Nechev, and R. Staniewicz, "Main aging mechanisms in li ion batteries," *Journal of power sources*, vol. 146, no. 1, pp. 90–96, 2005.

[21] S. B. Peterson, J. Apt, and J. Whitacre, "Lithium-ion battery cell degradation resulting from realistic vehicle and vehicle-to-grid utilization," *Journal of Power Sources*, vol. 195, no. 8, pp. 2385–2392, 2010.

[22] Y. Qi, H. Guo, L. G. Hector, and A. Timmons, "Threefold increase in the young's modulus of graphite negative electrode during lithium intercalation," *Journal of The Electrochemical Society*, vol. 157, no. 5, pp. A558–A566, 2010.

[23] A. Millner, "Modeling lithium ion battery degradation in electric vehicles," in *Innovative Technologies for an Efficient and Reliable Electricity Supply (CITRES), 2010 IEEE Conference on*, pp. 349–356, IEEE, 2010.

[24] J. Groot, "State-of-health estimation of li-ion batteries: Cycle life test methods," 2012.

[25] J. D. Dogger, B. Roossien, and F. D. Nieuwenhout, "Characterization of li-ion batteries for intelligent management of distributed grid-connected storage," *IEEE Transactions on Energy Conversion*, vol. 26, no. 1, pp. 256–263, 2011.

[26] L. Lam and P. Bauer, "Practical capacity fading model for li-ion battery cells in electric vehicles," *IEEE transactions on power electronics*, vol. 28, no. 12, pp. 5910–5918, 2013.

[27] P. Ramadass, B. Haran, R. White, and B. N. Popov, "Mathematical modeling of the capacity fade of li-ion cells," *Journal of Power Sources*, vol. 123, no. 2, pp. 230–240, 2003.

[28] E. Thomas, I. Bloom, J. Christophersen, and V. Battaglia, "Rate-based degradation modeling of lithium-ion cells," *Journal of Power Sources*, vol. 206, pp. 378–382, 2012.

[29] D. Andre, C. Appel, T. Soczka-Guth, and D. U. Sauer, "Advanced mathematical methods of soc and soh estimation for lithium-ion batteries," *Journal of Power Sources*, vol. 224, pp. 20–27, 2013.

[30] J. Weniger, T. Tjaden, and V. Quaschning, "Sizing of residential pv battery systems," *Energy Procedia*, vol. 46, pp. 78–87, 2014.

[31] J. Schiffer, D. U. Sauer, H. Bindner, T. Cronin, P. Lundsager, and R. Kaiser, "Model prediction for ranking lead-acid batteries according to expected lifetime in renewable energy systems and autonomous power-supply systems," *Journal of Power sources*, vol. 168, no. 1, pp. 66–78, 2007.

[32] H. Bindner, T. Cronin, P. Lundsager, J. F. Manwell, U. Abdulwahid, and I. Baring-Gould, "Lifetime modelling of lead acid batteries," *Benchmarking*, vol. 12, p. 82, 2005.

[33] D. Riccardo, L. Baumann, A. Damiano, and E. Boggasch, "A vanadium-redox-flow-battery model for evaluation of distributed storage implementation in residential energy systems," *IEEE Transactions on Energy Conversion*, vol. 30, no. 2, pp. 421–430, 2015.

[34] T. A. Nguyen, M. L. Crow, and A. C. Elmore, "Optimal sizing of a vanadium redox battery system for microgrid systems," *IEEE transactions on sustainable energy*, vol. 6, no. 3, pp. 729–737, 2015.

[35] X. Zhang, Y. Li, M. Skyllas-Kazacos, and J. Bao, "Optimal sizing of vanadium redox flow battery systems for residential applications based on battery electrochemical characteristics," *Energies*, vol. 9, no. 10, p. 857, 2016.

[36] M. Musallam and C. M. Johnson, "An efficient implementation of the rainflow counting algorithm for life consumption estimation," *IEEE Transactions on reliability*, vol. 61, no. 4, pp. 978–986, 2012.

[37] K. Bradbury, L. Pratson, and D. Patiño-Echeverri, "Economic viability of energy storage systems based on price arbitrage potential in real-time us electricity markets," *Applied Energy*, vol. 114, pp. 512–519, 2014.

[38] K.-H. Ahlert and C. Van Dinther, "Sensitivity analysis of the economic benefits from electricity storage at the end consumer level," in *PowerTech, 2009 IEEE Bucharest*, pp. 1–8, IEEE, 2009.

[39] W. Hu, Z. Chen, and B. Bak-Jensen, "Optimal operation strategy of battery energy storage system to real-time electricity price in denmark," in *Power and Energy Society General Meeting, 2010 IEEE*, pp. 1–7, IEEE, 2010.

[40] D. K. Maly and K.-S. Kwan, "Optimal battery energy storage system (bess) charge scheduling with dynamic programming," *IEE Proceedings-Science, Measurement and Technology*, vol. 142, no. 6, pp. 453–458, 1995.

[41] T. Huang and D. Liu, "Residential energy system control and management using adaptive dynamic programming," in *Neural Networks (IJCNN), The 2011 International Joint Conference on*, pp. 119–124, IEEE, 2011.

[42] T.-Y. Lee, "Operating schedule of battery energy storage system in a time-of-use rate industrial user with wind turbine generators: a multipass iteration particle swarm optimization approach," *IEEE Transactions on Energy Conversion*, vol. 22, no. 3, pp. 774–782, 2007.

[43] C. N. Truong, M. Naumann, R. C. Karl, M. Müller, A. Jossen, and H. C. Hesse, "Economics of residential photovoltaic battery systems in germany: The case of tesla's powerwall," *Batteries*, vol. 2, no. 2, p. 14, 2016.

[44] D. Akinyele, J. Belikov, and Y. Levron, "Battery storage technologies for electrical applications: Impact in stand-alone photovoltaic systems," *Energies*, vol. 10, no. 11, p. 1760, 2017.

[45] X. Luo, J. Wang, M. Dooner, and J. Clarke, "Overview of current development in electrical energy storage technologies and the application potential in power system operation," *Applied energy*, vol. 137, pp. 511–536, 2015.

[46] Eneco, "Residential electricity tariffs netherlands," *Available: https://www.eneco.nl/zonnepanelen/saldering/*.

[47] A. Energy, "Residential electricity tariffs texas," *Available: https://austinenergy.com/ae/residential/rates*.

[48] B. Zakeri and S. Syri, "Electrical energy storage systems: A comparative life cycle cost analysis," *Renewable and sustainable energy reviews*, vol. 42, pp. 569–596, 2015.

[49] J. Li, Z. Wu, S. Zhou, H. Fu, and X.-P. Zhang, "Aggregator service for pv and battery energy storage systems of residential building," *CSEE Journal of Power and Energy Systems*, vol. 1, no. 4, pp. 3–11, 2015.

[50] F. Shen, S. Huang, Q. Wu, S. Repo, Y. Xu, and J. Østergaard, "Comprehensive congestion management for distribution networks based on dynamic tariff, reconfiguration and re-profiling product," *IEEE Transactions on Smart Grid*, 2018.

[51] J. H. Yoon, R. Baldick, and A. Novoselac, "Dynamic demand response controller based on real-time retail price for residential buildings," *IEEE Transactions on Smart Grid*, vol. 5, no. 1, pp. 121–129, 2014.

[52] Y. Del Valle, G. K. Venayagamoorthy, S. Mohagheghi, J.-C. Hernandez, and R. G. Harley, "Particle swarm optimization: basic concepts, variants and applications in power systems," *IEEE Transactions on evolutionary computation*, vol. 12, no. 2, pp. 171–195, 2008.

[53] C. A. C. Coello, G. B. Lamont, D. A. Van Veldhuizen, *et al., Evolutionary algorithms for solving multi-objective problems*, vol. 5. Springer, 2007.

[54] P. Street, "Pecan street online database," *Pecan Street: Austin, TX, USA*, 2016.

6 Conclusions and Recommendations

6.1 Introduction

As discussed in Chapter 1, this thesis aims to develop an efficient, sustainable, safe, and economically feasible future smart house capable of supporting the future smart grid. Four key research elements are identified to realize the future smart house namely, (a) choice of system architecture, (b) development of a key power electronic technologies to integrate PV, battery, and grid, (c) integration of safe and efficient electric vehicle (EV) charging, and (d) optimal system sizing design to ensure techno-economic feasibility.

Chapter 2 identifies the functional requirements of a future smart house so that they can act as modules or agents to form a robust, decentralized Smart Grid (SG). Based on those metrics, the existing state of the art AC household architecture is evaluated. A case for DC based distribution is presented as it provides potentially higher energy efficiency due to inherent DC nature of sources like PV, storages like battery, and loads like electronic appliances. Several existing DC based architectures are reviewed in detail based on different functionalities. Finally, a smart power router based centralized nanogrid architecture is proposed.

Chapter 3 details the development of the smart power router introduced in the previous chapter. The multi-active bridge (MAB) converter is chosen as topology to act as the smart power router capable of functions like controlling bi-directional power flow, islanding during abnormal grid conditions, providing high-level energy management, supporting the grid autonomously based on price incentives, etc. Detailed analysis of the power flow coupling challenge in MAB converter is presented. A hardware based solution and a control based solution are introduced to eliminate the interaction between the port controllers. A 2 kW, Si-C device based four port MAB converter laboratory prototype is developed and tested extensively to validate the decoupling control strategies.

Battery-powered electric vehicles (EV) are envisioned to play a significant role in future smart residential grids. Ensuring safe and efficient EV charging integration is crucial for the success of future DC residential nanogrids. To that end, chapter 4 develops a wireless inductive power transfer (IPT) based EV charging station for residential applications. A multi-objective optimization (MOO) framework is developed in this chapter to provide a platform to design efficient, light, and misalignment tolerant

magnetic couplers for IPT based EV charging. The existing state of the art magnetic couplers are quantitatively compared using the developed MOO framework, and their relative advantages and disadvantages are highlighted.

Chapter 5 investigates the techno-economic feasibility of solar photo-voltaic (PV)-battery storage integrated household nanogrid. A multi-objective optimization-based framework is developed to draw simple PV-battery sizing guidelines considering the effect of solar potential, degree of temporal mismatch between load and PV generation, battery degradation, and tariff incentives. Economic metrics like simple payback time are considered to evaluate the economic feasibility of PV-battery powered smart homes. Additionally, the effect of meteorology on the optimal sizing problem is investigated by selecting two case studies in the Netherlands and the US.

6.2 Conclusions

The conclusions drawn from the work presented in the thesis can be grouped into four categories based on the thesis objectives presented in Chapter 1. The objectives are as follows:

1. *What is the optimal architecture for integrating PV, EV, battery, and loads to realize future smart grid-connected residential households?*
2. *How to design and construct key power electronic converter technology to realize a robust, safe, scalable, and reliable household nanogrid?*
3. *How to integrate EV charging in future homes while ensuring user safety and high efficiency?*
4. *What is the techno-economic feasibility of PV-battery integrated smart household nanogrids?*

6.2.1 Choice of smart home architecture

Smart grids need functionally independent households

Developing a universal, robust, efficient, decentralized smart grid requires a modular approach. High energy consuming households would play a significant role as a nanogrid modules. For the successful and sustainable operation of an intelligent grid, future houses and buildings need to be more self-reliant and provide additional functionalities. From a control perspective, household nanogrids need to be stable, able to coordinate between sources, storages and loads, work in islanding mode, and provide grid support based on price signals. Hardware functionalities include high energy efficiency, availability, flexibility, and scalability.

DC is more efficient than AC in grid-independent households

A close inspection of the type of household loads reveals that they are either DC in nature (e.g., LED lighting, smartphones, computers) or has an internal DC link (e.g., washing machines, dishwashers). Further, renewable sources like PV technology and storages like batteries are inherently DC. Therefore,

selecting DC distribution to power household loads locally via solar power generation and battery storage is more energy-efficient than using AC distribution.

Multi-bus DC architecture is required to integrate the power range of household loads

In the last few decades, the variety of household appliances has undergone a significant change with power requirements ranging from few watts (e.g., phone chargers, lighting) to as high as ten kilowatts (e.g., electric vehicle charging). Therefore, multiple DC bus voltages are required to supply power to different load groups to achieve both consumer safety and low distribution losses. Voltage levels between 350 V to 700 V can be used to high power residential EV charging, 300-400 V can be used to power the medium power loads like kitchen and laundry appliances, and 48/60 V can be used to power low power consumer electronics and lighting loads.

Nanogrids with a converter interface is better than nanogrids without one

Interfacing a DC nanogrid with a DC microgrid with a bi-directional converter would reduce energy efficiency for power flows between the microgrid and the nanogrid. However, a converter interfaced nanogrid can provide several functions like dynamic decoupling of the grid, superior grid support, bi-directional fault interruption capability, integrated protection, islanded operating capability, etc. Further, future household nanogrids are expected to be energy independent leading to minimized grid energy exchange. Thus, the advantages of converter interfaced nanogrids in the form of functional capabilities far outweigh the drawbacks due to energy efficiency.

Centralized nanogrid is essential for decentralized smart grid

To realize a stable, robust, flexible, decentralized smart grid, we need to maximize the functional abilities of individual nanogrids. Since nanogrids are inherently small in terms of physical size, a centralized internal architecture improves the overall operational capabilities of the nanogrid without accentuating the inherent drawbacks of a centralized system. Therefore, the smart power router-based DC nanogrid is a promising architecture for future residential households since it exploits the benefits of a centralized system to realize a robust overhead decentralized system.

6.2.2 Smart power router for DC residential nanogrids

Multi-active bridge (MAB) converter is a promising candidate as smart power router

The MAB converter integrates multiple DC sources, storages and loads using inverter bridges connected via a high frequency (HF) multi-winding transformer. Derived from the dual-active bridge (DAB) converter family, the MAB converter not only integrates and exchanges the energy from/to all ports, but also provides full isolation among all ports and matches the different port voltage levels. Additionally, the MAB converter realizes bidirectional power flow by adjusting the phase-shift angle between the high-frequency AC voltages generated by the inverter module at each port.

Inherent power flow coupling in MAB converters hinders scalability

A key challenge in the design and control of the MAB converter is the inherent cross-coupling of power flows between ports due to the inter-winding magnetic coupling of the transformer. Therefore, the MAB converter behaves as a multi-input multi-output (MIMO) system with coupled power loops, which is difficult to control. Existing decoupling strategies are all based on complex control implementation. The complexity of the control increases with the increase of the number of ports. Thus, they inhibit the scalability of the number of ports in MAB converters and reduces their applicability.

Asymmetric distribution of leakage inductances solves the coupling challenge in MAB converters

A modified hardware configuration for a MAB converter with asymmetrical leakage inductance distribution decouples the inter-port power flows. It is based on making a port as master with low leakage inductance (≤ 0.05 pu) act as a rigid-voltage source on the transformer magnetizing inductance while adding external inductors (1 pu) to the rest of the ports. The proposed MAB configuration has inherently magnetically decoupled power flows, enabling the regulation of power flows independently of the different port controller bandwidths. However, the hardware approach increases the switching losses of the master port MOSFETs and makes the multi-winding transformer design challenging.

Active disturbance rejection control (ADRC) provides a decentralized decoupling solution for MAB converters

Conventional decoupling control of MAB converters uses centralized model matrix based approach to decouple the power flows. In this thesis, active-disturbance rejection control (ADRC) based decoupling control is introduced which uses high bandwidth extended state observer (ESO) to observe the cross-coupling disturbance and compensates it in real-time. Thus, ADRC control decouples the power flows in a multi-active bridge (MAB) converter in a decentralized manner using minimal system information. The decentralized nature of the solution allows for scalability of ports without increasing control complexity.

ADRC based control has huge potential in power electronics applications

Traditionally power electronic systems have been controlled by proportional-plus-integral-derivative (PID) controllers due to their simplicity of implementation. However, PID control suffers from certain weaknesses like limited control precision in the presence of large disturbances/uncertainties, sensor noise degradation in the derivative control, etc. In recent times, research in control systems has advanced well beyond PID controllers to solve these problems. Active disturbance rejection control (ADRC) represents a relatively new paradigm to the control of complex systems. It inherits from PID control the qualities that make it such a success: the error-driven, rather than model-based, control law, and augments that with the best offering of modern control theory, the state observer. Together with advances in the computational power of controllers, they form a new set of tools and offer a potentially advantageous technique to obtain outstanding disturbance rejection and robustness performances in power electronic converters.

6.2.3 Residential EV charging intregration

Wireless EV charging is suitable for residential applications

Wireless inductive power transfer (IPT) technology for EV charging is more user-friendly and safe than conventional wired charging due to the absence of electrical or mechanical contacts. Especially in residential applications, wireless charging is a perfect solution as it provides easy, safe, and autonomous charging for low to medium power EVs (3-7 kW). Further, in future EVs are envisioned to be fully autonomous in nature, making a strong case for wireless EV charging for future homes.

IPT system design needs multi-variable multiple-objective optimization framework

The design of the magnetic couplers is crucial for the overall performance of IPT based charging systems. A high number of design variables need to be considered while designing the magnetic couplers. Further, there are multiple performance metrics like power transfer efficiency, cost and weight, misalignment tolerance, and low stray magnetic fields, which are mutually opposing in nature. Therefore, designing IPT systems require a multi-variable multi-objective optimization framework for a holistic design procedure. Parametric studies and simple design thumb rules for magnetic couplers are not adequate to ensure good performance.

Circular magnetic couplers provide the most efficient, cost-effective and safe solution

Considering all the metrics, circular couplers as transmitter/receiver provides a well-rounded performance among the popular magnetic couplers in IPT systems. Circular couplers have the best efficiencies due to high coupling for the same material effort. Additionally, circular couplers emit the lowest stray fields in both vertical and lateral direction for the same current excitation, which ensures safe operation. The misalignment performance of circular couplers is poor, with a rapidly falling coupling co-efficient with increasing misalignment. However, for static EV charging in residential homes, misalignment tolerance is not a priority performance metric. Therefore, the circular coupler is the most efficient, cost-effective, and safe solution for residential IPT based EV charging systems.

6.2.4 Techno-economic feasibility of smart DC homes

Vanadium redox flow batteries will compete with Li-ion batteries in residential storage

Among the battery technologies considered in this study, lithium-ion (Li-ion) battery based household system performs the best in all metrics. However, Li-ion is marginally better in the than vanadium redox flow batteries (VRFB) which suffers from high initial investment cost. As the VRFB technology matures further in future, it will be more competitive with Li-ion economically.

PV system designed for highest annual energy yield is a sub-optimal solution for smart homes

PV systems for residential grids are generally designed for the highest annual energy yield. However, results obtained in this thesis show that a better solution is to develop PV systems to have the highest

temporal match between the annual load profile and the solar generation profile. The higher temporal match comes at the cost of lower energy yield, but it leads to low storage requirements and lower system costs. For example, the azimuth angle (A_m) for the highest solar energy yield in the Netherlands is 185^o. However, given a dutch particular household load profile, the optimal azimuth angle turned out to be in the 200^o-220^o range.

Solar potential in the Netherlands is inadequate to make an average dutch household fully energy independent

It is challenging to achieve full energy autonomy for average dutch households due to the combination of two factors: (a) low solar potential of Netherlands, and (b) temporal mismatch between solar generation profile and energy usage profile. Consequently, sizing PV systems become challenging as during summer, when the solar generation is high, the energy consumption is lowest, and the pattern flips during winter. Therefore, to achieve full energy autonomy in Dutch households, battery-based storage is not sufficient and seasonal storage is required.

Tariffs should incentivize residential users to achieve power autonomy over energy autonomy

The main goal of designing the future smart homes is to make them more self-reliant and independent from the grid. To that end, users should be incentivized to achieve more power autonomy than energy autonomy. Two case studies analyzed in this thesis highlight the difference between the two approaches. The Dutch electricity provider Eneco incentivizes high energy autonomy with net-metering based tariff system. In contrast, the US, Texas tariff system incentivizes high power autonomy, a comparatively more difficult metric to achieve. Results show that the Dutch house nanogrid interacts heavily with the utility grid throughout the year, which results in low power autonomy. During winter, when the solar generation is small, and the load requirement is high, it depends solely on the grid to supply it. However, during the summer days when the load is comparatively lighter, and solar power is higher, the microgrid consistently dumps the excess solar energy to the utility grid. Therefore, the dutch household is highly energy-positive during the winter and highly energy-negative during the summer days, which eventually balances out due to the electricity tariff's sole dependence on energy autonomy rather than power autonomy. However, the US household has weaker interaction with the grid as the Texas electricity tariff incentivizes power autonomy, which leads to less dumping of solar power in the grid.

Thumb rules for PV-battery system sizing for Netherlands and Texas, US

In this thesis, simple thumb rules detailed for PV-battery system sizing are derived after extensive analysis of optimization results. A new metric called "storage hour" (S_h) is introduced, which is the ratio of the battery capacity to the peak PV power rating. Storage hour represents the optimal sizing of the battery capacity relative to the rated PV power to maximize the battery's utilization. The optimal value of storage hour for Cabauw, NL is between 2 to 4. In contrast, Austin, Texas, which has a 35 % higher solar yield than Cabauw, leads to an optimal storage hour between 4 to 6.

6.3 Thesis Contributions

The main scientific contributions of this thesis are summarized below:

- **Centralized nanogrids for decentralized smart DC grids:** Significant research has already been published regarding DC nanogrid architectures. However, most research focuses on the voltage levels and voltage polarity while assuming an AC utility grid. In this thesis, we step further towards envisioning DC nanogrid architectures within a universal DC smart grid. This thesis proposes a smart power router-based centralized DC nanogrid to exploit the advantages of a centralized system to realize a strong, robust decentralized smart grid.
- **Solving coupling problem of MAB converters:** A multi-active bridge (MAB) converter is used in this thesis for integrating PV system, battery, utility grid, and the household DC bus. A MAB converter in itself is not new, but this thesis, two new methods to solve the coupling problem inherent to MAB converters are proposed. The proposed decoupling strategies can be implemented with decentralized controllers, improving the scalability and applicability of MAB converters.
- **Holistic comparison of wireless magnetic couplers:** A comparison of different magnetic couplers for IPT systems can be found in the literature. However, most comparison research does not take into account misalignment tolerance as a performance factor. Additionally, the comparative framework used in those papers does not consider optimized designs, making it an unfair comparison. In this thesis, a holistic comparison of five magnetic couplers is presented considering multiple performance factors and optimized designs, revealing the relative strengths and weaknesses of different couplers. IPT design engineers can use the above information to select the optimal coupler topology during the initial design phase.
- **Derive simple thumb rules for system sizing:** Optimal system sizing is a complex mathematical problem as it is dependent on multiple variables and have to satisfy mutually competing objectives. Most PV-battery system sizing papers in scientific literature use methodologies are single-objective. Further, they do not take into account all the above design complexities. Therefore, the obtained results are case-specific and not very re-usable for system design engineers. This thesis proposes multi-objective optimization-based design methodology incorporating design depth in battery degradation, PV system alignment, electricity tariffs, etc. Extensive analysis of the obtained results reveals underlying trends used to derive simple generic thumb rules for system design that are readily usable by system engineers.

6.4 Recommendations for future research

The following recommendations for future research can be made: Regarding the design of multi-active bridge (MAB) converters as smart-power-router:

- ***Plug and play scalable MAB converter modules:***
  Multi-active bridge (MAB) converter based centralized nanogrid architecture is not easily scalable. The hardware-based decoupling approach proposed in this thesis solves the main obstacle

towards making MAB converters scalable in terms of the number of ports and power transfer capability. To that end, the design of a modular multi-active bridge (MMAB) converter with scalable modules with plug and play capability can be an exciting direction for future research. MMAB converter can be the AC backbone for future DC homes combining the plug and play capability of AC due to natural zero-crossing and the energy efficiency of DC.

- ***Develop modulation techniques to achieve soft-switching and higher efficiencies:***
  Traditionally, determining the soft-switching conditions of MAB converter ports is difficult as the inductor current shape of one port is dependent on the phase shifts of other ports. The hardware decoupling strategy of MAB converters magnetically decouples the ports from each other, resulting in a parallel combination of multiple dual active bridge (DAB) converters. Consequently, the waveform of the transformer winding currents of individual ports becomes independent of the ports' phase shifts. Therefore, independent decentralized modulation techniques to achieve soft-switching for each MAB port are easier to develop. Eliminating switching losses would lead to even higher efficiencies and allows the increase of switching frequency resulting in high power density and low-cost MAB converters.

Regarding the integration of wireless EV charging technology in smart homes:

- ***Space mapping technique to reduce optimization times:***
  Modeling the electromagnetic behavior of inductive power transfer (IPT) couplers is critical in designing highly efficient and safe IPT systems. Traditionally, numerical 3D models are used to model IPT couplers, which are accurate but computationally expensive. Axial symmetries of couplers are exploited to reduce the computational load to limited success. Therefore, research can be conducted towards using mathematical tools like space mapping technique to achieve a satisfactory optimal solution with a minimal number of computationally expensive "fine" model evaluations.

- ***Investigate inter-operability of different magnetic couplers:***
  Different types of couplers are proposed for IPT based EV charging. Detailed analysis of optimized couplers has shown that there is no single coupler topology, which is the objectively best in all performance metrics. For example, unipolar couplers like circular have the highest efficiencies for the same material effort while bi-polar coupler BPP has a high tolerance to misalignment. Due to a lack of standardization, it can be assumed different manufacturers can select different coupler topologies. Therefore, studying the interoperability of different coil combinations is essential.

Regarding the PV-battery system sizing for smart homes:

- ***Incorporate load-pv forecasting based intelligent power management algorithms:***
  A simple rule-based power management algorithm is used in this thesis to size the PV-battery system for smart homes optimally. A more intelligent algorithm that takes into account load and PV forecasting can lead to better utilization of battery and PV systems, which can reduce the storage size and thereby system cost.

- ***Study the effect of smart EV charging on optimal system sizing:***
  In this thesis, the electric vehicle (EV) is assumed to be a dumb load similar to the other household appliances. Incorporating smart charging of the EV with possible bi-directional vehicle to home (V2H) and vehicle to grid (V2G) services can positively reduce the storage requirements of the household leading to overall cost reduction.

A Discrete Time ADRC

A.1 Extended state observer (ESO) digital implementation

The decoupling performance of ADRC based controller in MAB converters is shown in simulation studies in continuous time domain. For practical implementation on the microcontroller, a discrete time ADRC formulation is constructed to observe all the relevant dynamics. The standard approach of discretizing the extended state observer is:

$$\hat{x}(k+1) = \mathbf{A}_\mathrm{d} \cdot \hat{x}(k) + \mathbf{B}_\mathrm{d}\, u(k) + \mathbf{L} \cdot [y(k) - \mathbf{C}_\mathrm{d} \hat{x}(k)] \tag{A.1}$$

where $\mathbf{A}_\mathrm{d}$, $\mathbf{B}_\mathrm{d}$ and $\mathbf{C}_\mathrm{d}$ are the discrete-time versions of the state-space model matrices in equation (3.32) which can be obtained by Euler's method of discretization [**?**]:

$$A_\mathrm{d} = I_i + \sum_{i=1}^{\infty} \frac{A^i \cdot T_s^i}{i!}, \quad B_\mathrm{d} = \sum_{i=1}^{\infty} \frac{A^{i-1} \cdot T_s^i}{i!} \cdot B, \quad C_\mathrm{d} = C, \quad D_\mathrm{d} = D \tag{A.2}$$

where T_s is the sampling time of the controller, i is the order of the system, and I_i is identity matrix of i-th order.

For the first-order plant, the discrete state-space matrcies can be presented as follows:

$$A_\mathrm{d} = \begin{bmatrix} 1 & T_\mathrm{s} \\ 0 & 1 \end{bmatrix}, \quad B_\mathrm{d} = \begin{bmatrix} b_0.T_\mathrm{s} \\ 0 \end{bmatrix}, \quad C_\mathrm{d} = [1 \quad 0], \quad D_\mathrm{d} = 0 \tag{A.3}$$

For the second-order plant, the discrete state-space matrcies can be presented as follows:

$$A_\mathrm{d} = \begin{bmatrix} 1 & T_\mathrm{s} & \frac{T_s^2}{2} \\ 0 & 1 & T_\mathrm{s} \\ 0 & 0 & 1 \end{bmatrix}, \quad B_\mathrm{d} = \begin{bmatrix} b_0.\frac{T_s^2}{2} \\ b_0.T_\mathrm{s} \\ 0 \end{bmatrix}, \quad C_\mathrm{d} = [1 \quad 0 \quad 0], \quad D_\mathrm{d} = 0 \tag{A.4}$$

The discrete observer described by equation (A.1) is known as the "prediction observer" since it predicts the state values at the subsequent time step $\hat{x}(k+1)$ using the current measurement $y(k)$. This approach is known to have performance issues as there are time delays introduced in the control loop since

$\hat{x}(k)$ does not depend on current measurement $y(k)$. To improve the performance of the observer, a "filtered" or "current" state observer is built based on the two steps. First, the prediction step:

$$\hat{x}(k+1|k) = \mathbf{A}_\mathrm{d} \cdot \hat{x}(k|k) + \mathbf{B}_\mathrm{d} \cdot \hat{u}(k) \qquad \text{(Prediction)} \tag{A.5}$$

which predicts $\hat{x}(k+1|k)$ based on measurements of previous time step k. Then, the following correction step is used to obtain the final estimate $\hat{x}(k+1|k+1)$ based on most recent measurement $y(k+1)$:

$$\hat{x}(k+1|k+1) = \hat{x}(k+1|k) + \mathbf{L} \cdot [y(k+1) - \mathbf{C}_\mathrm{d}\hat{x}(k+1|k)] \qquad \text{(Correction)} \tag{A.6}$$

If he prediction output is fed into the correction equation and renaming $\hat{x}(k+1|k+1) = \hat{x}(k+1)$, one update equation for the observer is obtained:

$$\hat{x}(k+1) = \mathbf{A}_\mathrm{ESO} \cdot \hat{x}(k) + \mathbf{B}_\mathrm{ESO} \cdot \hat{u}(k) + \mathbf{L}_\mathrm{ESO} \cdot \hat{y}(k) \tag{A.7}$$

where the ESO terms are as follows:

$$\mathbf{A}_\mathrm{ESO} = (\mathbf{A}_\mathrm{d} - \mathbf{L} \cdot \mathbf{C}_\mathrm{d} \cdot \mathbf{A}_\mathrm{d}), \qquad \mathbf{B}_\mathrm{ESO} = (\mathbf{B}_\mathrm{d} - \mathbf{L} \cdot \mathbf{C}_\mathrm{d} \cdot \mathbf{B}_\mathrm{d}), \qquad \mathbf{L}_\mathrm{ESO} = \mathbf{L} \tag{A.8}$$

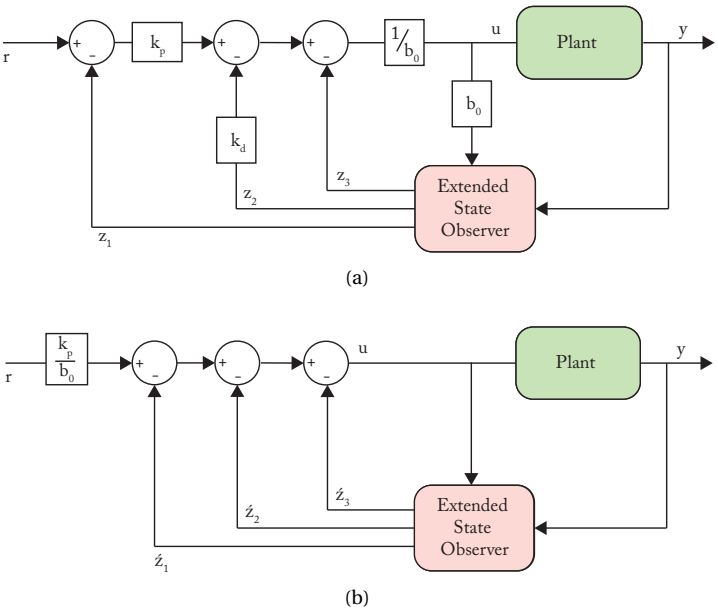

Figure A.1: (a) Conventional control structure of second order ADRC controller, (b) control loop with modified ADRC structure and transformed state variables $\acute{z}$ resulting in lower computation load.

A.2 Optimized low latency ADRC implementation

In a practical discrete-time implementation, the lag between sensor input and controller output should be as small as possible, which means that one should try to reduce the computational effort for a controller. Due to the observer-based approach, ADRC has a much bigger computational footprint than a classical PI type controller. Therefore, it is important to reduce the computational footprint of the observer on the micro-controller. Failure to do so might result in the crash of the controller as the sensor updates the new value of the measurement by the time the controller has generated a control action. Additionally, the variable values generated by the higer order state observers can have high data storage requirements which might also overload the micro-controller and affect its performance.

Figure A.1a shows the conventional second-order ADRC structure with controller gains. The controller structure can be simplified by scaling the outputs of the observers so that the multiplications by K_p, K_d and b_0 can be eliminated. Therefore, the overall latency due to coumputaional requirements is reduced. The new transformed state variables can be represented as the following depending on the plant order:

$$\acute{z}_1 = \frac{K_\mathrm{p}}{b_0} z_1, \qquad \acute{z}_2 = \frac{1}{b_0} z_2 \qquad \text{(First order ADRC)} \tag{A.9}$$

$$\acute{z}_1 = \frac{K_\mathrm{p}}{b_0} \acute{z}_1, \qquad z_2 = \frac{K_\mathrm{d}}{b_0} \acute{z}_2, \qquad \acute{z}_3 = \frac{1}{b_0} z_3 \qquad \text{(Second order ADRC)} \tag{A.10}$$

The controller structure of the modified ADRC is shown in Figure A.1b. The variable transformation matrix used to transform the old state variables z to the new state variables is represented as:

$$T = \frac{1}{b_0} \begin{bmatrix} K_\mathrm{p} & 0 \\ 0 & 1 \end{bmatrix}, \quad \text{(First order ADRC)} \tag{A.11}$$

$$T = \frac{1}{b_0} \begin{bmatrix} K_\mathrm{p} & 0 & 0 \\ 0 & K_\mathrm{d} & 0 \\ 0 & 0 & 1 \end{bmatrix}, \quad \text{(Second order ADRC)} \tag{A.12}$$

Using this transformation matrix T, the new state space equations of the optimized ESO can be obtained:

$$\acute{\mathbf{A}}_\mathrm{ESO} = T \cdot \mathbf{A}_\mathrm{ESO} \cdot T^{-1}, \qquad \acute{\mathbf{B}}_\mathrm{ESO} = T \cdot \mathbf{B}_\mathrm{ESO}, \qquad \acute{\mathbf{L}}_\mathrm{ESO} = T \cdot \mathbf{L}_\mathrm{ESO} \tag{A.13}$$

B Li-ion battery degradation model

The main goal of this modelling process is to estimate the lifetime as a function of the operating conditions associated with the application:

$$L_{\text{batt}} = f(\text{SoC}, \text{DoD}, C_{\text{tot}}) \tag{B.1}$$

where C_{tot} is the total Ah processed by the battery in that load cycle. It has been pointed out in [**?**] that SoC and DoD data of a load cycle is not sufficient to model capacity fading. To that end, instead of initial SoC and DoD of a battery, the terms SoC_{avg} and SoC_{dev} are introduced:

$$\text{SoC}_{\text{avg}} = \frac{1}{\Delta t_n} \sum_{t_{n-1}}^{t_n} \text{SoC}(t)\,dt \tag{B.2}$$

$$\text{SoC}_{\text{dev}} = 2\sqrt{\frac{3}{\Delta t_n} \sum_{t_{n-1}}^{t_n} (\text{SoC}(t) - \text{SoC}_{\text{avg}})^2\,dt} \tag{B.3}$$

where Δt_n is the time-period of individual timeslots. SoC_{dev} is the normalized standard deviation from SoC_{avg}. For example, a battery with an initial SoC of 100% cycled with 100% DoD corresponds to 50% SoC_{avg} with 50% SoC_{dev}.

The rate of capacity fading (ξ) is dependent on an exponential function consisting of SoC_{avg} and SoC_{dev}. The empirical equation provided in [**?**] is shown below:

$$\delta\xi(\text{SoC}_{\text{avg}}, \text{SoC}_{\text{dev}}) = k_1 \text{SoC}_{\text{dev}}.e^{k_2.\text{SoC}_{\text{avg}}} + k_3 e^{k_4.\text{SoC}_{\text{dev}}} \tag{B.4}$$

where constants $k_1 - k_4$ are obtained by curve fitting techniques on experimental data on $LiFePO_4$

Table B.1: Capacity fading model parameters

k_1	-4.092e-4	k_3	1.408e-5
k_2	-2.167	k_4	6.130

cells(Table B.1) The unit of capacity fading rate ($\delta\xi$) is Ah faded per Ah processed. For a particular cycle, the values of SoC_{avg} and SoC_{dev} determine the fading rate $\delta\xi$ and coupled with the Ah processed

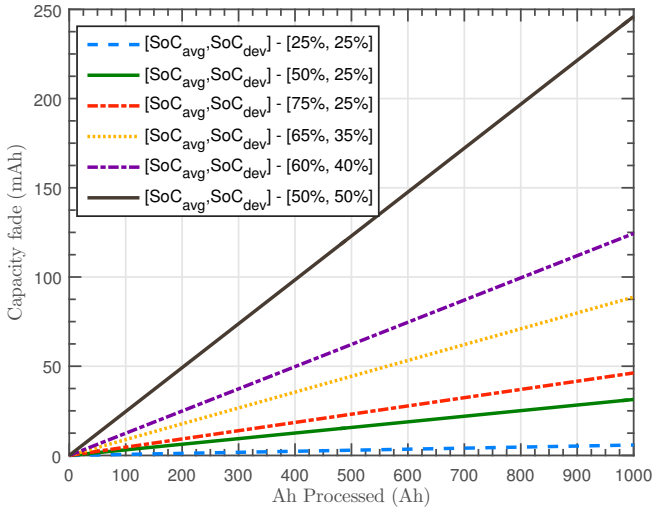

Figure B.1: Rate of capacity fading of a lithium-ion battery with Ah processed at different battery cycle characteristics based on empirical model developed in *Lam et al.*

in that cycle gives the total capacity fade in that particular cycle. Therefore, in case of nanogrid storage applications, the total capacity fade (ξ) after n cycles would be:

$$\xi = \sum_{i=1}^{n} \delta\xi = \sum_{i=1}^{n} (k_1 \mathrm{SoC}_{\mathrm{dev,i}}.e^{k_2.\mathrm{SoC}_{\mathrm{avg,i}}} + k_3 e^{k_4.\mathrm{SoC}_{\mathrm{dev,i}}}) Ah_i \tag{B.5}$$

Figure B.1 illustrates the effect of operating conditions like SoC_{avg} and SoC_{dev} on battery capacity fading rate. It can be seen from the plot that battery cycles with similar SoC_{dev} or DoD degrades the battery faster if the SoC_{avg} of the cycle is higher.

List of publications

Publications related to thesis

Journal papers

1. S. Bandyopadhyay, P. Purgat, Z. Qin and P. Bauer, "A Multiactive Bridge Converter With Inherently Decoupled Power Flows," in IEEE Transactions on Power Electronics, vol. 36, no. 2, pp. 2231-2245, Feb. 2021.

2. S. Bandyopadhyay, Z. Qin and P. Bauer, "Decoupling Control of Multi-Active Bridge Converters using Linear Active Disturbance Rejection," in IEEE Transactions on Industrial Electronics, Early access.

3. S. Bandyopadhyay, P. Venugopal, J. Dong and P. Bauer, "Comparison of Magnetic Couplers for IPT-Based EV Charging Using Multi-Objective Optimization," in IEEE Transactions on Vehicular Technology, vol. 68, no. 6, pp. 5416-5429, June 2019.

4. S. Bandyopadhyay, G. R. C. Mouli, Z. Qin, L. R. Elizondo and P. Bauer, "Techno-Economical Model Based Optimal Sizing of PV-Battery Systems for Microgrids," in IEEE Transactions on Sustainable Energy, vol. 11, no. 3, pp. 1657-1668, July 2020.

Conference papers

1. S. Bandyopadhyay, V. Prasanth, P. Bauer and J. A. Ferreira, "Multi-objective optimisation of a 1-kW wireless IPT systems for charging of electric vehicles," IEEE Transportation Electrification Conference and Expo (ITEC), Dearborn, MI, USA, 2016, pp. 1-7.

2. S. Bandyopadhyay, V. Prasanth, L. R. Elizondo and P. Bauer, "Design considerations for a misalignment tolerant wireless inductive power system for electric vehicle (EV) charging," 19th European Conference on Power Electronics and Applications (EPE'17 ECCE Europe), Warsaw, 2017, pp. P.1-P.10.

3. S. Bandyopadhyay, Z. Qin, L. Ramirez-Elizondo and P. Bauer, "Comparison of Battery Technologies for DC Microgrids with Integrated PV," IEEE Third International Conference on DC Microgrids (ICDCM), Matsue, Japan, 2019, pp. 1-9.

4. S. Bandyopadhyay, V. Prasanth, L. R. Elizondo and P. Bauer, "Design considerations for a misalignment tolerant wireless inductive power system for electric vehicle (EV) charging," 19th European Conference on Power Electronics and Applications (EPE'17 ECCE Europe), Warsaw, 2017, pp. P.1-P.10.

5. S. Bandyopadhyay, J. Dong, Z. Qin and P. Bauer, "Comparison of Optimized Chargepads for Wireless EV Charging Application," 10th International Conference on Power Electronics and ECCE Asia (ICPE 2019 - ECCE Asia), Busan, Korea (South), 2019, pp. 1-8.

6. S. Bandyopadhyay, J. Dong, L. Ramirez-Elizondo and P. Bauer, "Determining Relation Between Size of Polarized Inductive Couplers and Nominal Airgap," IEEE 18th International Power Electronics and Motion Control Conference (PEMC), Budapest, Hungary, 2018, pp. 248-255.

Publications collaborative projects

Journal papers

1. P. Purgat, S. Bandyopadhyay, Z. Qin and P. Bauer, "Zero Voltage Switching Criteria of Triple Active Bridge Converter," in IEEE Transactions on Power Electronics, vol. 36, no. 5, pp. 5425-5439, May 2021.

2. A. Shekhar, L. Ramírez-Elizondo, S. Bandyopadhyay, L. Mackay and P. Bauera, "Detection of Series Arcs Using Load Side Voltage Drop for Protection of Low Voltage DC Systems," in IEEE Transactions on Smart Grid, vol. 9, no. 6, pp. 6288-6297, Nov. 2018.

3. Venugopal, P.; Bandyopadhyay, S.; Bauer, P.; Ferreira, J.A. A Generic Matrix Method to Model the Magnetics of Multi-Coil Air-Cored Inductive Power Transfer Systems. Energies 2017, 10, 774.

Conference papers

1. V. Prasanth, S. Bandyopadhyay, P. Bauer and J. A. Ferreira, "Analysis and comparison of multi-coil inductive power transfer systems," IEEE International Power Electronics and Motion Control Conference (PEMC), Varna, Bulgaria, 2016, pp. 993-999.

2. E. L. Bianchi, H. Polinder and S. Bandyopadhyay, "Energy consumption of electric powertrain architectures: A comparative study," 19th European Conference on Power Electronics and Applications (EPE'17 ECCE Europe), Warsaw, 2017, pp. P.1-P.10.

3. P. Purgat, S. Bandyopadhyay, Z. Qin and P. Bauer, "Continuous Full Order Model of Triple Active Bridge Converter," 21st European Conference on Power Electronics and Applications (EPE '19 ECCE Europe), Genova, Italy, 2019, pp. P.1-P.9.

4. P. Purgat, S. Bandyopadhyay, Z. Qin and P. Bauer, "Power Flow Decoupling Controller for Triple Active Bridge Based on Fourier Decomposition of Transformer Currents," IEEE Applied Power Electronics Conference and Exposition (APEC), New Orleans, LA, USA, 2020, pp. 1201-1208.

5. W. Shi, J. Dong, S. Bandyopadhyay, F. Grazian, T. B. Soeiro and P. Bauer, "Comparative Study of Foreign Object and Misalignment in Inductive Power Transfer Systems," IECON - 45th Annual Conference of the IEEE Industrial Electronics Society, Lisbon, Portugal, 2019, pp. 2634-2639.

Patent

1. V. Prasanth, S. Bandyopadhyay, and P. Bauer, "Electrically driven vehicle, an inductive vehicle charging system and a method for wireless inductive charging," WO2019013626A1, 2018.
2. S. Bandyopadhyay, "Seamless integration of PV into any Electric vehicle," (patent submitted)

Acknowledgements

As one famous scientist has noted, it is a lot better to have written a thesis than actually to write one. Writing a thesis requires a significant amount of patience, discipline, and organization, virtues nobody can accuse me of. Therefore, I was highly dependent on many others who had these qualities in great measure and whose wisdom and unwavering support helped shape this thesis in many big and small ways. I want to thank and acknowledge these people in the following.

To begin with, I am deeply thankful for my promotor, Professor Pavol Bauer, first for fiving me the opportunity to join the DCE&S group as a researcher and later as a PhD. He has been an excellent promotor, providing a lot of research independence and support, both technical and personal. He has been receptive and open to ideas and gave the right motivation during the 'not-so-productive' stages of the research. Overall, he cared for his students, which helped me finish the work in time while enjoying it fully. I also thank all the participants and partners in the Smart Energy Management and Services in Buildings and Grids (SES-BE) project. I learned a lot during the bi-annual meetings from diverse disciplines within the project. I would especially like to thank the program leaders, Prof. dr. Madeleine Gibescu and Dr. Phuong Nguyen who were very supportive of our work.

Sometimes despite your best efforts in life, luck always plays a huge role in the outcome. I was fortunate to have Dr Zian Qin as my supervisor and co-promotor. I have learnt a lot from you, both technically and philosophically. Your approach and focus on the quality of research rather than quantity helped me enjoy research for what it is, an adventure. You were always there to help, be it answering queries or help out with experiments or improve manuscripts. Without your patience, knowledge, and dedication, it would be hard to imagine the outcome of this thesis. Thank you for being the supervisor every PhD student dreams of having.

All the countless hours in the lab won't be possible without the help and support of the lab managers. Bart Roodenburg, I want to thank you for making it easy for us in the lab with your support and technical knowledge nicely topped with dark humour. Joris Koeners, there was never a dull moment with you in the room. Thank you for all the discussions ranging from philosophy to Ajax. Harrie Olsthoorn, thank you for all the support you provided with your diverse electrical and mechanical engineering skills. A special thanks to Radek to arrange and organize the laboratories, especially during the tough times of the pandemic.

Sharmila Rattansingh, the DCE&S corridor would have been a sad place to work without your ever

cheerful and jolly presence. Thank you for always entertaining my endless administrative requests with a big smile. You glued the whole place together by arranging all the group events and your kindness. However, I have to say that I disapprove of your choice of beer. Radler is not beer, Sharmila!

During my tenure in the DCE&S group, I had the privilege to work with and learn from the best researchers in the field of electrical engineering. Jianning Dong, thank you for your humility, kindness and wisdom. It was fun discussing and listening to Mongolian rock with you. Thiago Batista Soeiro, I want to thank you for your help and immense technical expertise you were always happy to share. I learnt a lot from your 'no-nonsense' approach to problem-solving. I wish to thank Laura Ramirez-Elizondo for taking me on board for the SES-BE project. Mohamad Ghaffarian Niasar, I always enjoyed the spontaneous discussions about FEM modelling of wireless transmitters. Henk Polinder, thank you for laying down the building blocks for me to be a researcher. You helped me learn the advantage of being dispassionate about the scientific outcome and focus on enjoying the journey itself. Finally, I want to thank Prof.dr.ir. Braham Ferreira for being an inspiration for all young researchers like me.

Contrary to popular belief, the PhD journey is not a solo one. You learn and grow significantly more as a person when you are with fellow travellers, friends and colleagues. Udai, you were an integral part of the best years of my time in Delft. Thank you for being the anchor in literally all the trips to Locus, dinners, movies; we went together as a group. Your sense of fairness, selflessness, and camaraderie is enviable. Pavel Purgat, we started the journey together. You have been a part of all the good memories in between; Japan, Slovakia ski-trip, India, and countless trips to Locus Publicus. Thank you for your kindness and patience. You made the group bigger than the sum of its parts. Nils van der Blij, I have enjoyed our discussions and arguments in the coffee room. You always made sure that everyone in the group participates together during lunches or football matches. Most importantly, it was really fun working with you. Gautham, I learnt a lot from your equanimous, analytical and balanced approach towards life in general. I had an amazing time travelling with you: be it in Michigan or Japan. Prasanth, I want to thank you for being a mentor and friend since my days as a master student. Your love for teaching and patience for students (even the crazy ones) is commendable. Faisal, thank you for your companionship and, more importantly, for the fingerlicious lamb yakhni. Laurens, thank you for opening the world of dc for us. Your passion for technology and entrepreneurship is second to none. Mladen, you are an amazing team player and an excellent fellow traveller. However, I want to take this opportunity to ask you to not get your daily news from Russian Wikipedia. It is bad for health. Ilija, we shared an office in the last year of your stay in Delft. Every day was entertaining with you, be it your rants about master students or academia in general. There was not a single dull moment with you. Tsegay, I enjoyed your company and our discussions about the political history and future of Africa. Minos Kontos Epi (insert long name), I enjoyed our time in Delft, be it playing mini-basketball during office hours or revelling in schadenfreude when you wallowed in sadness watching Manchester United play football. Guillermo, memo, you are the only one fixed from my master' years to the end of my PhD. I enjoyed your free spirit and optimistic view of life. Aditya, thank you for being the real-life "Dwight Schrute" of our group. It was always entertaining waiting for the next faux pas you would commit non-intentionally or sometimes intentionally. Victor, thank you for your calm presence and rare but witty humour. It was really fun playing football with you. Nishant, thank you for always eager to share your knowledge of Japanese culture and chess. Lucia, thank you for bringing fresh energy to the group. Those frantic escape rooms were one of the premium highlights of my experience in Delft. Ibrahim, it was really fun working with you, and your dedication to learning hardcore electrical engineering

coming from a mechanical background was inspiring. Wiljan, your enthusiasm and independent way of thinking was inspiring. It was a pleasure working with you on the wireless project. Foremost, I am delighted that Lucia, Ibrahim, and Wiljan joined as PhDs after their master's collaboration with me. Yunhe and Junzhong, I enjoyed sharing the office with you both in the last two years of my thesis. You were kind and helpful. Marco, thank you for being the only football fan in the group after the departure of Minos. Francesca and Wenli, I want to thank you both for holding the flag of wireless research high and flying in the group. Dhanashree, it was always fun doing our experiments together in the laboratory. Christi, thank you for your kindness and humility; I am sad to see you go. Farshid, I thoroughly enjoyed our duels on the football field. I wish I had the same level of skill and technique as yours. When my time at Delft was coming to an end, Sachin, Dingsihao, and Yang started their journey. Your drive and enthusiasm reminded me of my experience during my initial years. A special thank goes to the high-voltage part of our group - Alessandro, Luis, and Djurre for being on the football pitch playing together and in drinks afterwards.

I had the opportunity to meet some amazing people in my life outside the university. Siddarth, dada, what would the Delft experience be without your Awadhi biriyani and watching cringe movies like 'Genius' together with Udai. I enjoyed and learned so much with you: philosophy, art, literature. My life during my masters would not be memorable without the presence of several people. I want to thank Avinash, Jaggu, Debu, Harsha, Murugan, Anil, Benjamin, Shreya, Nefeli, and George. I had so many lovely evenings cooking together, eating together, and put doing stupid things together in Marcushof and Roland Holstlaan. I will never forget those good moments we shared. I would also like to thank the members of our drama and culture club "Thespians"; Pritam da, Sanghamitra di, Sanchita di, Arijit da, Som di, Sankha da, Debashish da. You all provided the comfort and company of home in a distant land. For that, I will be forever in debt to you. One of the best experiences in Europe is meeting the amazing family of Lin, Orla, Lasse, and Benthe. Thank you for your kindness in welcoming us as one of your own and making us feel at home in Copenhagen. Orla, even though you are almost as old as a dinosaur, you are still my young friend, and I cannot wait to beat you in the next championship round of 'Settlers of Catan'. I would also like to thank Franz Bahner for his company and amazing sense of humour. It was a beautiful experience of visiting parents in Kierspe during Christmas 2018. Finally, I want to thank my oldest friends from my boarding school: Dr. B (Aritra), Mankin, Som, Arnab, Buddha. We have been through all the ups and downs of life together from a very tender age. It looks like we are destined to do this forever.

I want to thank my *Ma* and *Baba* for being there for me my whole life. Thank you, Ma, for teaching me the courage to stand up for what is right and the determination to see it through. Thank you, Baba, for your eternal calmness and kindness. I also would like to thank Lakshmi mashi and Netai mama for your unconditional love and support. I thank my sister, Anisha, for her love, support and companionship. You all form the core value system which makes me what I am today. I also want to thank my parents-in-law, Dalia and Kishore and my sister-in-law Chandrima for caring for me like their own son, and brother, respectively. Talking about family, Souvik, I want to thank you for being the brother I never had. You are the kind of friend who might not show up for the best days but will definitely show up to help during the worst ones.

Finally, I would like to thank my wife and best friend, Tulika, for being the rock for me during this journey. One paragraph is not enough for me to express what you mean for my life. It has been a long 13

years together, most of which in different countries. You have sacrificed a lot for this. You were always there to listen to me complaining about rejected papers, failed lab experiments, and politics. You lifted my spirits by saying, "this too shall pass" during the darkest days and made me soldier on. You were my biggest fan and critic. Thank you for making me a better and happier person. Now, I cannot wait to spend the rest of my life with you.

Delft, 12 January 2021 S. Bandyopadhyay.

Biography

Soumya Bandyopadhyay was born in Bankura, India, in 1989. He pursued his Bachelors in Electrical Engineering and went on to work as an Executive engineer at SIEMENS, India, from 2011 to 2013.

He received the MSc degree in Electrical Power Engineering in 2015 and from June 2016 he pursued a PhD degree on power electronics development for future DC smart homes at the Delft University of Technology, Delft, The Netherlands. His research interests include design and control of multiport DC–DC converter design for renewable sources and storages, smart charging of electric vehicles, and multiobjective design optimization of wireless power transfer systems.